

# Analysis Note of the Experiment

## Supplementary note on diffractive analyses of 2015 proton-proton data:

- [1] Measurement of diffractive Central Exclusive Production of  $h\bar{h}$  pairs ( $h = \pi, K, p$ ) in proton-proton collisions at  $\sqrt{s} = 200$  GeV with forward proton reconstruction in Roman Pot detectors
- [2] Measurement of particle production in diffractive proton-proton interactions at  $\sqrt{s} = 200$  GeV with forward proton reconstruction in Roman Pot detectors

Leszek Adamczyk , Łukasz Fulek , and Rafał Sikora

*AGH University of Science and Technology, FPACS, Kraków, Poland*

January 18, 2019

### Abstract

In this note we present supplementary material related to analyses of diffractive processes based on 2015 data from proton-proton collisions at  $\sqrt{s} = 200$  GeV. This dataset was collected with newly installed Roman Pot detectors in Phase II\* configuration which ensured efficient triggering and measuring diffractively scattered protons.

We focus on issues which are common in aforementioned analyses: calculation of efficiencies, corrections to Monte Carlo simulations and derivation of systematic uncertainties of our measurements.

ver. 0.99

# Contents

<b>List of contributions</b>	<b>4</b>
<b>Change log</b>	<b>4</b>
<b>1 Bad run list</b>	<b>5</b>
<b>2 TPC/TOF track and event selection</b>	<b>6</b>
2.1 TPC vertex selection (event selection) . . . . .	6
2.2 TPC track selection . . . . .	6
2.2.1 Quality cuts . . . . .	6
2.2.2 TOF hit matching . . . . .	6
2.2.3 Vertex matching quality . . . . .	6
2.3 Fiducial region of the measurement . . . . .	6
<b>3 Efficiencies</b>	<b>7</b>
3.1 General overview . . . . .	7
3.2 TPC track acceptance and reconstruction efficiency . . . . .	7
3.2.1 STAR nominal method . . . . .	7
3.2.1.1 Global track to true level particle matching . . . . .	7
3.2.2 Method used in this analysis . . . . .	9
3.2.3 Sample of efficiency plots . . . . .	13
3.3 TOF acceptance, hit reconstruction and track matching efficiency . . . . .	14
3.3.1 Sample of efficiency plots . . . . .	14
<b>4 Corrections to efficiencies</b>	<b>16</b>
4.1 Data driven corrections to TOF efficiency . . . . .	16
4.2 Data driven corrections to RP efficiency . . . . .	21
<b>5 Energy Loss Correction</b>	<b>22</b>
<b>6 Forward protons</b>	<b>23</b>
6.1 Detector layout . . . . .	23
6.2 Roman Pot data reconstruction . . . . .	23
6.2.1 Roman Pot track points and tracks . . . . .	23
6.2.2 Alignment . . . . .	24
6.3 Roman Pot simulation . . . . .	25
6.3.1 General description . . . . .	25
6.3.2 Detector model . . . . .	26
6.3.3 Aperture tuning . . . . .	26
6.3.4 Embedding technique . . . . .	28
<b>7 dE/dx adjustment</b>	<b>29</b>
<b>8 TPC track pointing resolution adjustment</b>	<b>33</b>
<b>9 Dead material in front of TPC</b>	<b>36</b>

<b>10 Systematic uncertainties</b>	<b>42</b>
10.1 TPC track reconstruction efficiency . . . . .	42
10.1.1 Pile-up effect . . . . .	42
10.1.2 Dead material effect on TPC track reconstruction efficiency . . . . .	46
10.2 TOF matching efficiency . . . . .	48
10.2.1 Embedding (pile-up) effect . . . . .	48
10.2.2 TOF system simulation accuracy . . . . .	49
10.3 Roman Pot track reconstruction efficiency . . . . .	52
10.3.1 Track reconstruction efficiency (absolute reconstruction efficiency) . . . . .	52
10.3.2 Track point reconstruction efficiency (relative reconstruction efficiency) . . . . .	55
10.4 Summary of the systematic uncertainties of efficiencies . . . . .	59
<b>Appendix A TPC track reconstruction efficiency</b>	<b>60</b>
<b>Appendix B TOF hit reconstruction and matching efficiency</b>	<b>85</b>
<b>Appendix C Energy Loss Correction</b>	<b>98</b>
<b>Appendix D Apertures tuning in Geant4 simulation</b>	<b>111</b>
<b>Appendix E Dead material effect on TPC track reconstruction efficiency</b>	<b>113</b>
<b>Appendix F Fits to <math>dE/dx</math> spectra, comparison of <math>dE/dx</math> and <math>n_X^\sigma</math> between data and MC</b>	<b>122</b>
<b>Appendix G Tag&amp;Probe fits for TOF hit reconstruction and matching efficiency</b>	<b>143</b>
<b>Appendix H RP track reconstruction efficiency comparison between data and MC</b>	<b>148</b>
<b>List of Figures</b>	<b>160</b>
<b>List of Tables</b>	<b>160</b>
<b>References</b>	<b>162</b>

# List of contributions

---

Leszek Adamczyk	Analysis coordination/supervision, production of picoDST, production of embedded MC samples
Lukasz Fulek <sup>1</sup>	pp2pp Geant4 simulation (user interface, beamline, magnet lattice, $B$ -field), TPC efficiency calculation, TOF efficiency calculation, matching between true-level particles and reconstructed TPC tracks, energy loss corrections, pile-up-related systematics to TPC and TOF efficiency
Rafal Sikora <sup>2</sup>	pp2pp Geant4 simulation (user interface, RP detectors, digitization and reconstruction, embedding), $dE/dx$ adjustment, TPC track resolution adjustment, pre-TPC dead material study, Tag&Probe studies (TOF and TPC), corrections to TOF efficiency and related systematics, RP efficiency systematics, list of bad runs

---

<sup>1</sup> - contact editor for Chapter: 2, 3 (Sec. 3.1-3.2.2), 5, 10 (Sec. 10.1-10.2.1)

<sup>2</sup> - contact editor for Chapter: 1, 2, 3 (Sec. 3.2.3-3.3), 4, 6, 7, 8, 9, 10 (Sec. 10.1.1,10.2.2-10.4)

## Change log

---

19 Jan 2019      ver. 1.0      Initial revision

---

## 1. Bad run list

Diffractive analyses [1,2] were performed with the use of data from runs with completion status “Successful” in the STAR run log [3]. During analysis of these runs no problems with the reconstructed data were found. The distributions of the TPC track-related quantities and performance of remaining subsystems used in analyses did not indicate issues preventing this data from inclusion to physics analyses.

We omitted from analyses data taken with Roman Pot detectors far from their typical positions. By the position we understand the vertical distance between the nominal beam trajectory and the closest edge of the Silicon Strip Detector housed inside Roman Pot. These positions were first measured during dedicated survey [4] and later precisely calculated for all runs and for all detectors using elastic proton-proton scattering events [5, 6].

Below we show histogram (Fig. 1.1a) and graph (Fig. 1.1b) of the beam-detector distance of all Roman Pots during runs<sup>1</sup> with active RP triggers. Based on these plots we set the limit on the actual position of the detector with respect to the beam to  $y_{\text{thr}} = 34$  mm. If any of 8 detectors was further from the beam than the threshold ( $|y| > y_{\text{thr}}$ ) the run was omitted from analysis. The benefit of that selection was reduction of the systematic effects related to low/asymmetric acceptance of detectors when they are at far/significantly differing distances from the nominal beam trajectory.

In the Fig. 1.1 one can notice that there were a few runs (16106026-16106033, fill 18915) with the closer-than-typical distance of detectors to the beamline. These runs correspond to a period dedicated for a study of elastic proton-proton scattering when an enhanced sample of RP\\_ET triggers was collected. For this particular process it was important to collect data with maximally reduced detector distance to the beamline and have continuous support of the Roman Pot experts in the control room throughout the runs. Although detector positions differ from the typical for these few runs, the active area of Roman Pots still covered the fiducial area defined for a physics measurement described in this note. We therefore preserve these runs.

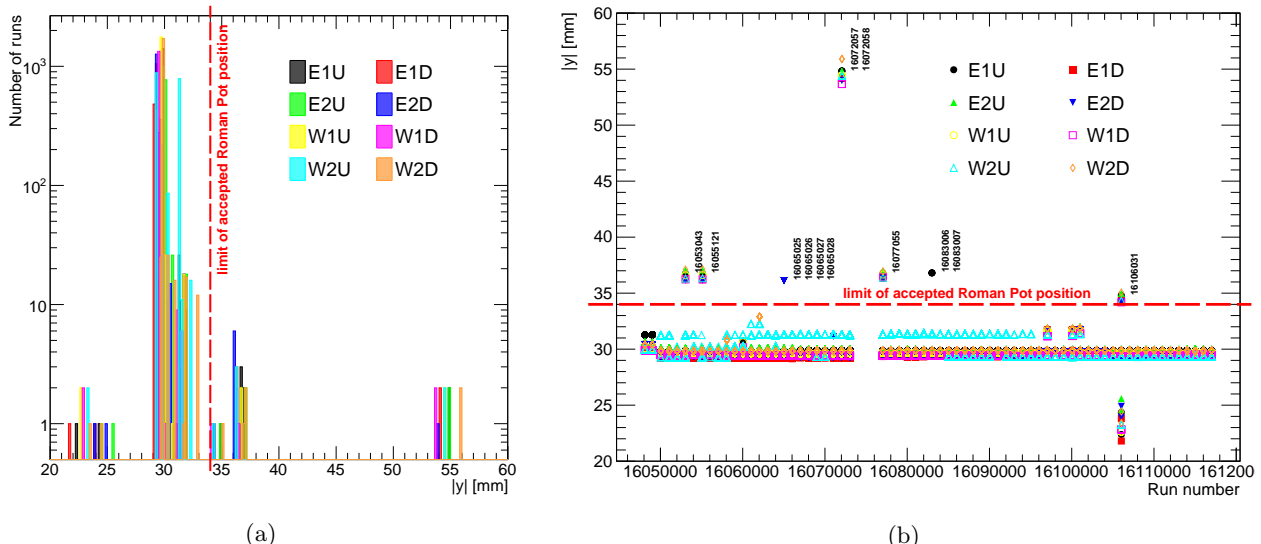


Figure 1.1: Histogram of beam-detector distance  $|y|$  (1.1a) and graph showing run-dependence of  $|y|$  (1.1b) for all Roman Pots

A summary list of runs in which detector positions did not fulfill beam-detector distance limits are listed below:

16053043 16055121 16065025 16065026 16065027 16065028  
16072057 16072058 16077055 16083006 16083007 16106031

Full list of runs with diffractive triggers (“RP\_xxxx”) and the list of runs for each trigger can be found at the web address given in Ref. [7].

---

<sup>1</sup>Roman Pots were not moved during the run. They were only moved between the runs.

# 2. TPC/TOF track and event selection

Charged particle tracks and primary vertices reconstructed with the TPC were selected in our analyses with the set of cuts listed below. These cuts were used in all sub-analyses described in this note and our physics analyses described in Ref. [1] and [2], unless stated differently. The goal of these criteria was to reject overlapping pile-up events, off-time pile-up tracks and ensure satisfactory resolution of the track momentum and specific energy loss.

Limit values of quantities in all selection cuts were chosen to balance the selection efficiency, background rejection power and related systematic uncertainties. Cuts in Sec. 2.2.1 and 2.2.3 were established based on histograms like the ones presented in Fig. 8.5. Cuts on  $z_{\text{vtx}}$  and track  $p_T$  and  $\eta$  were set based on the  $z_{\text{vtx}}$  distribution ( $\sigma(z_{\text{vtx}}) \approx 50$  cm) and joint acceptance and efficiency of the TPC and TOF (see e.g. Sec. 3.2.3). More detailed description of event and track selections are contained in physics analyses notes [1, 2].

## 2.1 TPC vertex selection (event selection)

An event was selected for analysis if the following criteria were satisfied:

- **Single primary vertex** (exactly one that contains at least one track matched with hit in TOF),
- $|z_{\text{vtx}}| < 80$  cm.

## 2.2 TPC track selection

### 2.2.1 Quality cuts

All TPC tracks used in analyses had to satisfy quality criteria:

- $N_{\text{hits}}^{\text{fit}} \geq 25$  - at least 25 hits used in the helix fit (for good momentum resolution),
- $N_{\text{hits}}^{\text{d}E/\text{dx}} \geq 15$  - at least 15 hits used in  $dE/dx$  calculation (for good  $dE/dx$  resolution),
- $|d_0| < 1.5$  cm - transverse impact parameter w.r.t. the beamline (see Fig. 8.1) not larger than 1.5 cm (for selection of tracks of real primary particles which by definition have origin in the interaction point which lies on the beamline).

### 2.2.2 TOF hit matching

TPC tracks had to be matched with hits reconstructed in TOF:

- **TOF match flag**  $\neq 0$ .

### 2.2.3 Vertex matching quality

Primary TPC tracks had to match well to the primary vertex:

- $\text{DCA}(R) < 1.5$  cm - radial component of the DCA vector between the global helix and the vertex not larger than 1.5 cm (value consistent with  $|d_0|$  limit),
- $|\text{DCA}(z)| < 1$  cm - absolute magnitude of longitudinal component of the DCA vector between the global helix and the vertex not larger than 1 cm.

## 2.3 Fiducial region of the measurement

TPC tracks had to be contained within the kinematic range:

- $|\eta| < 0.7$ ,
- pions:  $p_T > 0.2$  GeV, tracks without identification:  $p_T > 0.2$  GeV,  
kaons:  $p_T > 0.3$  GeV, protons:  $p_T > 0.4$  GeV.

# 3. Efficiencies

## 3.1 General overview

It is best to apply the corrections to the measured distributions that are based on real data analysis. However, due to the complexity of the processes we are studying, it is necessary to obtain corrections from the MC simulation. Whenever possible, we compare efficiencies obtained from MC with these from the data and introduce appropriate corrections to the MC if necessary.

It is preferred to get the detector to true-level corrections from the MC, which is dedicated to the studied physics process. However, for this purpose, the statistics in the MC should be several times greater (preferably an order of magnitude) than we have in the data for analysis. This is not possible with generally low total efficiency (TPC & TOF & RP). On the other hand, such efficiencies depend on the modeling of the studied process and require a good description of all generally multidimensional distributions by MC. Since that, the basic method of corrections that we use in the analyses is the method of factorization of global efficiency into the product of single-particle efficiencies (separate for each central particle and forward protons). Thereby, statistically precise multidimensional corrections on TPC, TOF and RP are obtained. Nevertheless, this method does not correct on the migration effects caused by the finite detector resolution and is sensitive to the binning. Whenever possible, we use both methods of correction (at least in the consistency tests for MC samples). In this note, only the single-particle corrections are described, which are common for both analyses.

## 3.2 TPC track acceptance and reconstruction efficiency

We defined joint acceptance and efficiency of reconstruction of a track in the TPC,  $\epsilon_{\text{TPC}}$ , as the probability that particle from the primary interaction generates signal in the detector which is reconstructed as a global track that satisfies all quality criteria (cuts 2.2.1). To derive this efficiency the single particle STARsim MC embedded into zero-bias trigger data taken simultaneously with physics triggers was used.

### 3.2.1 STAR nominal method

Technically, the common method used by the STAR to obtain  $\epsilon_{\text{TPC}}$  is the following procedure:

1. True-level primary particles of given ID and charge were selected (*set A*).
2. Each particle from *set A* was checked if any global TPC track with more than half of hit points associated to it was generated by true-level particle (definition of true level particle-track matching, `idTruth` from `StMuTrack` collection). All particles from *set A* which have associated global track satisfying quality criteria (cut 2.2.1) formed *set B*.
3. The joint TPC acceptance and efficiency was calculated as the ratio of the histograms of true level quantities (such as  $p_T$ ,  $\eta$ ,  $z_{\text{vtx}}$ ) for particles from *set B* and particles from *set A*:

$$\epsilon_{\text{TPC}}(p_T, \eta, z_{\text{vtx}}; \text{sign}, \text{PID}) = \frac{(p_T, \eta, z_{\text{vtx}}) \text{ histogram for particles of given sign and ID from } \textit{set B}}{(p_T, \eta, z_{\text{vtx}}) \text{ histogram for particles of given sign and ID from } \textit{set A}}. \quad (3.1)$$

#### 3.2.1.1 Global track to true level particle matching

It was found during the analysis that in about 1% events there are more than one reconstructed global track matched with the same true level particle, which is shown in Fig. 3.1, separately for true level pions, kaons and protons. This generally leads to few percent overestimation of corrected number of tracks since each reconstructed track is weighted by TPC efficiency. Therefore only one reconstructed track should be considered as good track and the rest should be treated as fake tracks.

The true level particle end vertex  $V_r^{\text{end}}$  is not specified if the particle neither interacted with the dead material nor decayed. The analysis showed that 1% of the reconstructed tracks are matched to the true particle which lost identity ( $V_r^{\text{end}} < 48$  cm) before entering TPC. We interpret such situation as matching of reconstructed daughter particle to true level parent particle, which is a clear bug in the STAR software rather than intentional feature. It is potentially dangerous since momentum and type of daughter particle might be significantly different from parent particle. Problem with wrong true level matching is also present for tracks with only one track matched to true level particle which do not decay or interact with material (no end vertex associated to true



Figure 3.1: Number of reconstructed global tracks, satisfying all quality criteria (cuts 2.2.1), matched with the same true level primary particle. The type of true level particle is indicated in the figure.

level particle). It is visible on Fig. 3.2 where  $dE/dx$  is shown that some reconstructed tracks have different PID than true level particle matched to it. Also, there are problems in the closure tests, where the reconstructed-level distributions of rapidity and transverse momenta weighted by the nominal efficiency corrections do not describe the true level distributions. Main reason for failing of closure tests is non-negligible (and significant for anti-protons) amount of global tracks matched with primary particles but no or little correlation in  $\eta - \phi$  space between matched pair. This correlation can be represented by the distance

$$\delta^2(\eta, \phi) = (\eta^{true} - \eta^{reco})^2 + (\phi^{true} - \phi^{reco})^2 \quad (3.2)$$

between the true level particle and global track assigned to it, shown in Fig. 3.3 for particles with only one matched global track and Fig. 3.4 for particles with at least two matched global tracks, indicates that some part of the tracks taken for the efficiency calculation are measured very badly ( $\delta^2(\eta, \phi)$  is very large), even if there is only one global track matched to the true-particle.



Figure 3.2:  $dE/dx$  of the track matched to true level particle. Lines indicate Bichsel function prediction for each particle species. Only tracks matched to true level particles without end vertex are shown. Black lines and arrows indicate region accepted in the analysis.

Because of several above mentioned problems with nominal STAR definition of matching between reconstructed tracks and true level particles we decided to use in the analysis modified matching definition by taking into the account the difference between reconstructed tracks and true particles in  $\eta - \phi$  space.



Figure 3.3:  $\delta^2(\eta, \phi)$  distributions between true level particles and tracks assigned to them. Only true level particles with only one reconstructed track matched to them were selected. Red lines and arrows indicate the cut value of  $0.15^2$ , which is used in the modified true level particle-track matching definition.



Figure 3.4:  $\delta^2(\eta, \phi)$  distributions between true level particles and tracks assigned to them. Only true level particles with at least two reconstructed tracks matched to them were selected. Red lines and arrows indicate the cut value of  $0.15^2$ , which is used in the modified true level particle-track matching definition.

### 3.2.2 Method used in this analysis

In this method, the definition of true level particle-track matching is modified. In addition to the requirement of the appropriate number of common hit points, the distance between true level particle and track is required to be smaller than  $0.15$ ,  $\delta^2(\eta, \phi) < (0.15)^2$ . It is quite an arbitrary value which should be small but not too small to loose good events. The value of  $\delta^2$  cut was chosen by the requirement that only acceptable small amount of CEP events which passed all selection criteria will not satisfy matching criteria. It was verified with

the CEP MC embedded into zero-bias triggers that with quoted value of cut on  $\delta^2(\eta, \phi)$  less than 0.3% of CEP events have at least one track which is not considered to be matched with true-level pion despite the standard matching (Fig. 3.5). We consider this an acceptably low effect.

Tracks, which do not satisfy the above criterion, are treated as fake tracks (even if they are matched to the true level particle in the standard way). In 99.97% cases, where the  $\delta^2(\eta, \phi) < (0.15)^2$ , there is only one track matched to true level particle (Fig. 3.6). Additionally, the  $dE/dx$  of the track is in 99.94% consistent with the true level PID (Fig. 3.7). Figure 3.8 shows the difference between TPC efficiencies obtained with the STAR standard and the modified definition of true particle-track matching. The maximum differences between TPC efficiencies in the analyzed  $p_T$  range are about 2% for pions, 3% for kaons, 2% and 4% for protons and antiprotons, respectively.



Figure 3.5: Distribution of  $\delta^2(\eta, \phi)$  for tracks matched with true-level pions (using standard matching) in CEP MC embedded into zero-bias triggers. Tracks were taken from events passing full CEP event selection, recognized as exclusive  $\pi^+\pi^-$ . The vertical red dashed line indicates the cut value of  $0.15^2 \approx 0.023$ , above which less than 0.14% of tracks is contained.

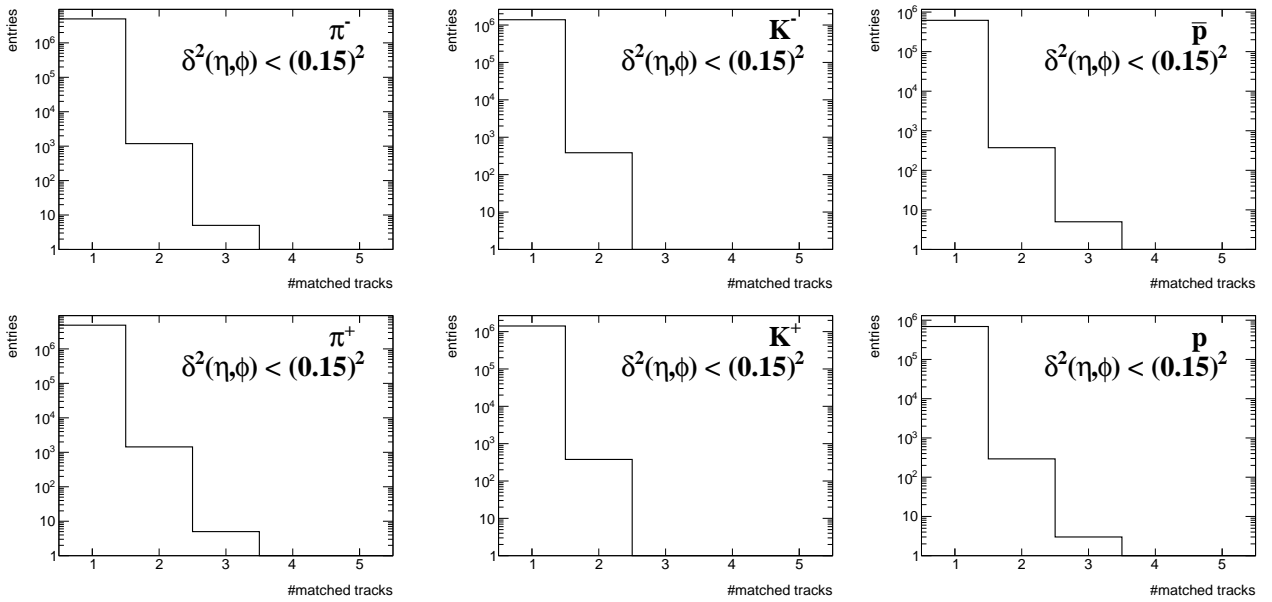


Figure 3.6: Number of reconstructed global tracks, satisfying all quality criteria (cuts 2.2.1) and  $\delta^2(\eta, \phi)$  cut, matched with the same true level primary particle.



Figure 3.7:  $dE/dx$  of the closest track matched to true level particle passing the  $\delta^2(\eta, \phi)$  cut. Lines indicate Bichsel function prediction for each particle species. Black lines and arrows indicate region accepted in the analysis.



Figure 3.8: TPC acceptance and reconstruction efficiency as a function of  $p_T$  ( $|V_z| < 80$  cm,  $|\eta| < 0.7$ ) obtained from two methods. Black lines and arrows indicate region accepted in the analysis.

### 3.2.3 Sample of efficiency plots

During Run 15 the inner sector #19 in the TPC was dead during some runs [8]. In Figure 3.9 we show density map of global TPC track first point  $(\eta, \varphi)$  coordinates for runs with dead sector #19 and with that sector back in operation. Since that, the TPC track acceptance and reconstruction efficiency was calculated for two periods: runs up to 16073050 and after 16073050.

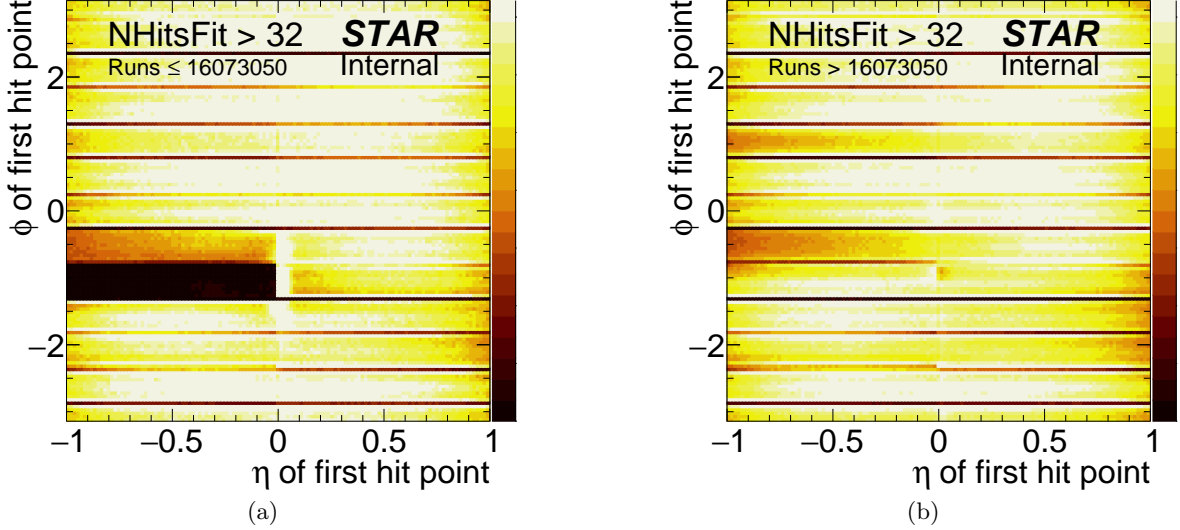


Figure 3.9: Density map of global TPC track first point  $(\eta, \varphi)$  coordinates for runs with dead sector #19 (up to 16073050, 3.9a) and with that sector back in operation (after run 16073050, 3.9b).

In Figure 3.10 we present sample plots of the TPC track acceptance and reconstruction efficiency calculated with modified definition of reconstructed track and true-level particle matching (according to description in Sec. 3.2.2), used in our analyses. Plots for all analyzed particle types, all bins of true  $z_{\text{vtx}}$  and all runs are contained in Appendix A.

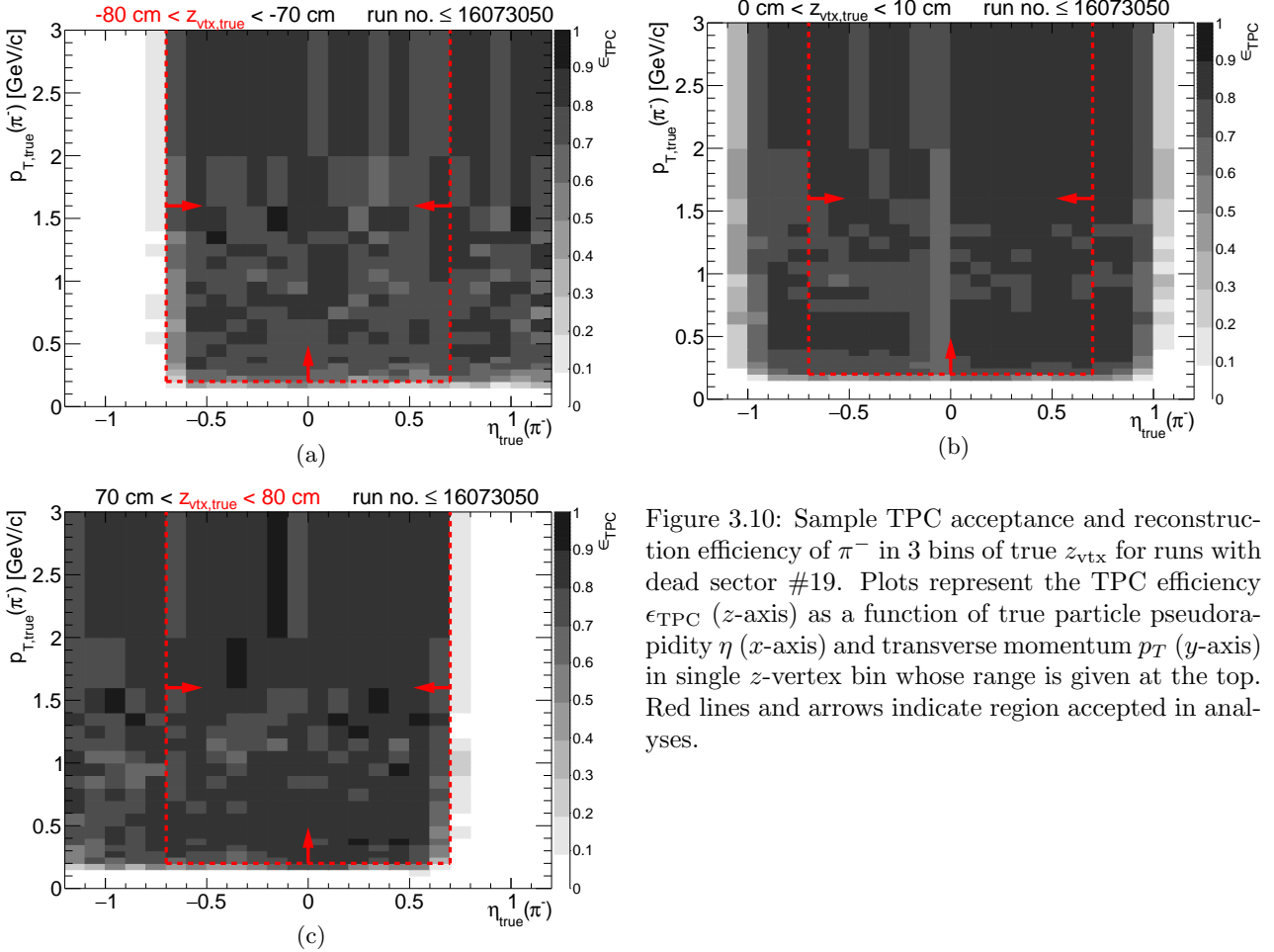


Figure 3.10: Sample TPC acceptance and reconstruction efficiency of  $\pi^-$  in 3 bins of true  $z_{\text{vtx}}$  for runs with dead sector #19. Plots represent the TPC efficiency  $\epsilon_{\text{TPC}}$  ( $z$ -axis) as a function of true particle pseudorapidity  $\eta$  ( $x$ -axis) and transverse momentum  $p_T$  ( $y$ -axis) in single  $z$ -vertex bin whose range is given at the top. Red lines and arrows indicate region accepted in analyses.

In order to maximize the statistics available for the measurement (possibly wide range of accepted longitudinal vertex position  $z_{\text{vtx}}$ ) with maximized probed phase-space in analyzed physics processes (wide range of track  $p_T$  and  $\eta$ ) and minimized systematic uncertainties related to the central detector (TPC and TOF), we have studied the efficiency plots like ones shown in Fig. 3.10 and Fig. 3.11. We thus decided to set the cut on  $z_{\text{vtx}}$  at  $\pm 80$  cm, which corresponds to 89% of the full integral of normal distribution with mean at 0 and standard deviation of 50 cm. At the same time we set the cuts on track  $p_T$  and  $\eta$  as listed in Sec. 2.3. These cuts are represented with red dashed lines in Fig. 3.10 and Fig. 3.11. Our goal was to operate within cuboid ( $z_{\text{vtx}}, p_T, \eta$ ) region of relatively high TPC and TOF efficiency ( $\geq 50\%$  of the maximum value). In other words, we required high acceptance and efficiency for a rectangular ( $p_T, \eta$ ) space with limits independent from  $z_{\text{vtx}}$ . One can see that the red lines in Fig. 3.10 and Fig. 3.11 always contain in their interior the region of relatively high acceptance.

### 3.3 TOF acceptance, hit reconstruction and track matching efficiency

Combined TOF acceptance, hit reconstruction efficiency and matching efficiency with TPC tracks,  $\epsilon_{\text{TOF}}$ , was defined as the probability that the global TPC track that satisfy quality criteria (cuts 2.2.1) is matched with hit in TOF (2.2.2). This quantity is generally referred as “TOF efficiency”.

It was calculated in the very similar way to TPC efficiency - single particle STARsim MC embedded into zero-bias triggers was used. Tracks belonging to *set B* from Sec. 3.2 were utilized. From these tracks a sub-sample of tracks with non-zero TOF matching flag (`StMuBTofPidTraits.mMatchFlag > 0`) was extracted (*set C*). The TOF efficiency was calculated as

$$\epsilon_{\text{TOF}}(p_T, \eta, z_{\text{vtx}}; \text{sign}, \text{PID}) = \frac{(p_T, \eta, z_{\text{vtx}}) \text{ histogram for particles of given sign and ID from set } C}{(p_T, \eta, z_{\text{vtx}}) \text{ histogram for particles of given sign and ID from set } B}. \quad (3.3)$$

An additional note has to be made here about the correction which is applied to TOF matching flag in MC analysis. It was found that in embedded simulation the dead TOF elements were not masked. To correct for this effect (hence obtain more reliable TOF efficiency) a data-based map of modules was created, separately for each RHIC fill. Map was filled with modules which were matched with TPC tracks in the data. In all MC sample analyses (including efficiency determination) each TPC track with non-zero TOF match flag was additionally checked if TOF module that track was matched with had any entries in the data-based map. If not - the TOF match flag was considered 0. All dead TOF modules masked in the MC are listed in Tab. B.1 in Appendix B.

#### 3.3.1 Sample of efficiency plots

The sample TOF efficiency plot is shown in Fig. 3.11. All remaining TOF efficiency plots are contained in Appendix B.

As shown in Sec. 4.1 the data-driven efficiency and MC efficiency differ significantly, therefore the final TOF efficiency which is used to correct the data is the one presented here (taken from single particle embedded MC) but additionally modified according to correction derived in the referred section.



Figure 3.11: Sample TOF acceptance, reconstruction and matching efficiency of  $\pi^-$  in 3 bins of true  $z_{\text{vtx}}$ . Plots represent the TOF efficiency  $\epsilon_{\text{TOF}}$  ( $z$ -axis) as a function of true particle pseudorapidity  $\eta$  ( $x$ -axis) and transverse momentum  $p_T$  ( $y$ -axis) in single  $z$ -vertex bin whose range is given at the top. Red lines and arrows indicate region accepted in analyses.

# 4. Corrections to efficiencies

## 4.1 Data driven corrections to TOF efficiency

The efficiency of TOF hit reconstruction and matching with the TPC tracks that was used in our analyses was (at the very beginning) taken directly from the STAR simulation. This made the inaccuracies in the description of real detector geometry and its response propagating to physics results and introducing a bias. We decided to derive the correction to the TOF efficiency obtained from the STAR simulation by extracting it in the very same way from the data and embedded MC and comparing the results.

Unfortunately, in 2015 there were no low-luminosity (heavy-ion) runs that would imply lack of off-time pile-up tracks in TPC and thus would allow calculating the TOF efficiency in straightforward way, namely by dividing number of selected TPC tracks that were matched with TOF hits by number of all selected TPC tracks (matched or unmatched). For this reason a variation of the “tag and probe” method was developed and used. This method utilizes some specific feature of the distribution of quantity describing two objects (whose trigger/reconstruction/identification/etc. efficiency is studied) which allows to quantify amount of these objects with satisfied/unsatisfied efficiency condition. This could be e.g.  $J/\psi$  peak in the invariant mass spectrum of the muon tracks, like in the study of muon identification efficiency in MTD [9].

In our variation of mentioned tag&probe method the CEP of  $\pi^+\pi^-$  events were used, with the missing transverse momentum  $p_T^{\text{miss}}$  used to determine signal event yield ( $p_T^{\text{miss}} = (\vec{p}_W + \vec{\pi}^+ + \vec{\pi}^- + \vec{p}_E)_T$ ). In short, events with forward proton track on each side of STAR and with a TOF-matched primary TPC track (tag) were selected. Among the remaining primary TPC tracks in the same vertex the opposite-sign TPC track (probe) was chosen as the one which provides the minimum total transverse momentum of all four tracks. The probe was checked whether it has been matched with the TOF hit or not. The ratio of the matched TPC tracks to all (matched or unmatched) TPC tracks defined the TOF efficiency, as given in Eq. (4.1):

$$\varepsilon^{\text{TOF}} = \frac{N_{\text{satisfied}}^{\text{probes}}}{N_{\text{produced}}^{\text{probes}}} = \frac{N_{\text{satisfied}}^{\text{probes}}}{N_{\text{satisfied}}^{\text{probes}} + N_{\text{failed}}^{\text{probes}}} = \frac{2N_{TT}^{\text{events}} + N_{TP_s}^{\text{events}}}{2N_{TT}^{\text{events}} + N_{TP_s}^{\text{events}} + N_{TP_f}^{\text{events}}} \quad (4.1)$$

Subscripts  $TT$ ,  $TP_s$  and  $TP_f$  denote possible combinations of tags and probes:

- $TT$  (both tracks satisfy tag criteria, and by definition the efficiency condition); such events provide two probes which satisfy efficiency condition which is the reason for the factor ‘2’ in front of  $N_{TT}^{\text{events}}$  in Eq. (4.1),
- $TP_s$  (one track is tag, the other is a probe and probe satisfies the efficiency condition),
- $TP_f$  (one track is tag, the other is a probe and probe fails to satisfy the eff. condition).



Figure 4.1: Sketch of the cross section of the central detector and CEP event with off-time pile-up tracks with drafted tag&probe method used to determine the TOF hit reconstruction and matching efficiency.

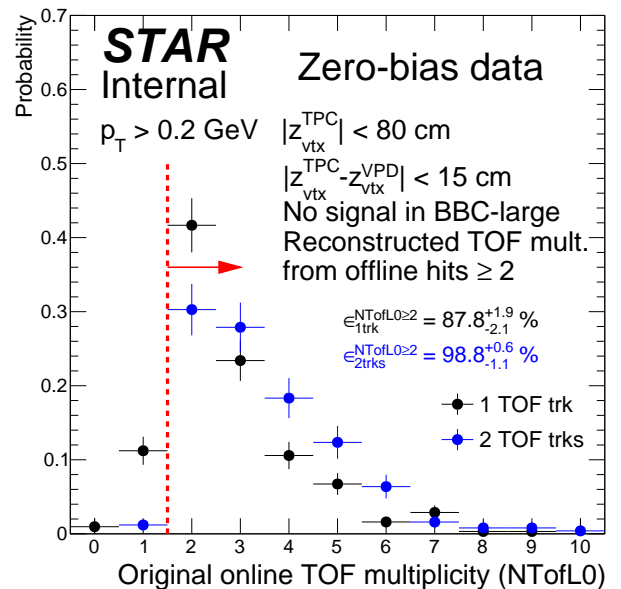


Figure 4.2: TOF L0 multiplicity in events with exactly 1 (black) or exactly 2 (blue) primary TPC track matched with offline TOF hits under condition of online TOF mult. reconstructed from offline hits  $\geq 2$ .

The method is illustrated in the sketch in Fig. 4.1. The detailed description of the procedure of the TOF efficiency extraction is listed below:

1. Data from RP\_CPT2 trigger were used. This trigger required at least 2 level-0 TOF hits (trigger details can be found in Tab. 2.1 of Ref. [1]). Requirement of 2 TOF hits in the trigger (to ensure presence of 2 tracks in TPC) does not comply with the basics of the tag&probe method, but as explained in #4 and in the following page the tight selection of tags as tracks providing online multiplicity 2 and firing the TOF trigger allowed to use this method. GenEx  $\pi^+\pi^-$  signal MC (embedded into zero-bias data from runs corresponding to RP\_CPT2 triggers), as well as Pythia CD for non-exclusive background, were subjected to the same trigger conditions, except online TOF multiplicity condition to avoid trigger bias.
2. Events were selected with the cuts from nominal CEP analysis (Ref. [1]), except cuts **C3** and **C7-C9** which were removed or modified as given below. This provided significant reduction of background events.
3. For each event passing above selection primary TOF-matched TPC tracks of good quality (cuts 2.2.1,2.2.3), contained within kinematic region of our measurement (cuts 2.3 with  $p_T$  threshold lowered to 0.18 GeV to also calculate efficiency in a point where it rapidly changes hence allow more precise fit to efficiency  $p_T$ -dependence) and compatible with pion hypothesis based on  $dE/dx$  ( $|n_{\text{pion}}^\sigma| < 3$ ) were selected. If any TOF-matched track incompatible with pion hypothesis was found, event was dropped from analysis. Also, event was not analyzed if more than 2 TOF-matched tracks were reconstructed (not two-prong CEP event).
4. Primary TOF-matched TPC tracks preselected in #3 were set as tag candidates. In the data they were additionally required to be matched with the TOF hit belonging to a TOF cluster that is expected to provide multiplicity 2 at the level 0 (to reduce trigger bias). In case only one track was found to be a tag candidate, steps #5-#6 were executed only with this single track being a tag. Otherwise steps #5-#6 were repeated for each of two tracks set as a tag.
5. From the remaining TPC tracks in the same vertex (preselected in #3) of the sign opposite to tag and of good quality (cuts 2.2.1,2.2.3), the one which provided the best transverse momentum balance together with 2 protons and a tag was selected as a probe (signature of exclusive  $\pi^+\pi^-$  is  $p_T^{\text{miss}} \sim 0$ ). If no primary TPC tracks passing this selection were found, an event was dropped.
6. 2-dimensional histograms of quantities of interest  $q$  (probe  $\eta$ , probe  $p_T$ ,  $z_{\text{vtx}}$ ) vs.  $p_T^{\text{miss}}$  were filled, separately for all probes and only for probes matched with TOF. Each probe (each entry to the histogram) was associated with the weight  $w$  taking into account the trigger efficiency and vertexing efficiency, as given in Eq. (4.3) and explained later in the text.
7. In each bin of quantity of interest  $q$  (as a function of which the efficiency was to be determined) the distribution of  $p_T^{\text{miss}}$  was fitted in the signal-free region with the function describing background shape. The background function was extrapolated to  $p_T^{\text{miss}} = 0$ . The signal yield in given bin of  $q$  was calculated as the integral of the histogram with subtracted integral of the background function, both in the range  $p_T^{\text{miss}} < 75$  MeV. The final efficiency in given bin of  $q$  was calculated according to Eq. (4.2):

$$\varepsilon_{\text{TOF}}(q) = \frac{N_{\text{weighted}}^{\text{matched}, p_T^{\text{miss}} < 75 \text{ MeV}} - N_{\text{bkgd,weighted}}^{\text{matched}, p_T^{\text{miss}} < 75 \text{ MeV}}}{N_{\text{weighted}}^{\text{all}, p_T^{\text{miss}} < 75 \text{ MeV}} - N_{\text{bkgd,weighted}}^{\text{all}, p_T^{\text{miss}} < 75 \text{ MeV}}} \quad (4.2)$$

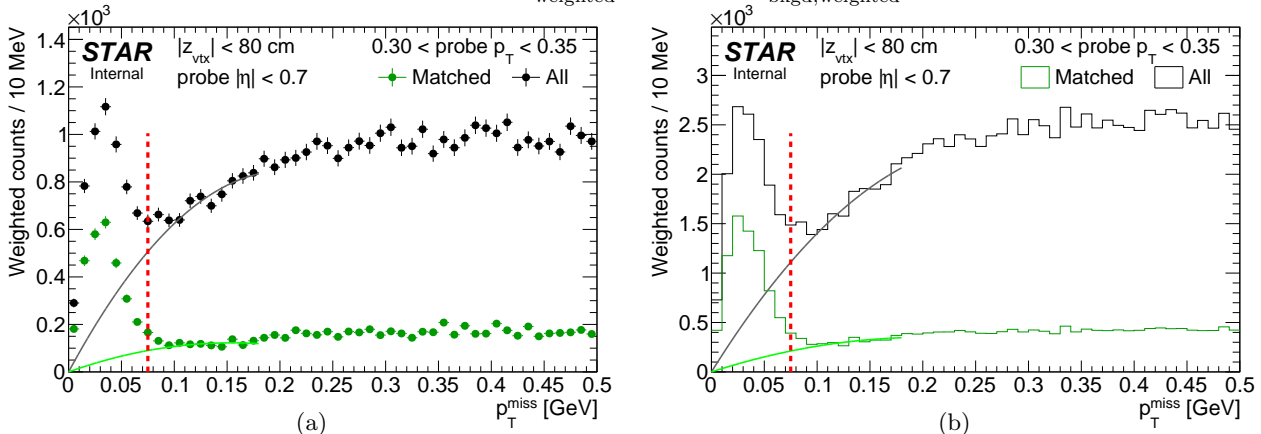


Figure 4.3: Sample distributions of total transverse momentum  $p_T^{\text{miss}}$  of the  $p+\text{Tag}+\text{Probe}+p$  system in the data (4.3a) and signal+background embedded MC (4.3b). TOF-matched and all (matched or unmatched) probes are represented by histograms in green and black color, respectively. The red dashed line shows the exclusivity cut value (75 MeV/c). Signal yield is determined via the integral of the histogram with subtracted integral of the solid line representing non-exclusive background in the  $p_T^{\text{miss}}$  range to the left from the vertical line. Background (solid line) is fitted with 2<sup>nd</sup> order polynomial in the signal-free region (the details can be found in Ref. [1] in Sec. 5.2). Full sets of histograms in different ranges of probe  $p_T$  and  $\eta$  are included in Appendix G.

As described in the algorithm of the tag&probe method, the RP\_CPT2 triggers were used in our study. The logic of that trigger required at least 2 TOF hits online. Since the system whose efficiency was studied has also been a part of the trigger, the tag should be, in principle, chosen as the track that is linked with 2 online TOF hits - to be sure that the tag satisfies the trigger condition and thus the probe is not biased by the trigger (in other words, the probe does not bias the resultant efficiency). Unfortunately, the TOF system works independently for the trigger and for the offline data stream (the readout electronics are independent), therefore there is no information about the connection between the TOF hits at L0 and offline.

Fortunately, a solution to the above limitation has been found. We made use of the TOF cluster<sup>1</sup> concept introduced in Ref. [1], Sec.XX, as well as of reconstruction/emulation of the online TOF multiplicity from the offline hits according to description of the TOF trigger system in Ref. [10]. With these tools we chose tags as the tracks that are matched with TOF hit associated with a TOF cluster that provides reconstructed online multiplicity  $\geq 2$ . We verified with zero-bias data that by requiring the reconstructed online multiplicity to be  $\geq 2$  we can efficiently select events in which the true online (L0) TOF multiplicity was also  $\geq 2$ . For this purpose we selected events with only one(two) TOF-matched TPC track(s), in addition forming a primary vertex. We also required no signal in large BBC tiles, the same as in physics analysis of CEP. To make sure that the single TOF-matched track is from beam-beam interaction that TOF electronics is adjusted to trigger on, we required the signal in VPD detectors on both sides of the IP. The  $z$ -positions of the primary vertex reconstructed in TPC and reconstructed from the time difference in west and east VPDs was required to be not larger than 15 cm. In Fig. 4.2 we show distribution of the TOF L0 multiplicity for such selected events. One can find in this figure that the probability of TOF L0 multiplicity  $\geq 2$  for a single TOF-matched track,  $\epsilon_{1\text{trk}}^{\text{NTofL0} \geq 2}$ , is high and equals 87.8%. For events with 2 reconstructed TOF-matched tracks the probability of TOF L0 multiplicity  $\geq 2$ ,  $\epsilon_{2\text{trks}}^{\text{NTofL0} \geq 2}$ , equals 98.8%. These efficiency factors were accounted in the event weighting, as shown in Eq. (4.3).

The vertexing efficiency was an additional efficiency factor which had to be taken into account in described analysis<sup>2</sup>. This efficiency for a single track depends on matching with TOF due to 'useBTOFmatchOnly' option used in reconstruction. It is different when both exclusive pion tracks are matched with TOF, comparing with the case when only one track is matched with TOF and the other is not. The vertexing efficiency defined as the probability that two global TPC tracks of true-level primary particles, matched with TOF and satisfying criteria 2.2.1, form the common primary vertex is presented in Ref. [1] in Fig.XXX as a function of the distance in  $z$  of the DCA points on the beamline,  $|\Delta z_0|$ . This efficiency extracted from embedded MC was used in this analysis in case when both tag and probe were matched with TOF. As shown in dedicated study presented in

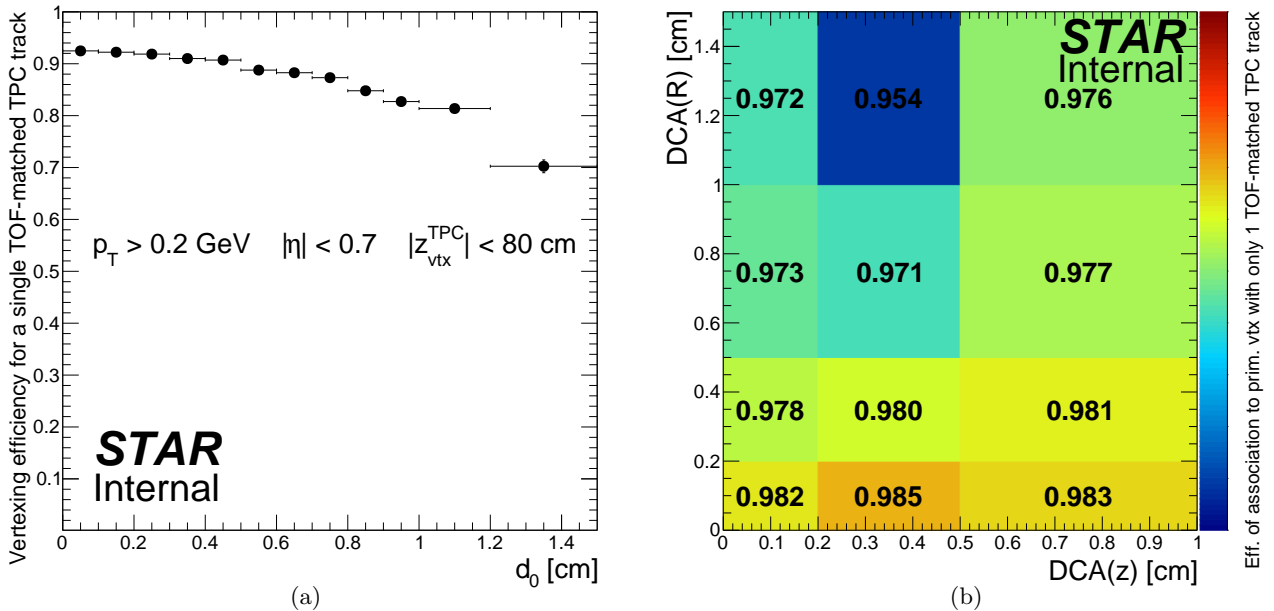


Figure 4.4: Efficiency  $\epsilon_{\text{vtx}}^{\text{nTOF}=1}$  of reconstruction of the primary vertex from a single TOF-matched TPC track as a function of the absolute value of the transverse impact parameter  $d_0$  (4.4a) and efficiency  $\epsilon_{\text{vtx}}^{\text{no-TOF}}$  of association with the vertex formed from single TOF-matched track of a TPC track not matched with TOF, as a function of radial and longitudinal DCA to the vertex (4.4b). The tracks were required to be matched with true-level primary particles (pions) as well as the quality and kinematic cuts were implied (2.2.1, 2.2.3, 2.3).

<sup>1</sup>Group of offline TOF hits adjacent/close to each other in space (and time)

<sup>2</sup>This analysis could be performed using solely global TPC tracks without requiring reconstructed primary vertex. Such solution was not chosen due to limitation of the picoDST data accessible for analysis (not all global tracks stored).

Ref [1] in Sec.XXX, the MC reproduces very well the vertexing efficiency obtained from the data.

For events with only one of exclusively produced pions being matched with TOF a different efficiency had to be used. In this case only the TOF-matched track participated in the vertexing, while the other was added to the primary vertex if it satisfied certain criteria. We therefore calculated the vertexing efficiency for the single TOF-matched track as a function of the transverse distance to the beamline  $|d_0|$  (Fig. 4.4a) and the efficiency of association of the TPC track not matched with TOF with the primary vertex made of single TOF-matched track (Fig. 4.4b). The final correction factor for a probe represented by the weight of an entry to  $q$  vs.  $p_T^{\text{miss}}$  histograms has the following form:

$$w = \begin{cases} \left[ \epsilon_{1\text{trk}}^{\text{NTofL0} \geq 2} \times \epsilon_{vtx}^{\text{nTOF}=2}(|\Delta z_0|) \right]^{-1} & \text{for } TT, TP_s \\ \left[ \epsilon_{2\text{trks}}^{\text{NTofL0} \geq 2} \times \epsilon_{vtx}^{\text{nTOF}=1}(|d_0|) \times \epsilon_{vtx}^{\text{no-TOF}}(\text{DCA}_z, \text{DCA}_R) \right]^{-1} & \text{for } TP_f \end{cases}, \quad (4.3)$$

where factors related to trigger efficiency are accounted only in the data analysis. A sample histograms of the  $p_T^{\text{miss}}$  distribution in the data and embedded MC filled with entries of weight  $w$  are shown in Fig. 4.3.

The dependence of the TOF efficiency on the track  $p_T$  was assumed to have the error function (erf) form:

$$\epsilon^{\text{TOF}}(p_T) = \frac{1}{2} \cdot P_1 \cdot \left( \text{erf}\left(\frac{p_T - P_2}{P_3}\right) + 1 \right) \quad (4.4)$$

In Fig. 4.5 we show the resultant TOF efficiency obtained with the Tag&Probe method.

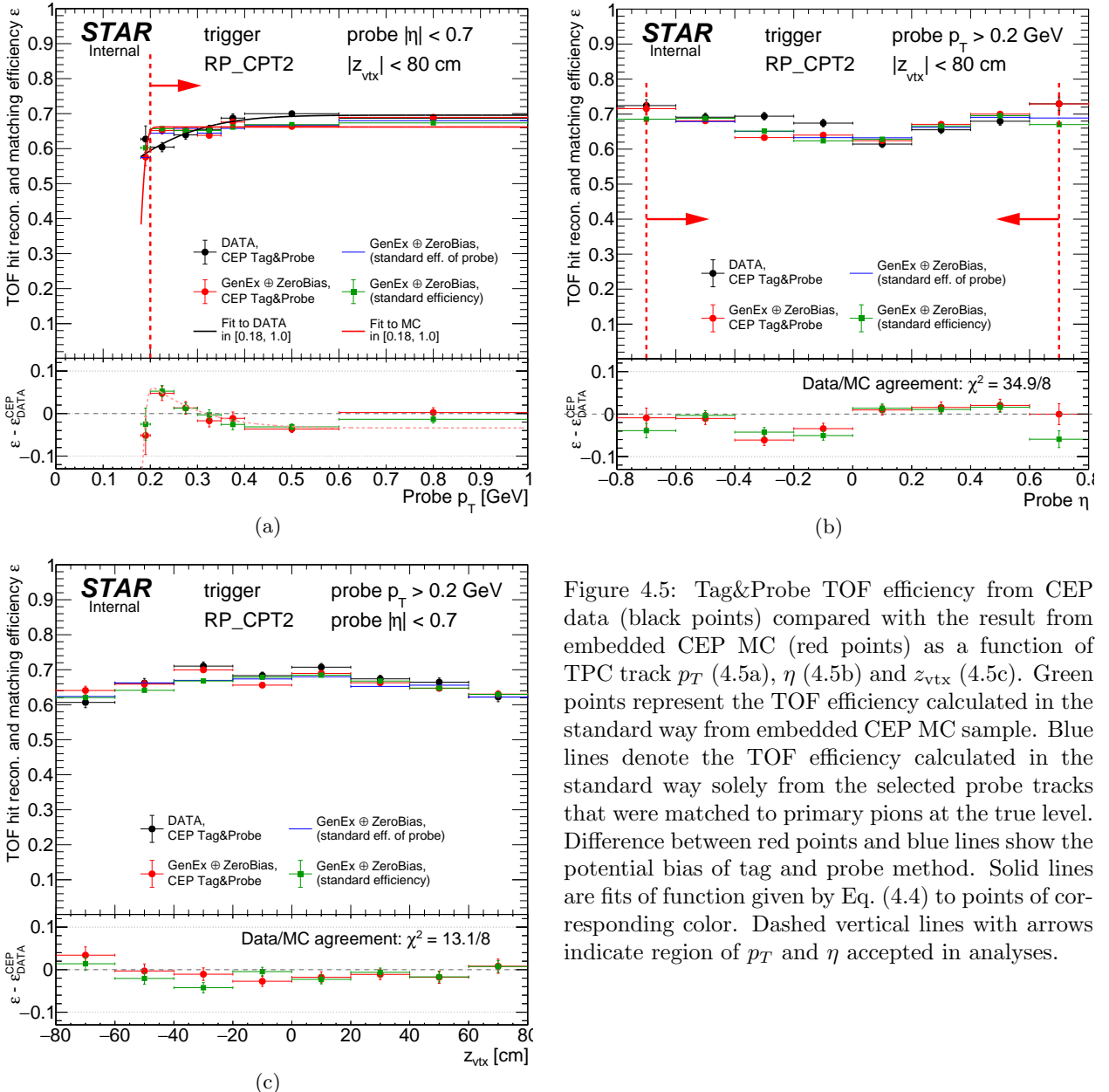


Figure 4.5: Tag&Probe TOF efficiency from CEP data (black points) compared with the result from embedded CEP MC (red points) as a function of TPC track  $p_T$  (4.5a),  $\eta$  (4.5b) and  $z_{\text{vtx}}$  (4.5c). Green points represent the TOF efficiency calculated in the standard way from embedded CEP MC sample. Blue lines denote the TOF efficiency calculated in the standard way solely from the selected probe tracks that were matched to primary pions at the true level. Difference between red points and blue lines show the potential bias of tag and probe method. Solid lines are fits of function given by Eq. (4.4) to points of corresponding color. Dashed vertical lines with arrows indicate region of  $p_T$  and  $\eta$  accepted in analyses.

From Fig. 4.5 one can find that the efficiency in the data and MC differ substantially. The comparison of the  $p_T$ -dependence of TOF efficiency in Fig. 4.5a suggests that saturation of the TOF efficiency with growing track  $p_T$  is slower than MC predicts, and that maximum (high- $p_T$ ) efficiency is generally higher by 3-4 percentage points in the data compared to MC. In the  $\eta$ -dependence we can see that there are some bins of  $\eta$  in which the agreement between MC and data is satisfactory, while in others the difference is large. The  $z_{\text{vtx}}$ -dependence (Fig. 4.5c) is in acceptable agreement between the data and MC.

The above observations led to perform the analysis of  $p_T$ -dependence of TOF efficiency in 4 bins of track pseudorapidity. The result is presented in Fig. 4.6. Parameters of functions fitted to data and MC points are contained in Tab. 4.1. The additive correction to the TOF efficiency presented in Sec. 3.3 has the form

$$\delta\varepsilon^{\text{TOF}}(p_T) = \varepsilon_{\text{DATA}}^{\text{TOF}}(p_T) - \varepsilon_{\text{MC}}^{\text{TOF}}(p_T), \quad (4.5)$$



Figure 4.6: Tag&Probe TOF efficiency from CEP data (black points) compared with the result from embedded CEP MC (red points) as a function of TPC track  $p_T$  for four ranges of the pseudorapidity  $\eta$  of the probe. Blue lines denote the TOF efficiency calculated in the standard way solely from the selected probe tracks that were matched to primary pions at the true level. Difference between red points and blue lines show the potential bias of tag and probe method. Solid lines are fits of function given by Eq. (4.4) to points of corresponding color, whose parameters are tabulated in Tab. 4.1. Dashed vertical lines with arrows indicate region of  $p_T$  and  $\eta$  accepted in analyses.

$\eta$ range	Data			MC		
	$P_1$	$P_2$	$P_3$	$P_1$	$P_2$	$P_3$
$[-0.7; -0.3]$	$0.736 \pm 0.011$	$0.013 \pm 0.083$	$0.329 \pm 0.106$	$0.686 \pm 0.010$	$0.180 \pm 0.036$	$0.011 \pm 0.039$
$[-0.3; 0.0]$	$0.696 \pm 0.011$	$0.090 \pm 0.070$	$0.164 \pm 0.079$	$0.629 \pm 0.003$	$0.180 \pm 0.004$	$0.029 \pm 0.011$
$[0.0; 0.3]$	$0.716 \pm 0.031$	$-0.050 \pm 0.137$	$0.508 \pm 0.233$	$0.670 \pm 0.005$	$-0.021 \pm 0.096$	$0.344 \pm 0.154$
$[0.3; 0.7]$	$0.683 \pm 0.008$	$0.132 \pm 0.055$	$0.084 \pm 0.056$	$0.690 \pm 0.009$	$0.167 \pm 0.002$	$0.000 \pm 0.000$

Table 4.1: Parameters of function (Eq. (4.4)) describing the TOF efficiency as a function of pion track  $p_T$  in bins of track  $\eta$  from Fig. 4.6. Paramaters of the functions fitted to both data and MC points are given. The TOF efficiency calculated as described in Sec. 3.3 is corrected during data analysis by the difference of values of functions  $\varepsilon^{\text{TOF}}(p_T)$  with parameters for data and MC, respectively (the difference is added).

where  $\varepsilon_{\text{DATA}}^{\text{TOF}}(p_T)$  and  $\varepsilon_{\text{MC}}^{\text{TOF}}(p_T)$  are of the form given by Eq. (4.4) with parameters from Tab. 4.1 for the data and MC, respectively. The same correction is used for positive and negative charge particles.

Due to much lower statistics a similiar study cannot be performed for kaons and protons. We therefore apply the same correction  $\delta\varepsilon^{\text{TOF}}(p_T)$  to the TOF efficiency for  $K^\pm$  and  $p(\bar{p})$ .

After our study of systematic uncertainty of the TOF efficiency we decided to introduce another correction, on top of the correction derived in this Section. The details can be found in in Sec. 10.2.2.

## 4.2 Data driven corrections to RP efficiency

Study of systematic uncertainty of the RP track reconstruction efficiency revealed that in some part of the fiducial area of RP detectors a correction needs to be applied to the efficiency obtained from the MC simulation. The details can be found in in Sec. 10.3.1.

## 5. Energy Loss Correction

Particles passing through the detector material lose energy as they travel. The track momentum  $p_T$  is reconstructed by fitting a helical path to the track points left in the detector. Fitting the track points to an ideal helical track tends to underestimate the momentum due to these energy loss effects. To minimize biases due to this effect, correction procedure is applied during standard track momentum reconstruction for both data and MC simulation. For this procedure pion hypothesis is used and the reconstructed momentum  $p_T^{meas}$  is corrected by the amount of energy loss specific for a pion. For all particles but a pion some rest bias is still present since energy loss is specific for each particle type. These biases can be determined from simulated tracks run through GEANT. The correction  $p_T^{meas} - p_T^{true}$  was calculated for each particle species as a function of  $p_T^{meas}$ ,  $\eta$  and  $z$ -vertex. The sample energy loss correction averaged over  $|\eta| < 0.7$  for  $K^-$  is shown in Fig. 5.1. The energy loss corrections for other particle species are shown in Figs. C.1 to C.10 in Appendix C.

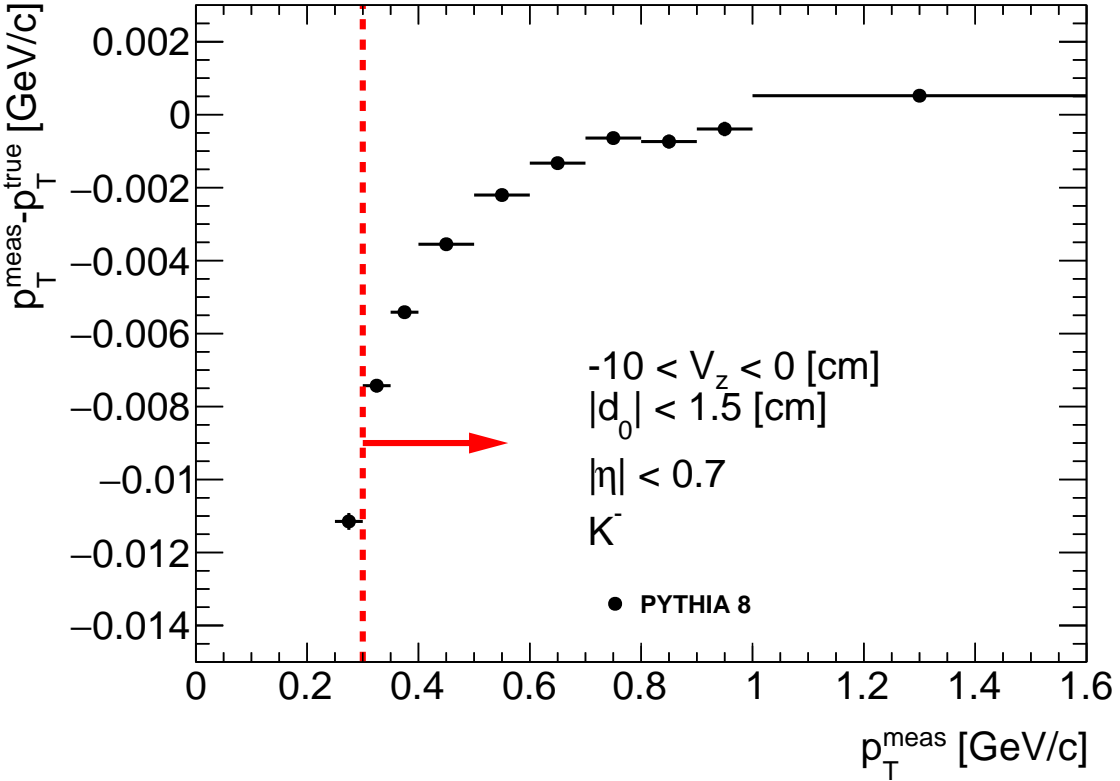


Figure 5.1: Sample energy loss correction  $p_T^{meas} - p_T^{true}$  for  $K^-$  as a function of reconstructed transverse momentum  $p_T^{meas}$  ( $|\eta| < 0.7$ ) in single  $z$ -vertex bin,  $-10 < V_z < 0$  cm. Red lines and arrows indicate region accepted in analyses.

# 6. Forward protons

One of the main detector systems used in our analyses is the Roman Pot setup in Phase II\* configuration (Roman Pots in Phase I took data with STAR during special runs in last days of  $p+p$  collisions in 2009, see e.g. Ref. [11–13]). It allowed to trigger on forward protons and reconstruct their momentum with high efficiency and precision.

## 6.1 Detector layout



Figure 6.1: Schematic representation (top view) of the Roman Pot Phase II\* at STAR (not to scale).

As presented in Figure 6.1 the Roman Pot Phase II\* setup consists of detectors located in two stations on each side of the interaction point (IP) in a distance of 15.8 m and 17.6 m from the IP. Each station has two Roman Pots positioned vertically, one above and the other below the beamline (Fig. 6.2). Detectors are situated downstream the DX dipole magnets responsible for head-on targeting of the incoming beams and bending outgoing beams back into the accelerator pipeline. The constant and uniform magnetic field of the DX magnet works as a spectrometer and thus knowledge on the track angle and position in the detector allows complete reconstruction of the proton momentum, including the fractional momentum loss  $\xi$  (as described in [14]). The naming convention of elements of RP setup is described in Ref. [15].

Single Roman Pot (the vessel, Fig. 6.5) houses a package of 4 silicon strip detector planes (Fig. 6.6) - one pair of SSDs with vertical and one with horizontal orientation of the strips, and hence measurement of the position of a proton hit is possible in both transverse spatial coordinates,  $x$  and  $y$ . The pitch (distance between neighbouring strips) in a single detector is  $100 \mu\text{m}$ , therefore intrinsic spatial resolution is at the level of  $100/\sqrt{12} \approx 30 \mu\text{m}$ . In addition to the silicon detectors, the package contains plastic scintillator that covers whole active area of the silicon, attached at the back. Two lightguides are glued at the top edge of scintillator which direct the light generated when ionizing particle passes through it to the photomultiplier tubes (PMTs) connected at the very end of each. This counter is used to trigger on forward protons and also provides the timing information.

## 6.2 Roman Pot data reconstruction

### 6.2.1 Roman Pot track points and tracks

Roman Pot data is stored in MuDST in StMuRpsCollection. This class contains objects reconstructed with St\_pp2pp\_Maker. The basic (low-level) data objects are the clusters characterized by their length (number of adjacent strips with signal above the threshold), energy (sum of ADC counts in each constituent strip) and

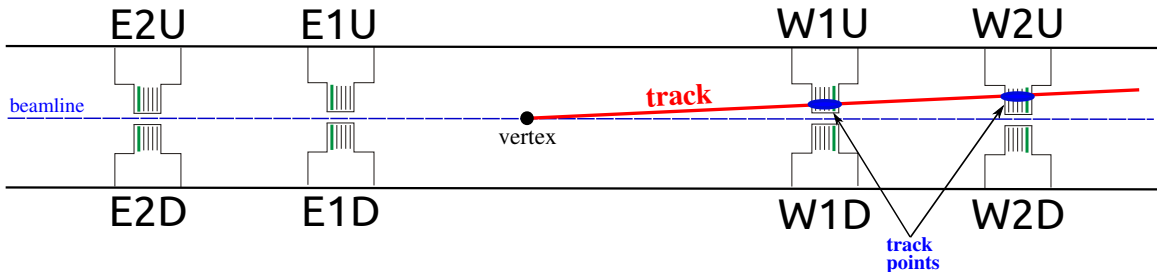


Figure 6.2: Side view of the Roman Pot Phase II\* setup (not to scale) with an illustration of Roman Pot track point and track.

position. Vectors of clusters are provided independently for each silicon plane. Another low-level data are informations about time (TAC) and signal strength (ADC) for each PMT.

Our physics analyses utilized mainly the high-level objects which are the track points (StMuRpsTrackPoint) and tracks (StMuRpsTrack) stored in vector members of StMuRpsCollection. In short, these objects represent real particles (e.g. their momentum vector) in the same way as the TPC tracks represent particles traversing TPC. Concept of track point and track is depicted in Fig. 6.2 and described in some more details in Ref. [16].

The algorithm for RP track reconstruction is implemented in St\_pp2pp\_Maker. It is a multi-track algorithm which first forms track points from clusters (there may be many track points in single RP), and then form tracks from all possible combinations of track points in Roman Pots in the same branch [16,17]. The track points and tracks are additionally tuned with Roman Pot “afterburner” package (StMuRpsUtil, [18]) which recalculates positions of hits and momenta of tracks according to the final alignment corrections and known vertex position.

### 6.2.2 Alignment

Precise knowledge of positioning of detectors in space is crucial for correct reconstruction of proton momentum. Therefore a process of detector alignment was done, which involved a few steps. At first, dedicated detector survey [4] was performed before the start of run 15, which provided initial calibration of the LVDTs installed



Figure 6.3: Correlation between the hit position of constituent track point in the first RP station ( $y$ -axis) and the local angle of track ( $x$ -axis) in elastic scattering events. The  $y$ -intercept has interpretation of the average position of the interaction vertex in given coordinate.

in Roman Pot movement system. This was sufficient to know the positioning of detectors at a  $\gtrsim 1$  mm level. Next, the alignment analysis using elastic scattering events was done, as described in the analysis note of elastic proton-proton scattering [19]. This analysis provided detectors alignment in the so called “elastic scattering reference frame”, by design close to the global (STAR) reference frame. In the last step determination of the average vertex position was done, as described below.

Vertex position is not necessary to correctly reconstruct forward proton observables in elastic scattering events e.g. squared four-momentum transfer  $|t|$  - this is because one can use momentum balance constraint of elastically scattered protons (collinearity constraint) and calculate scattering angle from the straight line fit to all track points of east and west proton tracks, without knowledge where the interaction vertex was. The same approach cannot be used in other processes like Single or Central Diffraction, since there is only single forward proton (SD) or two forward protons (CD, CEP) are independent in terms of scattering angles and momentum loss.

Need for a vertex position in the reconstruction of non-beam-momentum proton tracks led to development of the method of extraction of the average vertex position using the elastic scattering data, as presented in Ref. [20]. For this purpose RP\\_ET triggers from randomly chosen runs (16085056 and 16085057) were used with single (exactly one) global RP track reconstructed on each side of the IP. Tracks were required to be collinear at  $2\sigma$  level. Selected clean sample of elastic scattering events was used to prepare the plots of the position of the track point in near RP station vs. the local angle of the RP track with respect to the global  $z$ -axis (Fig. 6.3). The least squares fit of a line (with perpendicular offsets) to all data points in the scatterplot was performed. As a result four lines were obtained, one per arm per transverse coordinate. The slope of the line has interpretation of the distance from the nominal IP ( $z = 0$ ) to the 1<sup>st</sup> RP station at 15.8 m. One can see that the slopes are well consistent with this value. The intercept of the line equals to the average position of the vertex in given coordinate. One finds that  $\langle x \rangle_{IP}$  obtained from the fits to data points in two independent elastic arms are perfectly consistent, while in  $\langle y \rangle_{IP}$  parameters differ by 1.5 standard deviations. We conclude that extracted values of average positions of the vertex are trustworthy and we can average the numbers obtained from two independent arms. As a result we use in our analyses numbers  $\langle x \rangle_{IP} = 0.42$  mm,  $\langle y \rangle_{IP} = 0.45$  mm, both in the reconstruction/recalculation of proton tracks with StMuRpsUtil package, and generation of MC events.

In Ref. [20] the method of  $\langle z \rangle_{IP}$  extraction is also presented, however the result  $\langle z \rangle_{IP} = 3$  cm is much smaller than the distance between nominal IP and the Roman Pots (3 cm compared to 15.8 m). Such small offset does not bias proton momentum reconstruction, therefore we neglect it.

Due to time dependence of the beam conditions, automatic beam orbit corrections etc., the average position of the vertex may change from run to run. The measure of this variation is a by-product of Roman Pot alignment procedure which was done for every run. In Ref. [21] the middle points of the track (MPTs, position of the track at  $z = 0$ ) are plotted as a function of run number. One can see that MPTs in  $x$  and  $y$  are roughly constant along the entire data taking period in 2015 and consistent with numbers derived in Fig. 6.3. Another cross-check for the correctness of extracted  $\langle x \rangle_{IP}$  and  $\langle y \rangle_{IP}$  was done with the use of elastic scattering MC simulation in Geant4. Several MC samples were generated with differently positioned vertex. The same procedure was performed as the one described in this section and the output values of  $\langle x \rangle_{IP}$  and  $\langle y \rangle_{IP}$  were always consistent with the true values. Also the comparisons of the hit maps of elastic scattering protons were done between the data and MC, and the best matching was found for vertex generated at  $\langle x \rangle_{IP} = 0.42$  mm and  $\langle y \rangle_{IP} = 0.45$  mm (e.g. [22]).

## 6.3 Roman Pot simulation

### 6.3.1 General description

Simulation of the STAR detector (STARsim) implemented in Geant3 does not contain a model of the Roman Pot detectors. Because of this, a dedicated simulation program ”pp2pp” was prepared to enable precise measurements with the Roman Pot data. The development of this software started in 2012 as two independent projects for “Geant4 simulation tool kit” subject at AGH UST, which were later included in B.Sc. theses of the authors. One project was devoted to modeling of the Roman Pot and Silicon Strip Detector package [23], the other was aimed to implement simulation of the collider elements with full magnet lattice (including  $B$  field) [24] between the IP and Roman Pot location in Phase I configuration (at  $z = \pm 55$  m) based on the MAD-X twiss files. At that stage the two programs were used in analyses of 2009  $p + p$  data [13, 25] taken with Roman Pots during special high- $\beta^*$  runs. Both projects were merged in 2013 and since then are continuously developed by the Krakow group.

Currently the simulation program is a standalone Geant4 application that allows to simulate any type of particle, track it from the IP to the Roman Pots location (either in Phase I/run 2009 or Phase II\*/run 2015&17 configuration) and obtain the true level and reconstructed information in the standard STAR data format - MuDST classes stored the ROOT tree. In the reconstruction the original STAR St\\_pp2pp\\_Maker class is used. The program has multiple generation options: the input can be directly from STARsim, Pythia, HepMC format or a simple text file. There are also built-in modes, such as elastic scattering event generation. One can

customize the beam conditions, magnet settings (beam energy), Roman Pot positions, and many others. The application is installed at RCF and free to use by any STAR collaborator. Implementation of extensions desired by analyzers is possible after contact with authors. Some more information about the Roman Pot simulation (geometry, usage) can be found in the presentation from the LFS-UPC PWG weekly meeting (Ref. [26]).

### 6.3.2 Detector model

The geometry of the collider elements (beampipe, magnets) and Roman Pot detectors (vessel, SSD packages) is implemented in Geant4 according to the best available sources of information. The dimensions, positioning and material of the beam pipe and magnets were taken from the technical drawings available at RHIC C-AD and were discussed with the designers of these elements. In case of Roman Pot vessels and detector packages not only technical drawings were used to find the appropriate dimensions, but also dedicated survey was made in which some elements were measured with caliper.



Figure 6.4: View of the Geant4 implementation od the Roman Pot Phase II\* detector setup.

In Fig. 6.4 we show the general view of the "world" volume in Geant4 pp2pp simulation with labeled the most significant elements of the geometry. In Fig. 6.7 we show a few shots of the Roman Pot housing and the SSD package implemented in Geant4, together with the real photographs of the Roman Pot and SSD package in Figs. 6.5 and 6.6.

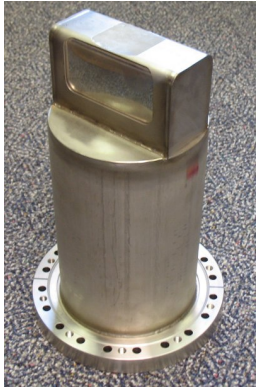


Figure 6.5: Roman Pot vessel (photo).

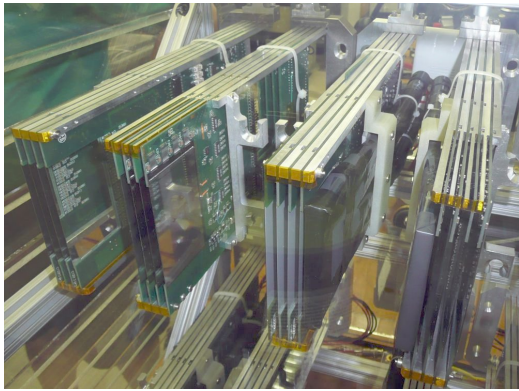


Figure 6.6: Silicon Strip Detector packages stored in the protective atmosphere (photo).

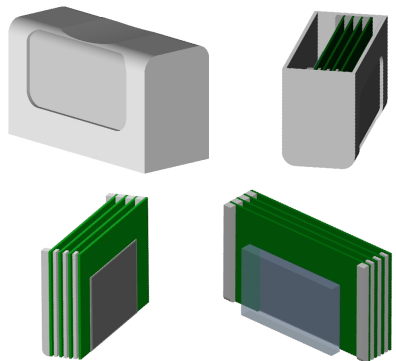


Figure 6.7: Geant4 implementations of the Roman Pot vessel and SSD package with trigger counter.

### 6.3.3 Aperture tuning

It turned out during initial validations of the Geant4 simulation for run 15 with elastic proton-proton scattering events that the distribution of the  $(x, y)$  position of the proton in Roman Pots does not agree between the data and MC at a satisfactory level. It was understood that the perfect positioning of the elements of the collider

assumed in the geometry model may need some tuning, especially the positioning DX magnet which particularly limits acceptance of the RP detectors. The DX magnets are moved each time the switch between symmetric (e.g.  $p + p$ ) and asymmetric (e.g.  $p + Au$ ) collisions takes place to accommodate for the non-zero tilt of the beams in asymmetric collisions required to close beam orbits and provide collisions in the STAR IR. Therefore lateral offset of this element was expected to be the most significant ingredient needed to correctly describe forward proton acceptance in the RP location.

In order to quantitatively determine the agreement between the true DX position and position implemented in Geant4 a dedicated analysis of the DX “shadow” in the proton hit maps was performed. This algorithm looked for the sharp drop of event counts along the  $x$  coordinate in the histogram of  $y$ - vs.  $x$ -position of the track points in collinear elastic scattering events with single proton tracks on both sides of the IP. The result (for a single RP station) is presented in Fig. 6.8a and 6.8b for the data and MC, respectively. The envelope of the DX shadow found by the algorithm is marked with black circles. The points were transformed by swapping  $x$  and  $y$  axis and fitted with a circle, as shown in Fig. 6.8c. The parameters of the circle (radius  $R$  and center point  $(x_0, y_0)$ ) do not reflect directly the position of the DX, but they were used to find the best shift of the



Figure 6.8: Sample hit map of track points of proton tracks in events selected as elastic scattering in the data (6.8a) and MC (6.8b) with the DX aperture “shadow” marked with black points. The DX aperture envelopes were fitted with circles (6.8c) which helped to establish the offsets of DX magnet positions in  $x$  and  $y$  with respect to the ideal (nominal) geometry, leading to nearly perfect agreement between the data and MC after introducing the offsets in Geant4 geometry (6.8d).

DX on the east and west side in the iterative method. The satisfactory agreement of the DX aperture envelopes between the data and MC was finally found when the shifts of the DX magnets with respect to their nominal positions were equal to  $\Delta x_{\text{DX}}^{\text{East}} = -3.1$  mm,  $\Delta y_{\text{DX}}^{\text{East}} = 4.0$  mm,  $\Delta x_{\text{DX}}^{\text{West}} = -2.4$  mm,  $\Delta y_{\text{DX}}^{\text{West}} = 0.4$  mm. The comparison of the DX shadow envelope after the tune is shown in Fig. 6.8d. All comparisons are presented in Appendix D.

### 6.3.4 Embedding technique

The pp2pp program has an option that allows to overlay the real data with the simulated detector response to MC events. The input data can be any trigger, but most common practice is to embed simulated signal into the zero bias triggers which by definition provide unbiased information about the real environment in which data were collected.

Merging of the simulated signal with the data signal is done for both the SSD data, as well as the PMT data. In case of the PMT data for each channel the ADC (energy) is set to the sum of values in the data and simulation, while the TAC (time) is set to larger value (earlier signal) of the two. In case of the SSD data the merging is done at the level of reconstructed clusters. At the end of simulation of an event a dedicated algorithm is run for every SSD plane which adds vectors of clusters from the data and from the simulation and merges overlapping clusters (recalculates their length, sums energy, updates cluster position). This new collection of clusters is saved in StMuRpsCollection together with new vectors of StMuRpsTrackPoints and StMuRpsTracks reconstructed from this new set of clusters.

# 7. $dE/dx$ adjustment

Particle identification in our analyses is done using merged information from the TPC (specific energy loss of tracks  $dE/dx$ ) and from the TOF (time of hit matched to TPC track). As can be seen in Fig. F.5,  $dE/dx$  information from the MC events simulated in STARsim (in red) poorly matches the data points (black). This results e.g. in large systematic error of estimate of particle identification efficiency.

This problem was discussed under ticket #3272 (Ref. [27]). There were trials to improve the TPC calibration in simulation, but the problem remained. It was finally concluded that the origin of the problem lies in the model of energy loss used in the STARsim, therefore any further action was postponed.

In order to tune simulated response of the TPC in terms of  $dE/dx$ , hence also reduce the systematic uncertainty related to particle identification, a correction method was developed based on proper transformation (recalculation) of simulated  $dE/dx$  to obtain new  $dE/dx$  whose distribution matches the data. We know that  $n_X^\sigma$  (where  $X = \pi, K, p, \dots$ ) variable for particle  $X$  follows a gaussian distribution

$$n_X^\sigma = \left( \ln \frac{dE/dx}{\langle dE/dx \rangle_X} \right) / \sigma_{dE/dx}, \quad f(n_X^\sigma) = \mathcal{N}(n_X^\sigma; \mu = 0, \sigma = 1), \quad (7.1)$$

therefore  $dE/dx$  itself by definition follows log-normal distribution:

$$f(dE/dx) = \mathcal{LogN}(dE/dx; \mu = \langle dE/dx \rangle, \sigma = \sigma_{dE/dx}) = \frac{1}{\sqrt{2\pi} \cdot \sigma \cdot dE/dx} e^{-\frac{\ln^2 \frac{dE/dx}{\langle dE/dx \rangle}}{2\sigma^2}}. \quad (7.2)$$

The desired transformation should preserve the shape of  $dE/dx$  distribution so that it is still described by  $\mathcal{LogN}$ , however it should change  $\mu$  and  $\sigma$  so that these values are equal to ones in the data. The transformation that satisfies above postulate is

$$dE/dx' = c \cdot (dE/dx)^a. \quad (7.3)$$

Parameters of the distribution  $\mathcal{LogN}(dE/dx')$  are then

$$\mu' = c \cdot \mu^a, \quad \sigma' = a \cdot \sigma. \quad (7.4)$$

From above we get formulae for parameters of the transformation:

$$a = \sigma'/\sigma, \quad c = \frac{\mu'}{\mu^a}. \quad (7.5)$$

To sum up, one has to find the MPV and width parameter of the  $dE/dx$  spectrum of each particle in the data and MC, and use relations (7.5) in order to find parameters of the transformation introduced in Eq. (7.3).

The most challenging part of the task was extraction of the  $\langle dE/dx \rangle$  and  $\sigma_{dE/dx}$  from the data. In case of MC one can select tracks matched to true-level particles of given ID and thus separate  $dE/dx$  of different particles, which makes extraction of the distribution shape straightforward. Unfortunately, it is not possible to apply the same method to the data - here one has to deal with overlapping of the reconstructed  $dE/dx$  from different particles. Therefore fits of sum of  $f(dE/dx)$  corresponding to different particles were performed to reconstructed track  $dE/dx$  in narrow momentum bins. The width of momentum bins was chosen to compromise statistics and validity of assumption of constant parameters of  $dE/dx$  distribution over bin range.

It was found during the fitting that log-normal distribution is not a perfect model of the reconstructed  $dE/dx$ . The problems with description of the data were mainly in the tail-part of the distribution from single particle. Precise model was necessary to obtain satisfactory quality of fits and trustworthy values of parameters. After some research the best model of  $dE/dx$  distribution from single particle was found to be

$$f(dE/dx) = \begin{cases} \frac{A}{\sqrt{2\pi} \cdot \sigma \cdot dE/dx} \exp \left( -\frac{1}{2} \left( \frac{\ln \frac{dE/dx}{\langle dE/dx \rangle}}{\sigma} \right)^2 \right) & \text{for } \frac{\ln \frac{dE/dx}{\langle dE/dx \rangle}}{\sigma} \leq k \\ \frac{A}{\sqrt{2\pi} \cdot \sigma \cdot dE/dx} \exp \left( -k \cdot \frac{\ln \frac{dE/dx}{\langle dE/dx \rangle}}{\sigma} + \frac{1}{2} k^2 \right) & \text{for } \frac{\ln \frac{dE/dx}{\langle dE/dx \rangle}}{\sigma} > k. \end{cases} \quad (7.6)$$

Such form was motivated by the function presented in Ref. [28], here adopted for the log-normal instead of normal distribution. Because the modification of the log-normal distribution is introduced only at high-end tail, the validity of the transformation discussed above still holds. To reduce fit complexity the  $k$  parameter was set the same for all particle species and fixed to value equal 2.2, which worked well for both data and embedded MC. Particles and their anti-particles were assumed to have the same  $dE/dx$  distributions for a given momentum and were analyzed together. The same track selection was used both for data and MC, with the quality criteria



Figure 7.1: Sample fit of sum of functions from Eq. (7.6) corresponding to different particle species to  $dE/dx$  spectra in the data in a single momentum bin.



Figure 7.2: Difference between MPV of  $dE/dx$  predicted by Bichsel parametrization and obtained from the fit of Eq. (7.6) to  $dE/dx$  distribution in the data (7.2c) and MC sample (7.2a) and  $dE/dx$  width parameter in data (7.2d) and MC (7.2b) as a function of reconstructed particle momentum for a few particle species. Solid lines represent fits to points of corresponding color. Only statistical errors are shown.

described in Sec. 2. The sample fit in a single momentum bin can be found in Fig. 7.1. Fits in all momentum bins can be found in Appendix F.

Results of the fits for all considered particle species (pions, kaons, protons, electrons and deuterons) are commonly presented in Fig. 7.2 with color markers. Figures 7.2c and 7.2a show the offset of the MPV of reconstructed  $dE/dx$  relative to the Bichsel parametrization in the data and embedded MC, respectively, and Fig. 7.2d and 7.2b show the width of reconstructed  $dE/dx$  (in the same order). Function able to qualitatively describe dependence of the parameters as a function of track momentum was empirically found to be given by Eq. (7.7):

$$g(p) = P_1 + P_2 \cdot \exp(-P_3 \cdot p) + P_4 \cdot \arctan(P_5 \cdot (p - P_6)) \quad (7.7)$$

This function was fitted to points corresponding to each particle type and fit result is shown in Fig. 7.2 with lines colored in accordance to markers. Values of parameters of above function are tabulated in Tab. 7.1.

PID	$\langle dE/dx \rangle_{\text{Bichsel}} - \langle dE/dx \rangle_{\text{MC}}$						$\sigma(dE/dx)_{\text{MC}}$					
	$P_1$	$P_2$	$P_3$	$P_4$	$P_5$	$P_6$	$P_1$	$P_2$	$P_3$	$P_4$	$P_5$	$P_6$
$\pi^\pm$	7.183e-8	-1.647e-4	41.68				0.0705			-1.42e-3	9.860	0.951
$K^\pm$	4.359e-8	-9.285e-6	7.697				0.0511	0.034	1.675	1.01e-2	4.934	0.528
$p, \bar{p}$	3.556e-8	-8.621e-6	3.980				0.0630	-7.725	27.17	3.37e-3	5.245	0.670
$e^\pm$	-6.219e-8	2.065e-7	3.241				0.0354	0.982	26.58	1.79e-2	41.515	0.095
$d, \bar{d}$	-1.305e-6	-5.268e-6	3.486				0.0967	-1526	18.75			

PID	$\langle dE/dx \rangle_{\text{Bichsel}} - \langle dE/dx \rangle_{\text{Data}}$						$\sigma(dE/dx)_{\text{Data}}$					
	$P_1$	$P_2$	$P_3$	$P_4$	$P_5$	$P_6$	$P_1$	$P_2$	$P_3$	$P_4$	$P_5$	$P_6$
$\pi^\pm$	-1.399e-8	2.012e-7	10.39				0.0734	1.907	31.86	-8.20e-4	22.788	0.653
$K^\pm$	2.325e-9	-3.690e-6	8.712				0.0808	-0.040	7.951	5.62e-3	-17.08	0.269
$p, \bar{p}$	-1.458e-7	0.6655	59.06	1.171e-7	4.660	0.644	0.0795	0.181	12.12			
$e^\pm$	9.005e-8	2.494e-7	8.834				0.0680	8.8e-4	1.549			
$d, \bar{d}$	-1.910e-7	5.637e-3	14.48				0.1161	-0.147	2.890			

(a)

(b)

Table 7.1: Parameters of functions from Fig. 7.2 describing reconstructed track  $dE/dx$  as a function of reconstructed momentum for a few particle species in the data (7.1b) and embedded MC (7.1a). Blank cells denote parameters equal 0. Units of parameters  $P_i$  are such that if one provides momentum in Eq. (7.7) in  $\text{GeV}/c$  the resultant offset of  $dE/dx$  MPV with respect to Bichsel parametrization is in  $\text{GeV}/\text{cm}$ , and the resultant  $\sigma$  parameter is unitless.

The correctness of the entire procedure described in this section was verified by comparing the reconstructed track  $dE/dx$  between the data and embedded MC without and with the  $dE/dx$  transformed using Eq. (7.3) and parameters from Tab. 7.1. Some difficulty arised in this comparison due to inconsistent relative content of different particle species in the data and embedded MC sample. Problem was ressolved by separating  $dE/dx$  histograms of different particle species in MC (in the same way as it was done for extraction of  $dE/dx$  MPV and  $\sigma$  for each particle ID) and fitting the sum of histograms from different particle types to the data histogram (in momentum bins). The only free parameters in the fit were relative contents of histogram from singe particle type in the data histogram. A sample comparison between the  $dE/dx$  in data and embedded MC is presented in Fig. 7.3. Comparison in all other momentum bins is contained in Appendix F (Fig. F.5). Fits were done for adjusted  $dE/dx$  (filled green). Histograms for unadjusted  $dE/dx$  (hashed red) were composed using the same relative content of particles as obtained from the fit of adjusted  $dE/dx$ . The ratio of the MC to the data shown in the lower pad of Fig. 7.3 and Fig. F.5 clearly demonstrates better agreement of the MC and the data in terms of position and width of peaks in  $dE/dx$  spectrum after the adjustment.

Exactly the same cross-check was done for  $n_X^\sigma$  variables, which are directly used to identify particles in our analyses. They carry information about the distance (in width units) of reconstructed  $dE/dx$  from the MPV of  $dE/dx$  according to Bichsel parametrization - they are kind of a pull variables. For every track  $n_X^\sigma$  was recalculated using its definition as shown in Eq. (7.8):

$$n_X^\sigma = \ln \left( \frac{dE/dx'}{\langle dE/dx \rangle_{\text{Bichsel}}^X} \right) / \delta(dE/dx), \quad (7.8)$$

where instead of original  $dE/dx$  the adjusted one ( $dE/dx'$ ) was used. Uncertainty of reconstructed  $dE/dx$ ,  $\delta(dE/dx)$ , was left unchanged. The sample comparison of  $n_{\text{pion}}^\sigma$ ,  $n_{\text{kaon}}^\sigma$  and  $n_{\text{proton}}^\sigma$  variables can be found in Fig. 7.4. Comparison in full set of momentum bins is placed in Appendix F. As in case of  $dE/dx$  comparison,

in the lower pads of Fig. 7.4 the ratio of the MC to the data also demonstrates better agreement of the MC and the data, which was the goal of the adjustment.

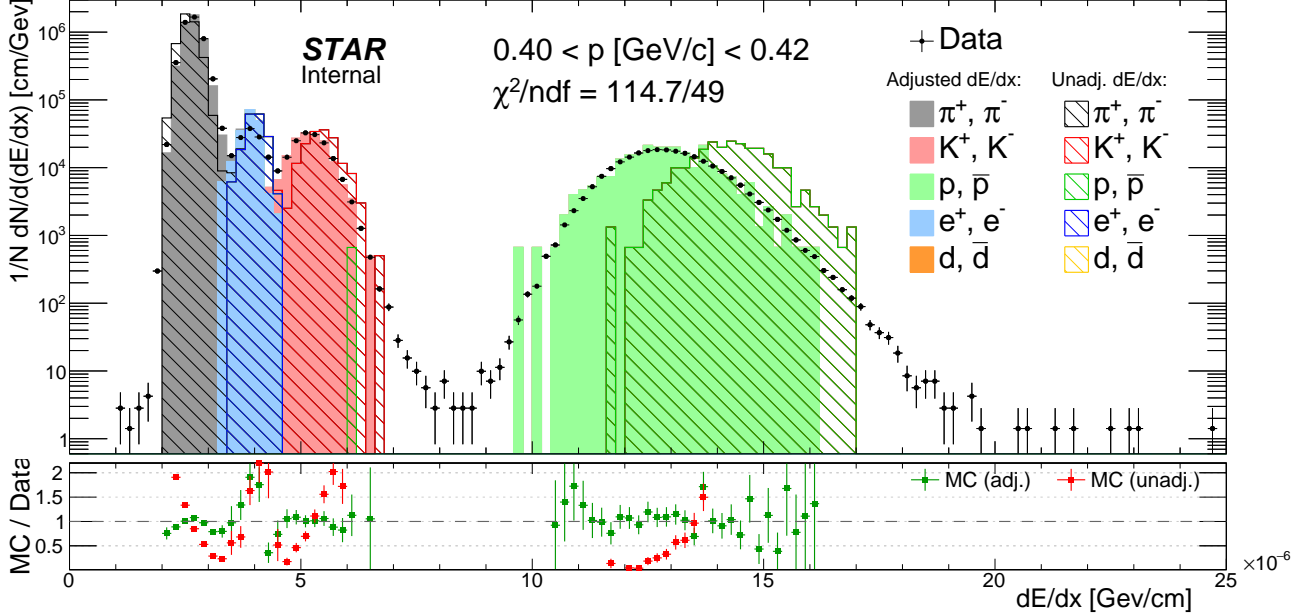


Figure 7.3: Sample comparison of  $dE/dx$  spectrum between data and embedded MC (before and after  $dE/dx$  adjustment) in a single momentum bin. Lower pad shows the ratio between embedded MC and data before and after  $dE/dx$  adjustment. In both upper and lower pads the same color code is used. Only statistical errors are shown. Due to limited statistics of embedded MC some data points do not have corresponding entries in MC.



Figure 7.4: Sample comparison of  $n_\sigma_{\text{pion}}$  (7.4a),  $n_\sigma_{\text{kaon}}$  (7.4b) and  $n_\sigma_{\text{proton}}$  (7.4c) distribution between data and embedded MC in single momentum bin. Lower pads show the ratio between embedded MC and data before and after  $dE/dx$  adjustment. In both upper and lower pads the same color code is used. Only statistical errors are shown.

# 8. TPC track pointing resolution adjustment

It was found during the analysis that distributions of quantities which describe the pointing resolution of the TPC tracks do not agree well between the data and embedded MC. Namely, the resolutions of the global helices associated with the tracks were found to be significantly better in the STAR simulation than in the data, what manifests as narrower DCA and  $d_0$  distribution in the embedded MC, comparing to corresponding distribution in the data (Fig. 8.5). This issue was discussed under ticket #3332 (Ref. [29]).

This problem could affect the momentum resolution and thus all other resolutions and response matrices used in data unfolding. Therefore the resolution adjustment procedure was performed to find appropriate parameters of the “artificial” helix deterioration and finally obtain agreement between DCA and  $d_0$  distributions (and all related resolutions) in the data and embedded MC.

In order to worsen pointing resolution in the MC a smearing of the helix radius  $\sigma(R)$  was introduced. Based on  $d_0$  comparison in Fig. 8.5a it was decided to account also for the small systematic bias of the helix radius  $\Delta\mu(R)$ <sup>1</sup>, which may be present e.g. due to differences in the material budget used the simulation and reconstruction. Both smearing and bias of the helix radius were introduced only for MC tracks which were matched with the true-level particles since only simulated tracks require adjustment (tracks from zero-bias event used in embedding already contain all detector effects).

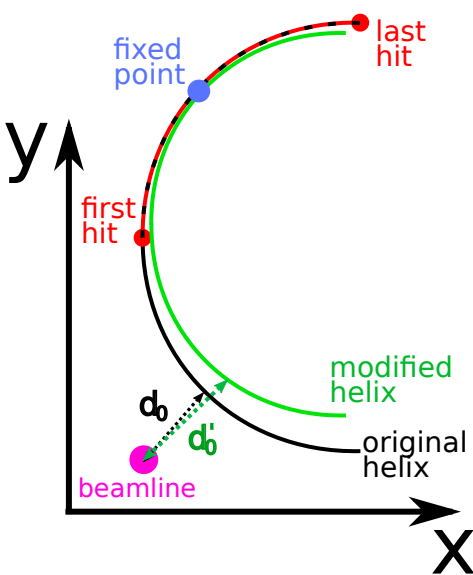


Figure 8.1: Sketch of helix modification procedure and  $d_0$  calculation.

Extraction of  $\Delta\mu(R)$  and  $\sigma(R)$  parameter required to achieve agreement of pointing resolution between embedded MC and the data involved a few steps, as listed below:

1. Series of  $d_0$  histograms in bins of  $p_T$  (100 MeV/c wide) was prepared, each for different size of distortion (different  $\Delta\mu(R)$  and  $\sigma(R)$ ) of global helix of the TPC tracks matched with true-level particles (example plot in single  $p_T$  bin is shown in Fig. 8.2):

- (a) for each set of parameters  $\Delta\mu(R)$  and  $\sigma(R)$  the helix radius  $R$  was recalculated independently for each track following the Eq. (8.1):

$$R' = R \times \mathcal{N}(1 + \Delta\mu(R), \sigma(R)), \quad (8.1)$$

- (b) new helix of a radius  $R'$  was assigned to a track and used to calculate  $d_0$ . The modified helix was obtained by changing the radius of original helix from  $R$  to  $R'$  with a fixed middle point between the first and last TPC hit of a global track represented by the helix (Fig. 8.1). The momentum of the track was also recalculated:

$$p'_T = p_T \times \frac{R'}{R}, \quad \eta' = \eta \times \frac{R'}{R}. \quad (8.2)$$

2. In each  $p_T$  bin the  $\chi^2/\text{NDF}$  was calculated between the data and MC  $d_0$  histogram in a range  $-1.5 \text{ cm} < d_0 < 1.5 \text{ cm}$  (corresponding to  $d_0$  cut used in analyses), for every point in parameter space of radius distortion (for every set of  $\Delta\mu(R)$  and  $\sigma(R)$ ). An example (single  $p_T$  bin) of map of  $-\chi^2/\text{NDF}$  in a parameter space is presented in Fig 8.3.
3. In each bin of recalculated  $p_T$  the 2-dim parabola  $z(x, y; a, b, x_0, y_0, z_0)$  given in Eq. (8.3) ( $z = \chi^2/\text{NDF}$ ,  $x = \Delta\mu(R)$ ,  $y = \sigma(R)$ ) was fitted to  $-\chi^2/\text{NDF}$  in the global minimum region to obtain the best-fit distortion parameters.  

$$z = z_0 - a(x - x_0)^2 - b(y - y_0)^2. \quad (8.3)$$
4. The best-fit smearing  $\sigma(R)$  (equal to parabola parameter  $y_0$ ) and best-fit bias  $\Delta\mu(R)$  ( $x_0$ ) from individual  $p_T$  bins was plotted as a function of global track  $p_T$  (Fig. 8.4). Each point was assigned with an error being a quadratic sum of two components: the error on  $x_0$  ( $y_0$ ) resulting from the parabola fit to  $-\chi^2/\text{NDF}$ , and length of corresponding semi-axis of ellipsis formed by the intersection of fitted parabola with the  $xy$ -plane at  $z = z_0 - 1/\text{NDF}$  (from definition of the parameter uncertainty given by the change of overall  $\chi^2$  by 1 unit). Resultant formulae for the error of each individual point in Fig. 8.4 are

<sup>1</sup>Transverse impact parameter  $d_0$  takes positive value if the beamline is contained inside the helix (in the  $yz$ -plane projection), otherwise it is negative. Any asymmetry in the  $d_0$  distribution in the MC with respect to the data indicates presence of systematic difference in reconstructed  $d_0$ , hence also in reconstructed  $R$ .



Figure 8.2: Example of comparison of  $d_0$  histograms in single  $p_T$  bin in the data (black points) and embedded MC (colored lines) in the procedure of TPC pointing resolution adjustment. Only MC histograms for  $\Delta\mu(R) = 0$  and  $\sigma(R) = 0, 5 \times 10^{-3}$  and  $10^{-2}$  were shown for explanatory purposes.

$$\delta(\Delta\mu(R)) = \sqrt{\delta_{\text{fit}}^2(x_0) + \frac{1}{2a\text{NDF}}}, \quad (8.4)$$

From Fig. 8.2 one can read that  $\text{NDF} = 14$ . In calculation of uncertainties correlation of  $\Delta\mu(R)$  and  $\sigma(R)$  have not been accounted.

5. The empirically determined functions were fitted to points representing  $\Delta\mu(R)$  and  $\sigma(R)$  dependence on the global track  $p_T$ . Their form and values of parameters are given in Fig. 8.4.

Helices of global TPC tracks were deteriorated according to Eq. (8.1) and the parametrizations of global track  $p_T$ -dependence of  $\Delta\mu(R)$  and  $\sigma(R)$  from Fig. 8.4, to verify if better agreement between the data and embedded MC is found after the adjustment. Filled histograms in Fig. 8.5 show  $d_0$  and DCA distributions after the described adjustment, and filled circles in the bottom pad show their ratio to the data points. Clearly, there is much better agreement between embedded MC and the data after the pointing resolution adjustment. Remaining differences may arise from incomplete theoretical model of the CEP process implemented in GenEx leading to different  $p_T$  spectra of the data and the model (e.g. model does not contain resonant  $\pi^+\pi^-$  production).

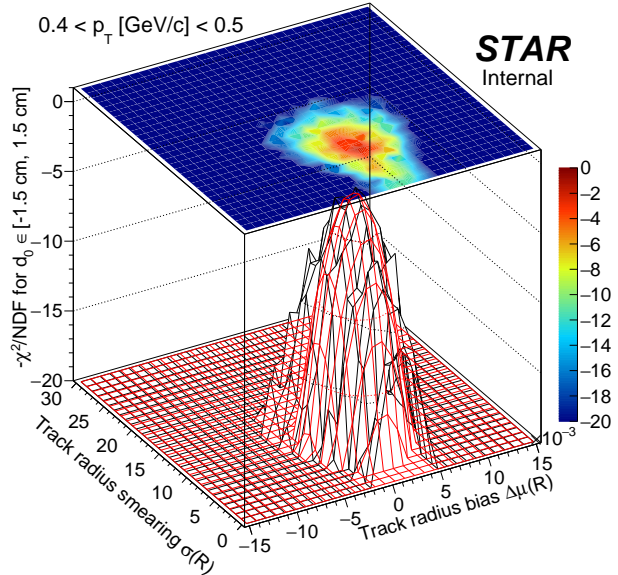


Figure 8.3: Example of  $-\chi^2/\text{NDF}$  map in a parameter space in the procedure of TPC pointing resolution adjustment. The red surface represents parabola fitted in the vicinity of the global minimum.

$$\delta(\sigma(R)) = \sqrt{\delta_{\text{fit}}^2(y_0) + \frac{1}{2b\text{NDF}}}. \quad (8.5)$$

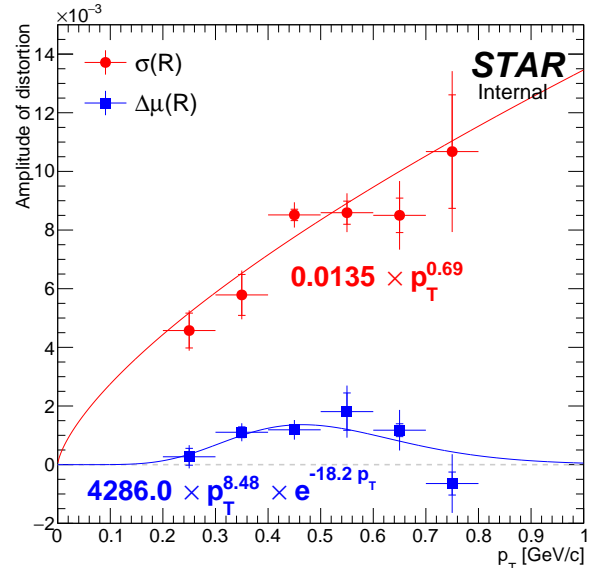
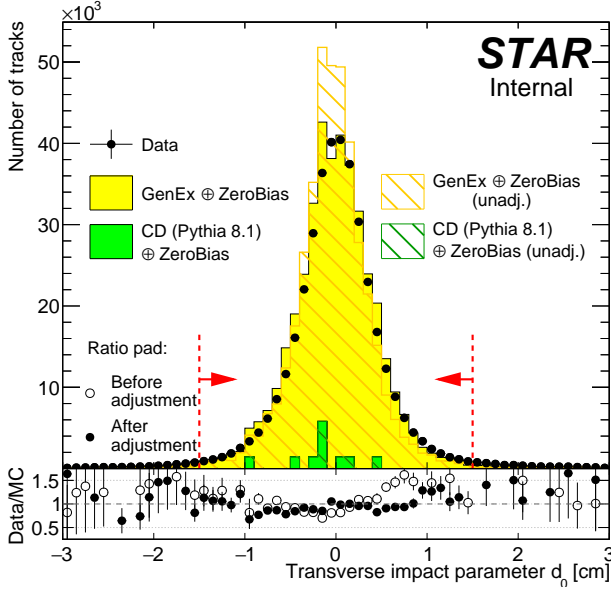
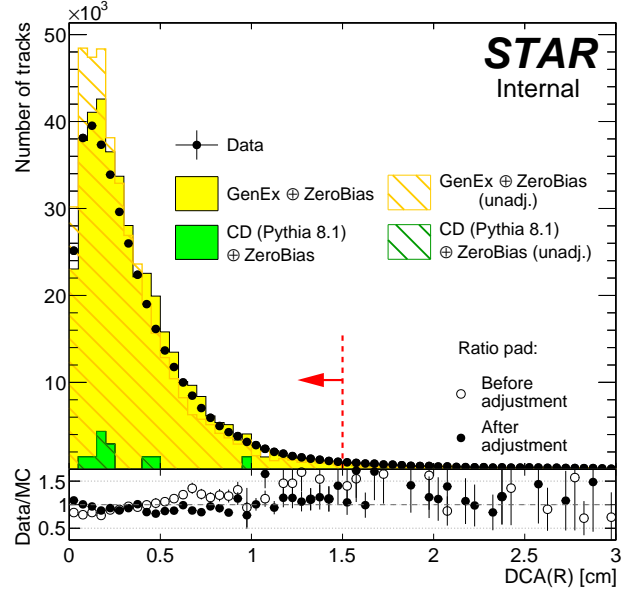


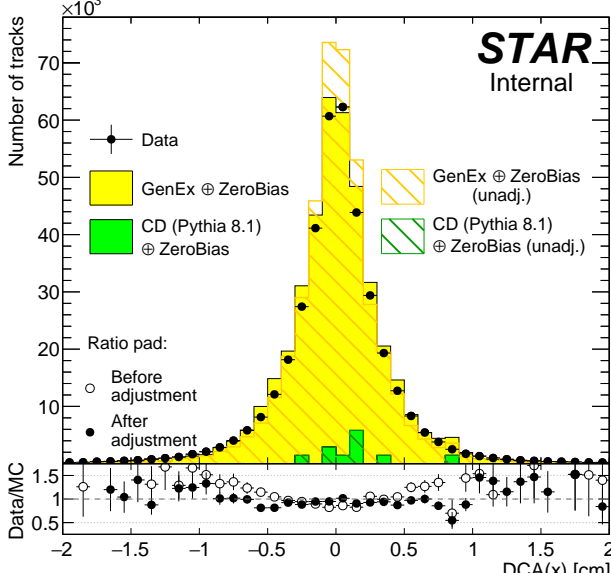
Figure 8.4: Best-fit parameters obtained in the procedure of the TPC track pointing resolution adjustment. Uncertainties on parameters resulting solely from the fit of Eq. (8.3) to  $-\chi^2/\text{NDF}$  are represented by the lines with perpendicular endings. Total uncertainties (Eqs. (8.4), (8.5)) extend beyond. The empirical functions fitted to points are drawn with corresponding colors, and formula of each is written aside.



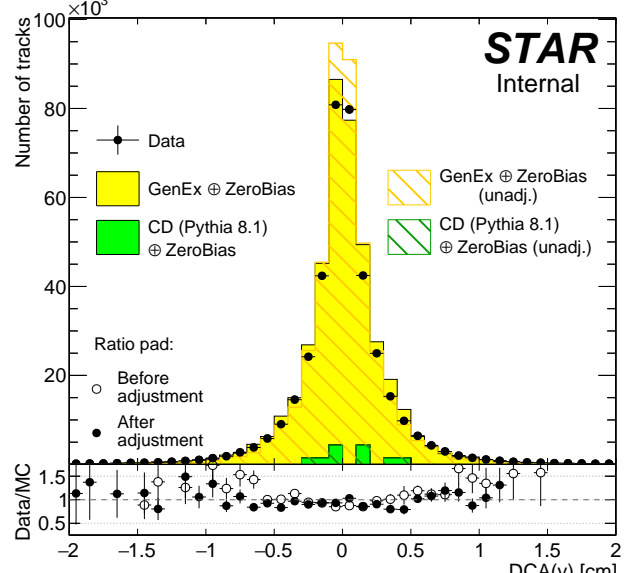
(a)



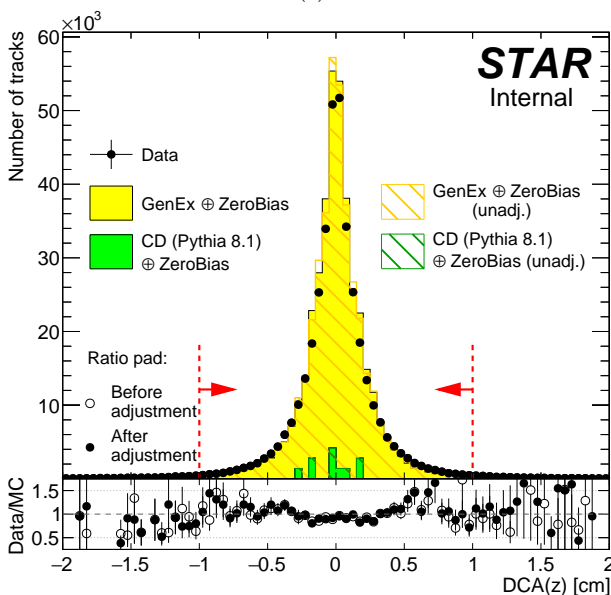
(b)



(c)



(d)



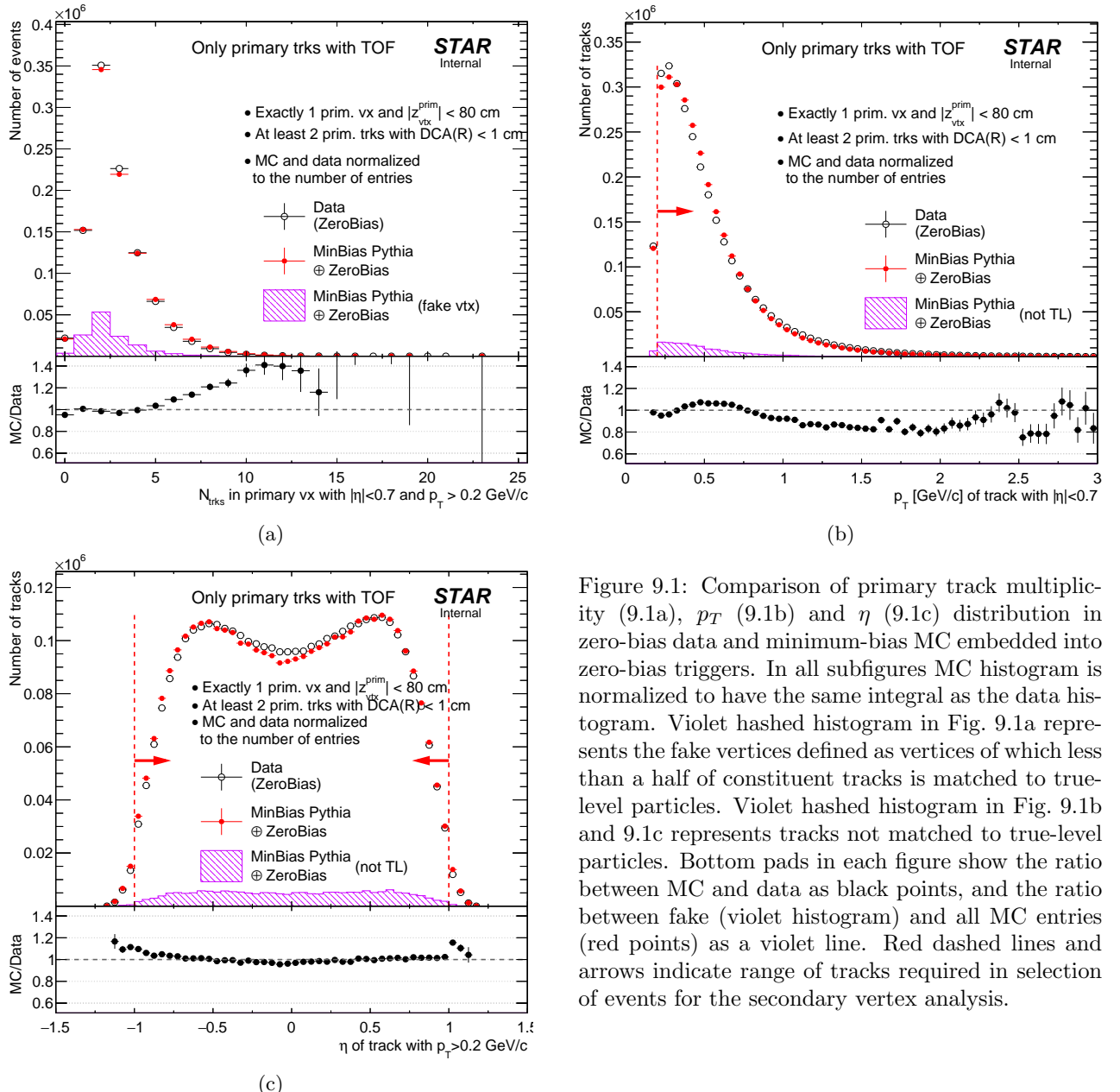
(e)

Figure 8.5: Comparison of distribution of pion transverse impact parameter  $d_0$  (8.5a) and transverse (8.5b),  $x$ - (8.5c),  $y$ - (8.5d) and  $z$ -component (8.5e) of the DCA vector between the global helix and primary vertex in the data (CEP) and embedded MC (GenEx). Distributions for unadjusted helices are drawn as hashed histograms, while filled histograms are for adjusted helices. Normalizations of the signal and backgrounds were established from the comparison of  $p_T^{\text{miss}}$  and  $\Delta\theta$  distributions after full selection (without cut on the presented quantity and without exclusivity cut), as described in Sec. XXX of Ref. [1]. Red dashed lines and red arrows indicate the range of each quantity which is accepted in analyses.

# 9. Dead material in front of TPC

Particle detected and reconstructed in the TPC must first pass through the detector material standing in between the accelerator vacuum and TPC gas. This affects track reconstruction efficiency, as the particle may interact with that material - in worst case inelastically, and induce secondary particles thus lower reconstruction efficiency. Accuracy of modeling of the detector material in the STAR simulation, especially in run 15 with the HFT installed, influences systematic error e.g. on the TPC track reconstruction efficiency. In this section the density of secondary vertices is compared between the data and embedded MC. The density of secondary vertices is directly proportional to the amount of the material in given volume, hence any discrepancy between secondary vertex distribution in the data and MC can be a hint for inaccuracies of the STAR simulation which should be accordingly covered by the systematic uncertainties. It should be stressed that this analysis is not aimed to tune the material budget in the STAR simulation, as there are much better data for this than high-luminosity proton-proton collisions from run 15. The aim of presented study is to obtain reasonable estimate of the component of systematic uncertainty of the TPC track reconstruction efficiency related to the error on the amount and distribution of inactive material.

Analysis of the distribution of secondary vertices was performed using both zero-bias (ZB) data and minimum-bias MC (Pythia) embedded into zero-bias triggers. Because of insufficient statistics of the ZB data, for the purpose of analysis presented in this section both standard ZB data sample (from ZB triggers in st\_rp stream) and the subsample of RP\_CP triggers (see Ref. [7] for trigger details) with identified elastic proton-proton scat-



tering events using loose RP track selection were used. The latter subsample is in good approximation a ZB sample in terms of central detector, as it was triggered only by the east and west coincidence of Roman Pots - any particle present in the TPC and TOF is predominantly a product of pile-up interaction. In all plots and later in the text we refer to this merged sample as ZB data sample.

Analysis started with the following selection of events:

1. Exactly 1 reconstructed primary vertex (with tracks matched to hits in TOF; beamline constraint was used in reconstruction therefore primary vertices lie on the beamline and tracks associated with them have global DCA ( $d_0$ ) not larger than  $\approx 1.5$  cm),
2.  $|z_{vx}| < 80$  cm,
3.  $\geq 2$  prim. TOF tracks with:  $DCA(R) < 1$  cm,  $|\eta| < 1$ ,  $p_T > 0.2$  GeV/c,  $N_{\text{hits}}^{\text{fit}} \geq 25$ ,  $N_{\text{hits}}^{\text{dE/dx}} \geq 15$ .

The aim of above criteria was to select pile-up-free events with well defined vertex. Cut on  $z$ -vertex is identical to one used in physics analyses. Figure 9.1 shows comparison of quantities characterizing an event. In general a moderate agreement between MC and data can be observed, considered sufficient for trustworthy result of described analysis.

As a next step the TPC tracks were selected for the search and reconstruction of secondary vertices. The requirements were as follows:

1. Global TPC tracks matched with TOF not associated with any primary TPC track,
2.  $|\eta| < 0.7$ ,  $p_T > 0.2$  GeV/c,  $N_{\text{hits}}^{\text{fit}} \geq 25$ ,  $N_{\text{hits}}^{\text{dE/dx}} \geq 15$ ,
3. Distance of closest approach to the STAR  $z$ -axis ( $x, y = (0, 0)$ ,  $d_0^{(0,0)}$ ), larger than inner radius of the beampipe:  $d_0^{(0,0)} > 2$  cm.

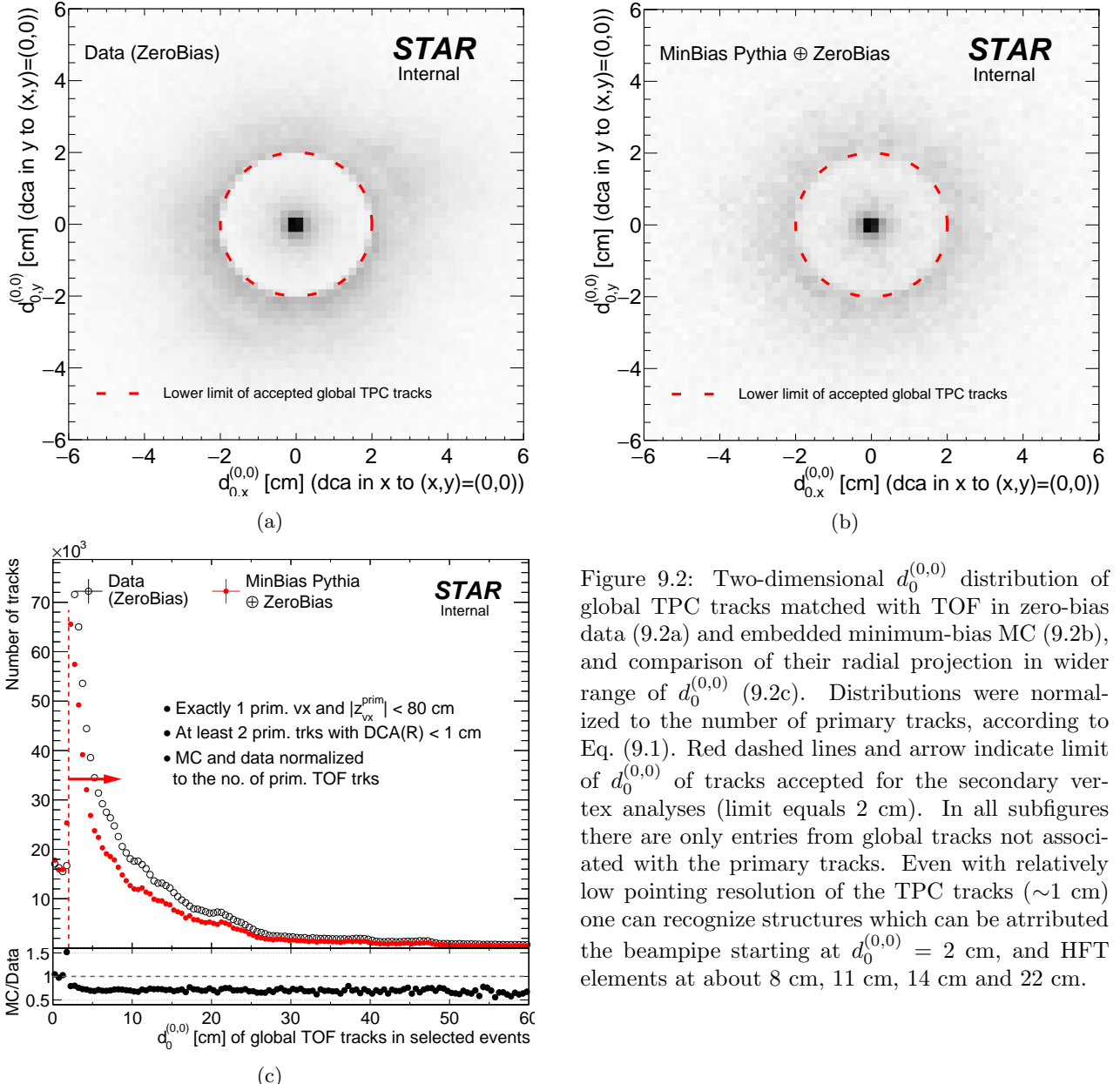


Figure 9.2: Two-dimensional  $d_0^{(0,0)}$  distribution of global TPC tracks matched with TOF in zero-bias data (9.2a) and embedded minimum-bias MC (9.2b), and comparison of their radial projection in wider range of  $d_0^{(0,0)}$  (9.2c). Distributions were normalized to the number of primary tracks, according to Eq. (9.1). Red dashed lines and arrow indicate limit of  $d_0^{(0,0)}$  of tracks accepted for the secondary vertex analyses (limit equals 2 cm). In all subfigures there are only entries from global tracks not associated with the primary tracks. Even with relatively low pointing resolution of the TPC tracks ( $\sim 1$  cm) one can recognize structures which can be attributed the beampipe starting at  $d_0^{(0,0)} = 2$  cm, and HFT elements at about 8 cm, 11 cm, 14 cm and 22 cm.

These cuts were intended to select in-time TPC tracks with high chance of being a product of secondary interaction of primary particle with the detector material. The higher limit of accepted  $d_0^{(0,0)}$  was set in analysis, the less background (fake secondary vertices) was found in the secondary vertex distribution for a price of limited access to secondary vertices of low radial distance from STAR  $z$ -axis. Cut of 2 cm was found a good compromise. In Fig. 9.2 we present comparison of  $d_0^{(0,0)}$  distribution of selected global TOF-matched TPC tracks in the data and embedded MC (without cut on  $d_0^{(0,0)}$ ). Number of secondary vertices is proportional to both material density and flux of primary particles. To remove bias due to the different fluxes of primary particles in data and simulation the latter was scaled by the following factor:

$$\text{MC normalization factor} = \frac{\langle N_{\text{trks/evt}}^{\text{DATA}} \rangle}{\langle N_{\text{trks/evt}}^{\text{MC}} \rangle} \times \frac{N_{\text{evts}}^{\text{DATA}}}{N_{\text{evts}}^{\text{MC}}} = \frac{3.78}{3.89} \times \frac{N_{\text{evts}}^{\text{DATA}}}{N_{\text{evts}}^{\text{MC}}} = \frac{N_{\text{trks}}^{\text{DATA}}}{N_{\text{trks}}^{\text{MC}}}. \quad (9.1)$$

Especially in Fig. 9.2c one can find structures/peaks that might be attributed to subdetectors (PXL, IST, SST) of the HFT. Notable is different yield of histograms which on first glance indicate different amount of simulated dead material with respect to real conditions. Another reason for this difference in yields was found in imperfect simulation of the pointing resolution of the TPC tracks. As shown in Chap. 8 the track pointing resolution is better in the STAR simulation comparing to the data, therefore in MC more true primary tracks are reconstructed as primary tracks (are forming/attached to the primary vertices), hence less such tracks are available in the selection of global tracks for secondary vertex reconstruction (comparing to data). The pointing resolution worsening which is introduced to MC tracks (see Chap. 8) does not help in this case because the track smearing is introduced after primary vertices are reconstructed (after MuDst are produced). This effect is accounted later in the background subtraction procedure to reveal the studied difference in the amount of existing and simulated dead material.

After secondary track candidates were selected, the following algorithm for secondary vertex reconstruction was used:

1. Loop over all pairs of secondary track candidates, store pairs whose DCA is less than 0.5 cm (nearby tracks passing a proximity cut),
2. Link pairs of nearby tracks into sets of tracks connected by the common nearby tracks,
3. Loop over all sets defined in 2., in each set loop over all pairs from given set, reject worst-matching tracks (these with largest DCA to others) until all pairs of tracks have DCA less than 0.5 cm,
4. Based on number of tracks in secondary vertex, total charge, specific energy loss,  $dE/dx$ , cosine of the opening angle of two tracks  $\cos(\Delta\theta)$  and invariant mass of two tracks  $m_{\text{inv}}$  determine if the vertex is from resonance decay, photoconversion or is of nuclear/hadronic nature:
  - (a) if  $\geq 2$  tracks in the vertex, or 2 tracks of the same sign, or 2 tracks of the opposite sign and cosine of the opening angle between two tracks  $\cos(\Delta\theta) < -0.99$  (tracks back-to-back) vertex is recognized as hadronic; otherwise (sub-sample of 2 opposite-sign tracks case remains)
  - (b) if  $|n_{\text{pion}}^\sigma| < 3$  for both tracks and invariant mass (assuming pion mass) is within  $[0.470, 0.515]$  GeV (Fig. 9.3a) the vertex is recognized as originating from the decay of  $K_S^0$ ; otherwise
  - (c) if  $|n_{\text{pion}}^\sigma| < 3$  for one track and  $|n_{\text{proton}}^\sigma| < 3$  for the other, and invariant mass (assuming pion and proton mass, respectively) is within  $[1.107, 1.123]$  GeV (Fig. 9.3b) the vertex is recognized as originating from the  $\Lambda/\bar{\Lambda}$  decay; otherwise

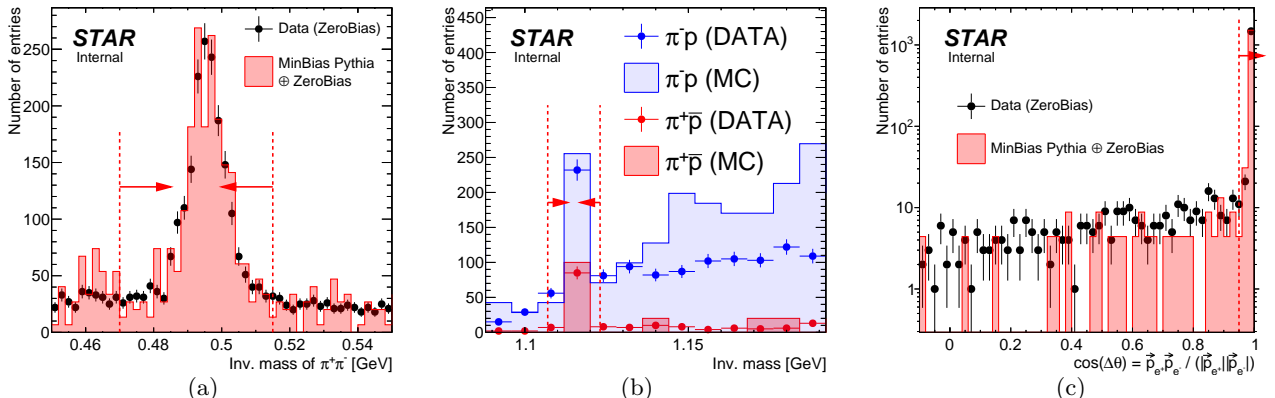


Figure 9.3: Invariant mass of two opposite-sign tracks recognized as  $\pi^+\pi^-$  (9.3a) and  $\pi^+\bar{p}/\pi^-\bar{p}$  pair (9.3b), and cosine of the opening angle between two opposite-sign tracks recognized as  $e^+e^-$  pair (9.3c), forming a secondary vertex. Dashed red lines and red arrows indicate ranges of quantities which define particular nature of the secondary vertex (photoconversion/resonance decay/hadronic). All three plots represent zero-bias data.

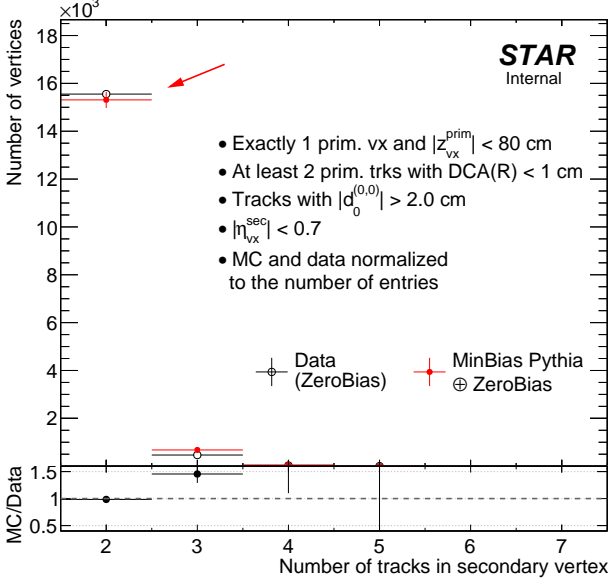
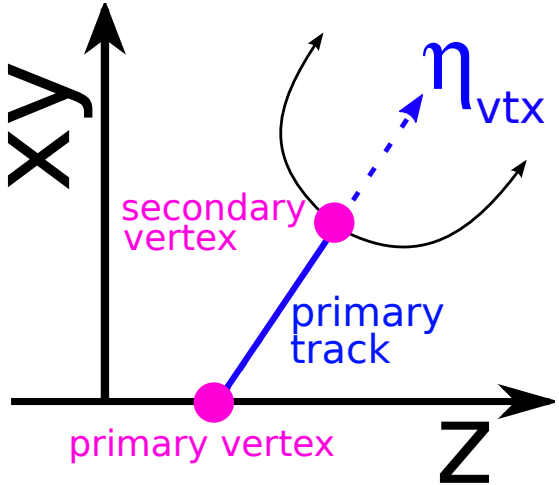


Figure 9.4: Multiplicity of tracks in reconstructed secondary vertices. Red arrow points to bin with vertices used in final analyses of vertex distribution.



- (d) if  $|n_{\text{electron}}^\sigma| < 3$  for both tracks and invariant mass (assuming electron mass) is less than 0.09 GeV and cosine of the opening angle between two tracks  $\cos(\Delta\theta) > 0.95$  (Fig. 9.3c) the vertex is recognized as originating from photoconversion; otherwise the vertex is recognized as hadronic.
- 5. Calculate the vertex position as the average DCA point of all track pairs in the vertex.

As a result secondary vertices were reconstructed, whose track multiplicity distribution is depicted in Fig. 9.4. Analysis was continued only with vertices of multiplicity equal 2. The first reason was that most of vertices consist of just a pair of tracks. Another reason was the background subtraction method developed only for vertices made of two tracks. In addition to this, only vertices representing primary particles in the pseudorapidity range  $-0.7 < \eta < 0.7$  were analyzed. To enable such selection a variable  $\eta_{\text{vtx}}$  was defined, as shown in Fig. 9.5.

Raw distributions of  $R_{\text{vtx}}^{\text{secondary}}$  and  $z_{\text{vtx}}^{\text{secondary}}$  are shown in Fig. 9.6a and Fig. 9.6b, respectively. In  $R_{\text{vtx}}^{\text{secondary}}$  spectrum one can find peaks in the regions where the HFT subdetectors are placed. Peaks seem to lie on top of a tail whose origin has been identified with the secondary vertices made of pair of tracks, one of which was a true primary tracks that was not associated with any primary vertex and unfortunately passed selection of

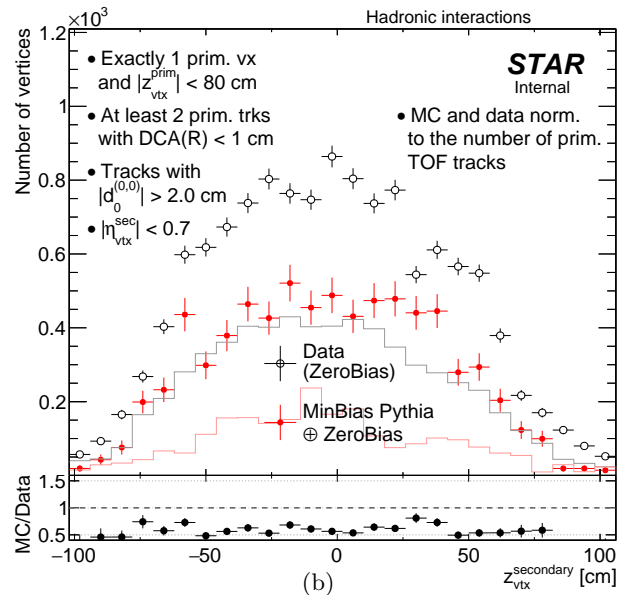
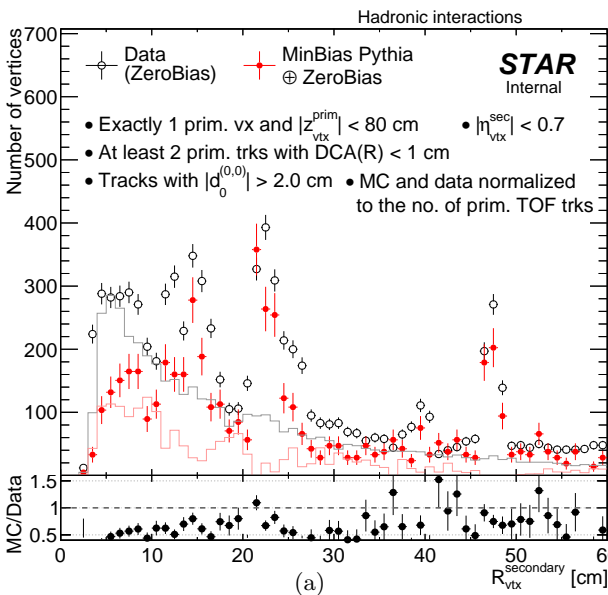


Figure 9.6: Comparison of raw  $R_{\text{vtx}}^{\text{secondary}}$  (9.6a) and  $z_{\text{vtx}}^{\text{secondary}}$  (9.6b) distribution in the data (opened black circles) and embedded MC (filled red circles). Only vertices recognized as products of hadronic interactions are shown in the figure. Solid lines denote estimated background content in the distribution of corresponding color.

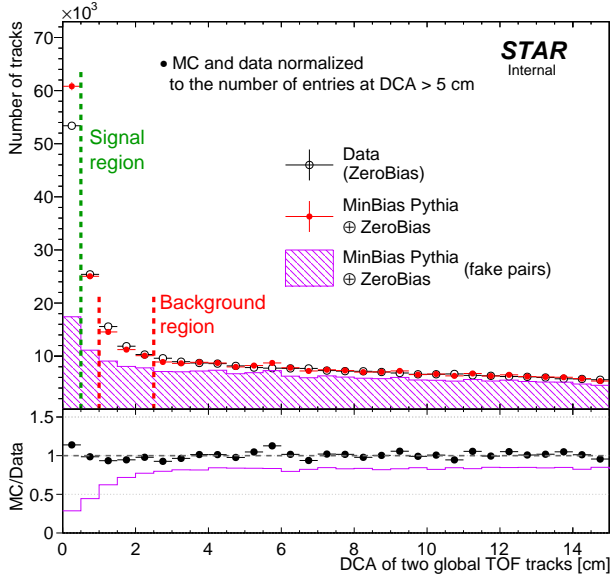


Figure 9.7: Comparison of DCA between all pairs of secondary track candidates selected for the secondary vertex reconstruction in the data and embedded MC. MC histogram is normalized to the data at  $DCA > 5$  cm. Violet hashed histogram depicts pairs contained in MC histogram and not originating from the same vertex. Solid violet line in the lower pad denotes ratio of violet and red histogram.

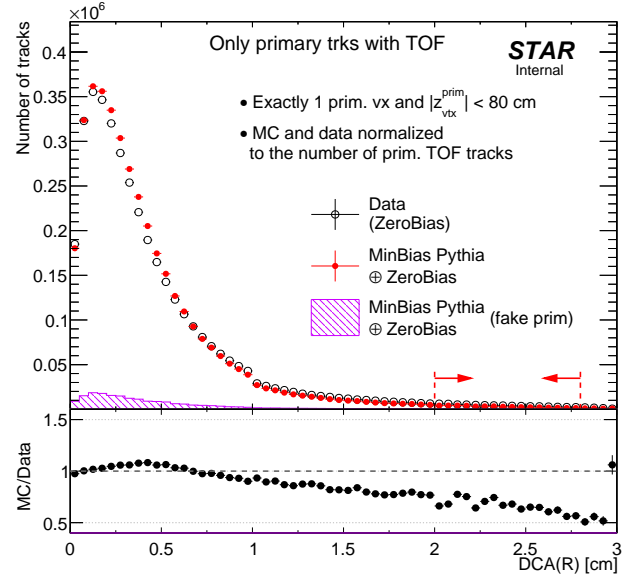


Figure 9.8: Comparison of radial DCA of all primary tracks matched with TOF and passing quality criteria in events selected for secondary vertex analysis, between the data and embedded MC. Violet hashed histogram represents tracks not matched to true-level particles. Red dashed lines and arrows limit region used to find normalization that compensates different background yield in reconstructed secondary vertex distributions in data and embedded MC. Discontinuity at 1 cm is due to selection of events with at least 2 tracks of  $DCA(R) < 1$  cm

global tracks for the secondary vertex reconstruction. For this reason a method of estimation of the background was invented, as described in the next paragraph. Without this background subtracted, the ratio of MC to data varies mostly between 0.5 and 0.7.

Background estimation makes use of different content of fake secondary vertices depending on the proximity cut used in the secondary vertex reconstruction. This method is enabled by good agreement of the shape of the tails in distributions of the DCA between two tracks forming a secondary vertex in data and MC, as shown in Figure 9.7. The most optimal cut to select pairs from the secondary vertices is as low as about 0.5 cm, however one can change the proximity cut to form vertices from tracks of DCA within some higher limits, which results in different ratio of signal to background vertices. In Fig. 9.7 the nominal proximity cut is marked with the green line (signal region), while the modified proximity cut is marked with red lines (background region). With such two versions of cuts used in vertexing the two independent distributions of secondary vertices can be obtained: one with the standard proximity cut -  $\mathcal{H}_1$ , the other with modified proximity cut, in our case  $1.0 \text{ cm} < DCA < 2.5 \text{ cm}$  -  $\mathcal{H}_2$ . Limits in modified proximity cut were set to such values in order to ensure similar statistics in signal and background region, as well as provide the same (very similar) resolution of secondary vertex position calculated as a middle point between DCA points on helices associated with the tracks. One can note that the content of histograms (normalized to the same number of entries,  $\int \mathcal{H}_2 = \int \mathcal{H}_1$ ) can be described by the set of equations given below:

$$\begin{cases} \mathcal{H}_1 = (1 - \kappa B) \times signal + \kappa B \times background, \\ \mathcal{H}_2 = (1 - \kappa B') \times signal + \kappa B' \times background, \end{cases} \quad (9.2)$$

$$(9.3)$$

in which parameters  $B$  and  $B'$  ( $B \neq B'$ ) denote the fraction of fake secondary vertices in the distribution resultant from analysis utilizing nominal and modified proximity cut, respectively, and *signal* and *background* denote distributions of only true and only fake secondary vertices, respectively. Meaning of the  $\kappa$  parameter (equal to 1 for the time being) is explained in the next paragraph. The solution to set of Eqs. (9.2), (9.3) is the following:

$$\left\{ \begin{array}{l} signal = \frac{B' \times \mathcal{H}_1 - B \times \mathcal{H}_2}{B' - B} \\ background = \frac{(1 - \kappa B) \times \mathcal{H}_2 - (1 - \kappa B') \times \mathcal{H}_1}{\kappa(B' - B)} \end{array} \right. \quad (9.4)$$

$$(9.5)$$

An important remark here is that the background fraction extracted from the ratio of violet and red histograms in Fig. 9.7 can be used directly in Eqs. (9.2)-(9.5) only for background estimation in MC. In other words, parameter  $\kappa$  is equal to 1 only when solving Eqs. (9.4)-(9.5) for MC. In case of background estimation in data parameters  $B$  and  $B'$  have to be corrected for the “leakage” of true primary tracks to set of selected secondary track candidates due to worse TPC track pointing resolution in the data, and thus lower probability/efficiency of attaching the true primary tracks to primary vertices at large DCA( $R$ ), as it was described in one of preceding paragraphs. The correction factor  $\kappa$  is extracted from the ratio of the radial DCA of the primary TPC tracks in events selected for the secondary vertex study (Fig. 9.8). This ratio at large DCA( $R$ ) provides estimate of how many more true primary TPC tracks in the data is not recognized as primary tracks (comparing to MC) and hence overpopulate/enrich sample of global tracks which are selected for the reconstruction of secondary vertices, by definition increasing number of fake, background secondary vertices. Histogram range selected for calculation of the ratio was set to  $2.0 \text{ cm} < \text{DCA}(R) < 2.6 \text{ cm}$ , as this range coincides with the  $d_0^{(0,0)}$  of global tracks accepted for the analysis ( $d_0^{(0,0)} > 2 \text{ cm}$ ).  $\kappa$  calculated in this range equals 1.5. It is clear from Fig. 9.8 that value of  $\kappa$  depends on the limits of DCA( $R$ ) selected for the ratio calculation, therefore we determined and subtracted the background using also values 1.2 and 1.8, which are the extreme cases in the bottom pad of aforementioned plot. In case  $\kappa B$  or  $\kappa B'$  exceeded 1, the unity was set to the product. The difference between these results and results for nominal  $\kappa = 1.5$  are considered as a systematic uncertainty of the number of secondary vertices.

Background determined with the described method is shown in Fig. 9.1 with the solid lines colored according to corresponding markers (for nominal  $\kappa$ ). This background was subtracted and resulting distributions of the secondary vertex positions in the transverse and longitudinal direction are presented in Fig. 9.9. Gray boxes represent systematic uncertainty on number of secondary vertices in the data due to  $\kappa$  parameter uncertainty. Most relevant region - the HFT detector extending between  $\sim 2 \text{ cm}$  and  $\sim 30 \text{ cm}$  is satisfactorily well described by MC. Also, the inner wall of the TPC at  $\sim 48 \text{ cm}$  well matches between data and MC. Looking at the ratios in the bottom panels of Figs. 9.1 one can conclude that the differences between the dead material density in the data and STAR simulation generally vary between  $\pm 25\%$ , which we consider a systematic uncertainty on the amount of the dead material in front of TPC. Related systematic uncertainty on the TPC track reconstruction efficiency is described in Sec. 10.1.2.

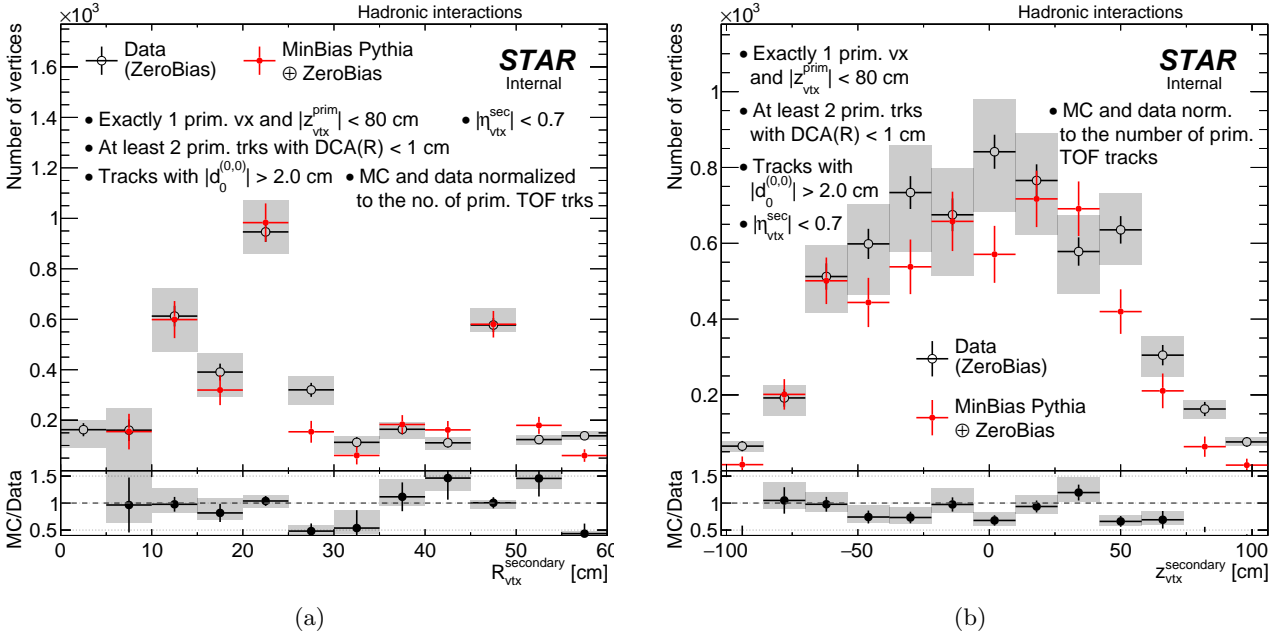


Figure 9.9: Comparison of background-subtracted  $R_{\text{vtx}}^{\text{secondary}}$  (9.9a) and  $z_{\text{vtx}}^{\text{secondary}}$  (9.9b) distribution in the data (open black circles) and embedded MC (filled red circles). Only vertices recognized as products of hadronic interactions are shown in the figure.

# 10. Systematic uncertainties

In this chapter we describe the common systematic uncertainties for two analyses [1, 2], related to: TPC track reconstruction efficiency, TOF matching efficiency and RP track reconstruction efficiency.

## 10.1 TPC track reconstruction efficiency

The TPC track reconstruction inefficiency is caused by:

- Spaces between the TPC sectors which are required to mount the wires and fiducial cuts applied during track reconstruction.
- Dead channels.
- Presence of off-time pile-up hits in TPC. This results in lowering the number of hits associated with reconstructed track (Sti algorithm was used) and track rejection caused by track quality selection.
- Particle interactions with dead material in front of the TPC.
- Particle decays.

In the following sections, we describe the systematic uncertainties related to the pile-up effect and amount of dead material in front of the TPC. The systematic uncertainty related to other sources of TPC inefficiencies is not considered since they should be well simulated by the MC.

### 10.1.1 Pile-up effect

The in-time pile-up does not affect the TPC reconstruction efficiency. In contrast, the off-time pile-up significantly reduces that efficiency due to high density of pile-up hits. That effect is taken into account by using embedding of MC events into Zerobias real data. To calculate the systematic uncertainty related to this procedure we compare relative changes of the track selection efficiencies between data driven tag&probe method and embedding method caused by different density of pile-up TPC hits. The MC and data were divided into three samples based on mean BBC coincidence rate:  $\langle \text{BBC\_AND} \rangle = 700 \text{ kHz}$ ,  $\langle \text{BBC\_AND} \rangle = 1100 \text{ kHz}$ ,  $\langle \text{BBC\_AND} \rangle = 1400 \text{ kHz}$ , as shown in Fig. 10.1. The main effect of different pile-up in those samples, shown in Fig. 10.2, is the change of the number of hits used in the helix fit.

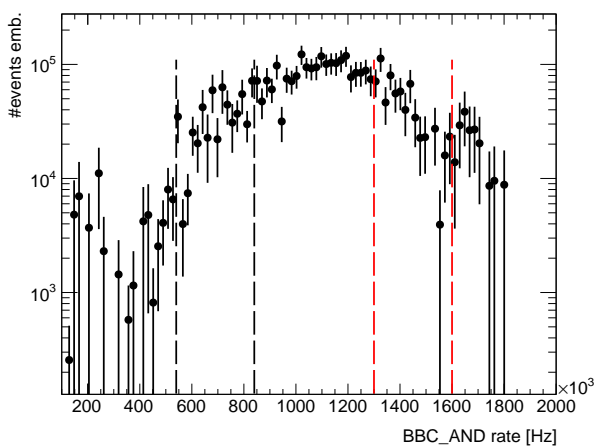


Figure 10.1: Number of events in embedded MC as a function of BBC\_AND rate. The black and red lines represent the events with  $\langle \text{BBC\_AND} \rangle = 700 \text{ kHz}$  and  $\langle \text{BBC\_AND} \rangle = 1400 \text{ kHz}$ , respectively. The region between these two corresponds to events with  $\langle \text{BBC\_AND} \rangle = 1100 \text{ kHz}$ .

The same quality cut on  $N_{\text{hits}}^{\text{fit}}$  (Sec. 2.2.1) in three above samples results in a significantly different TPC track reconstruction efficiency. To estimate the systematic uncertainty, the  $N_{\text{hits}}^{\text{fit}}$  cut was modified for events with  $\langle \text{BBC\_AND} \rangle = 700 \text{ kHz}$  and  $\langle \text{BBC\_AND} \rangle = 1400 \text{ kHz}$  by the amount obtained with data driven tag&probe method.

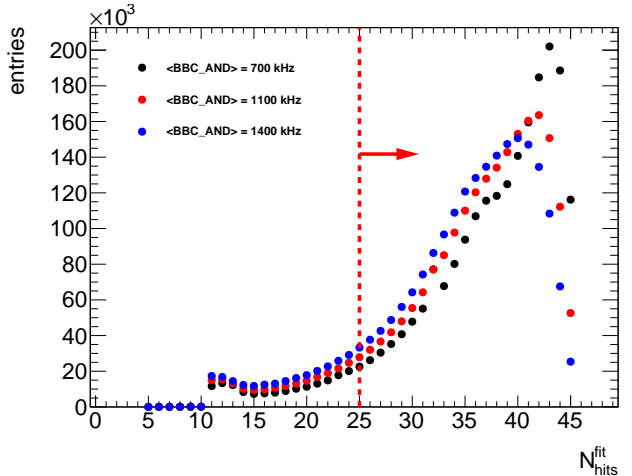


Figure 10.2: Number of hits used in the helix fit  $N_{\text{hits}}^{\text{fit}}$  for embedded MC samples selected with respect to average rate in BBC. Red line and arrow indicate the region accepted in the analysis for nominal  $N_{\text{hits}}^{\text{fit}}$  cut value.

In order to find cut value of  $N_{\text{hits}}^{\text{fit}}$  that should provide the same selection efficiency for in-time TPC tracks depending on the average rate in BBC, we utilized tag&probe method. With this method we studied the efficiency of selecting an in-time signal TPC tracks under the condition that the track was reconstructed. We modified variation of the tag&probe method presented in Sec. 4.1, preserving the general idea of using the process of CEP of  $\pi^+\pi^-$  and extracting the signal yield from  $p_T^{\text{miss}}$  distribution. The efficiency of TPC quality cuts was calculated according to Eq. (4.1) with modified definitions of the tag track and probe track, as explained in the following algorithm:

1. Data from RP\_CPT2 trigger were used. Events were selected with the cuts from nominal CEP analysis (Ref. [1]), except cuts **C3** and **C7-C9** which were removed or modified as given below.
2. For each event passing above selection global TPC tracks matched with TOF hits were selected. Exactly 2 such tracks, one of positive and one of negative charge, were required. Both tracks were required to be compatible with pion hypothesis based on  $dE/dx$  ( $|n_{\text{pion}}^\sigma| < 3$ ). If any of tracks was found incompatible with pion hypothesis - event was dropped from analysis. Also, the tracks were required to be likely a product of the same primary interaction, therefore cut on longitudinal separation along the beamline  $|\Delta z_0| < 3$  cm was imposed. Also, the  $z$ -position of the vertex was required to be contained within nominal margins,  $\frac{1}{2}|z_0^+ + z_0^-| < 80$  cm. We did not use primary tracks here as there are some quality cuts already applied at the level of vertexing, which could introduce bias in the resultant efficiency.
3. Global TOF-matched TPC tracks preselected in #2 were checked if they satisfy track quality cuts (2.2.1) with removed cut on  $N_{\text{hits}}^{\text{dE}/\text{dx}}$  and modified cut value of  $N_{\text{hits}}^{\text{fit}}$  denoted  $N_{\text{thr}}$  ( $N_{\text{hits}}^{\text{fit}} \geq N_{\text{thr}}$ ). Tracks which pass the quality cuts were set as a tag candidates. In case only one track was found to be a tag candidate, step #4 was executed only with this single track being a tag. Otherwise step #4 was repeated for each of two tracks set as a tag.
4. The TPC track of the sign opposite to tag (preselected in #2) was checked if it also passes the cuts for a good quality track (cuts 2.2.1 with removed  $N_{\text{hits}}^{\text{dE}/\text{dx}}$  cut and modified  $N_{\text{thr}}$  cut). 2-dimensional histograms of quantities of interest  $q$  (probe  $\eta$  if probe  $p_T > 0.2$  GeV, probe  $p_T$  if probe  $|\eta| < 0.7$ ) vs.  $p_T^{\text{miss}}$  were filled, separately for all probes and only for probes satisfying quality cuts.
5. In each bin of quantity of interest  $q$  (as a function of which the efficiency was to be determined) the distribution of  $p_T^{\text{miss}}$  was fitted in the signal-free region with the function describing background shape. The background function was extrapolated to  $p_T^{\text{miss}} = 0$ . The signal yield in given bin of  $q$  was calculated as the integral of the histogram with subtracted integral of the background function, both in the range  $p_T^{\text{miss}} < 75$  MeV. The final efficiency in given bin of  $q$  was calculated according to Eq. (4.2) (Sec. 4.1), with superscript “matched” understood as “passing quality cuts”.

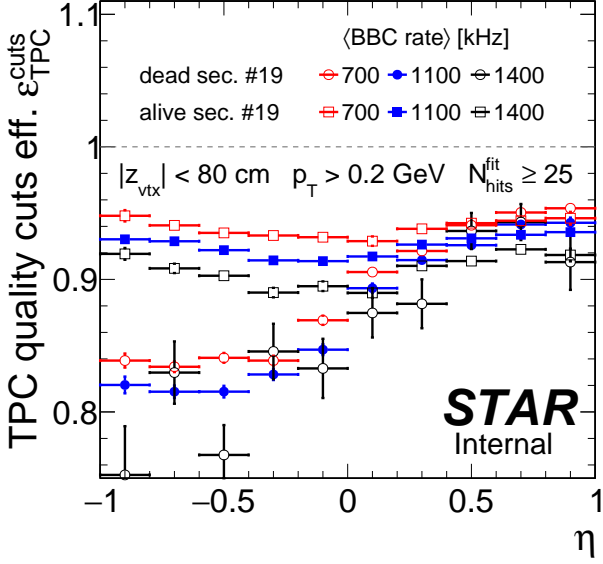


Figure 10.3: Sample comparison of TPC track quality cuts efficiency as a function of track pseudorapidity  $\eta$ , obtained with tag&probe method on CEP  $\pi^+\pi^-$  events, for a few data samples selected with respect to average rate in BBC and run period. Efficiencies for nominal value of 25 for minimum  $N_{\text{hits}}^{\text{fit}}$  are drawn to emphasize effect of the BBC rate (TPC occupancy) on the TPC track reconstruction efficiency.

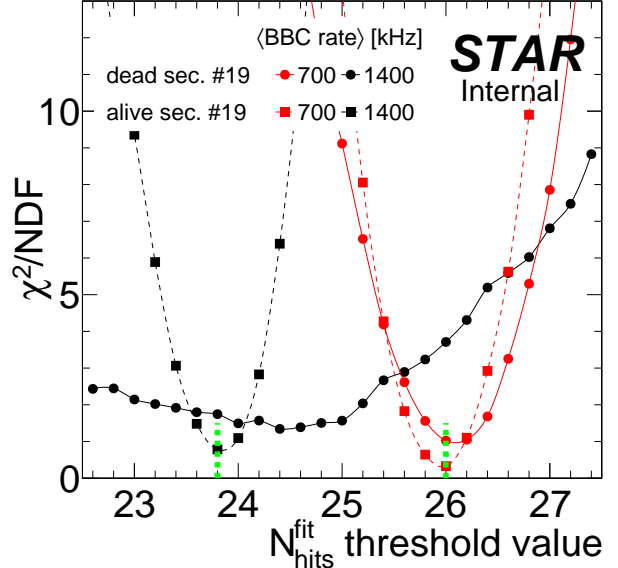


Figure 10.4:  $\chi^2/\text{NDF}$  between the TPC track quality cuts efficiencies obtained with tag&probe method as a function of the  $N_{\text{hits}}^{\text{fit}}$  cut value. Dashed green vertical lines show approximate  $N_{\text{hits}}^{\text{fit}}$  values for which  $\chi^2/\text{NDF}$  reaches minimum, separately for low- and high-BBC rate runs. Smooth lines connect points from the same data sample (they are not a fitted curves).

A few efficiency curves obtained with above method using a nominal cut on  $N_{\text{hits}}^{\text{fit}}$  ( $\geq 25$ ) are plotted in Fig. 10.3. A notable decrease of selection efficiency at negative pseudorapidities is visible in this Figure for a run period with dead TPC sector #19 (days up to 73). Also, a sizeable differences are present for the same run periods with different average rates in BBC. Values of  $N_{\text{thr}}$  which equalize the TPC track selection efficiency for different average BBC rates, were determined with the procedure described in the next paragraph.

Although number of hit points used in helical track fit is an integer, the value of  $N_{\text{thr}}$  which provides the same track selection efficiency at high/low BBC rates as at medium (moderate) rates, may lie in between two integers differing by 1 hit point and thus be a floating point number. To account for this possibility, for the purpose of this study we assigned to each global TPC track a new number of hit points used in a fit ( $N'_{\text{hits}}$ ) being a sum of an original numer of hit points (integer  $N_{\text{hits}}^{\text{fit}}$ ) and a random number between 0 and 1 drawn from the uniform distribution (float  $U[0, 1]$ ). With this modification introduced, we performed a scan of the TPC track selection efficiency with the tag&probe method for a set of  $N_{\text{thr}}$  values, starting from 22.6 with a step of 0.2, up to 27.4. For each value of parameter  $N_{\text{thr}}$  a quantity  $\chi^2/\text{NDF}$  was calculated between the  $\eta$ -dependent efficiency obtained for a modified  $N_{\text{hits}}^{\text{fit}}$  cut value ( $\geq N_{\text{thr}}$ ) and given BBC rate sample (low/high), and the one obtained with nominal cut value ( $\geq 25$ ) for a medium BBC rate sample. The result of the scan is shown in Fig. 10.4, where the  $\chi^2/\text{NDF}$  is drawn as a function of the  $N_{\text{hits}}^{\text{fit}}$  threshold value in quality cuts 2.2.1. For both run periods (before/after day 73) we found similar modified values of  $N_{\text{thr}}$  which provide the same track selection efficiency: 23.8 for high BBC rate runs, and 26 for low BBC rate runs, as marked with dashed green lines. Significantly different width of  $\chi^2/\text{NDF}$  for runs up to 16073050 and high BBC rates is due to lower statistics of this subsample (higher statistical uncertainties on efficiency points).

Figure 10.5 shows the TPC track reconstruction efficiency with nominal, for  $\langle \text{BBC\_AND} \rangle = 1100 kHz sample, and modified quality cut on the number of hits used in the helix fit, for  $\langle \text{BBC\_AND} \rangle = 700$  kHz and  $\langle \text{BBC\_AND} \rangle = 1400$  kHz samples, for two periods of data collection (with dead sector #19 and with that sector back in operation).$

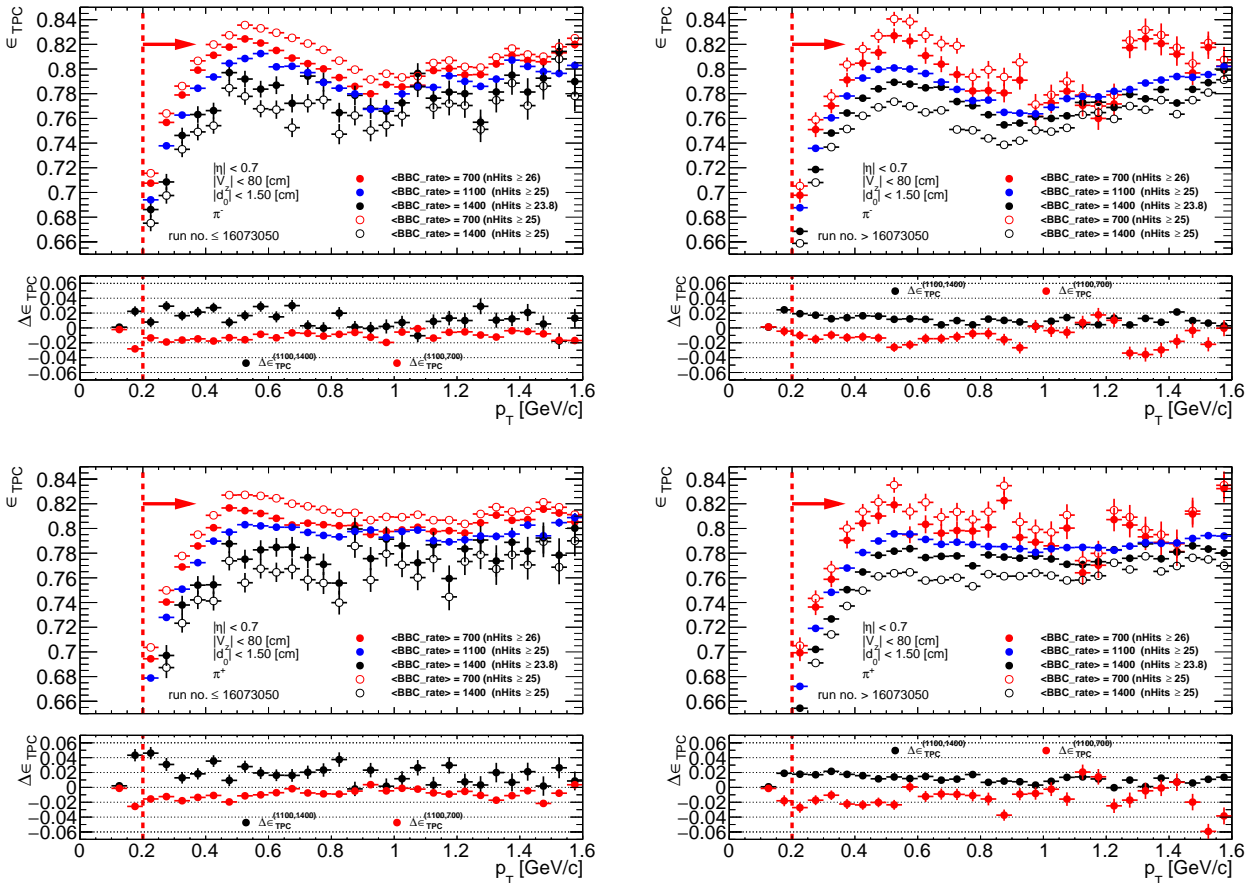


Figure 10.5:  $\pi^\pm$  TPC track reconstruction efficiency as a function of  $p_T$  ( $|\eta| < 0.7$ ,  $|V_z| < 80$  cm) for embedded MC samples with  $\langle \text{BBC\_AND} \rangle = 700$  kHz,  $\langle \text{BBC\_AND} \rangle = 1100$  kHz and  $\langle \text{BBC\_AND} \rangle = 1400$  kHz. The efficiencies from corresponding MC samples with changed cut on the number of hits used in the helix fit were also shown. Additionally, the offsets from Eq. 10.1 were drawn in the bottom of each plot. Red lines and arrows indicate region accepted in the analysis.

The offset between medium and low, high pile-up runs was separately calculated as:

$$\Delta\epsilon_{TPC}^{(1100,i)} = \epsilon_{TPC}^{1100,\text{nHitsFit}\geq 25} - \epsilon_{TPC}^i \quad (10.1)$$

where:

$\epsilon_{TPC}^{1100,\text{nHitsFit}\geq 25}$  - TPC track reconstruction efficiency calculated from sample with  $\langle \text{BBC\_AND} \rangle = 1100 \text{ kHz}$  with default  $N_{\text{hits}}^{\text{fit}}$  quality cut,

$\epsilon_{TPC}^i$  - TPC track reconstruction efficiency calculated from samples with  $\langle \text{BBC\_AND} \rangle = 1400 \text{ kHz}$  and  $\langle \text{BBC\_AND} \rangle = 700 \text{ kHz}$  with modified  $N_{\text{hits}}^{\text{fit}}$  quality cut.

Ideally above offset should be compatible with zero. This would mean that embedding procedure is compatible with data driven tag&probe method. As shown in the bottom of each plot in Figure 10.5 for  $\pi^\pm$ , above offset varies between 1 – 2% and was taken as systematic uncertainty on TPC track reconstruction efficiency related to embedding procedure.

Only small fraction of Zerobias data was available for embedded MC production. Therefore, additional systematic uncertainty should be calculated related to the proper representation of whole data sample in embedding. The comparison of the BBC\_AND rate for SD and CD in the data and embedded MC is shown in Fig. 10.6. The mean BBC\_AND rate varies between embedded MC and data by about 5% and 10% for SD and CD, respectively. As shown in Fig. 10.5, the effect of different TPC track reconstruction efficiency depending on TPC occupancy (the BBC rate) is about 10%. Thus, the additional systematic error due to different mean BBC\_AND rate in the data and embedded MC was introduced as 0.5% and 1% for SD and CD, respectively.

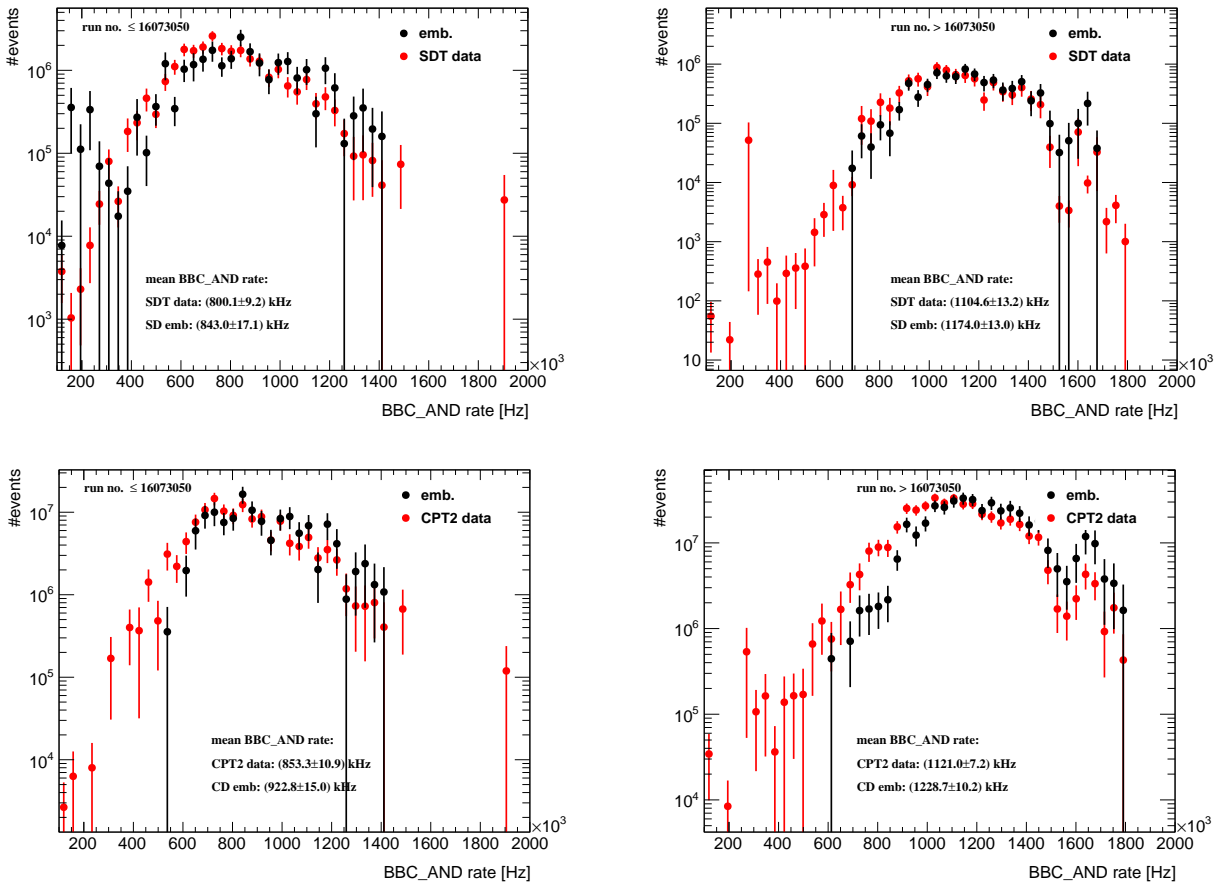


Figure 10.6: Comparison of the BBC\_AND rate in the data and embedded MC for SD and CD. The mean BBC\_AND rate for data and MC is given on each plot.

### 10.1.2 Dead material effect on TPC track reconstruction efficiency

The amount of dead material in front of TPC differs up to 25% between data and simulation (see Sec. 9). First, the amount of lost particles,  $\delta\epsilon_{TPC}$ , due to the interaction with dead material in front of TPC was estimated using no-pile-up MC samples. The sample result for  $\pi^-$  in CD and SD is shown in Fig. 10.7. The remaining plots for other  $z$ -vertex bins and other particles are contained in Appendix E. The symmetric systematic uncertainty on the TPC track reconstruction efficiency due to dead material was introduced as  $\pm 0.25 \cdot \delta\epsilon_{TPC}$ . In Fig. 10.8 the systematic uncertainty is shown for each particle species in CD and SD as a function of  $p_T$  ( $|\eta| < 0.7$ ,  $|V_z| < 80$  cm).

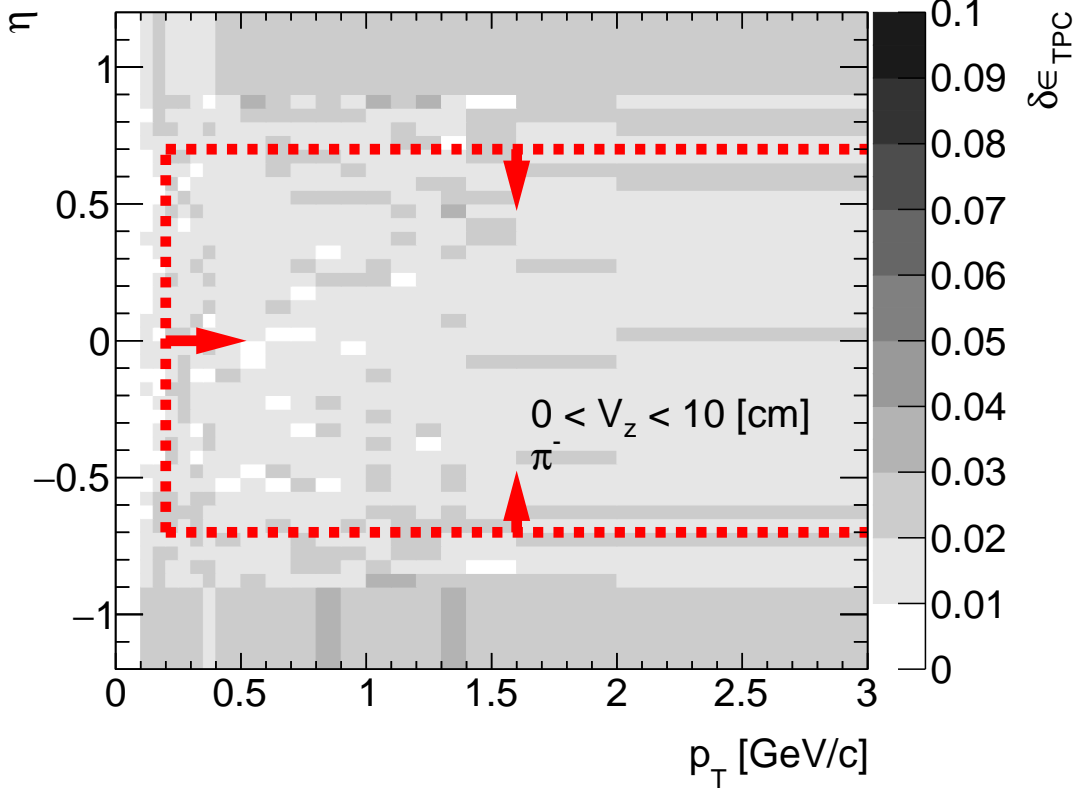


Figure 10.7: The amount of lost  $\pi^-$  due to the interaction with dead material in front of TPC. Sample plot represents the fraction of lost  $\pi^-$ ,  $\delta\epsilon_{TPC}$  ( $z$ -axis), as a function of true particle pseudorapidity  $\eta$  ( $y$ -axis) and transverse momentum  $p_T$  ( $x$ -axis) in single  $z$ -vertex bin. Red lines and arrows indicate region accepted in the analysis.

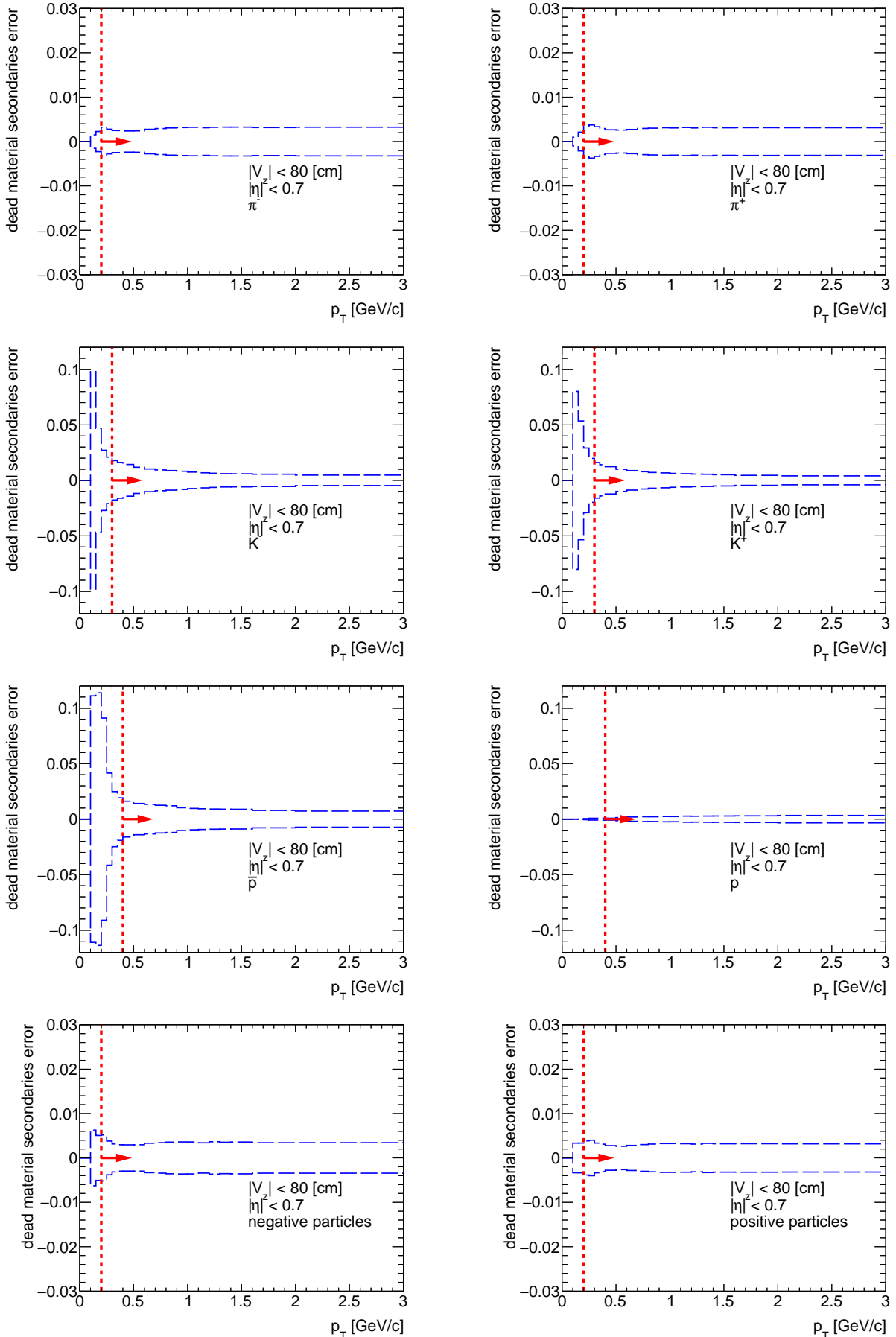


Figure 10.8: The systematic uncertainty to the TPC track reconstruction efficiency due to amount of dead material in front of TPC using MC samples for CD and SD. Each plot represents the systematic uncertainty as a function of true particle  $p_T$  ( $|\eta| < 0.7$ ,  $|V_z| < 80$  cm) for given particle species:  $\pi^-$ ,  $\pi^+$ ,  $K^-$ ,  $K^+$ ,  $\bar{p}$ ,  $p$ , negative and positive particles without identification. Red lines and arrows indicate region accepted in the analysis.

## 10.2 TOF matching efficiency

In this section the systematic uncertainties on TOF matching efficiency due to the embedding procedure and the simulation accuracy are described.

### 10.2.1 Embedding (pile-up) effect

The effects of pile-up on TOF efficiency is taken into account by using single particle MC embedded into Zerobias data. To estimate the systematic uncertainty of the TOF efficiency related to the embedding procedure, the offset from the linearity of TOF efficiency as a function of the mean BBC\_AND rate,  $\langle \text{BBC\_AND} \rangle$ , was calculated. The embedded MC was divided into two samples in which  $\langle \text{BBC\_AND} \rangle$  rate differs by a factor of two:  $\langle \text{BBC\_AND} \rangle = 700$  kHz and  $\langle \text{BBC\_AND} \rangle = 1400$  kHz as shown in Fig. 10.1 (Sec. 10.1.1). Next, it was checked whether the difference between TOF efficiency in pile-up and no-pile-up MC also changes by a factor of two between these two samples.

The TOF matching efficiency is conditional and depends on TPC track reconstruction efficiency. Since that, the difference between pile-up and no-pile-up MC was calculated as:

$$\Delta\epsilon_{TOF}^{1400/700 \text{ kHz}} = \frac{N_{TPC-TOF}^{no-pile-up}}{N_{TPC}^{no-pile-up}} - \frac{N_{TPC-TOF}^{pile-up}}{N_{TPC}^{pile-up}} \quad (10.2)$$

where:

$N_{TPC-TOF}^{pile-up}$  - number of reconstructed tracks, matched with MC tracks and TOF hit in pile-up MC,

$N_{TPC-TOF}^{no-pile-up}$  - number of reconstructed tracks, matched with MC tracks and TOF hit in no-pile-up MC,

$N_{TPC}^{pile-up}$  - number of reconstructed tracks, matched with MC tracks in pile-up MC,

$N_{TPC}^{no-pile-up}$  - number of reconstructed tracks, matched with MC tracks in no-pile-up MC.

Next the offset between high and low pile-up events was calculated with the formula:

$$\Delta\epsilon_{TOF} = \Delta\epsilon_{TOF}^{1400 \text{ kHz}} - 2 \cdot \Delta\epsilon_{TOF}^{700 \text{ kHz}} \quad (10.3)$$

and is shown in Figs. 10.9 and 10.10. Finally, the obtained value of  $\Delta\epsilon_{TOF}$  is smaller than 0.5% and can be neglected in comparison with other systematic uncertainties.

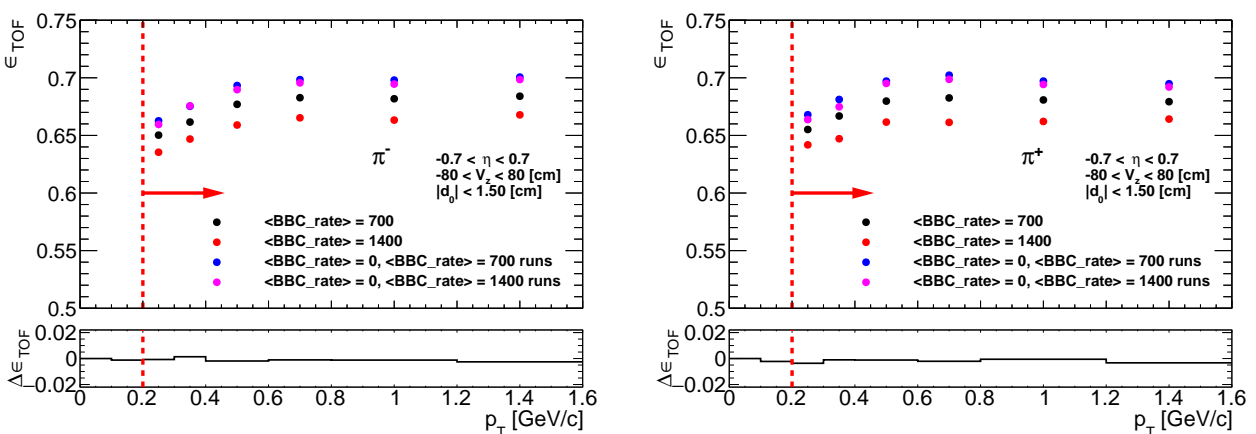


Figure 10.9:  $\pi^\pm$  TOF matching efficiency as a function of  $p_T$  ( $|\eta| < 0.7$ ,  $|V_z| < 80$  cm) for embedded MC samples with  $\langle \text{BBC\_AND} \rangle = 700$  kHz and  $\langle \text{BBC\_AND} \rangle = 1400$  kHz. The efficiencies from corresponding no-pile-up MC samples were also shown. Additionally, the offset from Eq. 10.3 was drawn in the bottom of each plot. Red lines and arrows indicate region accepted in the analysis.

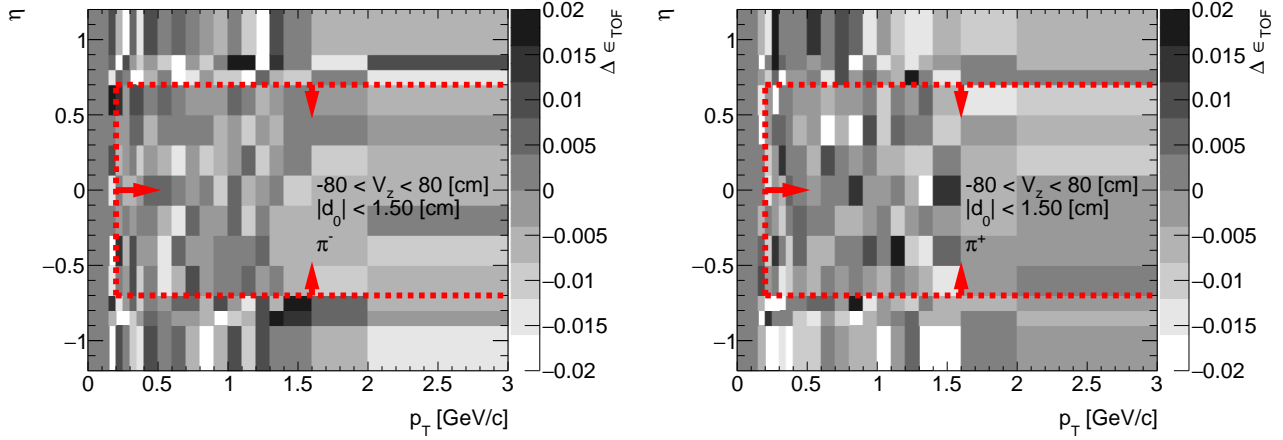


Figure 10.10: The offset  $\Delta\epsilon_{TOF} = \Delta\epsilon_{TOF}^{1400 \text{ kHz}} - 2 \cdot \Delta\epsilon_{TOF}^{700 \text{ kHz}}$  for  $\pi^\pm$  as a function of  $p_T$  and  $\eta$  ( $|V_z| < 80 \text{ cm}$ ). Red lines and arrows indicate region accepted in the analysis.

### 10.2.2 TOF system simulation accuracy

Systematic uncertainty of the TOF efficiency related to the accuracy of the TOF system simulation in STARsim and the data driven correction to it derived in Sec. 4.1 was estimated by comparing that nominal TOF efficiency with the one obtained with an independent method described below.

In some STAR analyses the TOF hit reconstruction and matching efficiency is determined from the data with the use of BEMC: real (in-time) tracks are selected based on the fact that they match to BEMC cluster. If they do, the TOF efficiency is calculated as a ratio of number of TOF-matched tracks to number of all tracks. This solution may provide slightly biased efficiency, because the signal in the detector placed behind TOF, such as BEMC, ensures that particle still followed the original helical path past the last hit of the track in TPC (Fig. 10.11). Also, BEMC clusters are more efficiently reconstructed as the energy deposits in the calorimeter increase, which may favor tracks which generated secondaries in front of the BEMC, hence possibly also in front of TOF thus increasing a chance to reconstruct hit in TOF.

To estimate systematic error of the TOF efficiency we decided to calculate efficiency utilizing the TPC tracks containing hits in HFT. The HFT is a group of silicon detectors (PXL, IST, SST) which differ from the gaseous detectors (like TPC) in many aspects. The difference that is most important for this study is the time of response/memory - much shorter in HFT than in TPC. Therefore if the TPC track contain hits in the silicon of

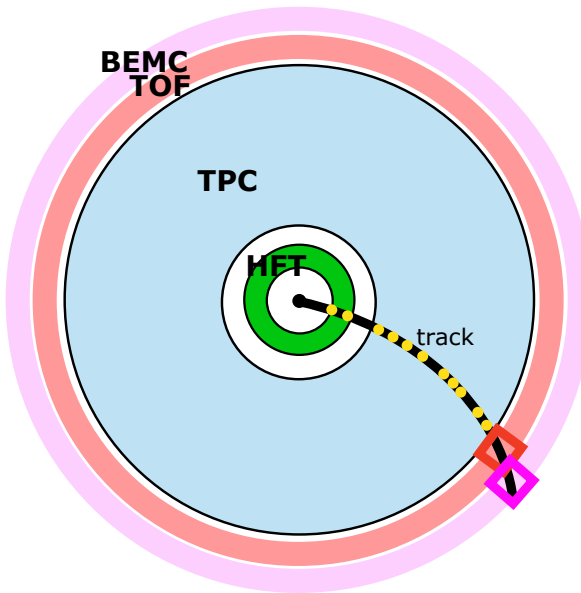


Figure 10.11: Sketch of the cross section of the central detector and the track reconstructed with points in HFT. Presence of HFT points in a reconstructed track can be used as a tagger of the in-time tracks.

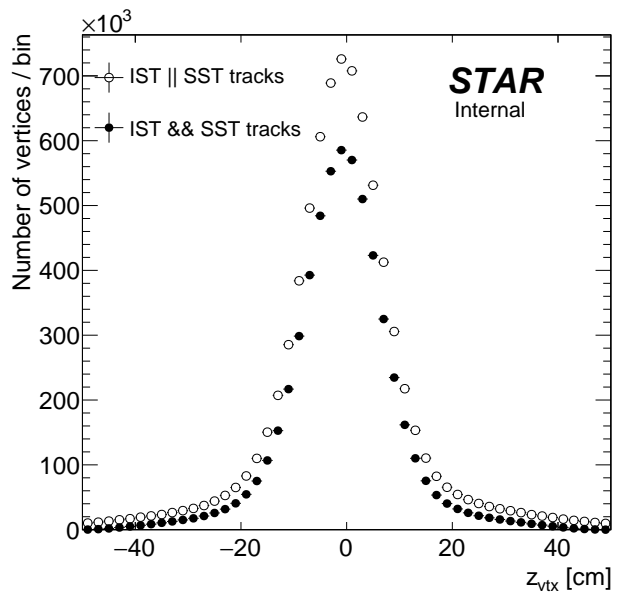


Figure 10.12: Distribution of  $z$ -position of vertices containing TPC tracks with HFT hits (st\_ssd stream). Open circles represent vertices with tracks with hits in IST or SST, full circles - IST and SST.

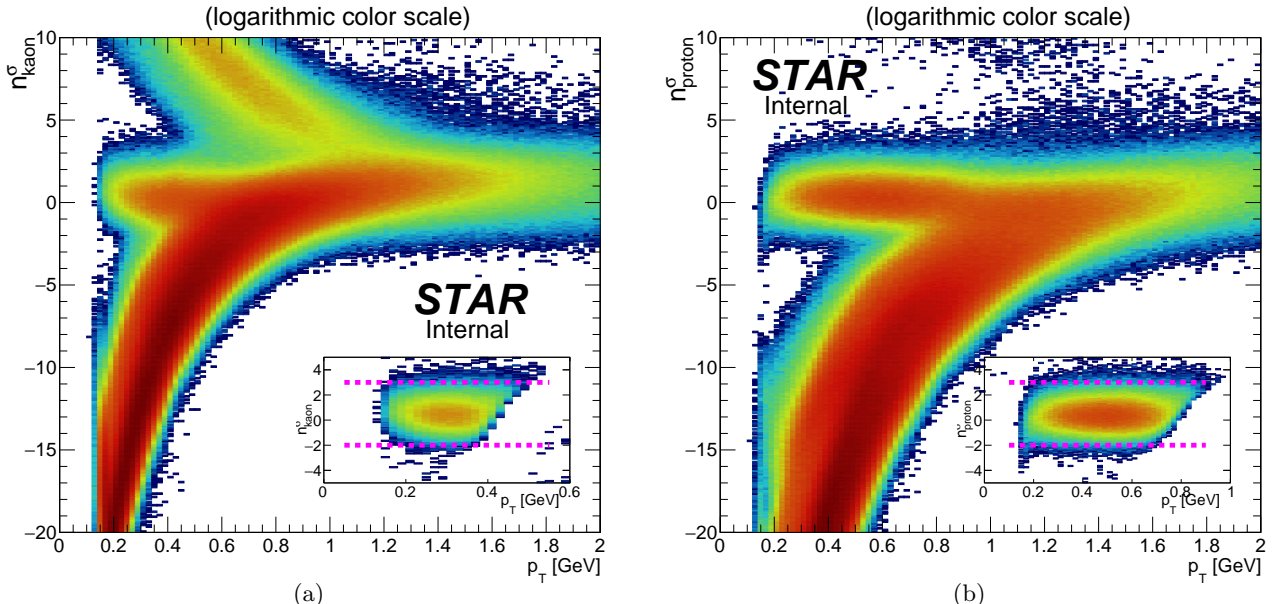


Figure 10.13: Distribution of  $n_\sigma^{\text{kaon}}$  (10.13a) and  $n_\sigma^{\text{proton}}$  (10.13b) vs. track  $p_T$  for tracks containing HFT hits. The insert in each subfigure shows the corresponding  $n_\sigma$  vs.  $p_T$  distribution after preselection of tracks of given species (without cut on variable in  $y$ -axis) according to description provided in the text in preceding page. Dashed magenta lines represent final cuts on corresponding  $n_\sigma$  quantity used to select tracks of given species.

HFT it is very probably a real track of particle produced in the proton-proton interaction in the corresponding bunch crossing. With this HFT-tagged tracks we omit potential bias related to matching with BEMC cluster.

We used the data from st\_ssdbm stream (VPDMB-5-ssd trigger) from the same runs as the data used in our physics analyses. The HFT-tagged tracks were selected as the primary tracks passing the quality cuts 2.2.1 (only the TPC hits were counted). These tracks were required to contain hits in two HFT layers: IST and SST, which vastly reduced probability to select an off-time track in TPC (PXL was not used in reconstruction due to problems in firmware). As shown in Fig. 10.12, the  $z_{\text{vtx}}$  coverage of the HFT-tagged tracks is limited to about  $\pm 20$  cm. We impose cut on the  $z$  position of the vertex  $|z_{\text{vtx}}| < 20$  cm to remove tracks from the tails, which generally have large  $|\eta|$ .

Identification of particles was done using the specific energy loss measured in the TPC ( $n_\sigma$  variables were used). The following requirements were imposed on  $n_\sigma$  variables in order to select three species of particles whose tracks were selected for the TOF efficiency analysis:

- pions:  $|n_{\text{pion}}^\sigma| < 2$ ,
- kaons:  $-2 < n_{\text{proton}}^\sigma < 2.5 \quad \&\& \quad |n_{\text{pion}}^\sigma| > 3.5 \quad \&\& \quad |n_{\text{electron}}^\sigma| > 3.5 \quad \&\& \quad |n_{\text{proton}}^\sigma| > 3.5$ ,
- protons:  $-2 < n_{\text{proton}}^\sigma < 3 \quad \&\& \quad |n_{\text{pion}}^\sigma| > 3.5 \quad \&\& \quad |n_{\text{electron}}^\sigma| > 3.5 \quad \&\& \quad |n_{\text{kaon}}^\sigma| > 3.5$ .

Selection of pions by cut solely on  $n_{\text{pion}}^\sigma$  (without additional cuts on  $n_\sigma$  for kaon, proton and electron hypothesis) is driven by the dominance of pion production over other species and by the fact that the  $dE/dx$  of pions overlap with kaons and protons at momenta which are relatively large, hence the TOF efficiency is saturated and the same for all particle species. More sophisticated selection was used for kaons and protons. Figure 10.13 shows the  $n_\sigma$  variables before and after the selection of kaons (10.13a) and protons (10.13b), where one can find proof that clean samples of these particles were selected, for the price of limited coverage in track  $p_T$ .

From selected sample of pion, kaon and proton tracks the TOF hit reconstruction and matching efficiency was calculated using the standard method - as a ratio of number of tracks matched with TOF and number of all tracks. This efficiency was compared with the efficiency extracted from the zero-bias-embedded single particle MC, calculated for  $|z_{\text{vtx}}| < 20$  cm and averaged between positive- and negative-charge particles. The result of comparison - the difference between efficiency calculated with HFT-tagged tracks and efficiency from single particle MC, is presented in Fig. 10.14 (subfigures 10.14b-10.14d). This difference could be interpreted as a data-driven correction to the TOF efficiency calculated from single particle MC, alternative to correction derived with tag&probe method on CEP events, described in Sec. 4.1.

The difference between an alternative correction in Figs. 10.14b-10.14d and the correction from tag&probe (Fig. 10.14a) method,  $\Delta\delta\varepsilon_{\text{TOF}}$ , can be used as a measure of the uncertainty of the overall TOF efficiency. Aforementioned difference is depicted in Fig. 10.15. We decided to symmetrize the systematic uncertainty of

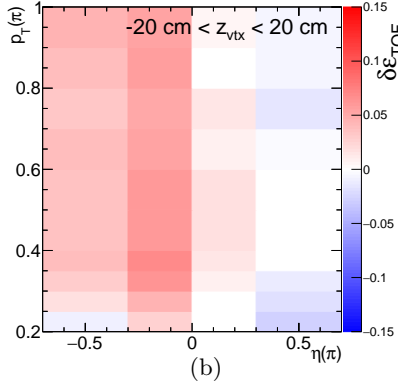
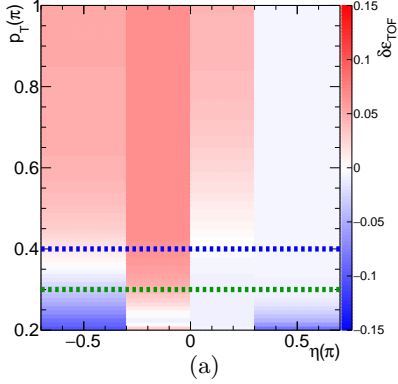
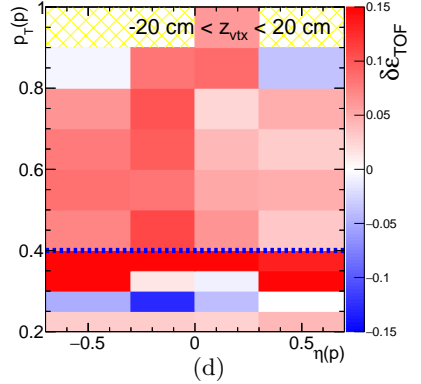
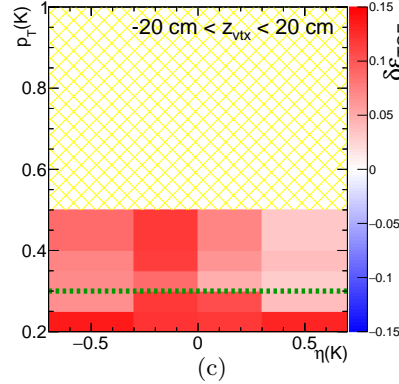


Figure 10.14: Comparison of the TOF efficiency correction obtained with tag&probe method on CEP  $\pi^+\pi^-$  events (10.14a, description in Sec. 4.1) and the difference between TOF efficiency calculated using standard method from the HFT-tagged tracks and efficiency from embedded single particle MC for pions (10.14b), kaons (10.14c) and protons (10.14d). Yellow hatched area mark empty bins. Dashed horizontal lines represent minimum track  $p_T$  thresholds used in our analyses: 0.3 GeV for kaons (green) and 0.4 GeV for protons (blue).



the TOF efficiency. For this purpose, on top of the correction to the TOF efficiency from CEP tag&probe method, we add the half of the difference from Fig. 10.15 to the TOF efficiency of corresponding particle type. We then assign a systematic uncertainty of the TOF efficiency to each  $(\eta, p_T)$  bin as an absolute value of the half of that difference,  $\frac{1}{2}|\Delta\delta\epsilon_{TOF}|$ . We assume that the systematic uncertainty for tracks whose  $|z_{vtx}| > 20$  cm is the same as for HFT tracks studied here ( $|z_{vtx}| < 20$  cm). For high track  $p_T$ , when there are no estimates of  $\Delta\delta\epsilon_{TOF}$ , the average value from the 2 last non-empty  $p_T$  bin (at given  $\eta$  bin) is used as a correction, and maximum absolute value among the last 3 non-empty  $p_T$  bins (at given  $\eta$  bin) is used as a systematic uncertainty.

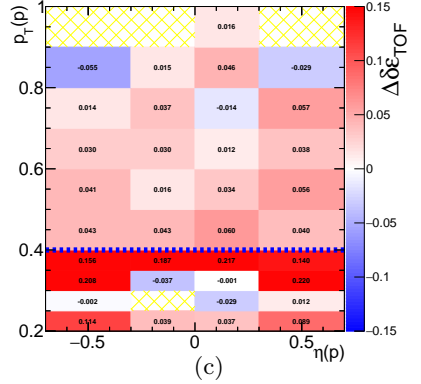
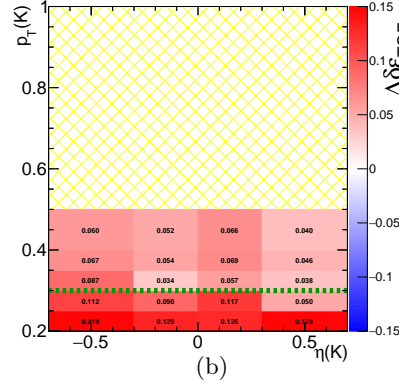
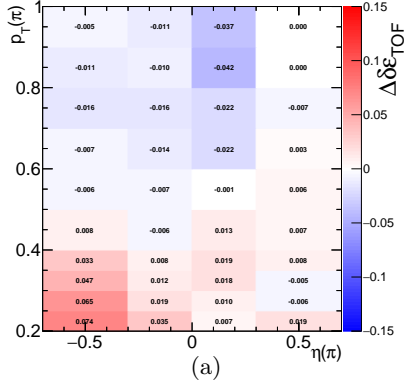


Figure 10.15: Difference between the TOF eff. correction estimated with the HFT-tagged tracks for pions (10.15a), kaons (10.15b) and protons (10.15c), and the correton from tag&probe method on CEP  $\pi^+\pi^-$  events. Figure 10.15a is the difference between 10.14b and 10.14a, Figure 10.15b is the difference between 10.14c and 10.14a, and Figure 10.15c is the difference between 10.14d and 10.14a. Yellow hatched area mark bins which were empty in histograms for HFT-tagged tracks (thus difference is incalculable). Dashed horizontal lines represent minimum track  $p_T$  thresholds used in our analyses: 0.3 GeV for kaons (green) and 0.4 GeV for protons (blue).

The effective systematic uncertainty calculated as an average uncertainty weighted with the MC events is shown in Fig. 10.16. From the Figure one reads that the uncertainty for a pion, kaon and proton track is of the order of 1%, 3% and 2%, respectively.

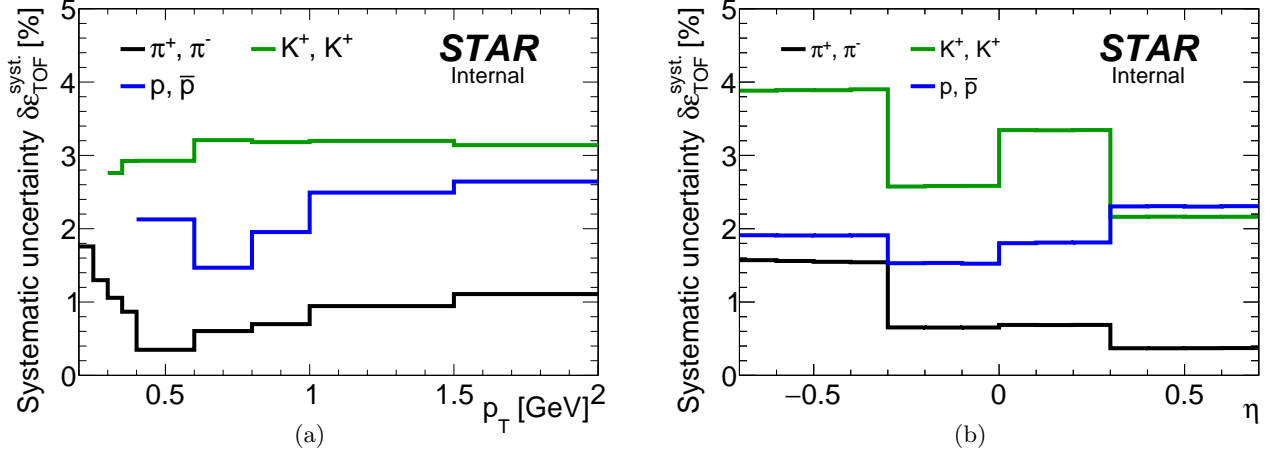


Figure 10.16: Effective systematic uncertainty of the TOF efficiency related to the simulation accuracy, drawn as a function of the track  $p_T$  (10.16a) and track  $\eta$  (10.16b). The  $p_T$ -dependence was calculated for tracks within  $|\eta| < 0.7$ , while  $\eta$ -dependence was calculated for tracks with  $p_T$  greater than the threshold established for given particle type (see Sec. 2.2.1).

## 10.3 Roman Pot track reconstruction efficiency

### 10.3.1 Track reconstruction efficiency (absolute reconstruction efficiency)

Nominally the RP track reconstruction efficiency is calculated with the zero-bias-embedded MC events as a probability that forward scattered proton is transported from the IP to the RP stations and produces hits in SSDs that are reconstructed as a track point(s) that form a track which passes selection cuts. The systematic uncertainty of this efficiency, which reflects the accuracy of the simulation (modeling of the dead material, signal digitization etc.), has been estimated using elastic scattering events. The same analysis scheme was used for the data and for embedded elastic scattering MC events. The difference between efficiency estimates extracted from the data and simulation was established as a measure of the systematic uncertainty of the nominal RP track reconstruction efficiency.

Obviously, in our physics analyses we study processes other than elastic proton-proton scattering, nevertheless the difference between the result obtained with data and simulated elastic scattering MC events are a good measure of the systematic uncertainty also for other processes. We choose elastic scattering for this study as it is the cleanest process involving forward protons - backgrounds can be suppressed relatively easy with the collinearity constraint. In addition to this, parameters of the proton track (its momentum, position in the detector) can be reconstructed even in case of lack of signal in one or both detectors in a branch. An additional argument to use elastic scattering is that in CEP of low central masses ( $\lesssim 3$  GeV) forward protons have  $\xi \approx 0$ , rarely exceeding 0.05 in studied rapidity range of the central state.

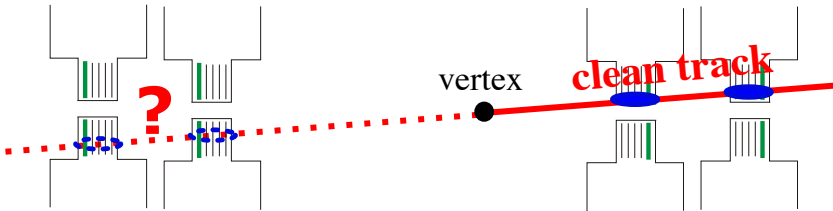


Figure 10.17: Sketch of the Roman Pot system with drafted method of estimation of the RP track reconstruction efficiency using elastic scattering events.

An idea of presented analysis was to select elastic proton-proton scattering events by requiring the elastic trigger (signal in PMTs in two opposite RP branches) and clean RP track of  $\xi$  consistent with 0 within  $3.5\sigma_\xi$  on one side of the IP, and counting how often there is reconstructed and successfully selected collinear RP track in the opposite branch with trigger signal. The method is illustrated in Fig. 10.17. Detailed description of the algorithm is provided below:

1. RP\\_ET triggers were used. Elastic proton-proton scattering MC events (generated with  $B = 14.3 \text{ GeV}^{-2}$  as it was measured in independent analysis, see Ref. [19]) simulated in Geant4 and embedded into zero-bias data were subjected to the same trigger conditions (signal in trigger counters in opposite RP branches was required). The zero-bias data used in embedding was taken from the same runs for which RP\\_ET triggers were analyzed. Also number of simulated events for each run was proportional to number of elastic scattering events in given run.

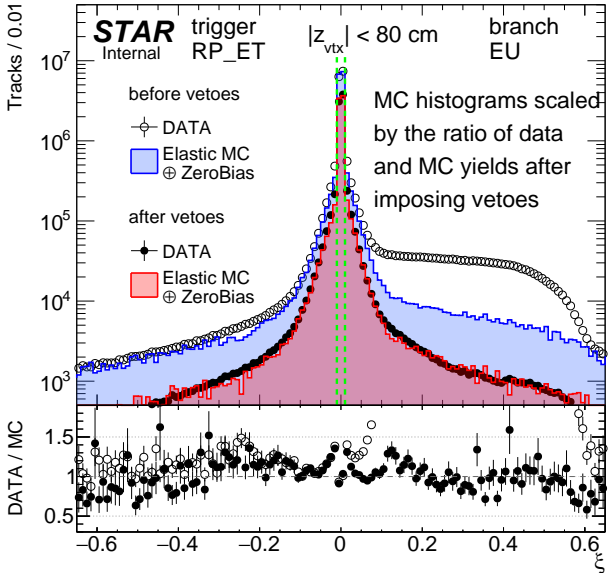


Figure 10.18: Fractional momentum loss  $\xi$  of clean proton tracks in branch EU before and after applying vetoes. Data are represented by opened and filled circles, while elastic MC embedded into zero-bias data is drawn as filled histograms. MC histograms are scaled by the ratio of data and MC yields after imposing vetoes in other STAR detector subsystems. Lower pad shows the ratio of corresponding distributions in the data and MC. Before vetoes are applied a significant contribution of non-elastic forward protons in the data sample is clearly visible (exceeds over MC for  $\xi > 0.01$ ). Satisfactory agreement between the data and MC is found after imposing vetoes, which indicates successful purification of data sample. Dashed green vertical lines show the  $\xi$  range of tracks accepted for the RP track (and also track point) efficiency studies,  $|\xi| < 0.01$ . Similar plot for the remaining branches can be found in Appendix H.

2. Since RP\\_ET triggers can be fired not only by elastic interactions but also, for instance, by central diffraction events, minimum bias events with forward remnants of protons, overlap of single diffraction events with beam halo protons, etc., a list of vetoes was exerted to suppress non-elastic interaction/pile-up:
  - TOF L0 multiplicity = 0
  - n. of TPC-TOF tracks = 0
  - n. of recon. TOF hits = 0
  - empty ZDC
  - empty VPD
  - empty BBC (small, large)
  - false state of RP\\_IT trigger bit (trigger signal only in RP branches forming an elastic trigger bit RP\\_ET)

As shown in Fig. 10.18, the mentioned types of background events that fire RP\\_ET trigger are vastly suppressed with the above vetoes.

3. From the difference between average time of the trigger signal in west and east RPs the  $z$ -position of the vertex was reconstructed and required to satisfy condition  $|z_{\text{vtx}}| < 80$  cm, which is the same as the range of  $z_{\text{vtx}}$  accepted in our physics analyses.
4. One side (a 'tagging' side, or a reference side) was checked if a clean set of track points was reconstructed in a branch with trigger signal. By clean set of track points we understand either 1 and 0, 0 and 1, or 1 and 1 reconstructed track point in the 1<sup>st</sup> and 2<sup>nd</sup> RP in given branch, respectively. If yes, from this(es) track point(s) a RP track was formed, reconstructed with the  $z$ -position of the vertex assumed to be as it was reconstructed in #3. Fractional momentum loss of this track was required to be  $|\xi| < 0.01$  (Fig.10.18).
5. Checked if in the 'probed' branch (that has a trigger signal, opposite to the reference branch) there is RP track which passes the track selection used in CEP analysis, and there is exactly 1 such track (as in CEP analysis):
  - RP track contains only track-points with at least 3 (out of maximum 4) planes used in reconstruction,
  - Local angles are consistent with the forward proton track originating from the IP:

$$-2 \text{ mrad} < \theta_x^{\text{RP}} - x^{\text{RP}}/|z^{\text{RP}}| < 4 \text{ mrad}, \quad -2 \text{ mrad} < \theta_y^{\text{RP}} - y^{\text{RP}}/|z^{\text{RP}}| < 2 \text{ mrad}$$

If the above was satisfied, the collinearity was calculated between the track reconstructed in the branch under study and the reference track (Fig. 10.19). If the collinearity was within 3.5 standard deviations ( $\sigma_{\Delta\theta_x} \approx \sigma_{\Delta\theta_y} \approx 180 \mu\text{rad}$ ) the elastic track was claimed reconstructed.

6. The RP track reconstruction efficiency  $\varepsilon$  was defined as a probability that in the studied branch exactly 1 RP track was reconstructed and selected, and found collinear with the reference track within 3.5 standard deviations (as required in #5). It was calculated as a ratio of the number of events with reconstructed track in a probed branch and clean track in tagging branch, to all number of events with clean track in tagging branch.
7. Steps #4-#6 were repeated for the other side.

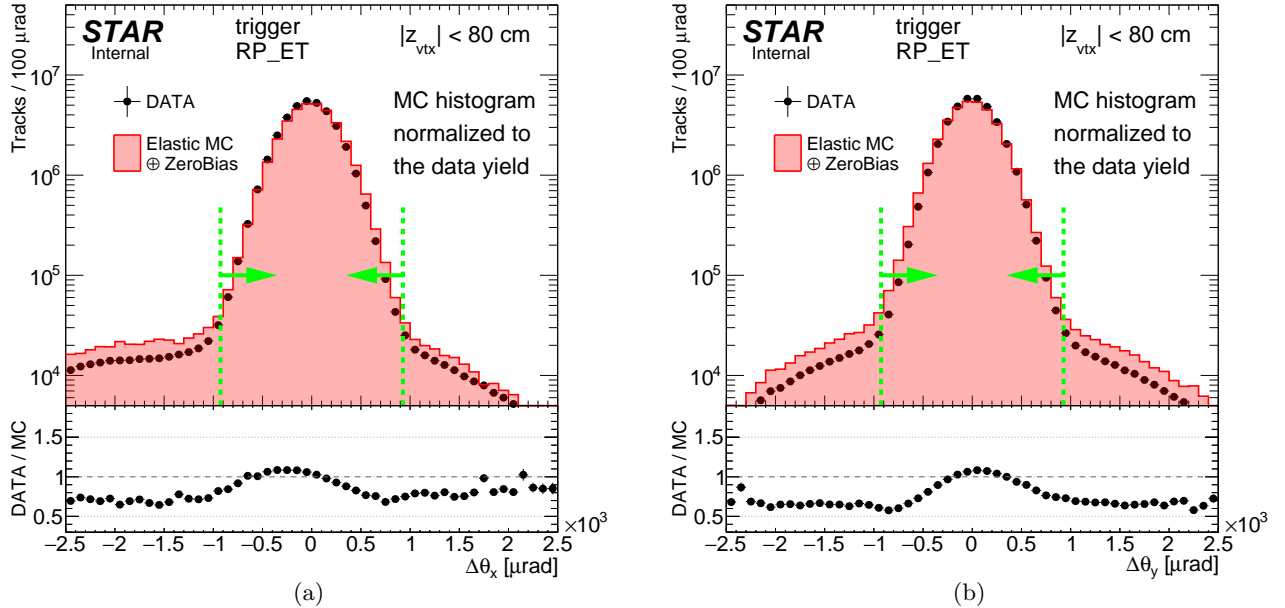


Figure 10.19: Collinearity of a reference track (the clean track which is required to have  $|\xi| < 0.01$ ) and track reconstructed in branch for which reconstruction efficiency is studied, separately in  $xz$ -plane (Fig. 10.19a) and  $yz$ -plane (Fig. 10.19b). An elastic track is claimed as reconstructed if the collinearity of two tracks does not exceed 3.5 standard deviations, as marked with dashed green vertical lines and arrows.

The efficiencies obtained with the described method were calculated as a function of the expected transverse momentum components of the proton in the branch under study. These components were assumed to be equal to the  $(p_x, p_y)$  of the track in the tagging branch taken with the “-” sign to reflect the fact that elastically scattered protons have opposite momentum,  $(p_x^E, p_y^E, p_z^E) = (-p_x^W, -p_y^W, -p_z^W)$  (in the center-of-mass reference frame, which here is identical with the laboratory frame). The sample result for a single branch is presented in Fig. 10.20. The remaining results were placed in Appendix H.

From the figures one can read that the difference between the RP track reconstruction efficiency estimated from the data and from embedded MC do not differ by more than  $\sim 5\%$ . In the central part of the fiducial region used in CEP analysis, defined by Ineqs. (10.4) as

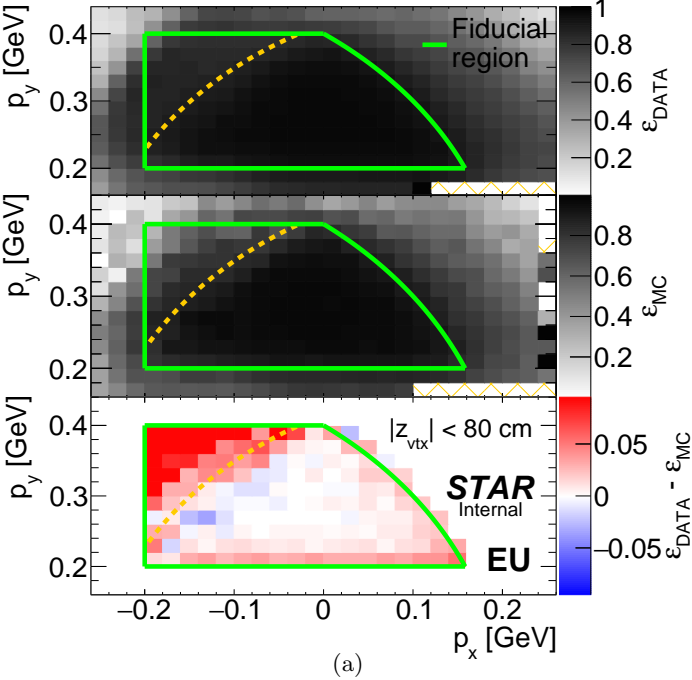
$$0.2 < |p_y| < 0.4, \quad -0.2 < p_x, \quad (p_x + 0.3)^2 + p_y^2 < 0.5^2 \quad (\text{all in GeV}), \quad (10.4)$$

where sensitivity to the edge effects (uncertainty on aperture positions), to dead material effects and to inaccuracies in simulated angular beam divergence is suppressed, the difference is not larger than  $\sim 1\%$ . Such number was taken as the uncertainty on the track reconstruction efficiency related to the signal digitization and embedding and the track reconstruction algorithm. The largest difference between the data and simulation is observed in the corner of the fiducial region satisfying Ineq. (10.5)

$$(p_x - 0.2)^2 + p_y^2 > 0.46^2 \quad (\text{all in GeV}), \quad (10.5)$$

where the RF shield is present between the 1<sup>st</sup> and 2<sup>nd</sup> RP station, and possibly also the front part of the DX-D0 chamber is present. This may indicate that the thickness/density of these elements is not accurately modeled (too thick/dense pieces of material implemented in the simulation). We decided to introduce correction to the RP track reconstruction efficiency in the corner of the fiducial region (Ineq. 10.5), equal to the difference between data and MC track reconstruction efficiency estimates presented in Fig. 10.20a (and corresponding plots for other branches). We assign a conservative systematic uncertainty to the efficiency in this corner region equal to the absolute value of the efficiency correction. We may conduct an independent analysis of this corner region in order to have better, more realistic estimate of the systematic uncertainty.

For the remaining part of the fiducial  $(p_x, p_y)$  region we also assign a systematic uncertainty of the RP track reconstruction efficiency equal to the absolute value of the difference between data and MC track reconstruction efficiency estimates shown in Fig. 10.20a and in Appendix H. These differences should also cover uncertainties related to the angular beam divergence effects and error on positions of limiting apertures.



(a)

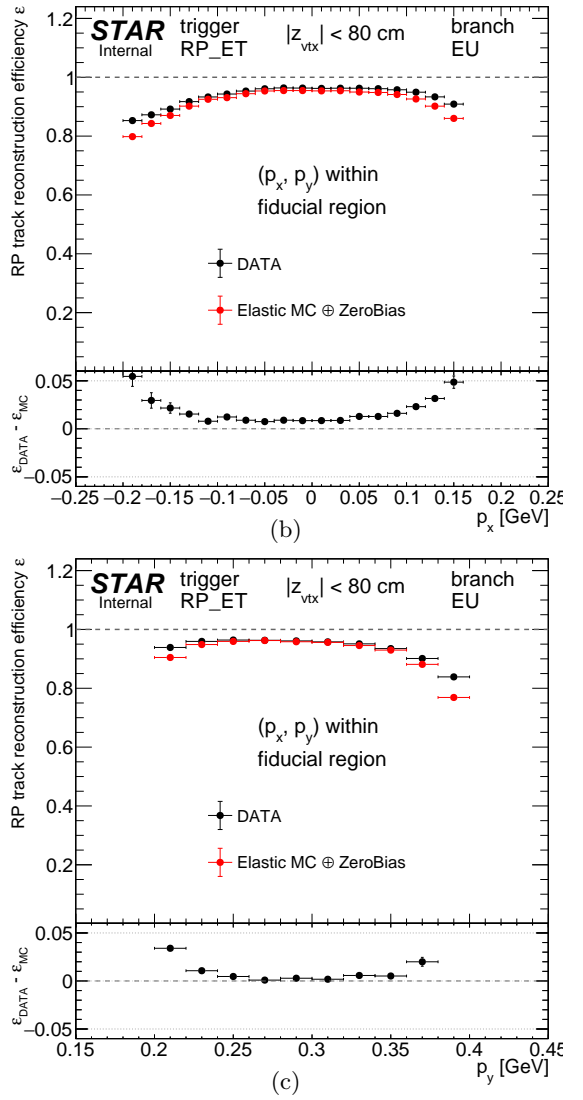


Figure 10.20: Sample comparison of RP track reconstruction efficiency (branch EU) estimated with the method described in the text as a function of  $(p_x, p_y)$  of proton track (10.20a) and comparison of 1-dimensional projections of efficiencies in a fiducial region marked with green envelope:  $p_x$  (10.20b) and  $p_y$  (10.20c). Dashed orange line marks the border of the fiducial region part where the correction to RP track reconstruction efficiency is required. Lower pad in each sub-figure shows the difference between efficiency extracted from the data and elastic scattering MC embedded into zero-bias data. Hatched orange area marks bins without any entries (efficiency incalculable). The difference between efficiencies in Fig. 10.20a was calculated only for entries in the fiducial region. Similar plots for the remaining branches can be found in Appendix H.

### 10.3.2 Track point reconstruction efficiency (relative reconstruction efficiency)

A single track point reconstruction efficiency can be studied in a way similar to the track reconstruction efficiency. In contrast to the latter, to estimate track point reconstruction efficiency one can reconstruct elastic scattering event independently from the studied detector, which provides even higher purity of the sample in comparison to the track reconstruction efficiency.

The comparison between track point reconstruction efficiency in the data and simulation provides better insight to discrepancies in detector geometry and amount of material than comparison of track reconstruction efficiency, as in this case the effect of angular beam divergence is reduced by using proton track observables reconstructed on the side of studied RP detector. Relative RP efficiency is mostly sensitive to material in between the RPs in the same branch, as the presence of elastic track reconstructed in the studied branch assures that proton survived transport from the IP to RP stations. This study gives us also information about performance of the track-point reconstruction algorithm itself.

Unfortunately, information about the track point reconstruction efficiency is limited - there is no access to some part of the fiducial region, approximately described by inequality  $p_x \lesssim -0.08$  GeV. This is caused by the fact that RPs in the 1<sup>st</sup> and the 2<sup>nd</sup> station do not fully overlap - they are shifted with respect to each other, with the most significant offset in  $x$  direction ( $\approx 2$  cm) due to restrictions imposed on DX-D0 chamber at the design level, mainly to accommodate space for ZDC detectors placed close behind the 2<sup>nd</sup> RP stations.

In this analysis elastic proton-proton scattering events were selected by requiring the elastic trigger (signal in PMTs in two opposite RP branches) and clean RP track of  $|\xi| < 0.01$  on one side of the IP, and clean track point with trigger signal in at least one RP (a reference RP) in the opposite branch. A track was formed from this clean track point and the two tracks were required collinear within 3.5 standard deviations. In the other

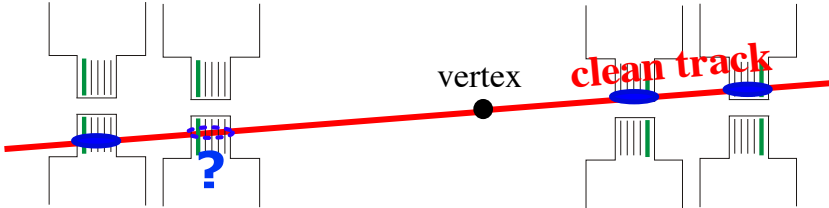


Figure 10.21: Sketch of the Roman Pot system with drafted method of estimation of the RP track point reconstruction efficiency using elastic scattering events.

RP detector in a studied branch a trigger was required. The probability to have exactly 1 track point in the studied RP with position consistent with that extrapolated from the reference RP was referred to as the track point reconstruction efficiency. The method is illustrated in Fig. 10.21. Detailed description of the algorithm is provided below, excluding steps #1-#4 which are the same as in Sec. 10.3.1:

5. Selected one RP station with a trigger signal in the studied branch (opposite to the tagging branch). We call it a reference detector. A clean track point in that RP was required. By clean track point we understand exactly 1 track point, in addition reconstructed with at least 3 (out of 4) silicon planes. A track was formed from the track point in the reference detector. Collinearity was calculated between the tagging track and the track reconstructed from the clean track point in studied branch (Fig. 10.19). If the collinearity was satisfied within 3.5 standard deviations the reference elastic track was claimed reconstructed.
6. The trigger signal was required in the detector under study (the other detector in the same branch as a reference detector). The RP track point reconstruction efficiency  $\varepsilon$  was defined as a probability that in the studied RP, among unlimited number of reconstructed track points exactly 1 track point had reconstructed  $(x, y)$  position consistent with the position extrapolated from the reference detector  $(x_{\text{extr}}, y_{\text{extr}})$  within 1.2 mm (Fig. 10.22). It was calculated as a ratio of the number of selected elastic scattering events with a trigger signal in a studied detector, and exactly 1 track point of reconstructed position matching the expected, to all number of selected elastic scattering events with a trigger signal in the studied detector.
7. Steps #5-#6 were repeated for the other detector in studied branch.
8. Steps #5-#7 were repeated for the other side.

The estimates of track point reconstruction efficiency obtained with the described method are shown in Figs. 10.23 (E1U), 10.24 (E2U) and Appendix H (for the remaining). They are presented 2-dimensionally: in

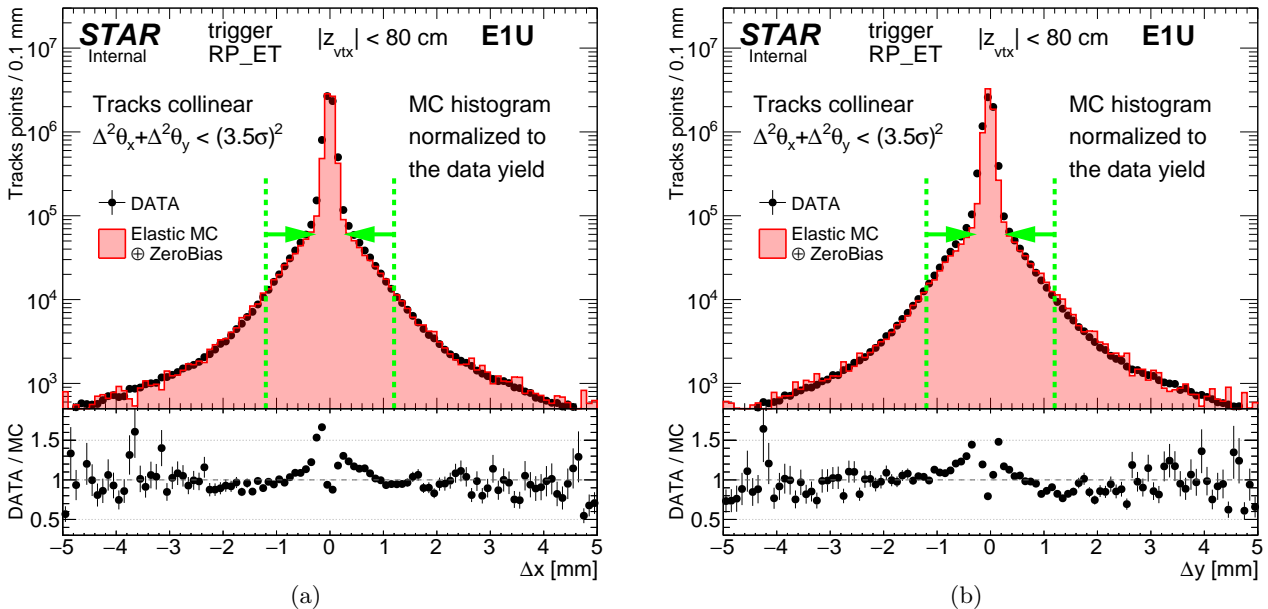


Figure 10.22: Difference between position of a track point (with clusters in 3 out 4 silicon planes) reconstructed in E1U (if E1U has a trigger signal) and expected track point position extrapolated from a reference track point reconstructed in E2U, for elastic scattering events with the collinearity of the track in the opposite branch and track reconstructed from a reference track point better than 3.5 standard deviations. A track point is claimed as reconstructed if the position difference is not larger than 1.2 mm, as marked with dashed green vertical lines and arrows.

$(p_x, p_y)$  (Figs. 10.23a, 10.24a) and  $(x, y)$  (Figs. 10.23b, 10.24b), as well as 1-dimensionally: in  $x$  (Figs. 10.23c, 10.24c) and  $y$  (Figs. 10.23d, 10.24d).

In the area of detector accessible in this study an excellent agreement ( $< 0.5\%$  difference) between the efficiency estimates from data and MC is found in the region of no material on the proton path from IP to the RPs. This reflects correct simulation of the silicon signal digitization, cluster reconstruction and matching, track point reconstruction and embedding. The differences between data and MC are more significant in the region of aperture shadows, e.g. DX shadow visible the best in Fig. 10.23c at  $x \gtrsim 20$  mm (possibly too much simulated material), or DX-D0 chamber entry/RF shield shadow visible in Fig. 10.23d at  $y \gtrsim 60$  mm (probably also too much simulated material).

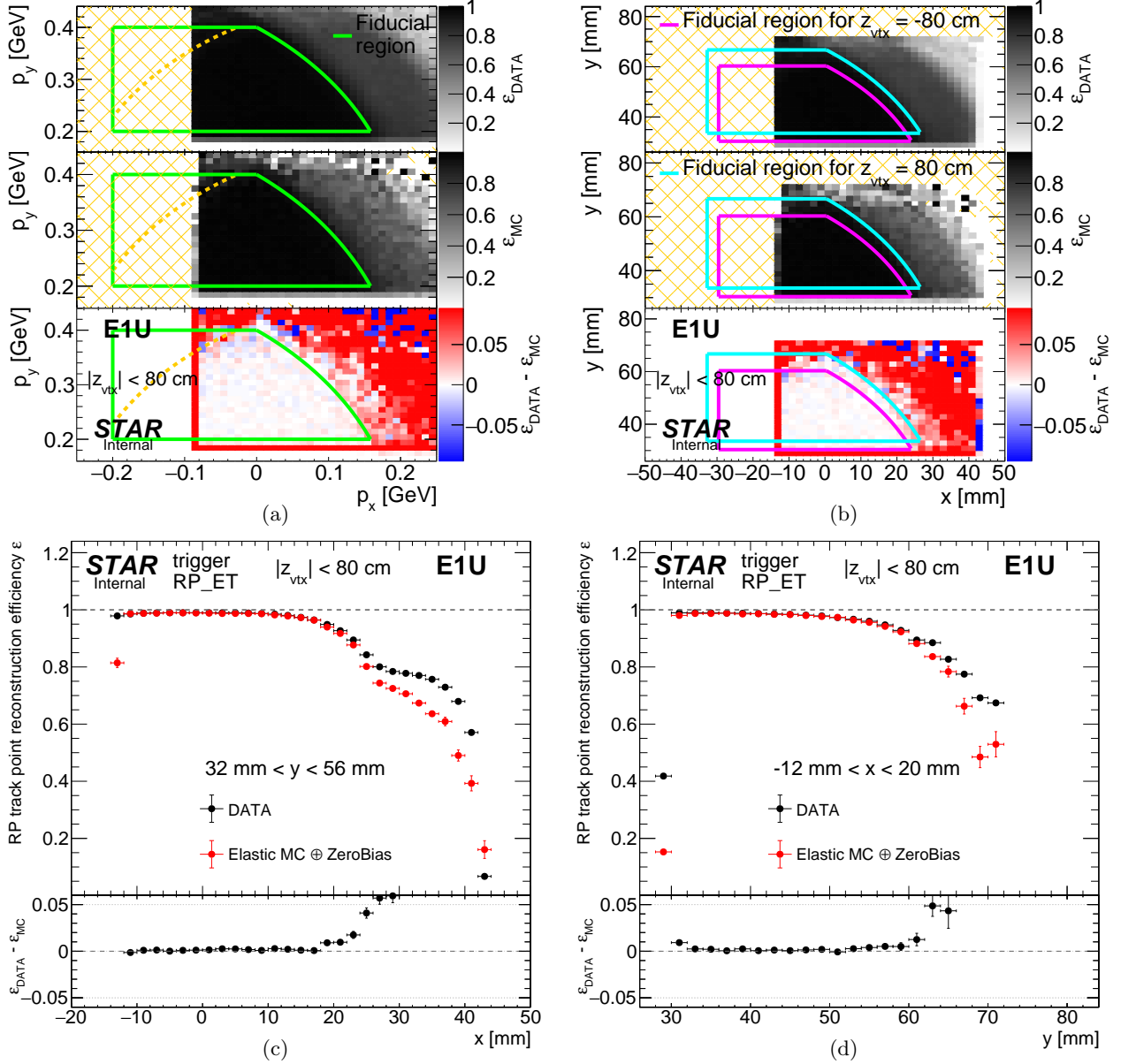


Figure 10.23: Sample comparison of RP track point reconstruction efficiency (detector E1U) estimated with the method described in the text as a function of  $(p_x, p_y)$  of proton track (10.23a),  $(x, y)$  position extrapolated from the reference RP (E2U) to the studied RP (10.23b), and comparison of 1-dimensional projections of efficiencies in selected ranges of hit position (given in the plot):  $x$  (10.23c) and  $y$  (10.23d). Lower pad in each subfigure shows the difference between efficiency extracted from the data and elastic scattering MC embedded into zero-bias data. Hatched orange area marks bins without any entries (efficiency incalculable). The fiducial region in  $(x, y)$  plot is represented by two envelopes which correspond to the extreme accepted values of  $z_{vtx}$ . Similar plots for the remaining detectors can be found in Appendix H.

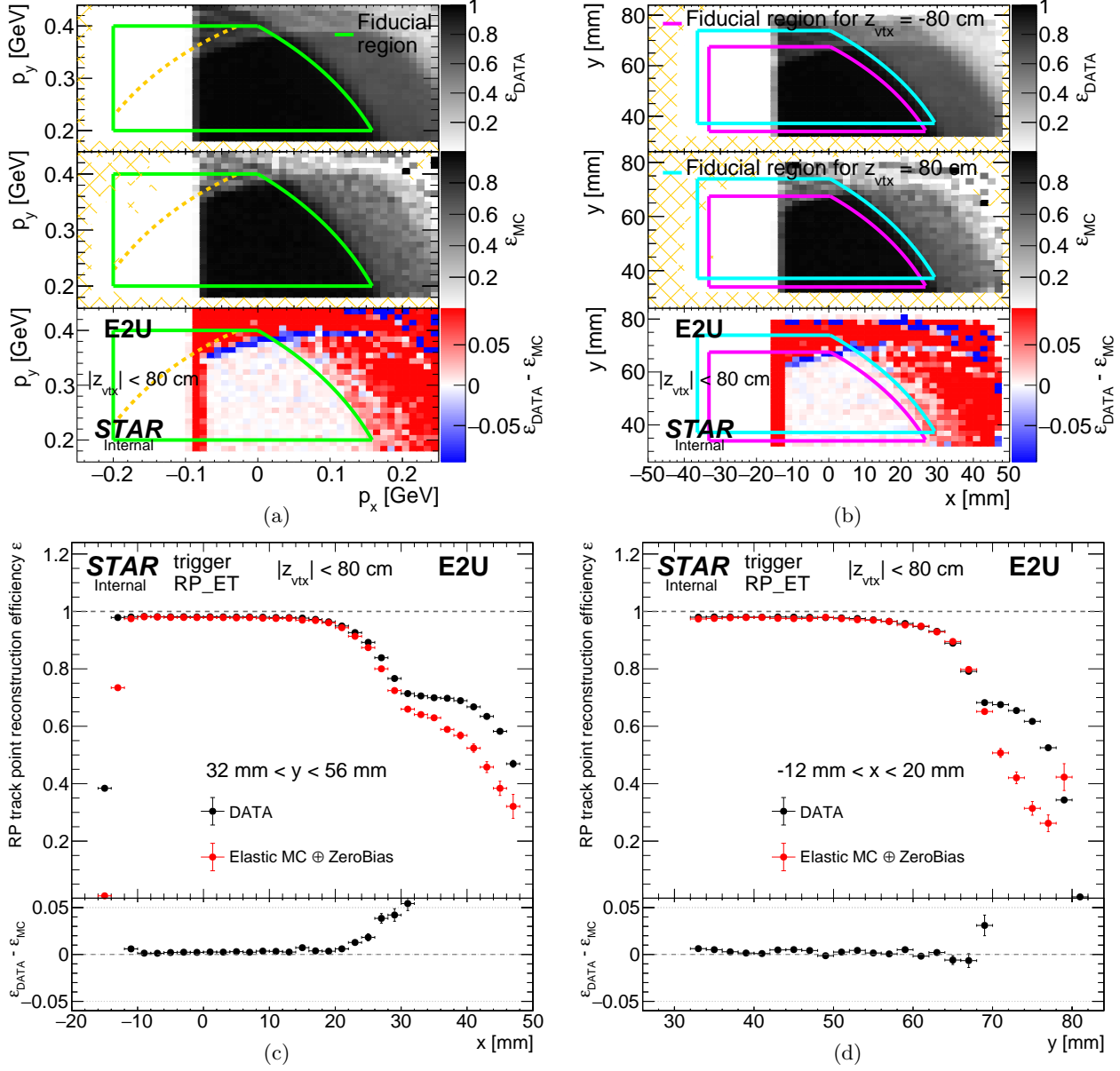


Figure 10.24: Sample comparison of RP track point reconstruction efficiency (detector E2U) estimated with the method described in the text as a function of  $(p_x, p_y)$  of proton track (10.24a),  $(x, y)$  position extrapolated from the reference RP (E1U) to the studied RP (10.24b), and comparison of 1-dimensional projections of efficiencies in selected ranges of hit position (given in the plot):  $x$  (10.24c) and  $y$  (10.24d). Lower pad in each subfigure shows the difference between efficiency extracted from the data and elastic scattering MC embedded into zero-bias data. Hatched orange area marks bins without any entries (efficiency incalculable). The fiducial region in  $(x, y)$  plot is represented by two envelopes which correspond to the extreme accepted values of  $z_{\text{vtx}}$ . Similar plots for the remaining detectors can be found in Appendix H.

## 10.4 Summary of the systematic uncertainties of efficiencies

In Tab. 10.1 we summarize all systematic uncertainties of TPC, TOF and RP efficiency which were discussed in this note.

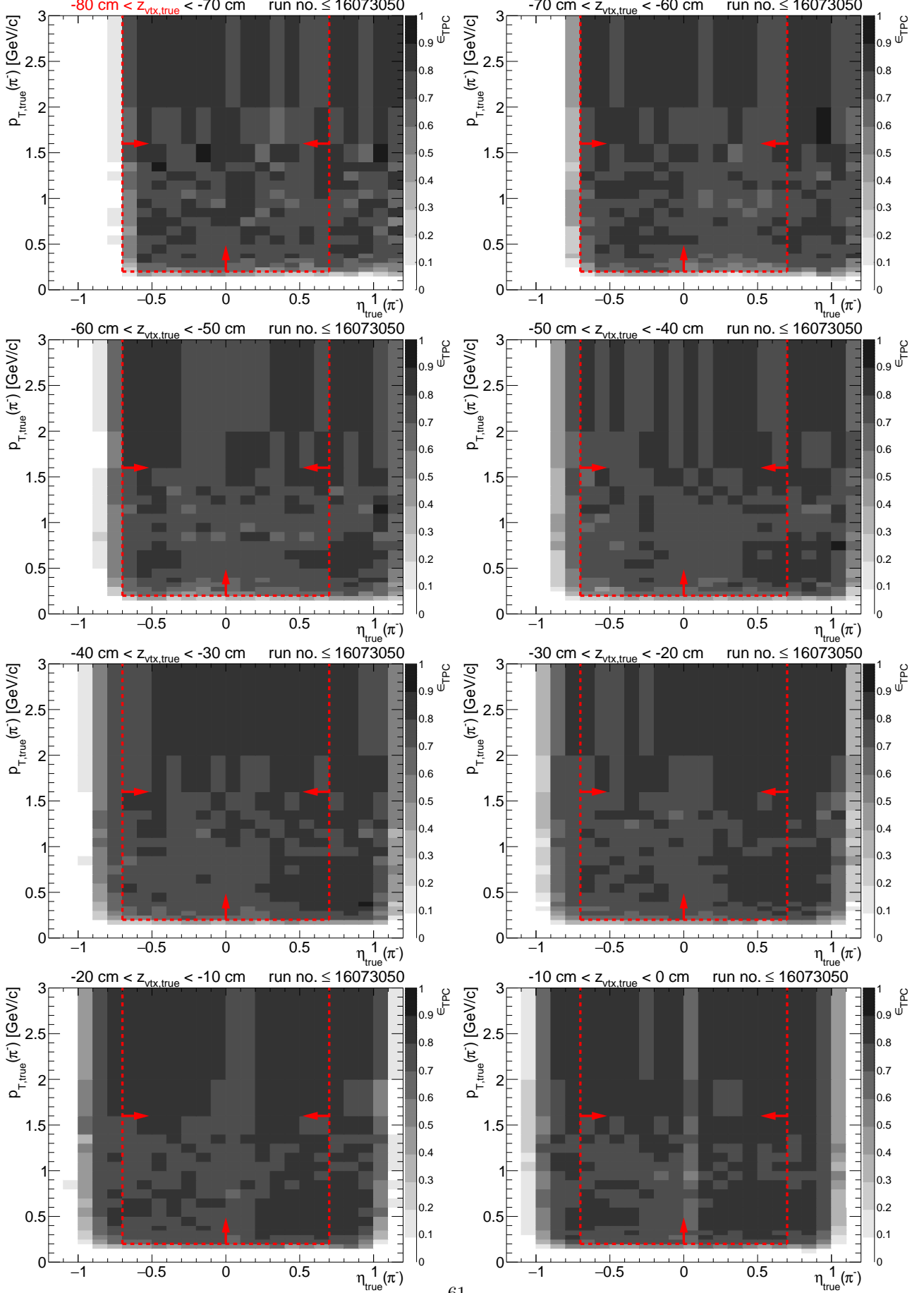
System	Source of systematic uncertainty	Maximum $\delta^{\text{syst.}}$			Average $\delta^{\text{syst.}}$			Total average $\delta^{\text{syst.}}$					
		$\pi$	$K$	$p$	$\pi$	$K$	$p$	$\pi$	$K$	$p$			
TPC	MC signal embedding into real data	3%			1.8%			2.1%	2.3%	2.3%			
	representativeness of embedded MC in terms of TPC occupancy	$\leq 1\%$			$\leq 1\%$								
	dead material modeling	0.4%	2%	2%	0.3%	1%	1%						
TOF	MC signal embedding into real data	< 0.5%			< 0.5%			1%	2%	3%			
	detector simulation accuracy	3%	4.5%	4%	1%	2%	3%						
RP	MC signal embedding into real data	-	-	0.5%	-	-	0.5%	-	-	2%			
	detector simulation accuracy (joint effect of alignment, beam ang. div., and others)	-	-	20%	-	-	2%						

Table 10.1: Summary of the systematic uncertainty of the TPC, TOF and RP track reconstruction/matching efficiency. All numbers reflect uncertainties determined for tracks within the fiducial range of kinematic variables defined for a physics measurement. Systematic uncertainties for three particle species are separately given for the central tracks, while in case of the RP track efficiency uncertainty for forward scattered protons is provided. The total uncertainty is a quadratic sum of all uncertainty components for a given detector system. All numbers are absolute uncertainties of efficiencies (e.g. syst. uncertainty  $\delta^{\text{syst.}} = 3\%$  for efficiency  $\varepsilon = 50\%$  should be read  $\varepsilon = 0.50 \pm 0.03$ ).

# **Appendix A**

## **TPC track reconstruction efficiency**

Figure A.1: TPC acceptance and reconstruction efficiency of  $\pi^-$  for runs with dead sector #19. Each plot represents the TPC efficiency  $\epsilon_{\text{TPC}}$  ( $z$ -axis) as a function of true particle pseudorapidity  $\eta$  ( $x$ -axis) and transverse momentum  $p_T$  ( $y$ -axis) in single  $z$ -vertex bin whose range is given at the top. Red lines and arrows indicate region accepted in analyses.



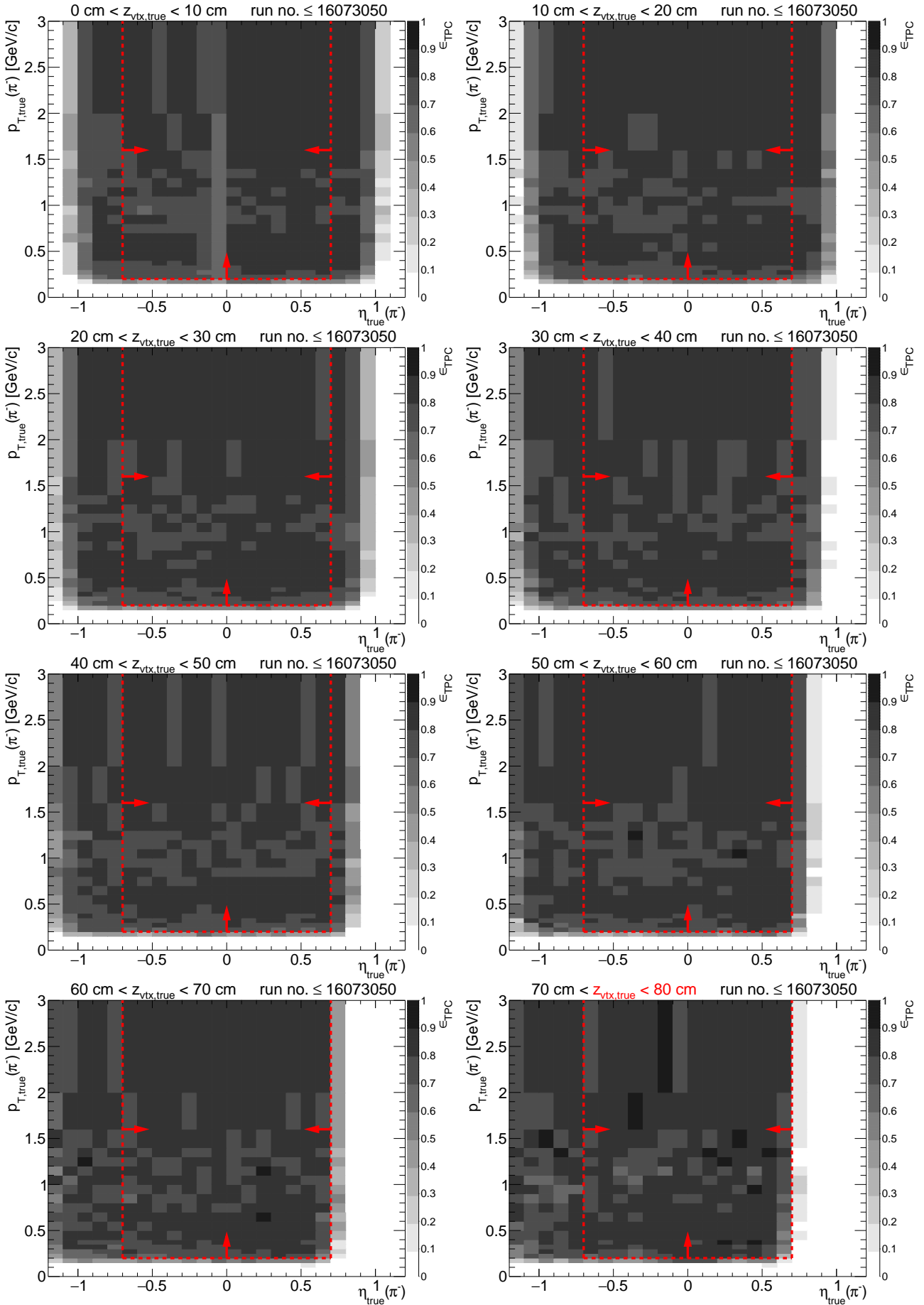
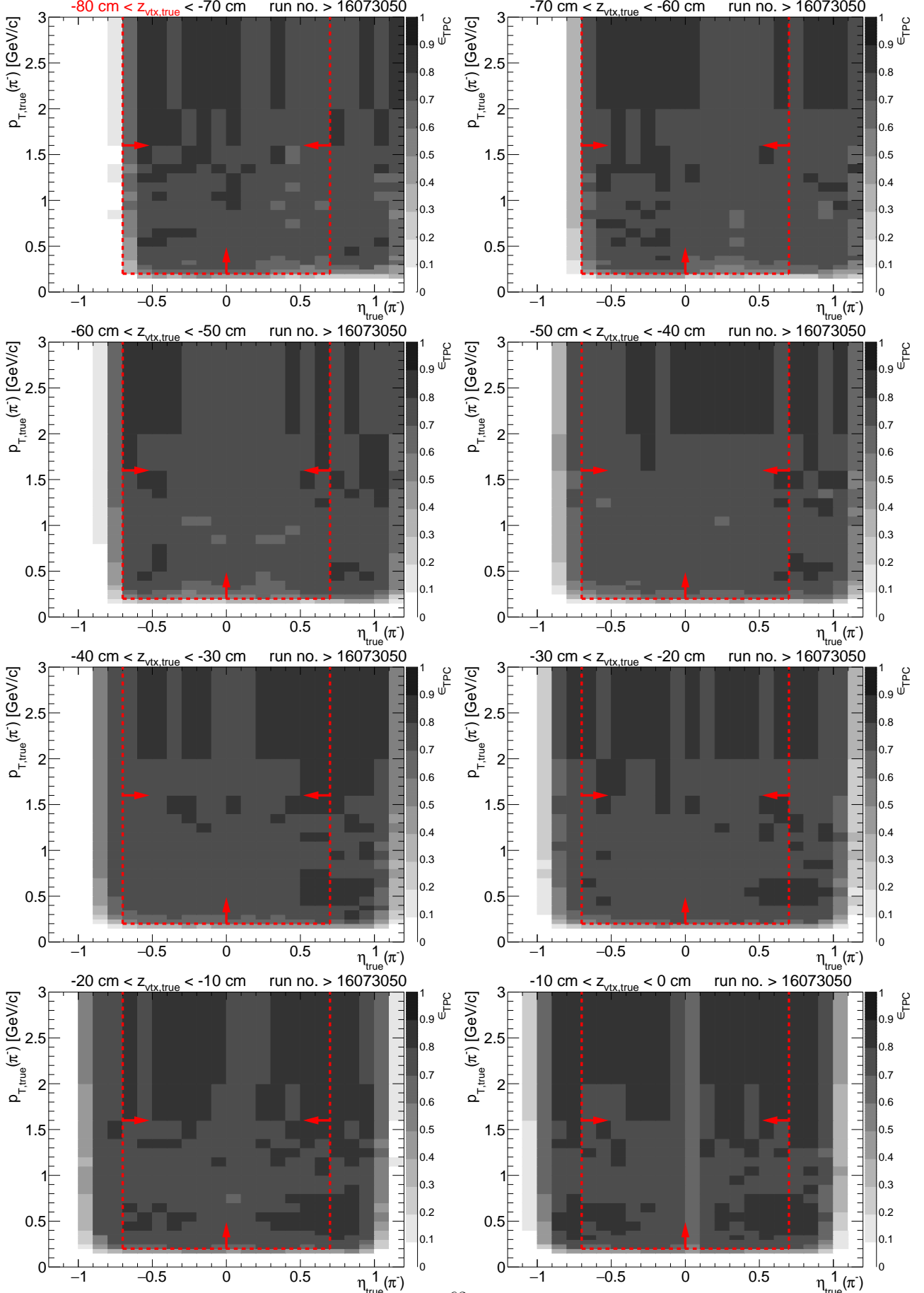


Figure A.2: TPC acceptance and reconstruction efficiency of  $\pi^-$  for runs with sector #19 back in operation. Each plot represents the TPC efficiency  $\epsilon_{\text{TPC}}$  ( $z$ -axis) as a function of true particle pseudorapidity  $\eta$  ( $x$ -axis) and transverse momentum  $p_T$  ( $y$ -axis) in single  $z$ -vertex bin whose range is given at the top. Red lines and arrows indicate region accepted in analyses.



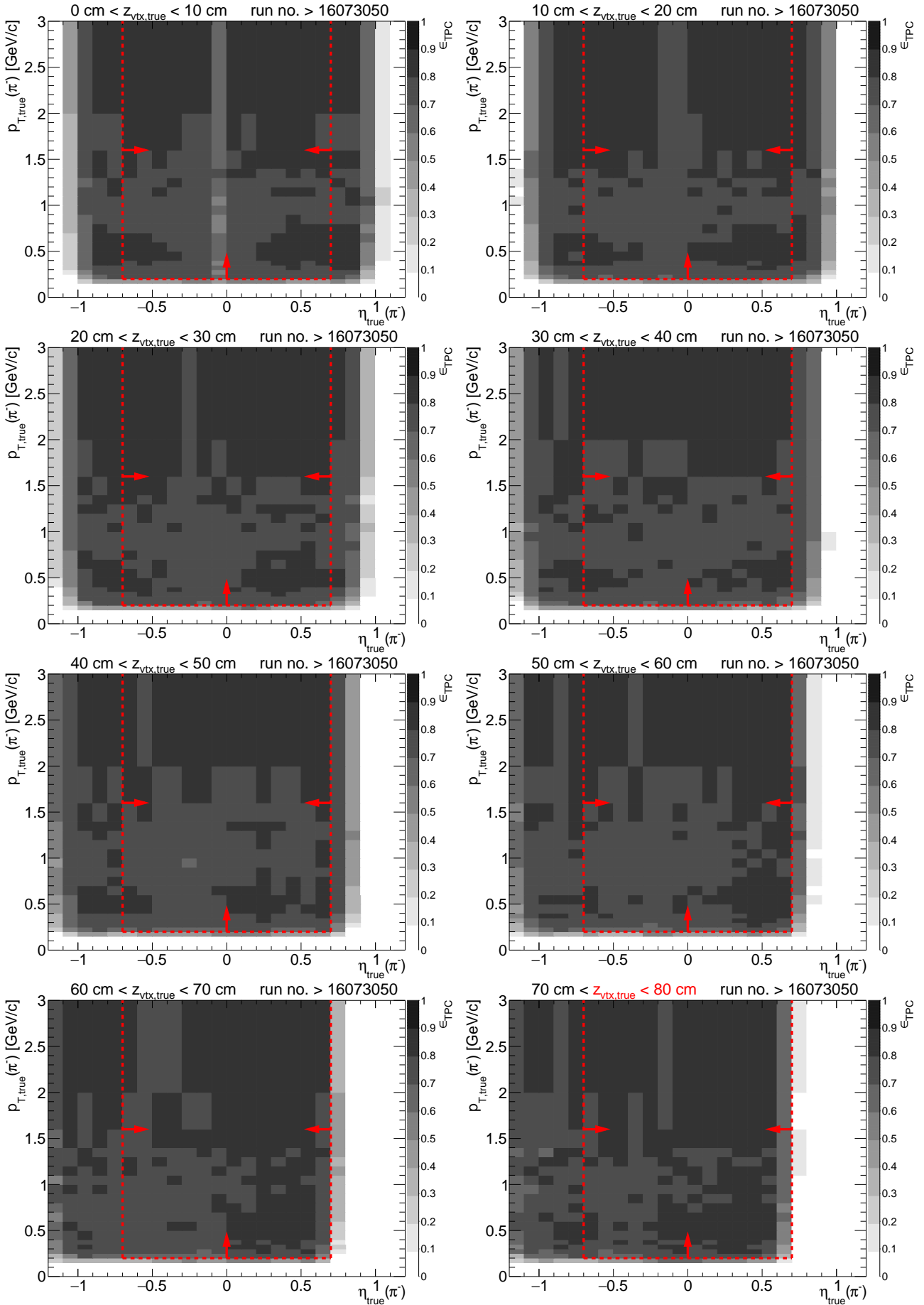
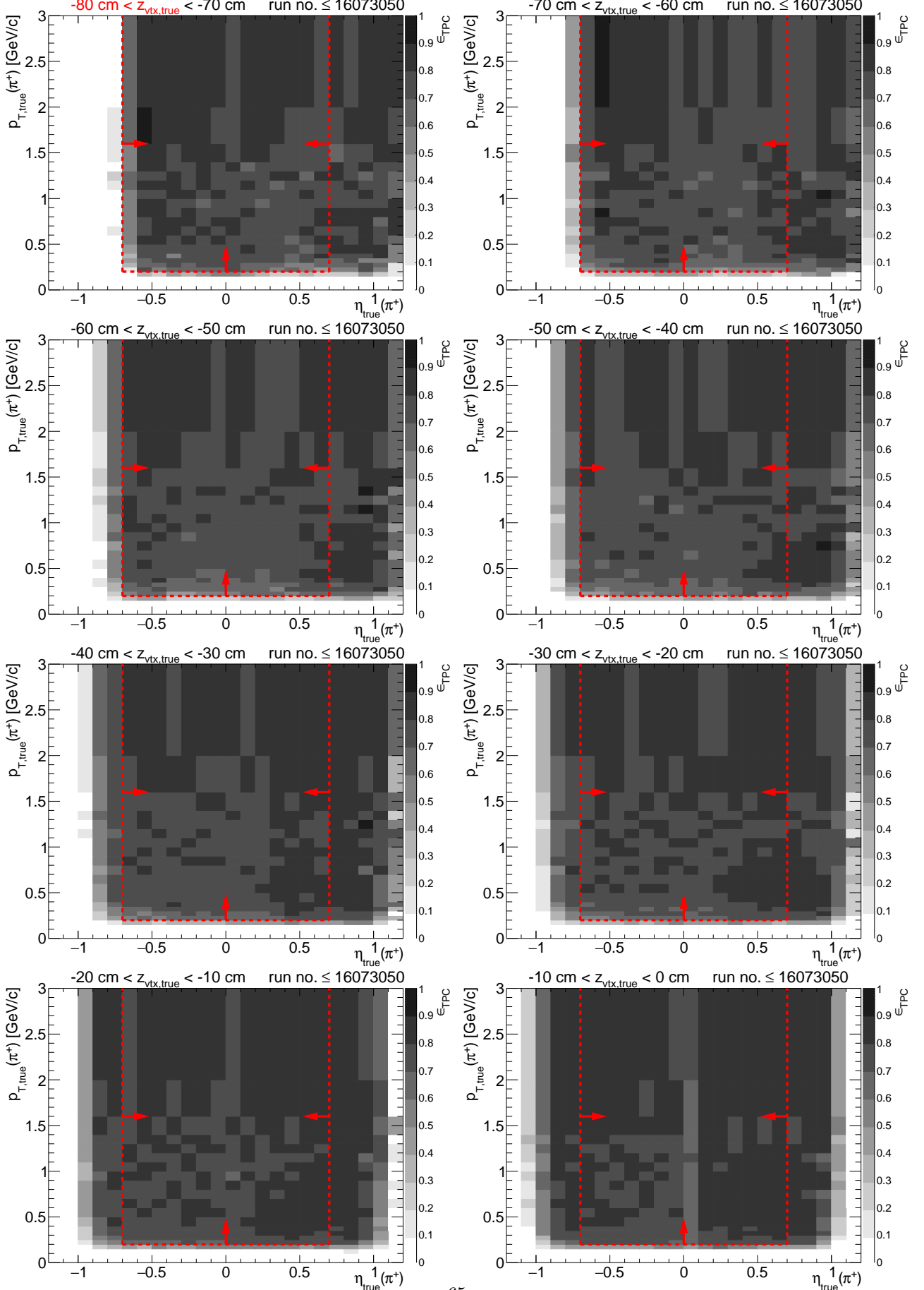


Figure A.3: TPC acceptance and reconstruction efficiency of  $\pi^+$  for runs with dead sector #19. Each plot represents the TPC efficiency  $\epsilon_{\text{TPC}}$  ( $z$ -axis) as a function of true particle pseudorapidity  $\eta$  ( $x$ -axis) and transverse momentum  $p_T$  ( $y$ -axis) in single  $z$ -vertex bin whose range is given at the top. Red lines and arrows indicate region accepted in analyses.



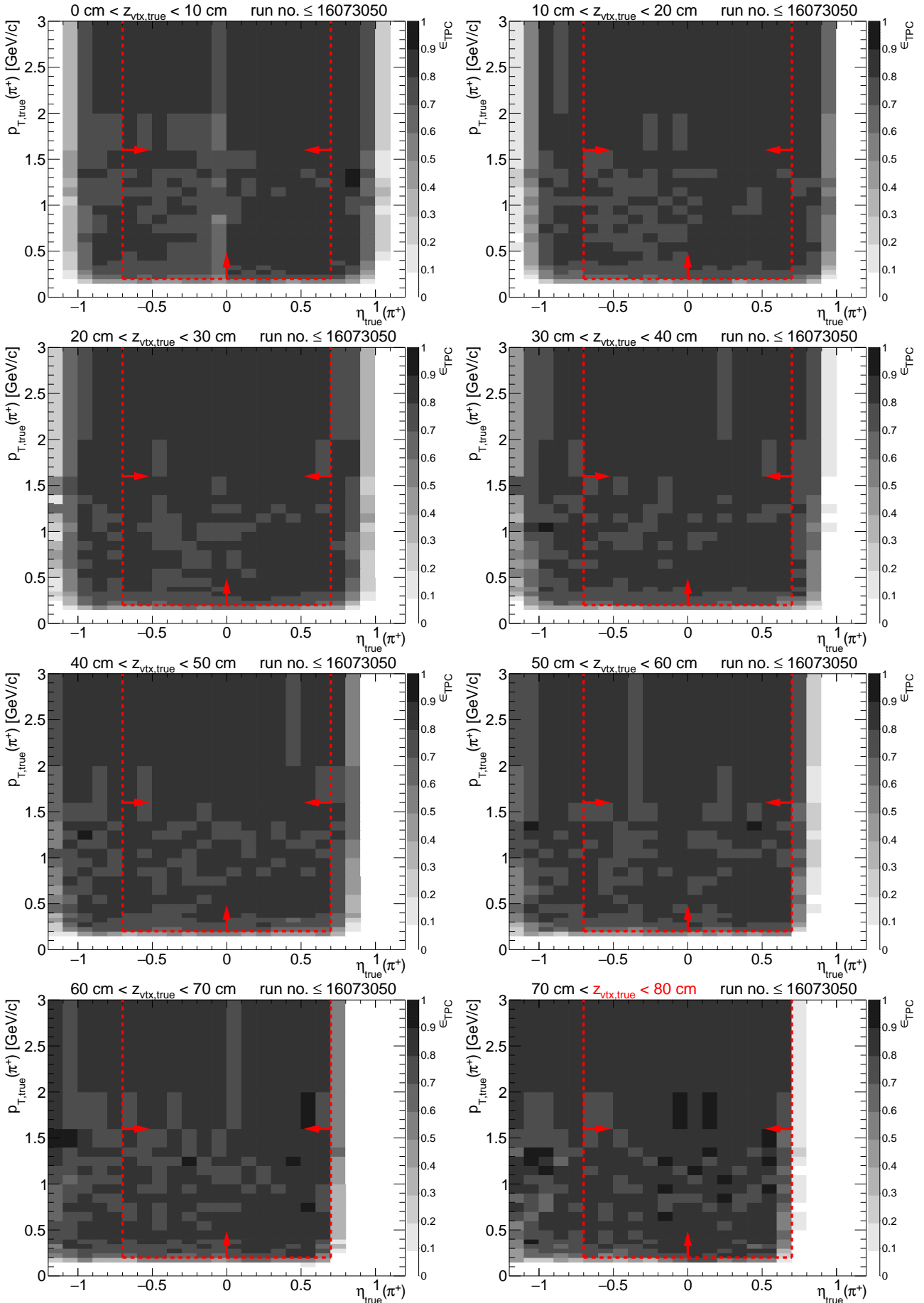
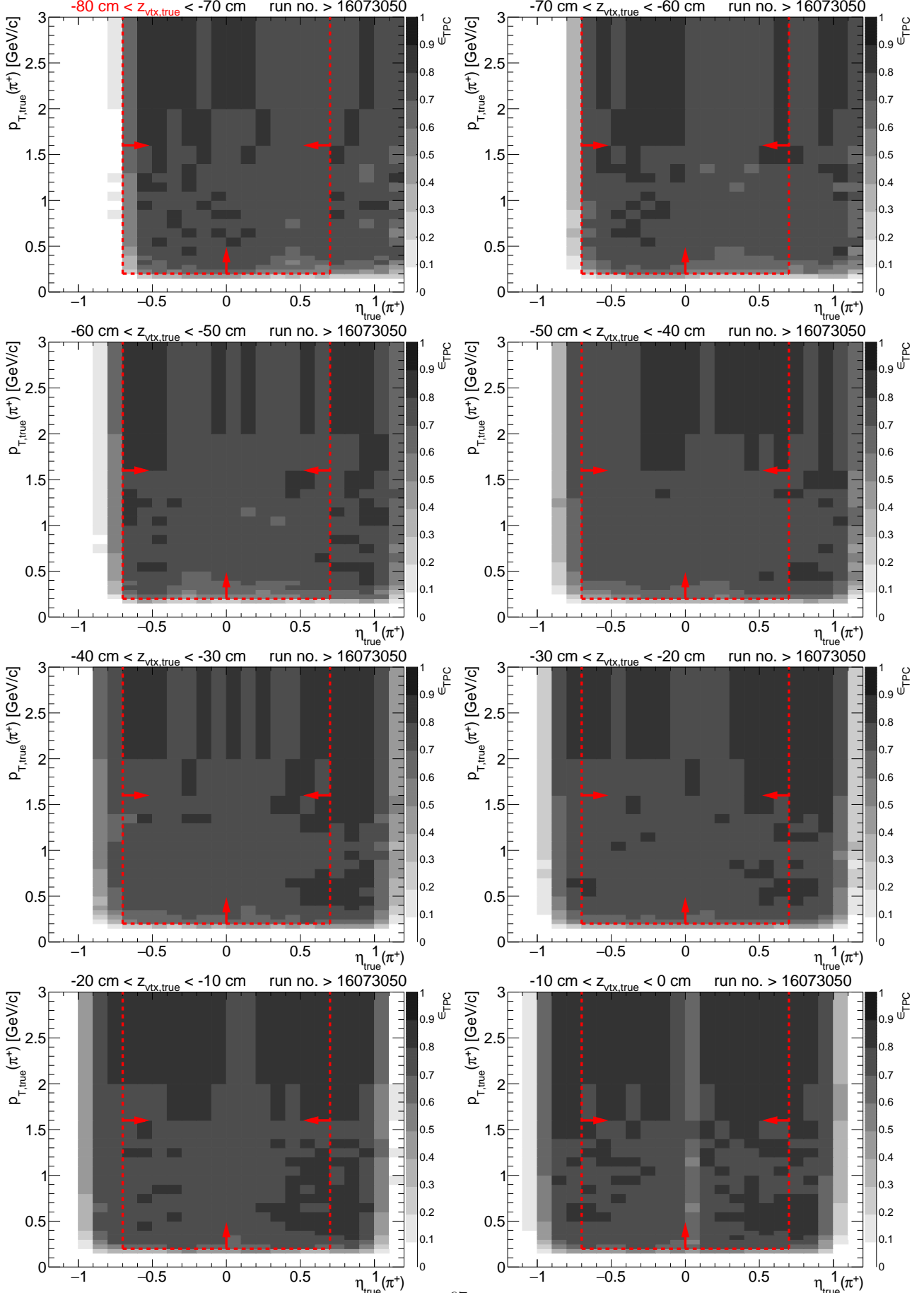


Figure A.4: TPC acceptance and reconstruction efficiency of  $\pi^+$  for runs with sector #19 back in operation. Each plot represents the TPC efficiency  $\epsilon_{\text{TPC}}$  ( $z$ -axis) as a function of true particle pseudorapidity  $\eta$  ( $x$ -axis) and transverse momentum  $p_T$  ( $y$ -axis) in single  $z$ -vertex bin whose range is given at the top. Red lines and arrows indicate region accepted in analyses.



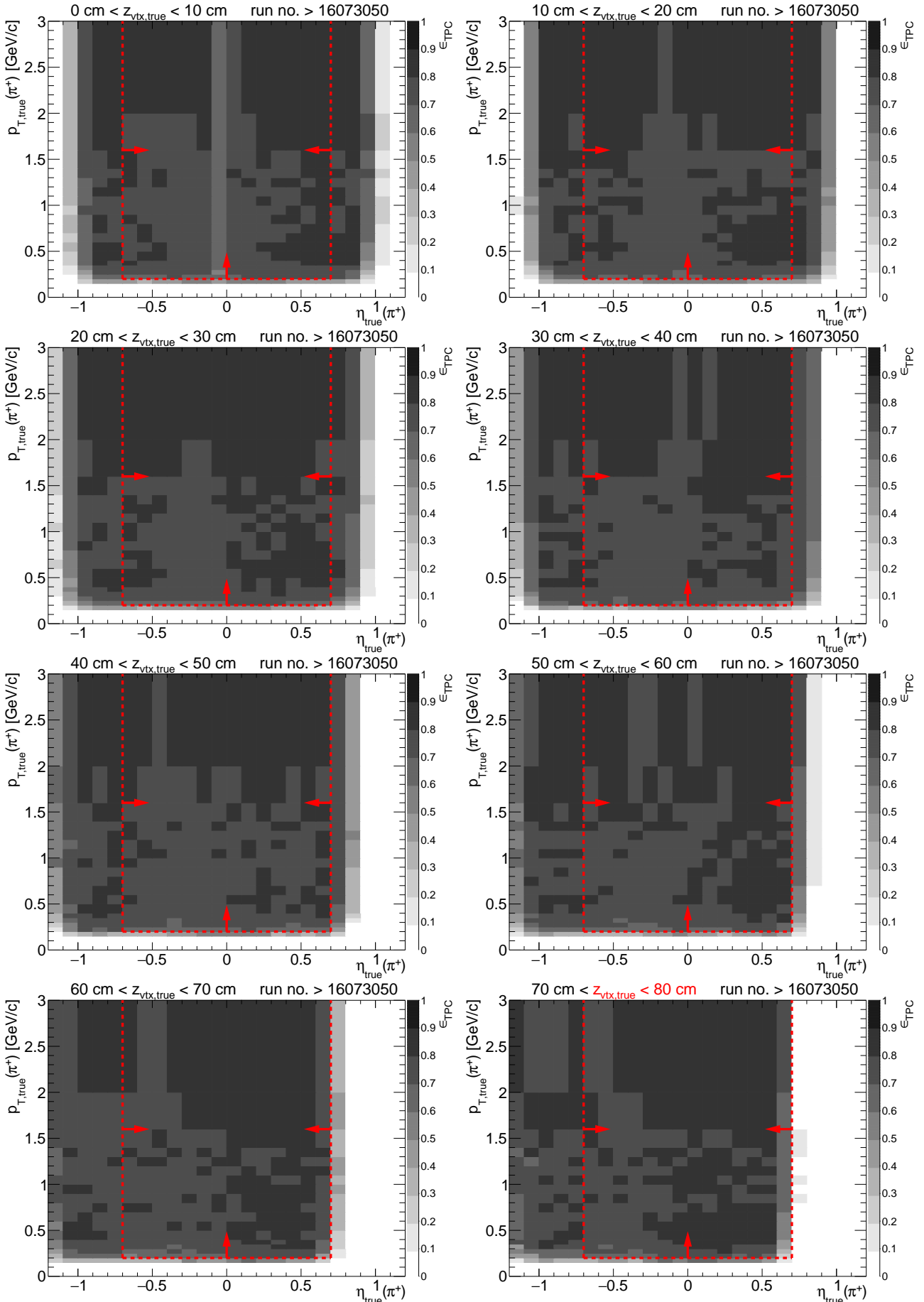
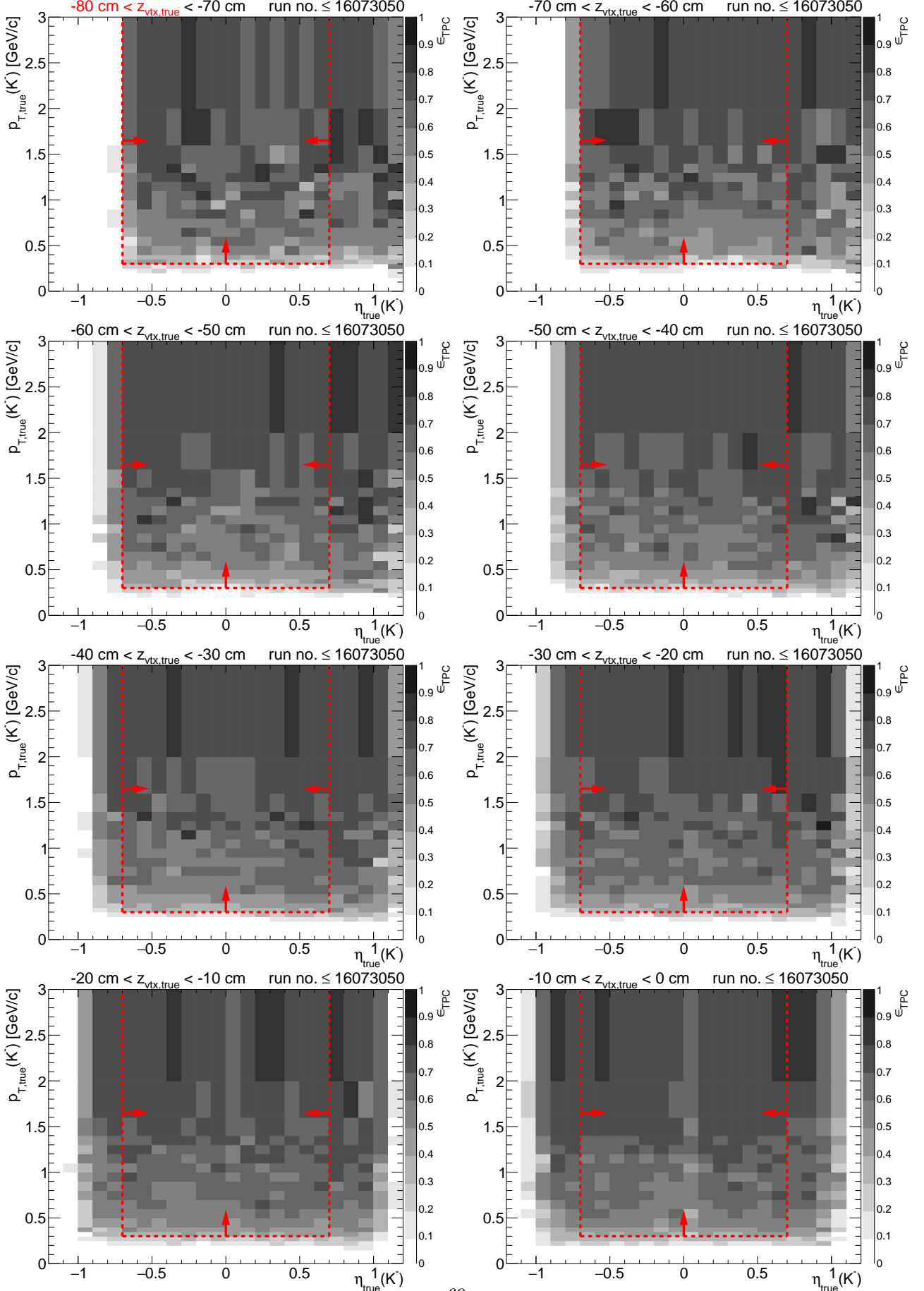


Figure A.5: TPC acceptance and reconstruction efficiency of  $K^-$  for runs with dead sector #19. Each plot represents the TPC efficiency  $\epsilon_{\text{TPC}}$  ( $z$ -axis) as a function of true particle pseudorapidity  $\eta$  ( $x$ -axis) and transverse momentum  $p_T$  ( $y$ -axis) in single  $z$ -vertex bin whose range is given at the top. Red lines and arrows indicate region accepted in analyses.



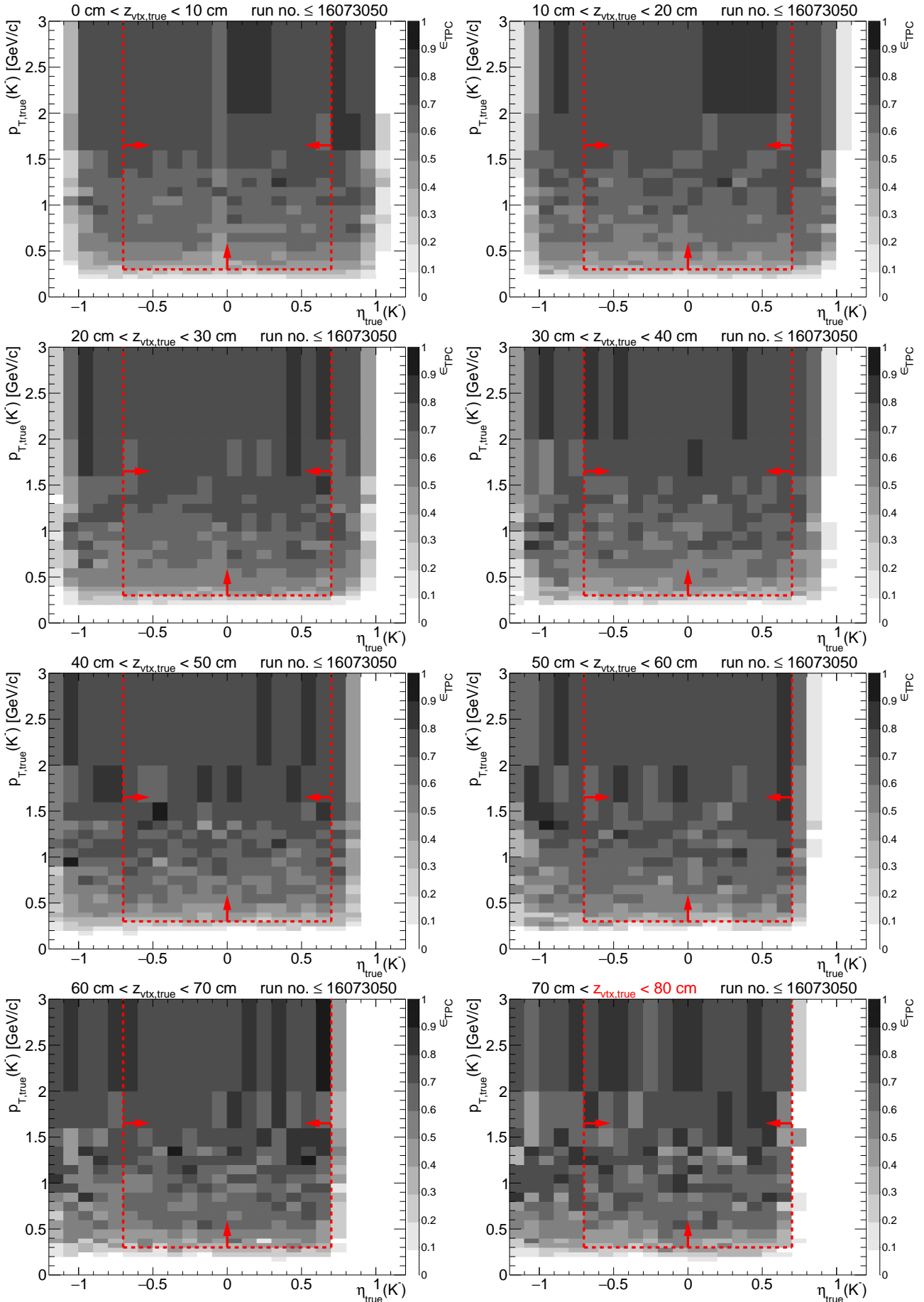
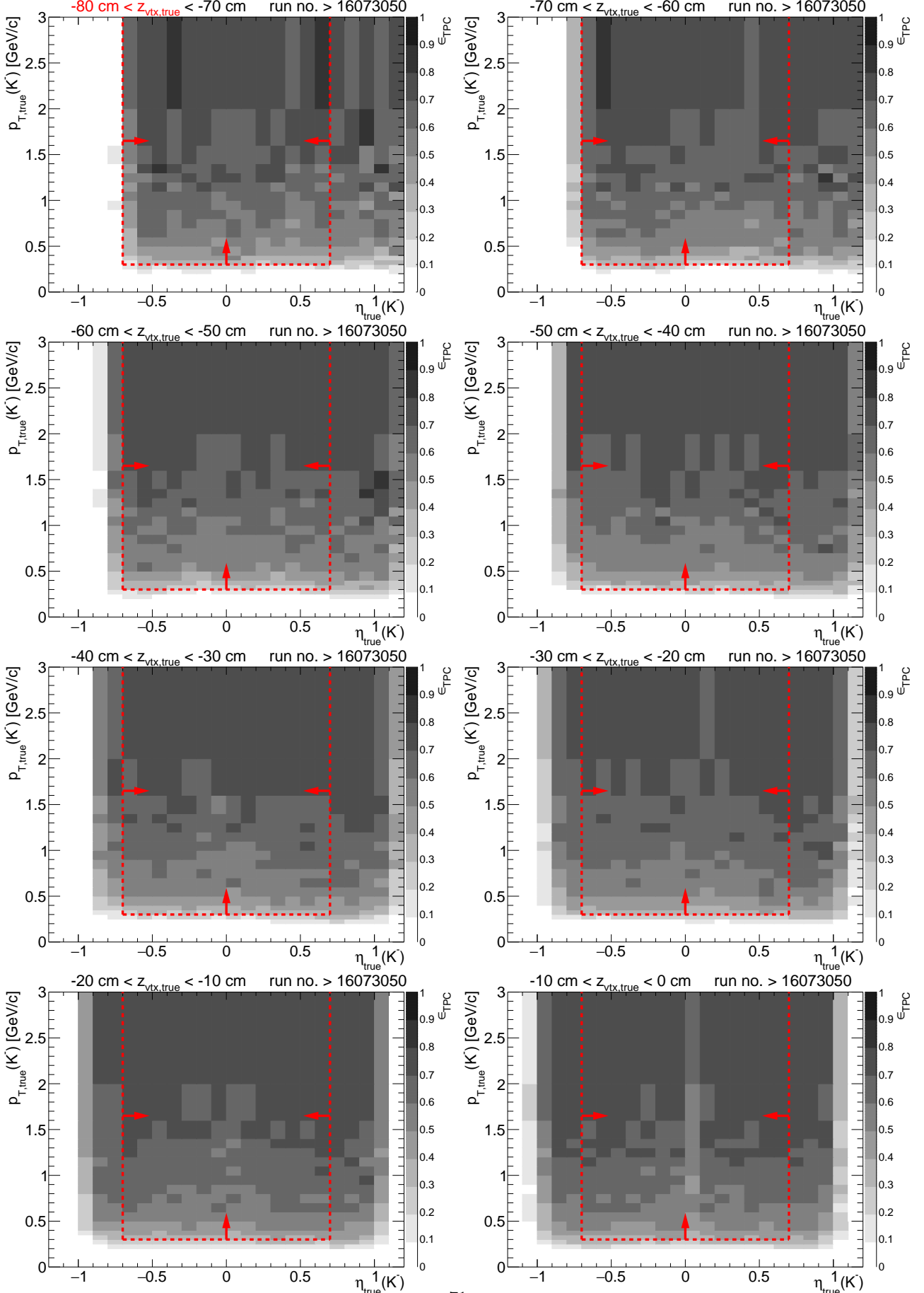


Figure A.6: TPC acceptance and reconstruction efficiency of  $K^-$  for runs with sector #19 back in operation. Each plot represents the TPC efficiency  $\epsilon_{\text{TPC}}$  ( $z$ -axis) as a function of true particle pseudorapidity  $\eta$  ( $x$ -axis) and transverse momentum  $p_T$  ( $y$ -axis) in single  $z$ -vertex bin whose range is given at the top. Red lines and arrows indicate region accepted in analyses.



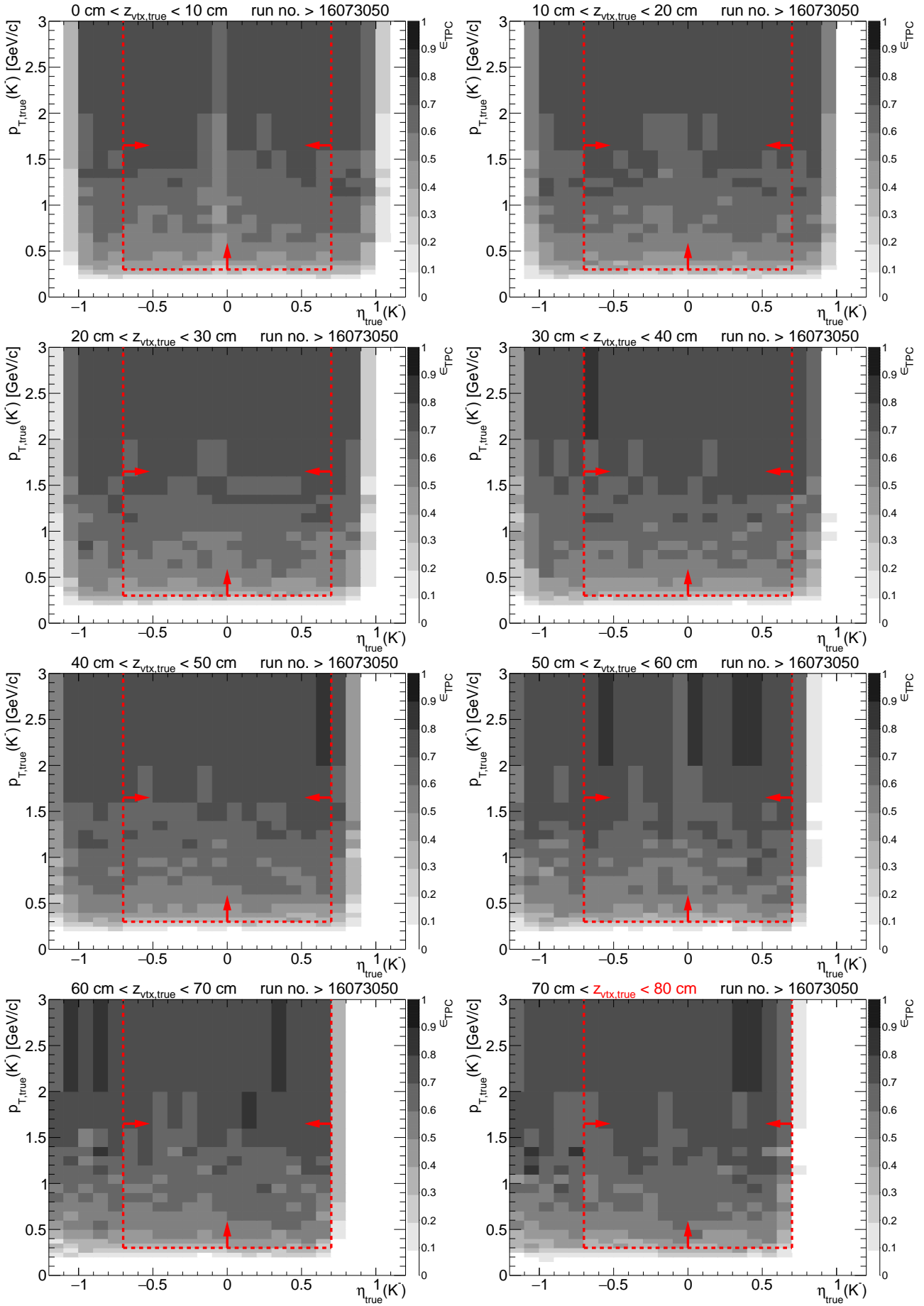
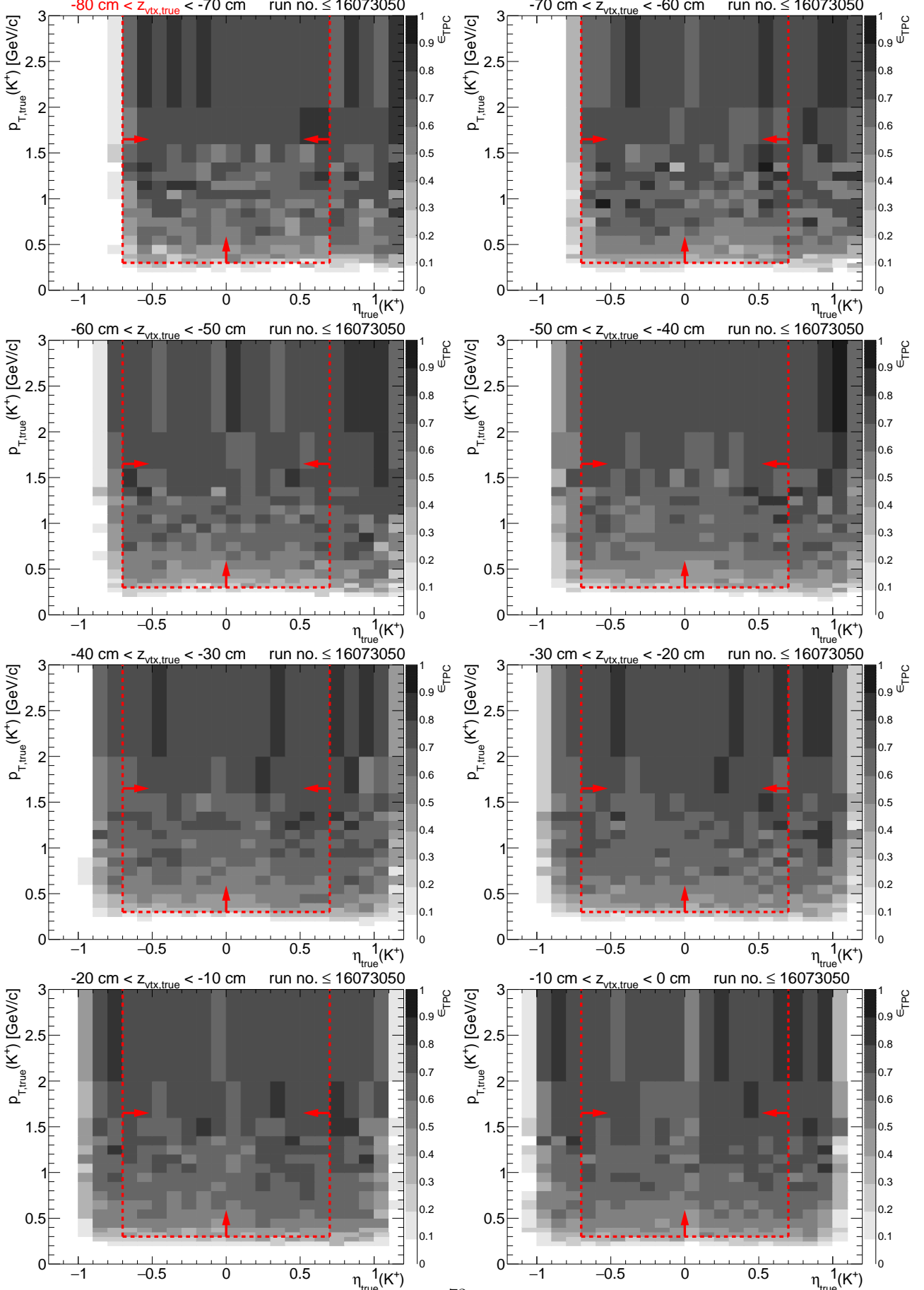


Figure A.7: TPC acceptance and reconstruction efficiency of  $K^+$  for runs with dead sector #19. Each plot represents the TPC efficiency  $\epsilon_{\text{TPC}}$  ( $z$ -axis) as a function of true particle pseudorapidity  $\eta$  ( $x$ -axis) and transverse momentum  $p_T$  ( $y$ -axis) in single  $z$ -vertex bin whose range is given at the top. Red lines and arrows indicate region accepted in analyses.



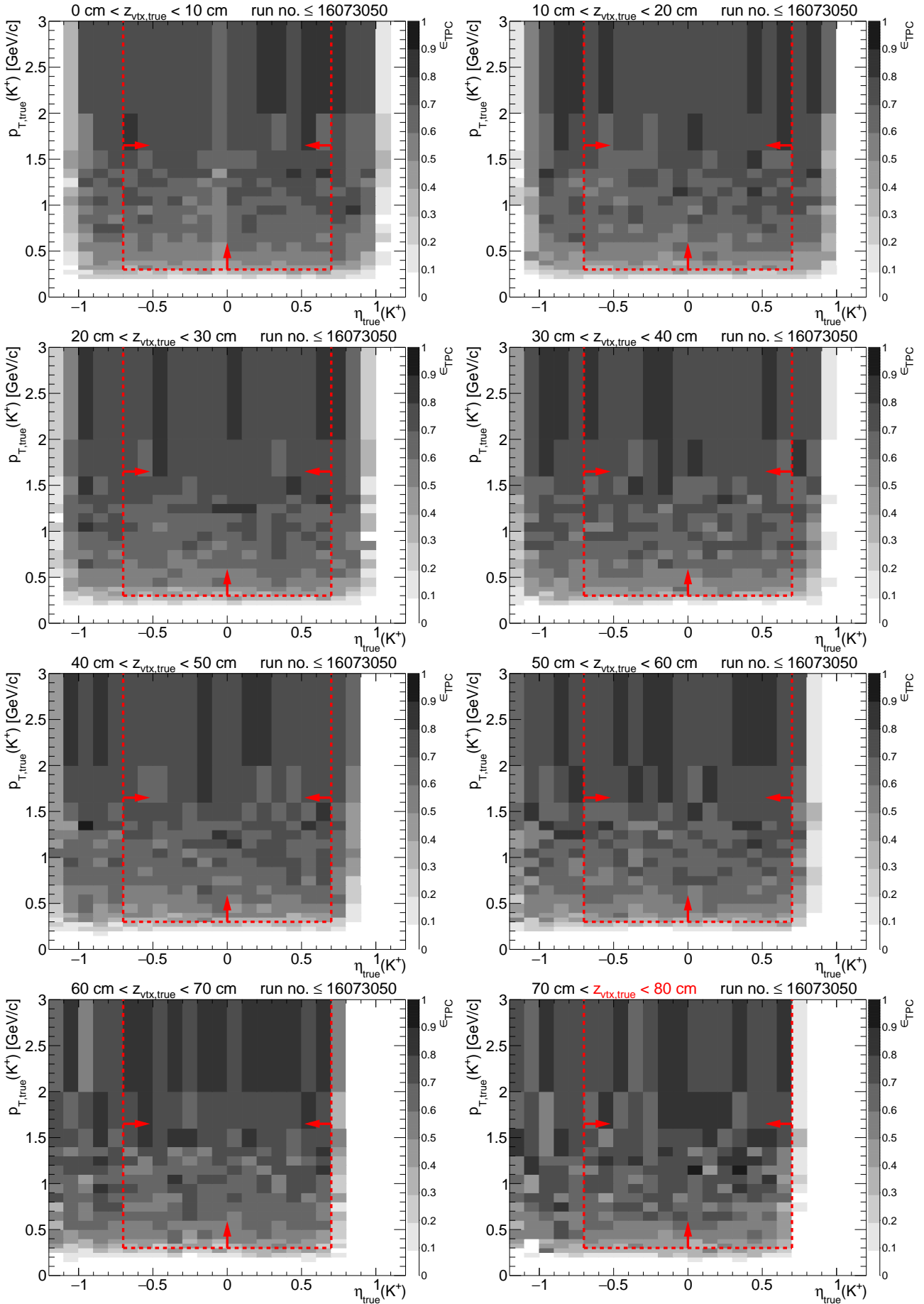
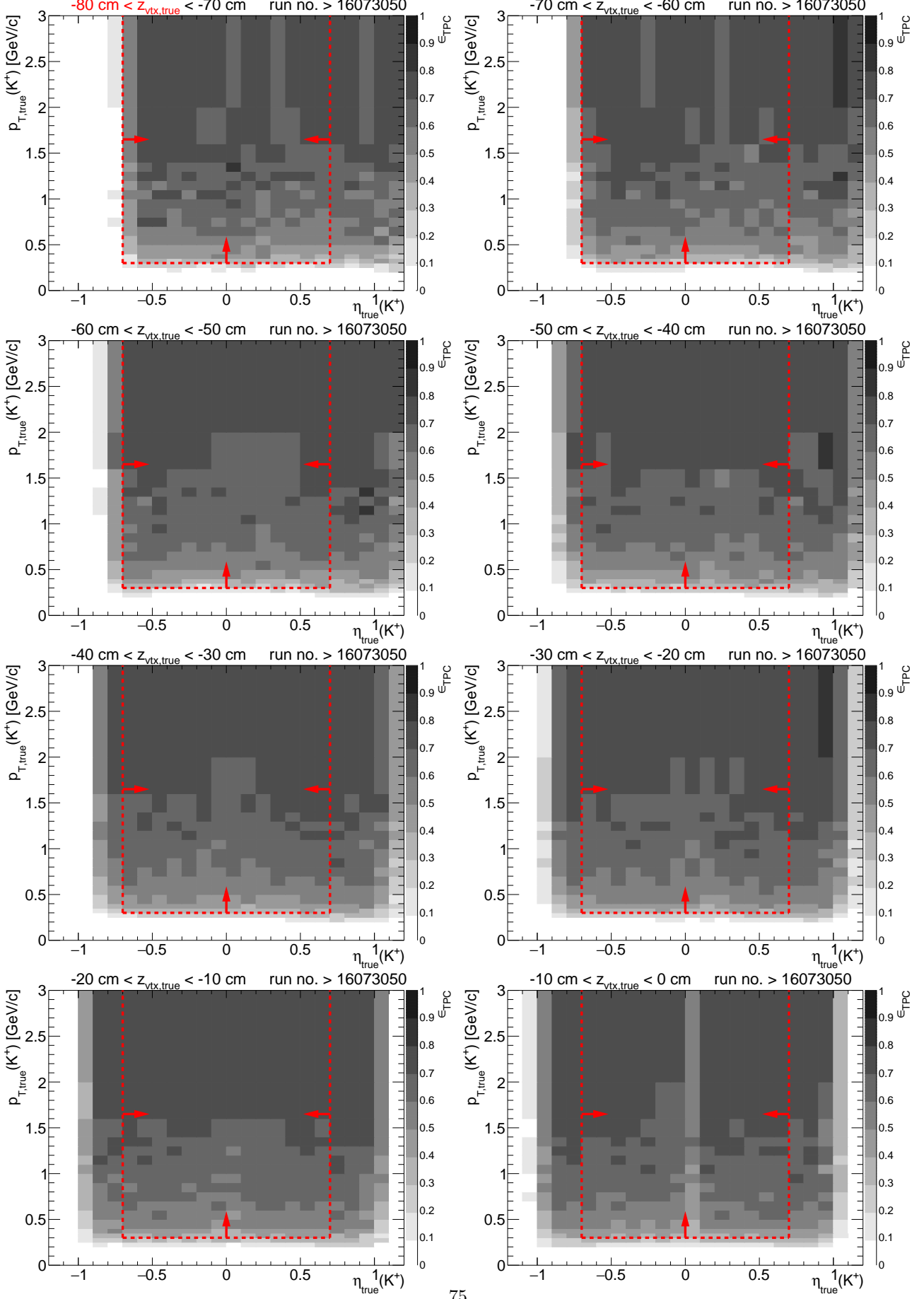


Figure A.8: TPC acceptance and reconstruction efficiency of  $K^+$  for runs with sector #19 back in operation. Each plot represents the TPC efficiency  $\epsilon_{\text{TPC}}$  ( $z$ -axis) as a function of true particle pseudorapidity  $\eta$  ( $x$ -axis) and transverse momentum  $p_T$  ( $y$ -axis) in single  $z$ -vertex bin whose range is given at the top. Red lines and arrows indicate region accepted in analyses.



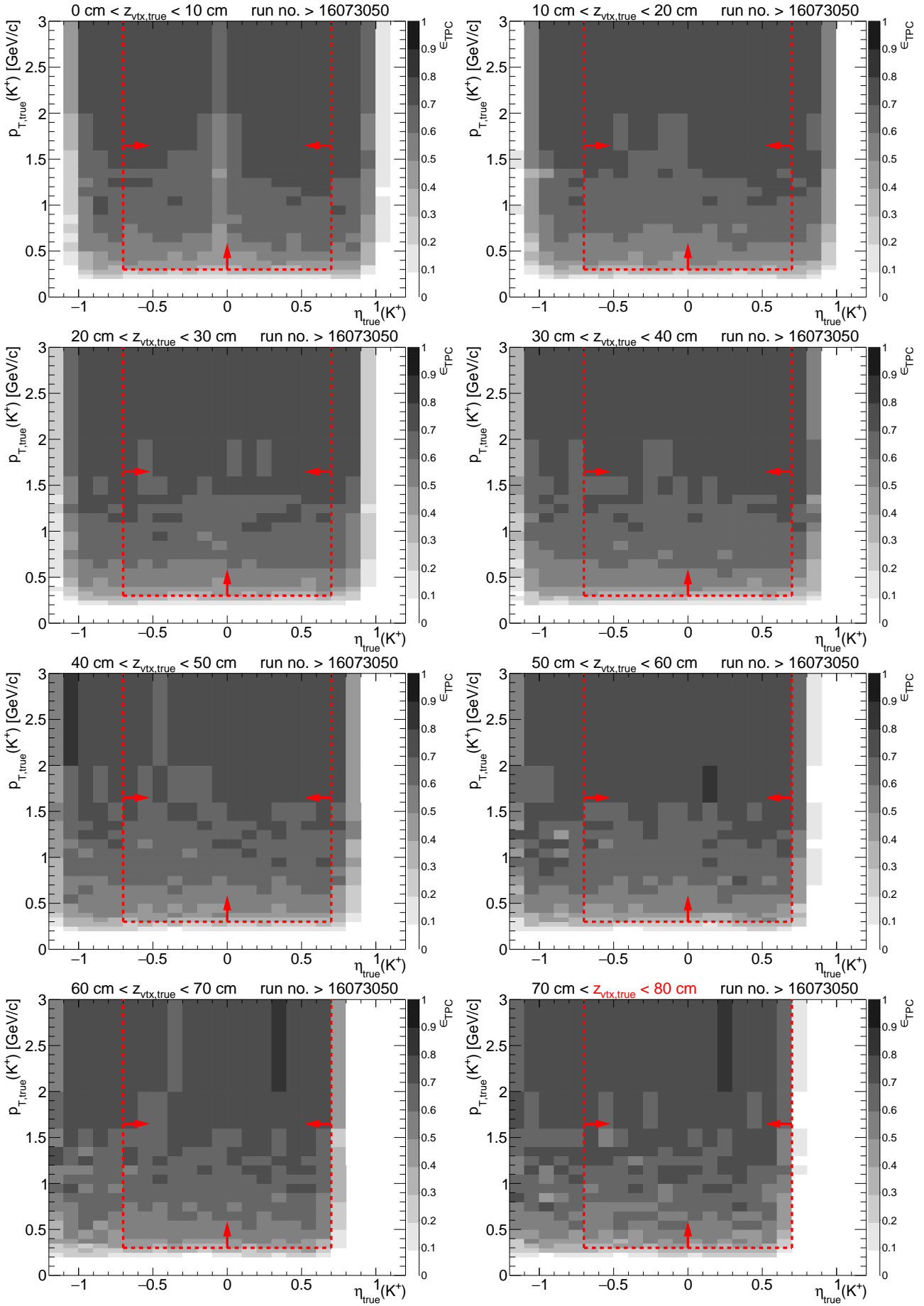
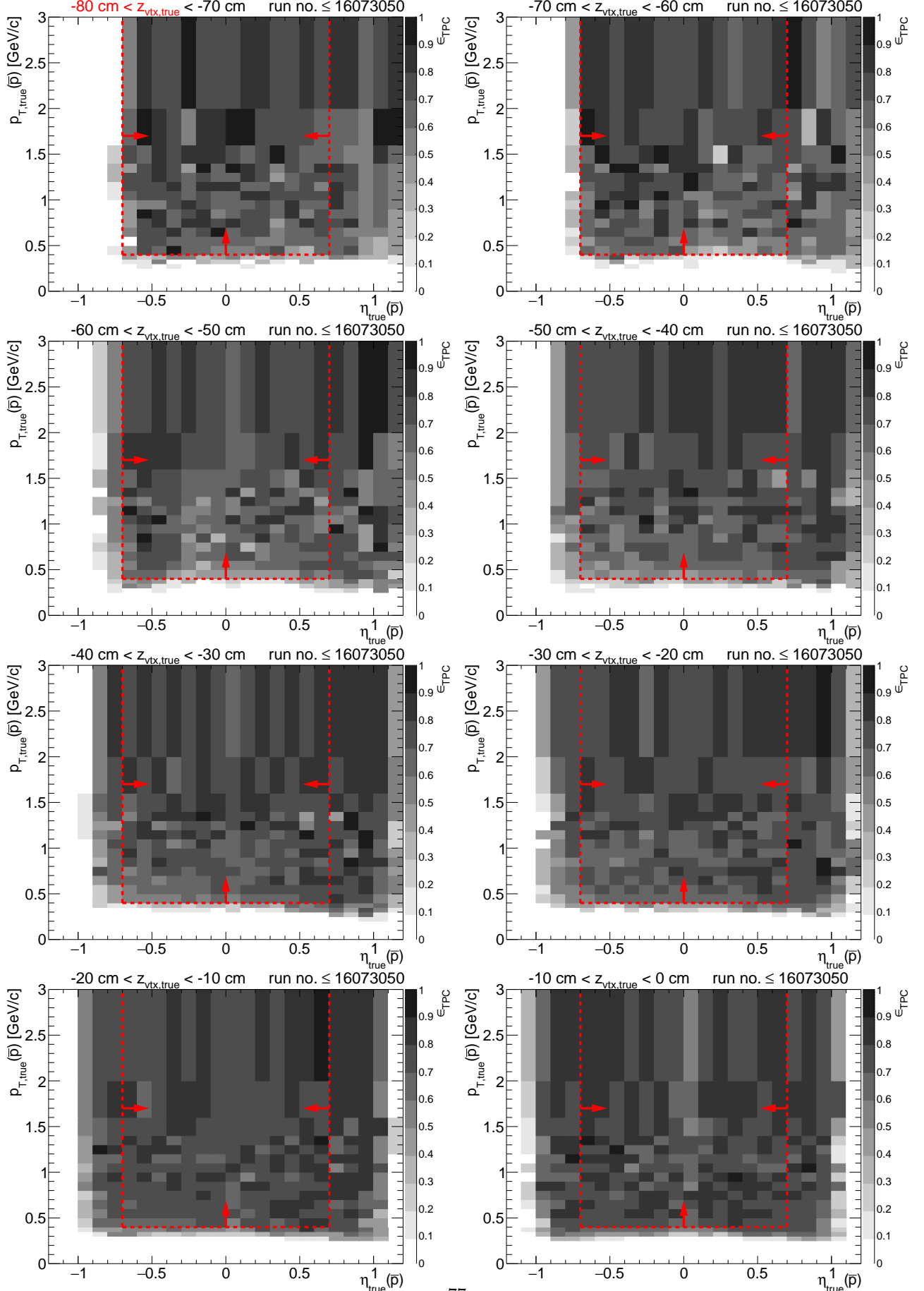


Figure A.9: TPC acceptance and reconstruction efficiency of  $\bar{p}$  for runs with dead sector #19. Each plot represents the TPC efficiency  $\epsilon_{\text{TPC}}$  ( $z$ -axis) as a function of true particle pseudorapidity  $\eta$  ( $x$ -axis) and transverse momentum  $p_T$  ( $y$ -axis) in single  $z$ -vertex bin whose range is given at the top. Red lines and arrows indicate region accepted in analyses.



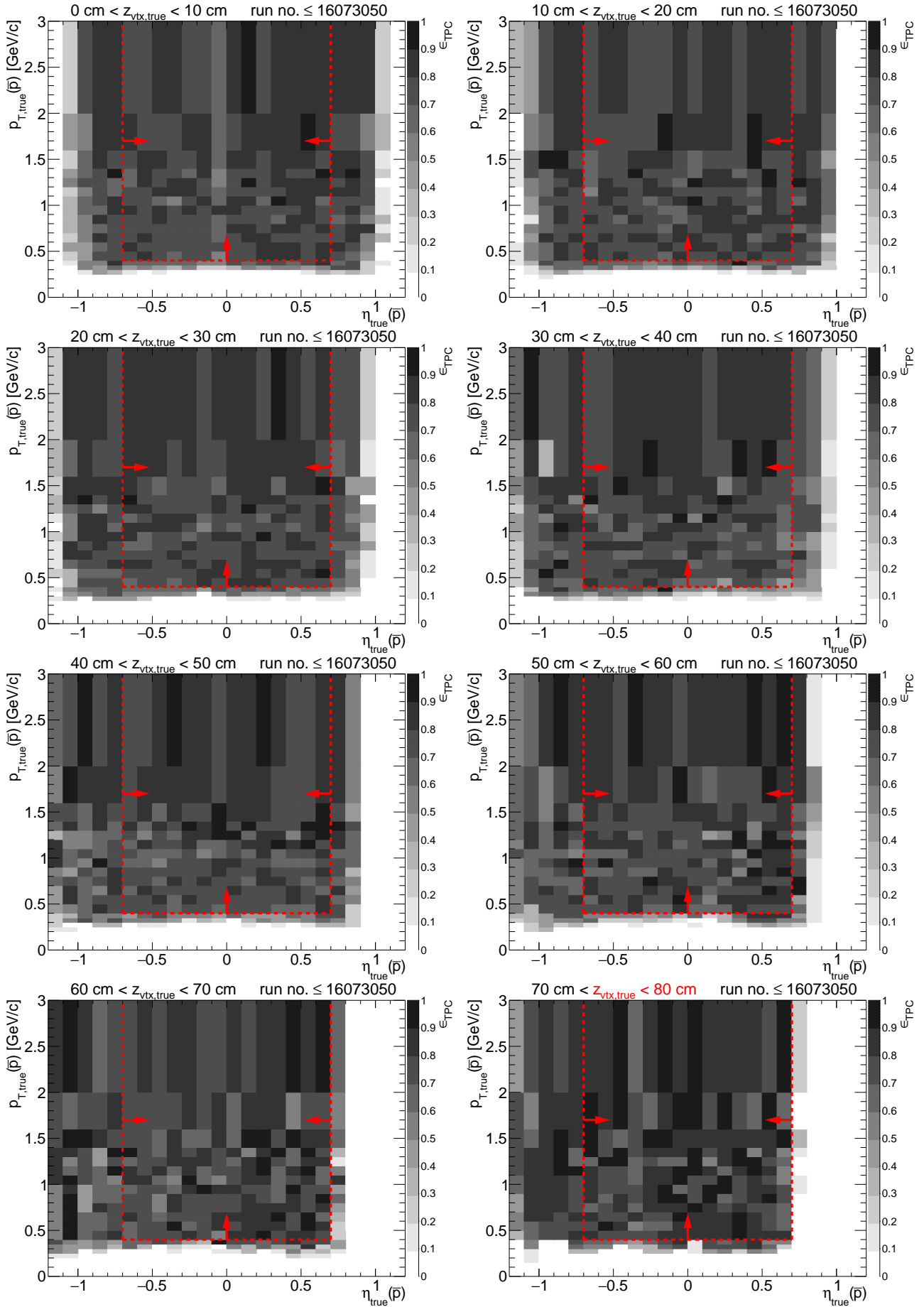
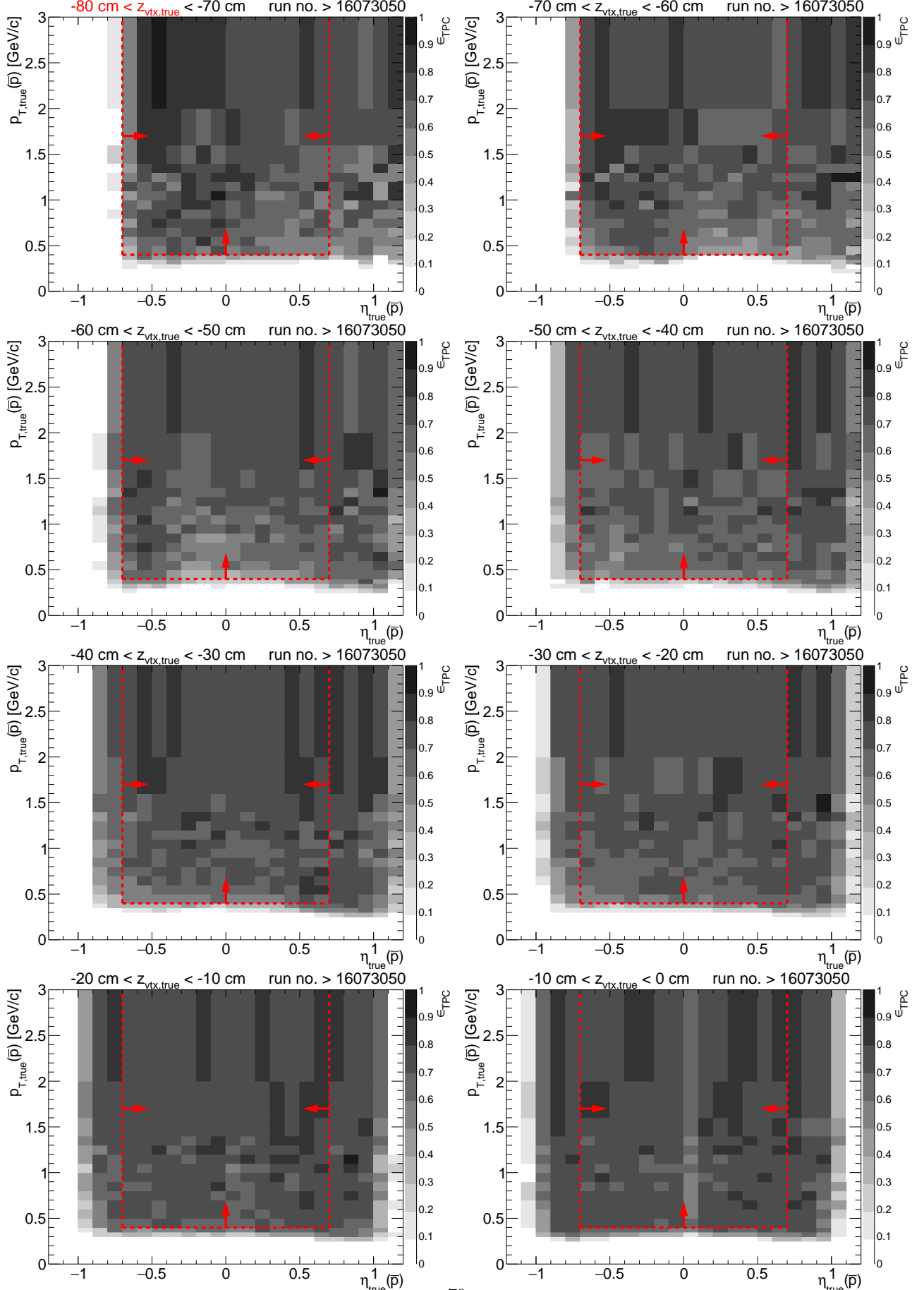


Figure A.10: TPC acceptance and reconstruction efficiency of  $\bar{p}$  for runs with sector #19 back in operation. Each plot represents the TPC efficiency  $\epsilon_{\text{TPC}}$  ( $z$ -axis) as a function of true particle pseudorapidity  $\eta$  ( $x$ -axis) and transverse momentum  $p_T$  ( $y$ -axis) in single  $z$ -vertex bin whose range is given at the top. Red lines and arrows indicate region accepted in analyses.



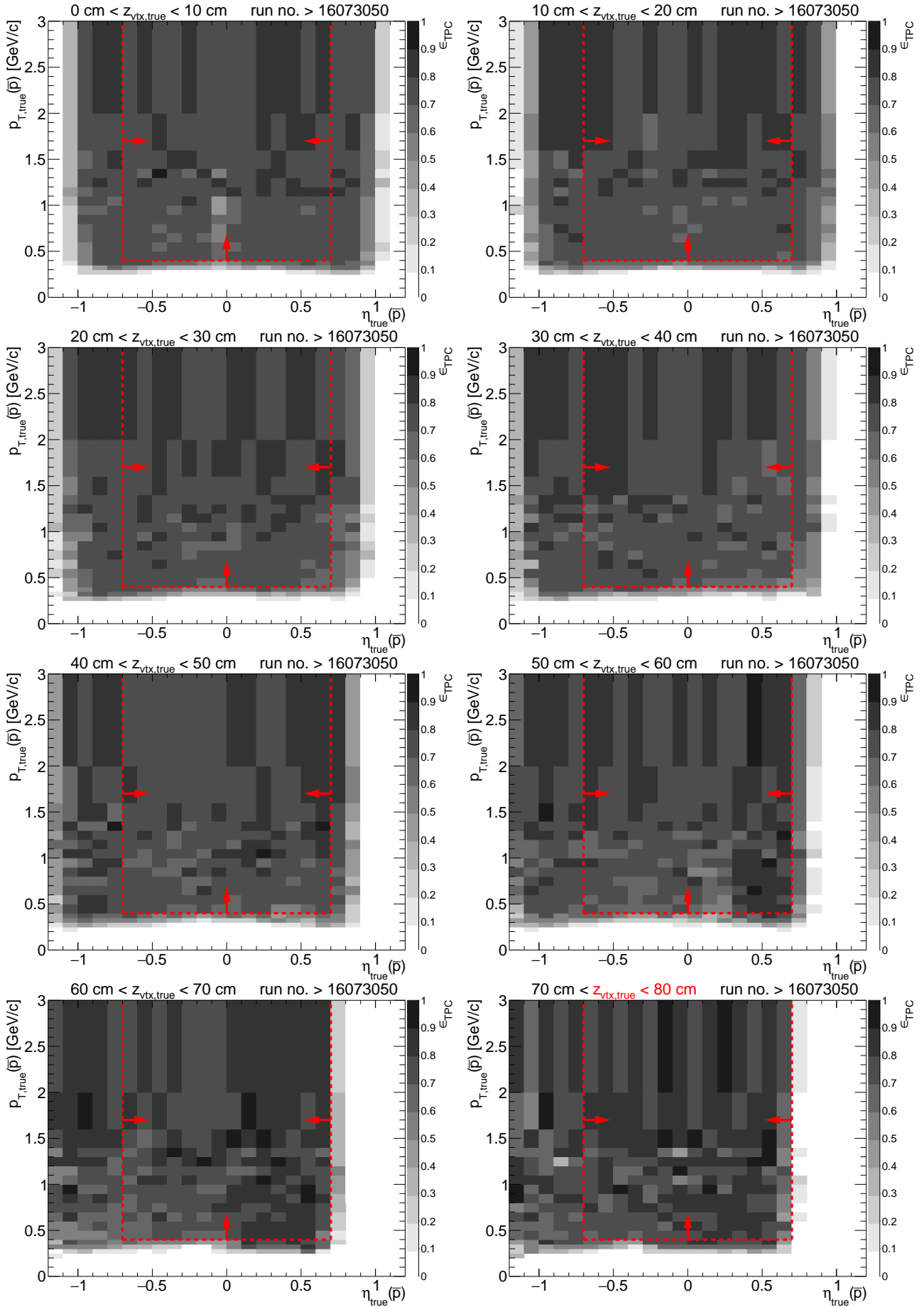
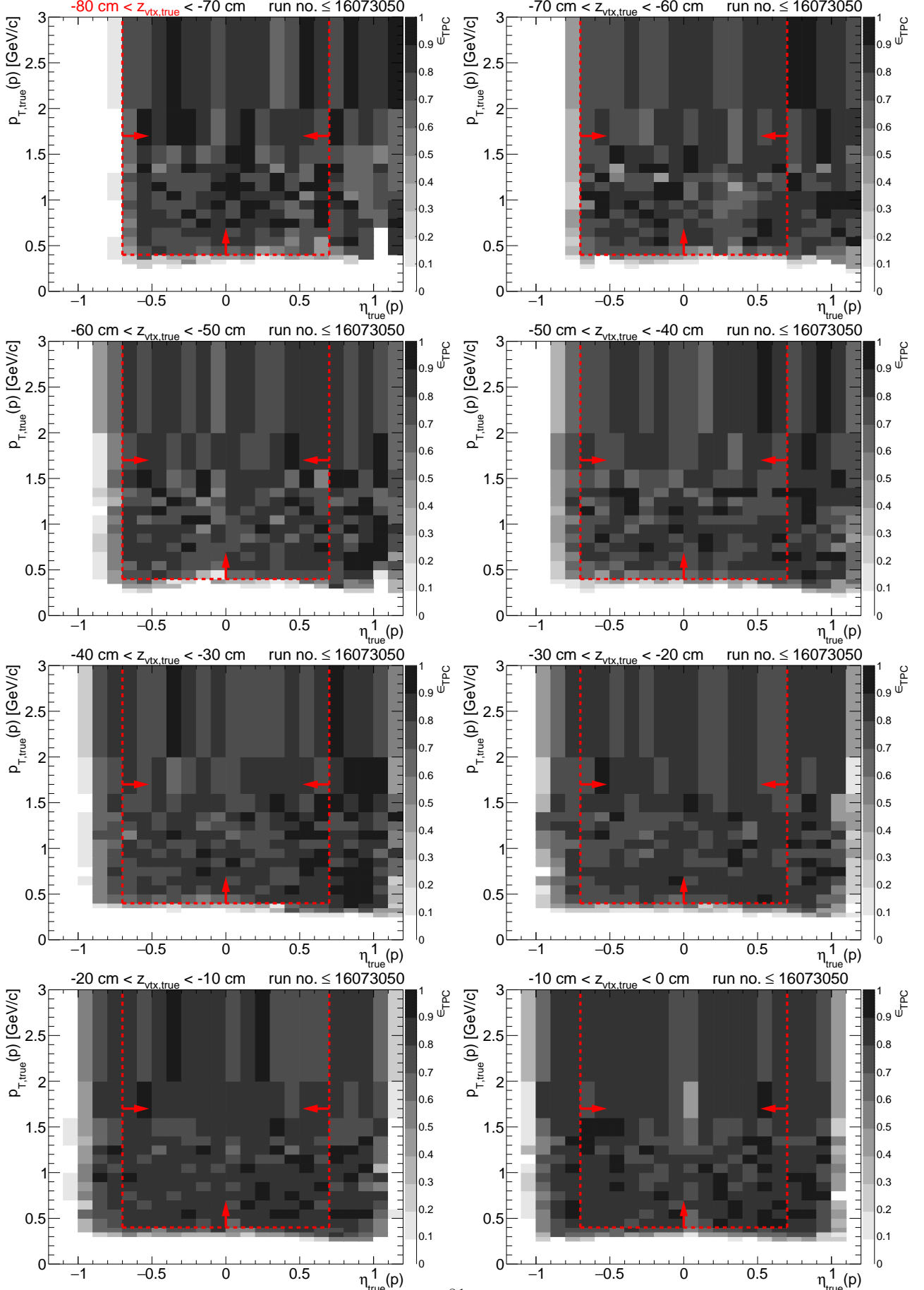


Figure A.11: TPC acceptance and reconstruction efficiency of  $p$  for runs with dead sector #19. Each plot represents the TPC efficiency  $\epsilon_{\text{TPC}}$  ( $z$ -axis) as a function of true particle pseudorapidity  $\eta$  ( $x$ -axis) and transverse momentum  $p_T$  ( $y$ -axis) in single  $z$ -vertex bin whose range is given at the top. Red lines and arrows indicate region accepted in analyses.



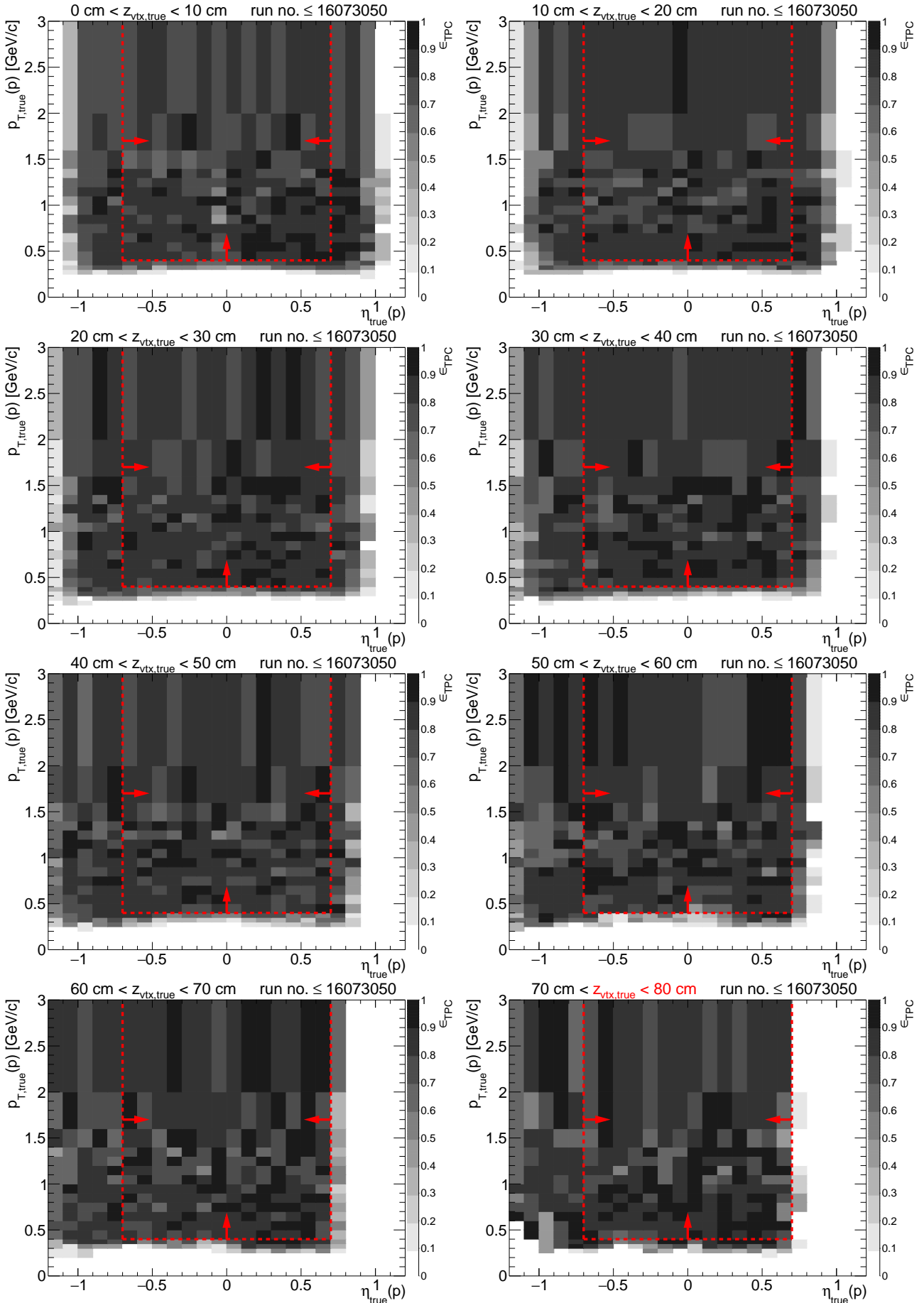
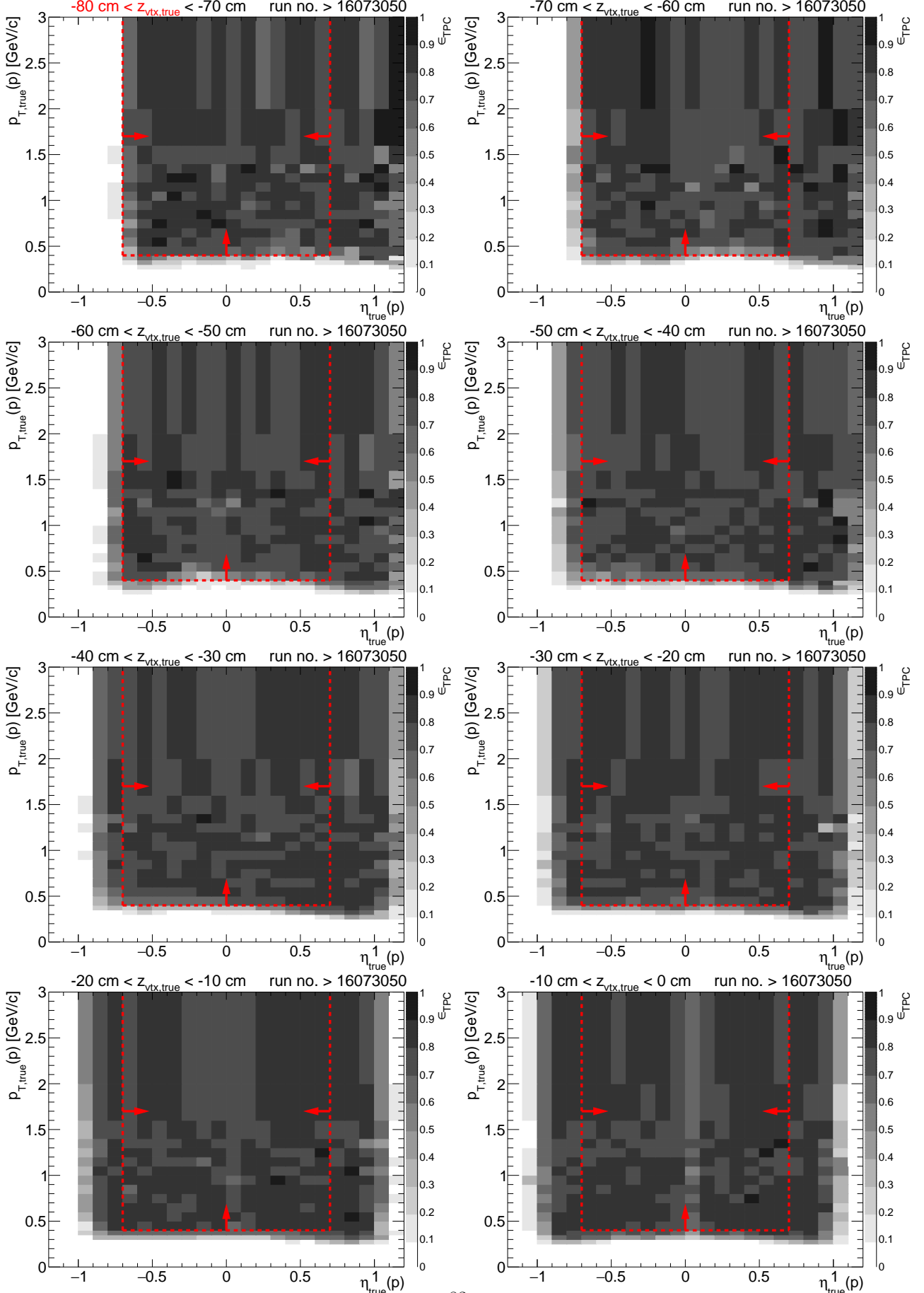
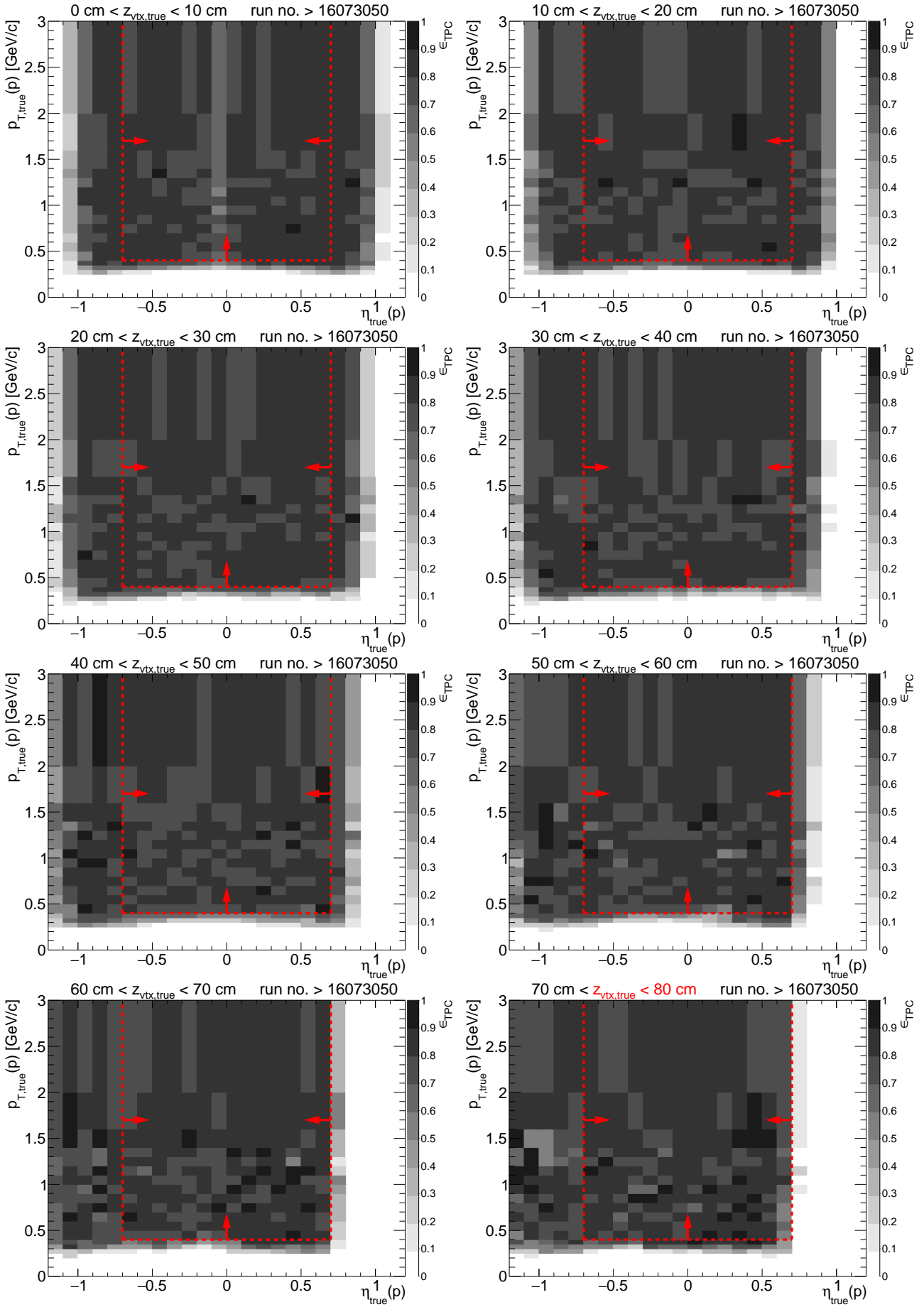


Figure A.12: TPC acceptance and reconstruction efficiency of  $p$  for runs with sector #19 back in operation. Each plot represents the TPC efficiency  $\epsilon_{\text{TPC}}$  ( $z$ -axis) as a function of true particle pseudorapidity  $\eta$  ( $x$ -axis) and transverse momentum  $p_T$  ( $y$ -axis) in single  $z$ -vertex bin whose range is given at the top. Red lines and arrows indicate region accepted in analyses.





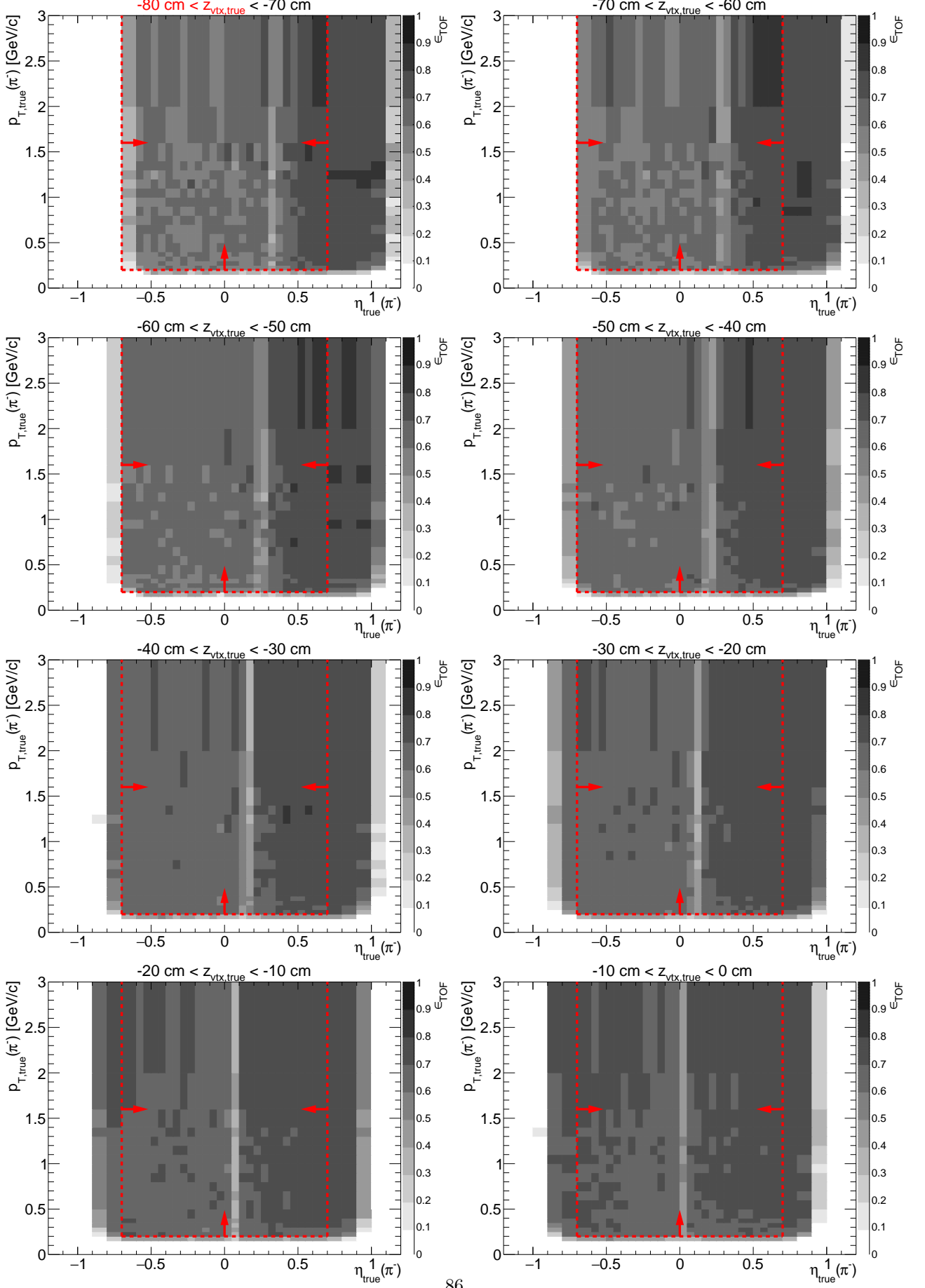
# Appendix B

## TOF hit reconstruction and matching efficiency

Tray No.	Module No.	RHIC fills
8	1 – 4, 29 – 32	18686 – 18953
23	1 – 4, 29 – 32	18686 – 18953
38	1 – 32	18686 – 18953
39	13	18686 – 18715, 18719 – 18795, 18797 – 18827, 18829 – 18854, 18856 – 18878, 18883 – 18892, 18895 – 18901, 18904 – 18924, 18926 – 18953
41	1 – 32	18686 – 18953
45	1 – 32	18877 – 18909
46	1 – 32	18853 – 18909
93	1 – 4, 29 – 32	18686 – 18953
102	1 – 32	18686 – 18953
108	1 – 4, 29 – 32	18686 – 18953

Table B.1: Dead TOF modules masked in the MC. Table was filled with modules which were not matched with TPC tracks in the data.

Figure B.1: TOF acceptance, reconstruction and matching efficiency of  $\pi^-$ . Each plot represents the TOF efficiency  $\epsilon_{\text{TOF}}$  ( $z$ -axis) as a function of true particle pseudorapidity  $\eta$  ( $x$ -axis) and transverse momentum  $p_T$  ( $y$ -axis) in single  $z$ -vertex bin whose range is given at the top. Red lines and arrows indicate region accepted in analyses.



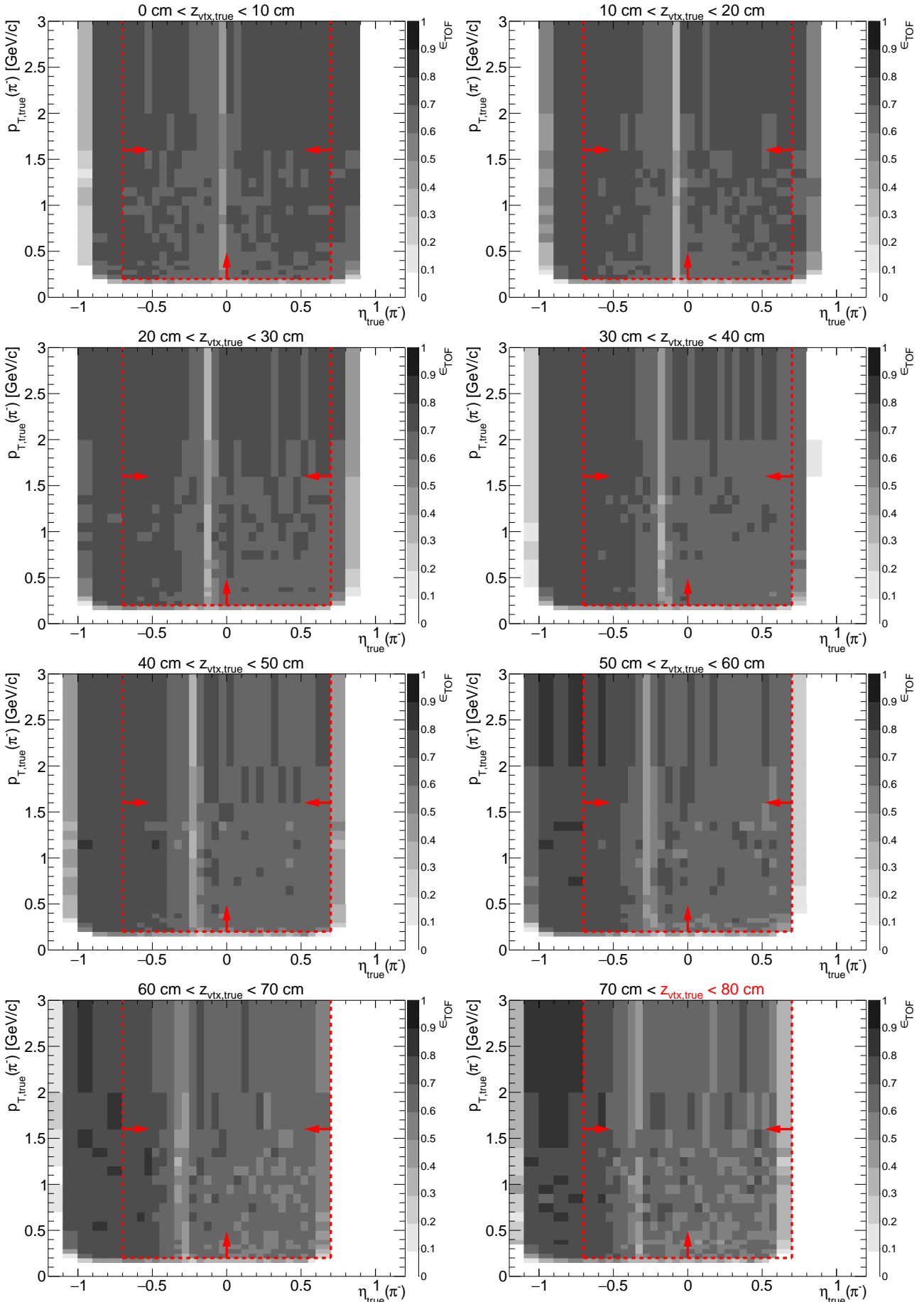
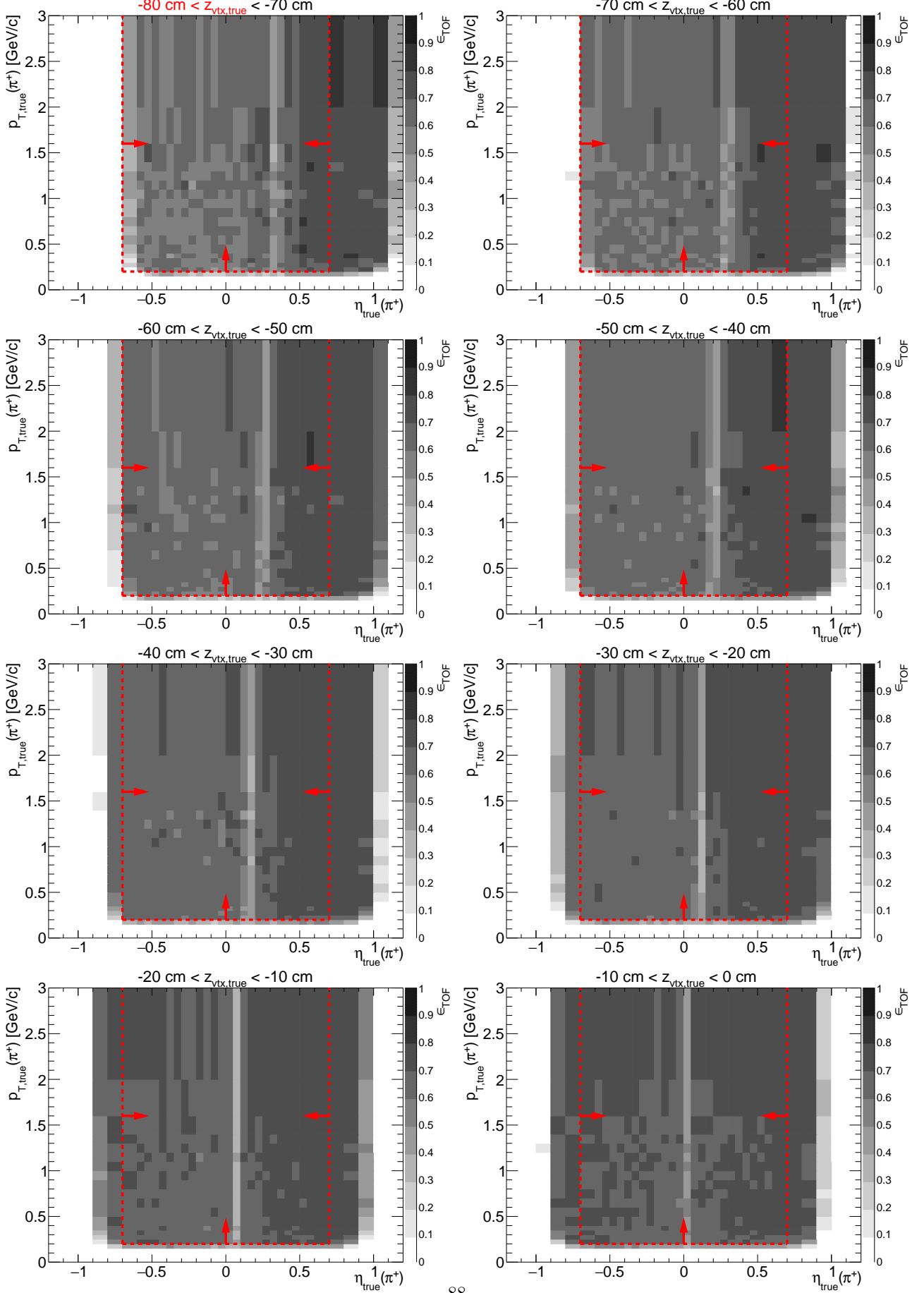


Figure B.2: TOF acceptance, reconstruction and matching efficiency of  $\pi^+$ . Each plot represents the TOF efficiency  $\epsilon_{\text{TOF}}$  ( $z$ -axis) as a function of true particle pseudorapidity  $\eta$  ( $x$ -axis) and transverse momentum  $p_T$  ( $y$ -axis) in single  $z$ -vertex bin whose range is given at the top. Red lines and arrows indicate region accepted in analyses.



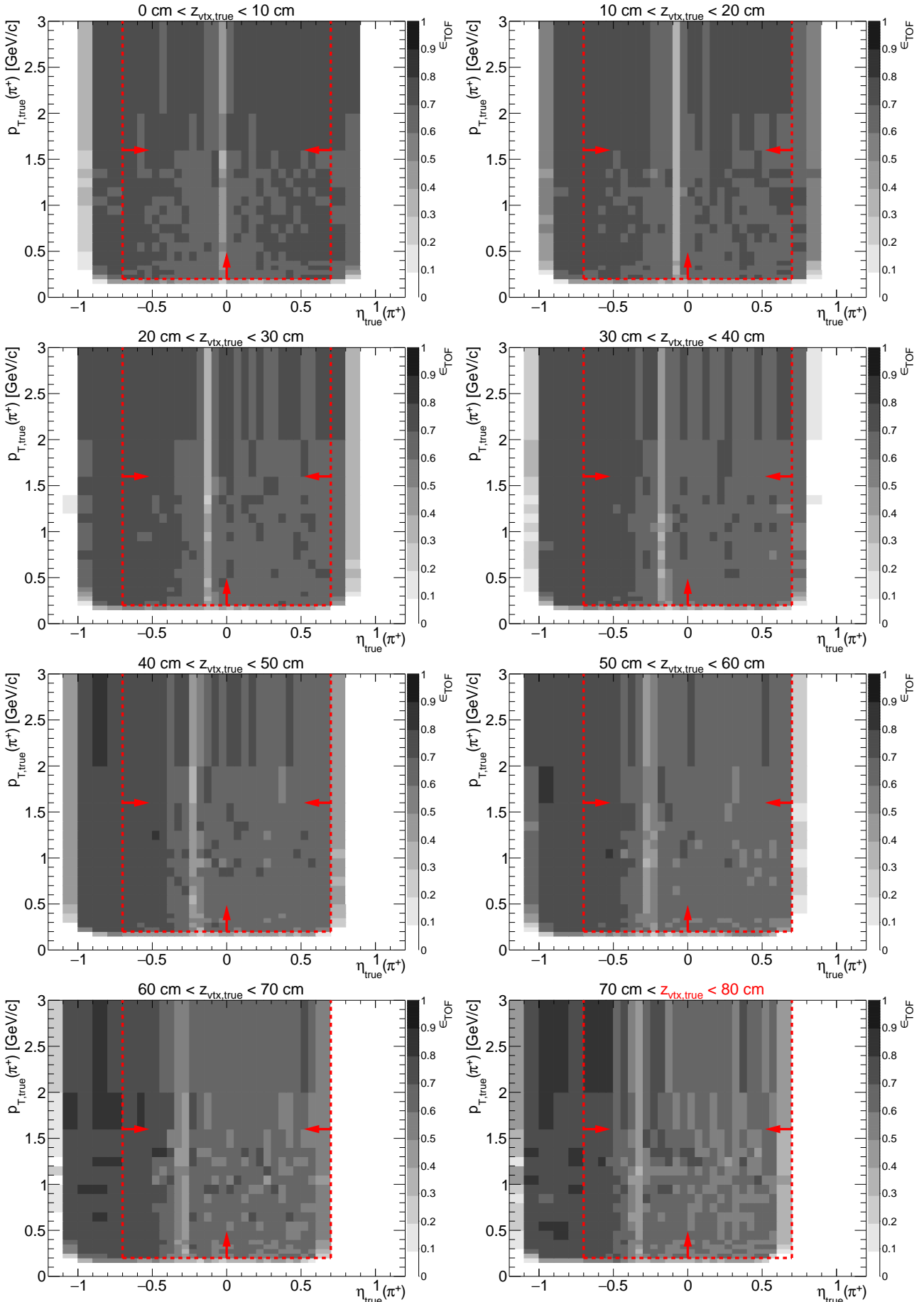
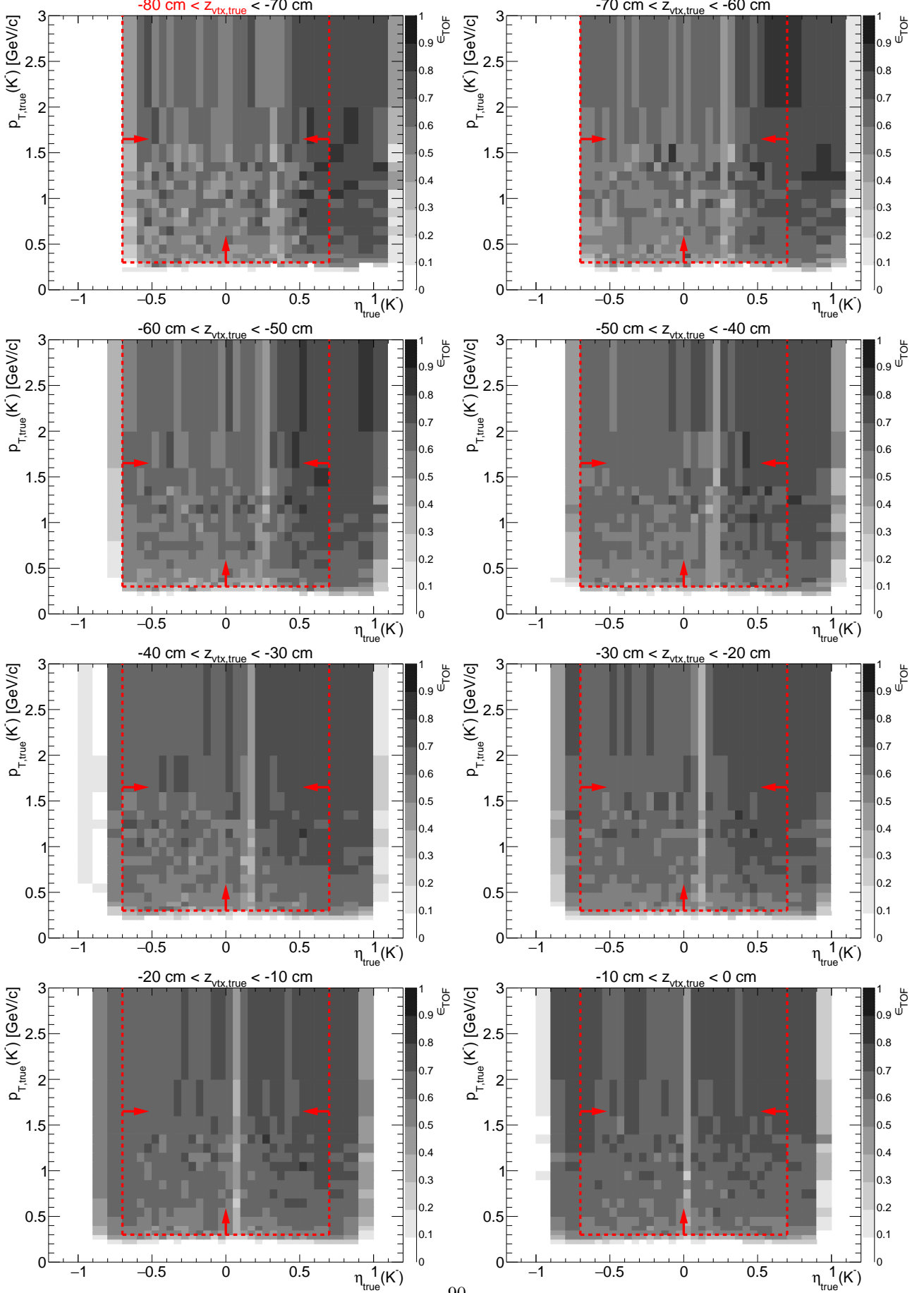


Figure B.3: TOF acceptance, reconstruction and matching efficiency of  $K^-$ . Each plot represents the TOF efficiency  $\epsilon_{\text{TOF}}$  ( $z$ -axis) as a function of true particle pseudorapidity  $\eta$  ( $x$ -axis) and transverse momentum  $p_T$  ( $y$ -axis) in single  $z$ -vertex bin whose range is given at the top. Red lines and arrows indicate region accepted in analyses.



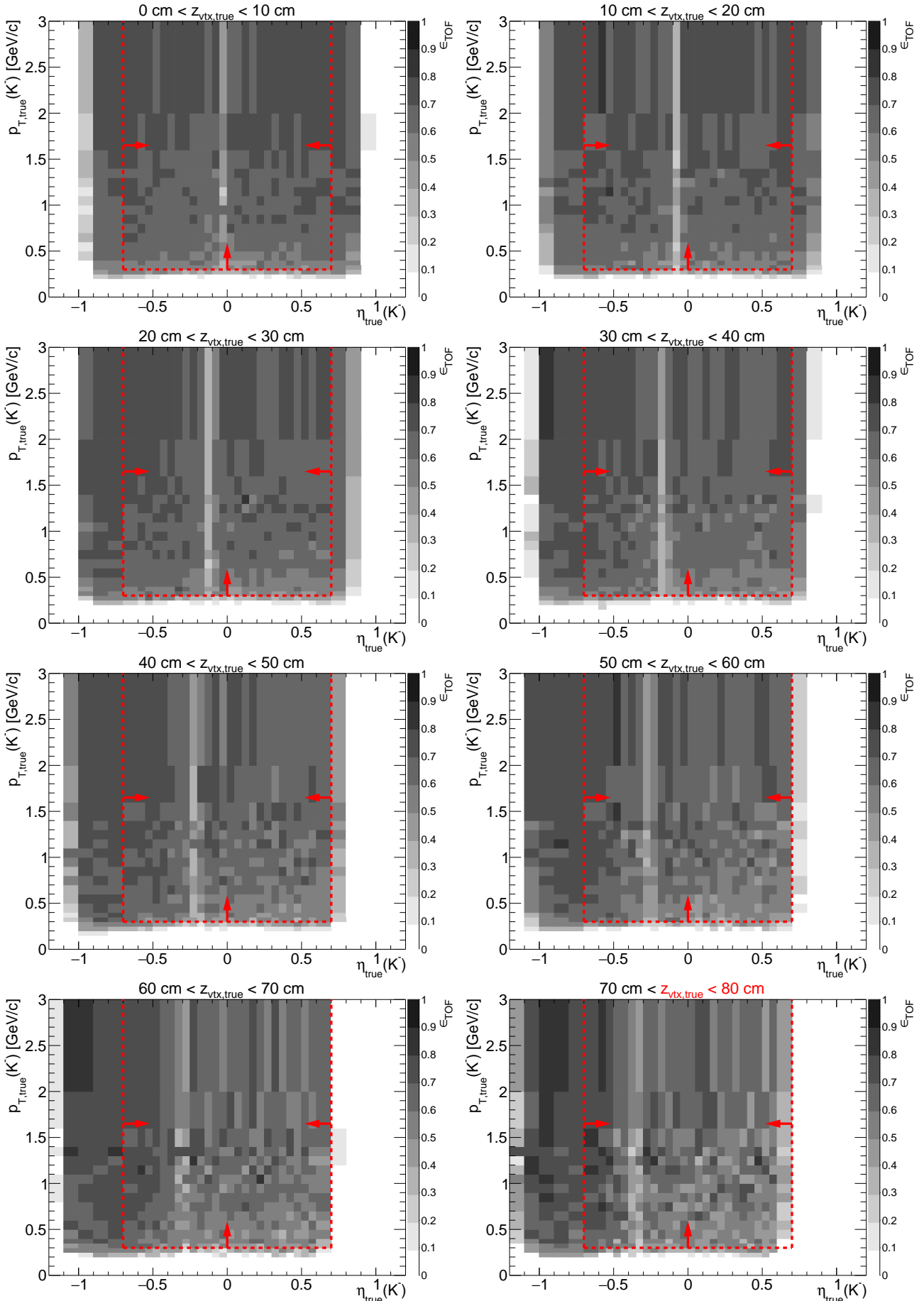
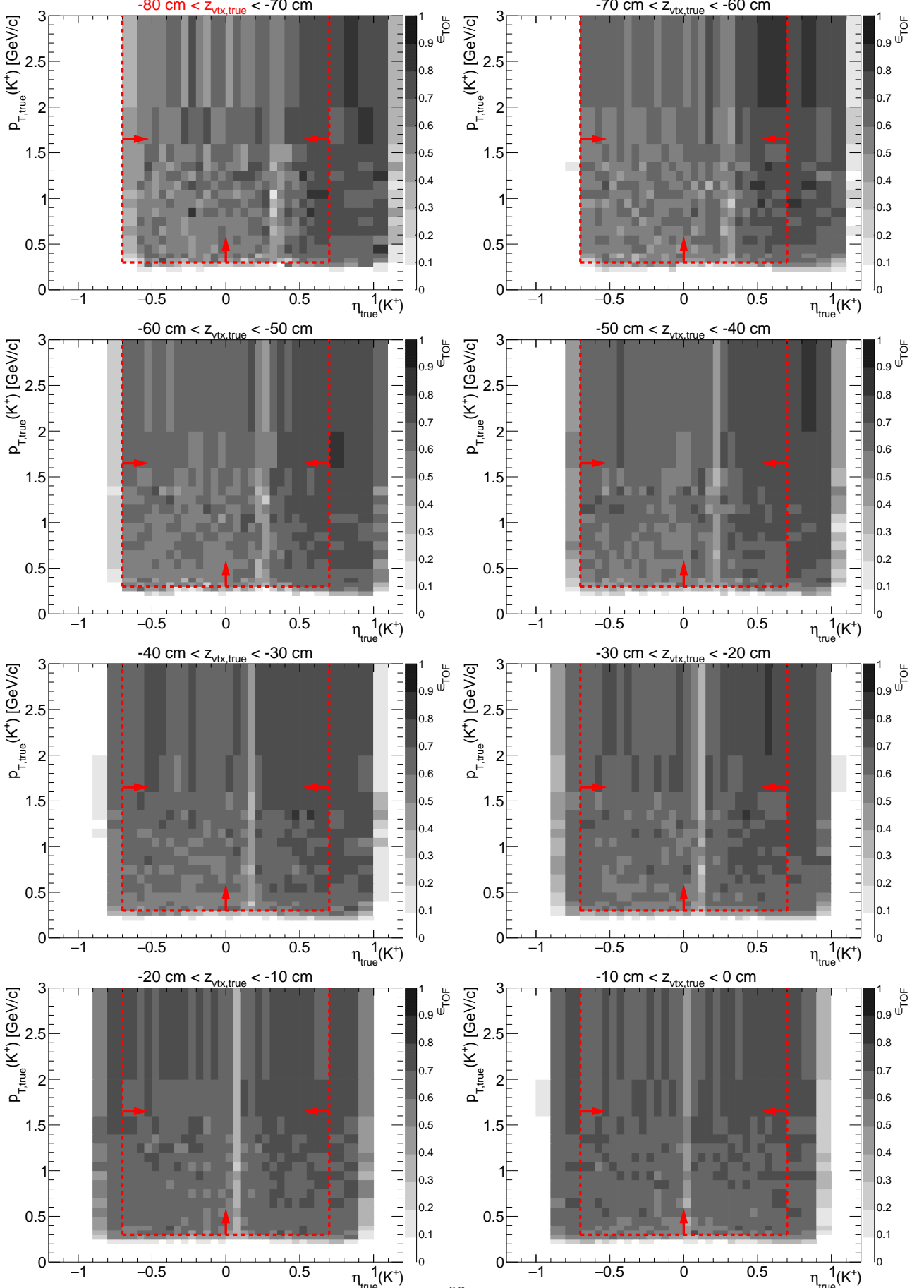


Figure B.4: TOF acceptance, reconstruction and matching efficiency of  $K^+$ . Each plot represents the TOF efficiency  $\epsilon_{\text{TOF}}$  ( $z$ -axis) as a function of true particle pseudorapidity  $\eta$  ( $x$ -axis) and transverse momentum  $p_T$  ( $y$ -axis) in single  $z$ -vertex bin whose range is given at the top. Red lines and arrows indicate region accepted in analyses.



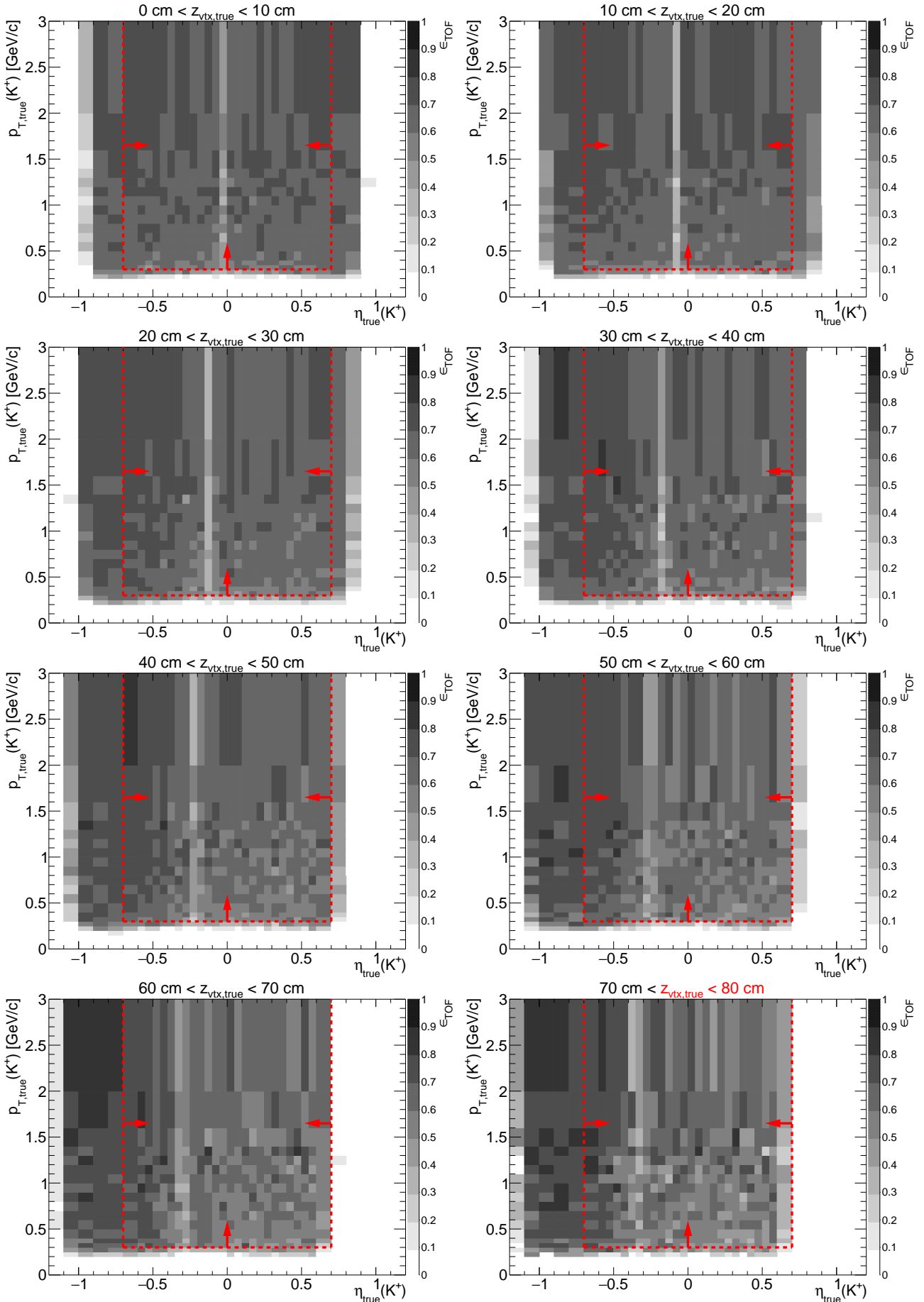
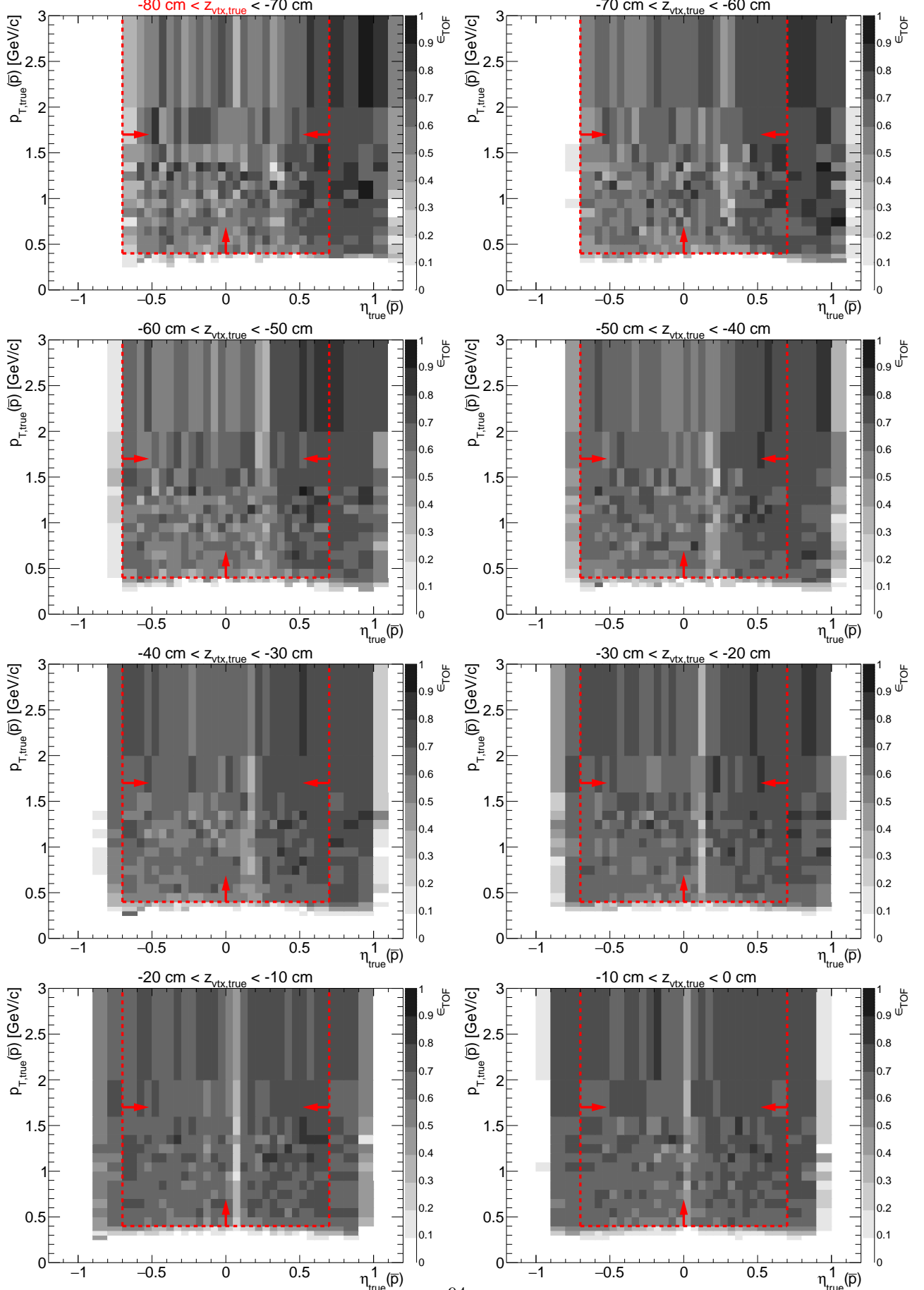


Figure B.5: TOF acceptance, reconstruction and matching efficiency of  $\bar{p}$ . Each plot represents the TOF efficiency  $\epsilon_{\text{TOF}}$  ( $z$ -axis) as a function of true particle pseudorapidity  $\eta$  ( $x$ -axis) and transverse momentum  $p_T$  ( $y$ -axis) in single  $z$ -vertex bin whose range is given at the top. Red lines and arrows indicate region accepted in analyses.



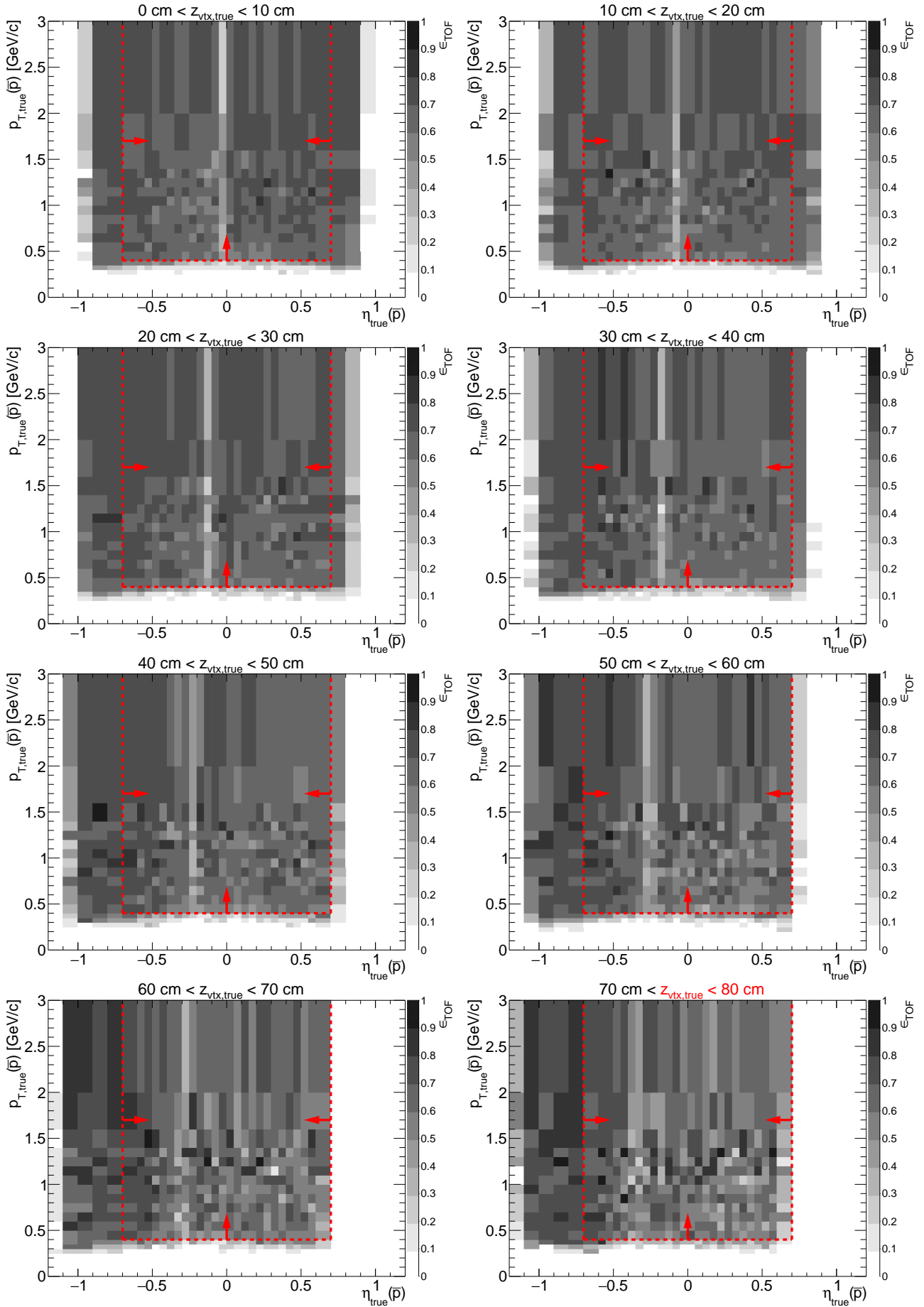
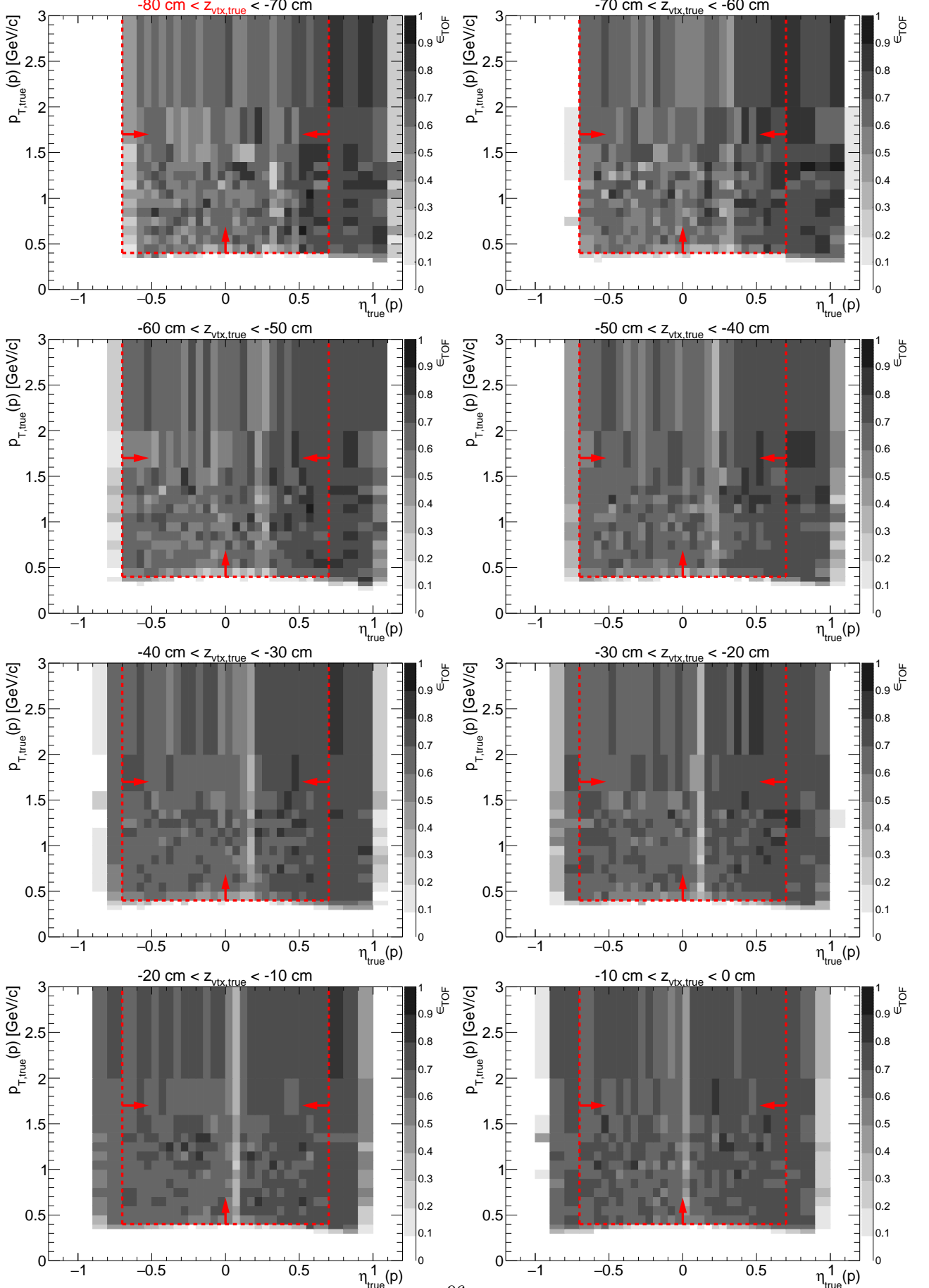
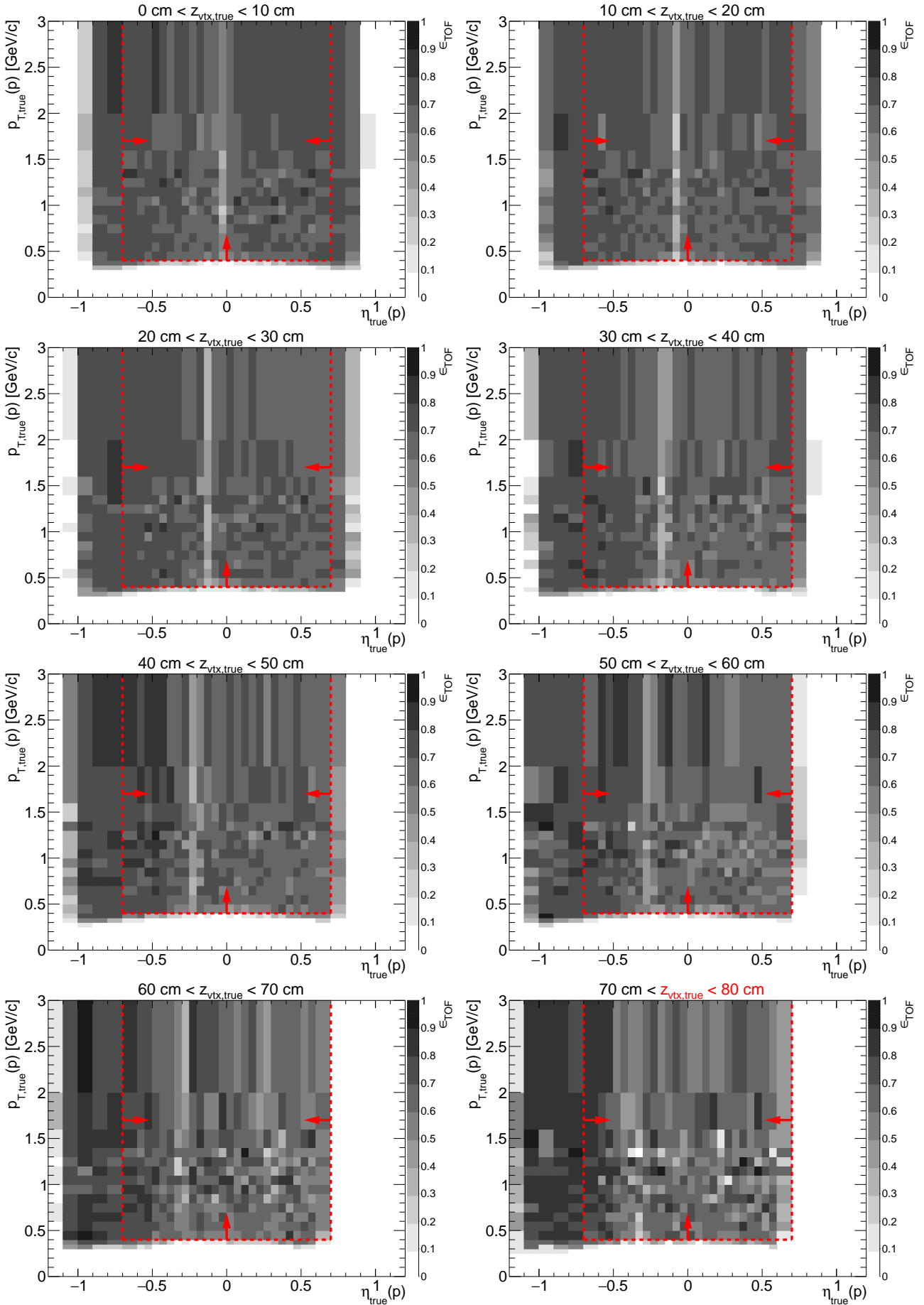


Figure B.6: TOF acceptance, reconstruction and matching efficiency of  $p$ . Each plot represents the TOF efficiency  $\epsilon_{\text{TOF}}$  ( $z$ -axis) as a function of true particle pseudorapidity  $\eta$  ( $x$ -axis) and transverse momentum  $p_T$  ( $y$ -axis) in single  $z$ -vertex bin whose range is given at the top. Red lines and arrows indicate region accepted in analyses.

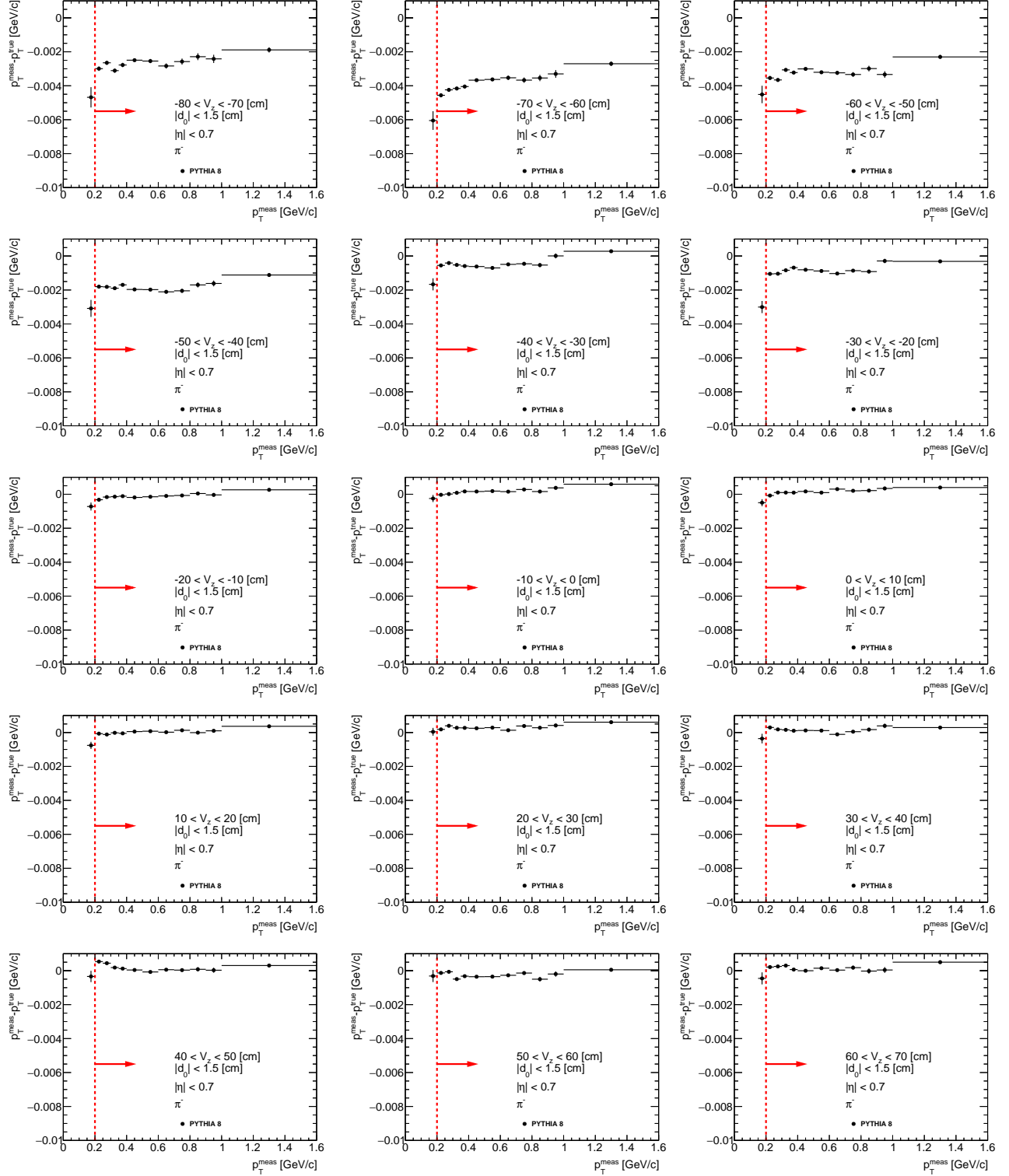




# Appendix C

## Energy Loss Correction

Figure C.1: Energy loss correction  $p_T^{meas} - p_T^{true}$  for  $\pi^-$  as a function of reconstructed transverse momentum  $p_T^{meas}$  ( $|\eta| < 0.7$ ) in single  $z$ -vertex bin whose range is given on each plot. Red lines and arrows indicate region accepted in analyses. One can notice an offset of about 3 – 4 MeV for negative  $z$ -vertex. It is a known issue with STAR simulation where HFT support material is badly described for negative  $z < -30$  cm.



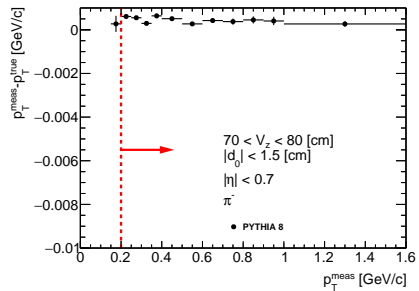


Figure C.2: Energy loss correction  $p_T^{meas} - p_T^{true}$  for  $\pi^+$  as a function of reconstructed transverse momentum  $p_T^{meas}$  ( $|\eta| < 0.7$ ) in single  $z$ -vertex bin whose range is given on each plot. Red lines and arrows indicate region accepted in analyses. One can notice an offset of about 3 – 4 MeV for negative  $z$ -vertex. It is a known issue with STAR simulation where HFT support material is badly described for negative  $z < -30$  cm.

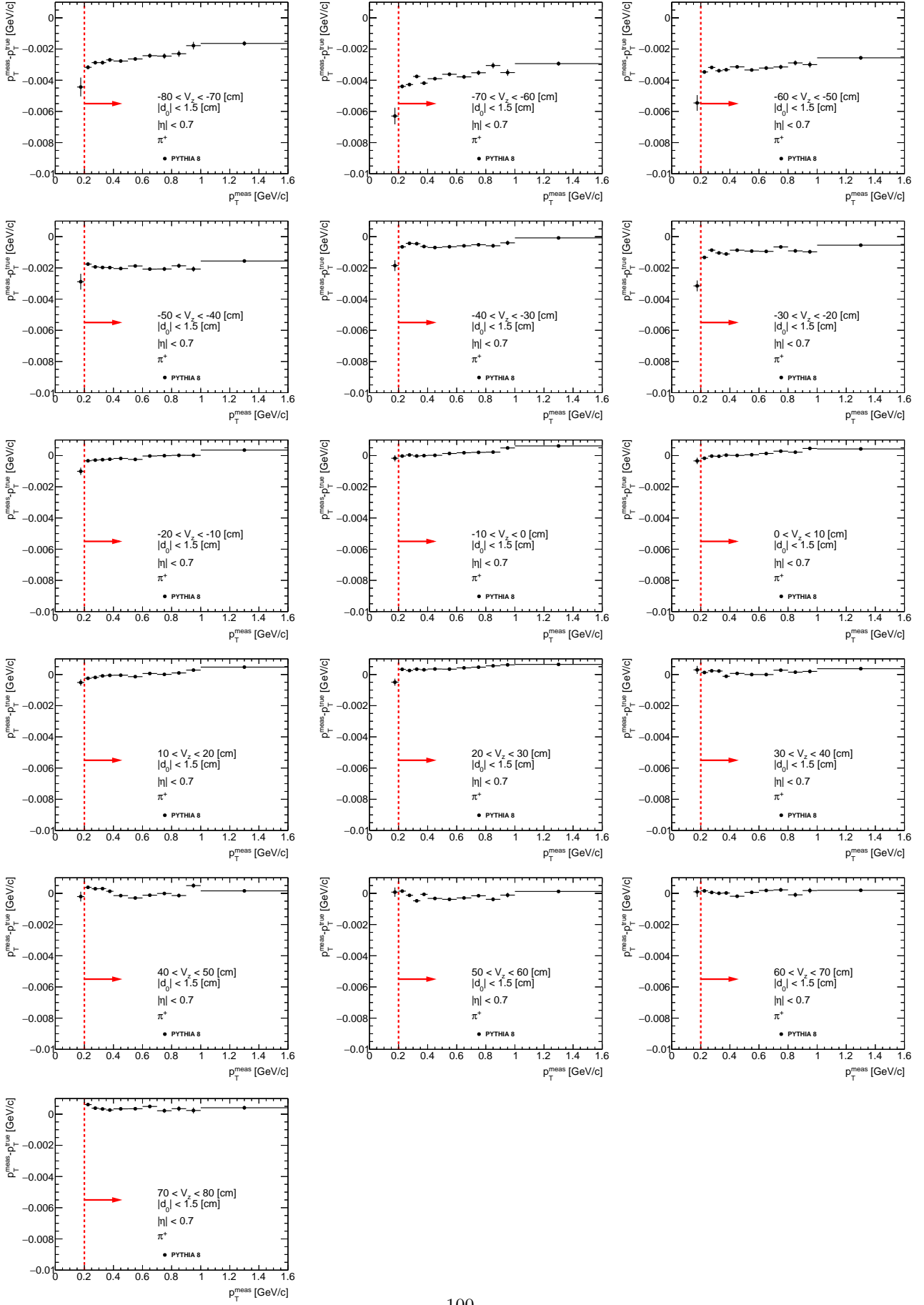


Figure C.3: Energy loss correction  $p_T^{meas} - p_T^{true}$  for  $K^-$  as a function of reconstructed transverse momentum  $p_T^{meas}$  ( $|\eta| < 0.7$ ) in single  $z$ -vertex bin whose range is given on each plot. Red lines and arrows indicate region accepted in analyses.

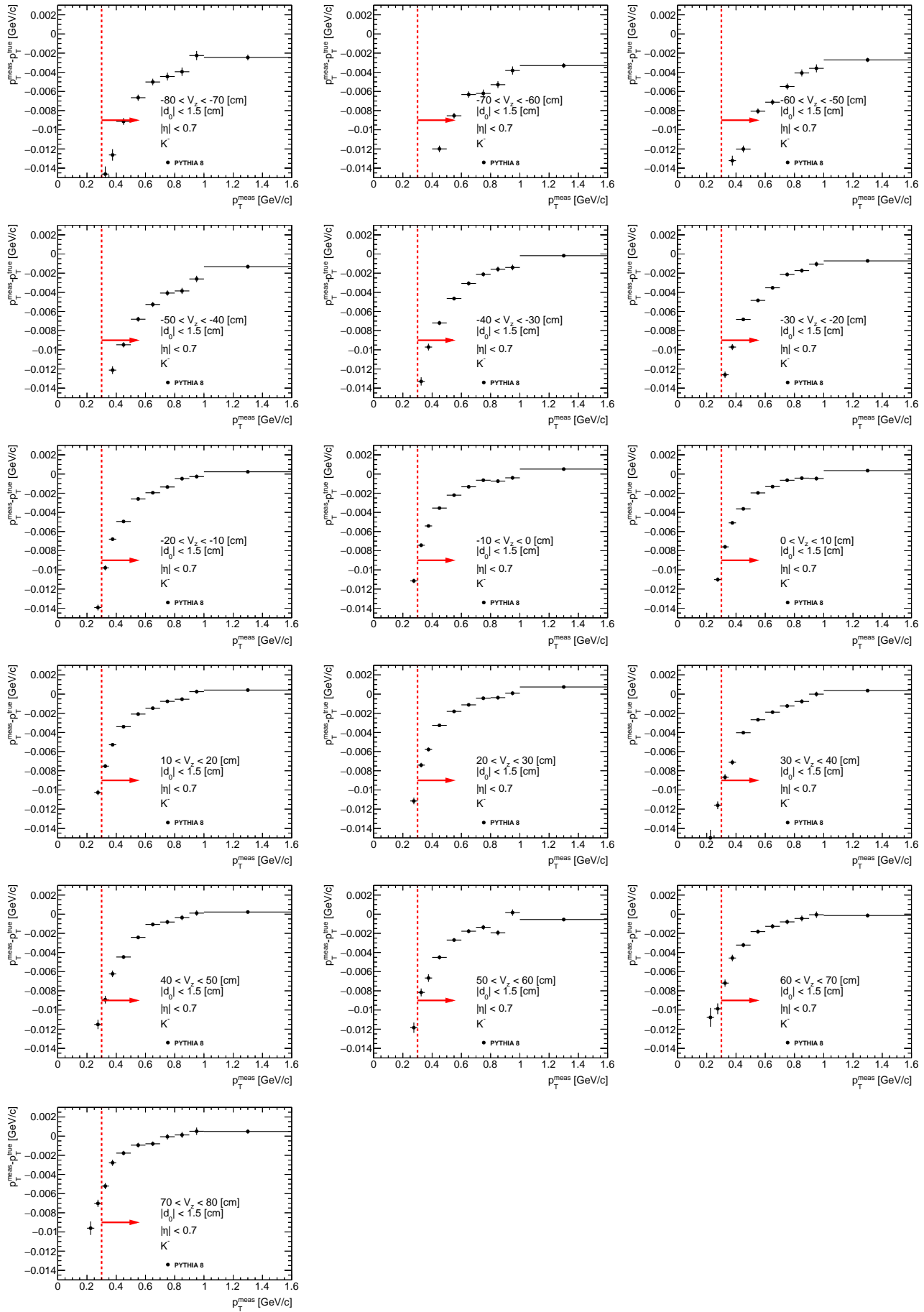


Figure C.4: Energy loss correction  $p_T^{meas} - p_T^{true}$  for  $K^+$  as a function of reconstructed transverse momentum  $p_T^{meas}$  ( $|\eta| < 0.7$ ) in single  $z$ -vertex bin whose range is given on each plot. Red lines and arrows indicate region accepted in analyses.

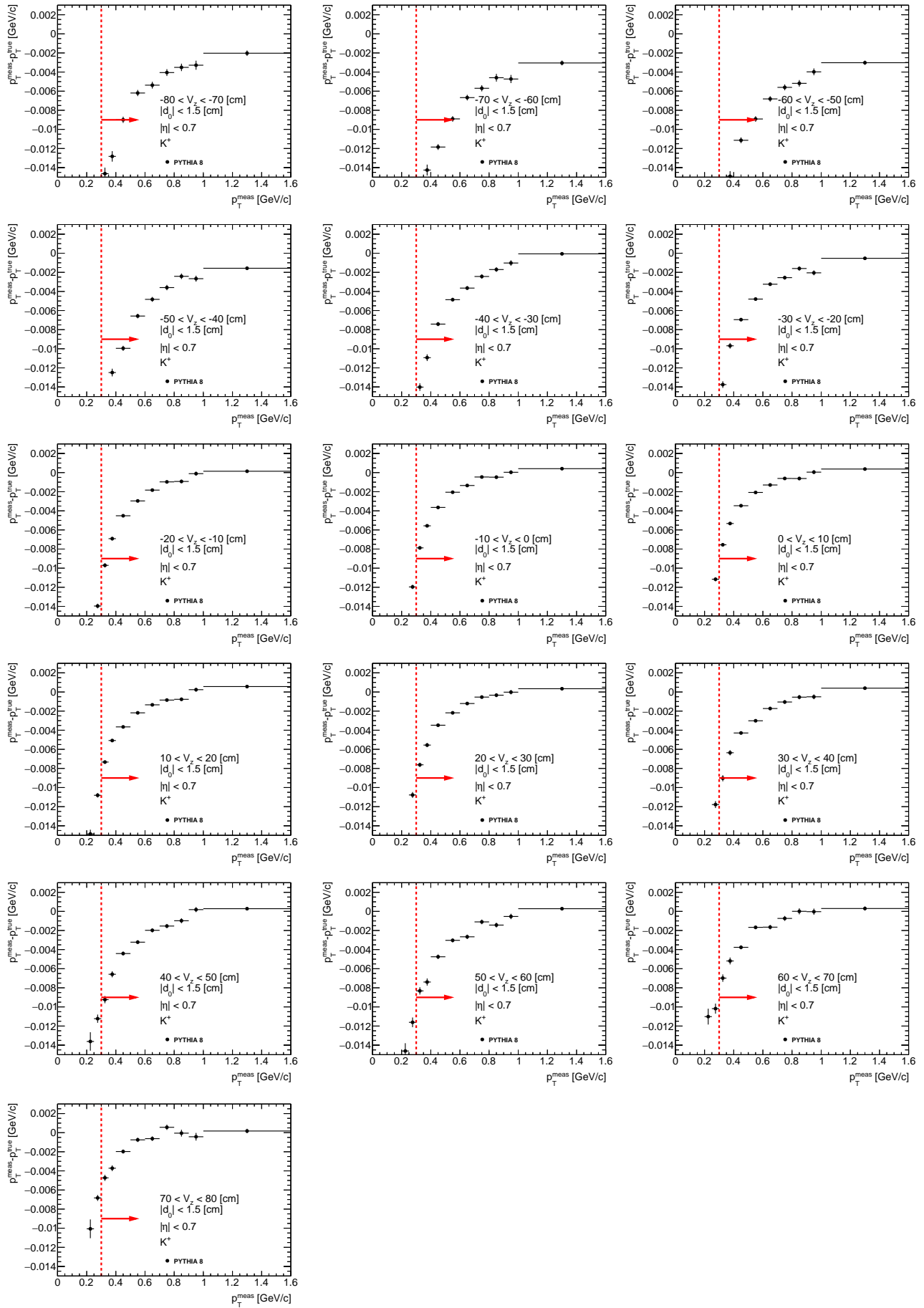


Figure C.5: Energy loss correction  $p_T^{meas} - p_T^{true}$  for  $\bar{p}$  as a function of reconstructed transverse momentum  $p_T^{meas}$  ( $|\eta| < 0.7$ ) in single  $z$ -vertex bin whose range is given on each plot. Red lines and arrows indicate region accepted in analyses.

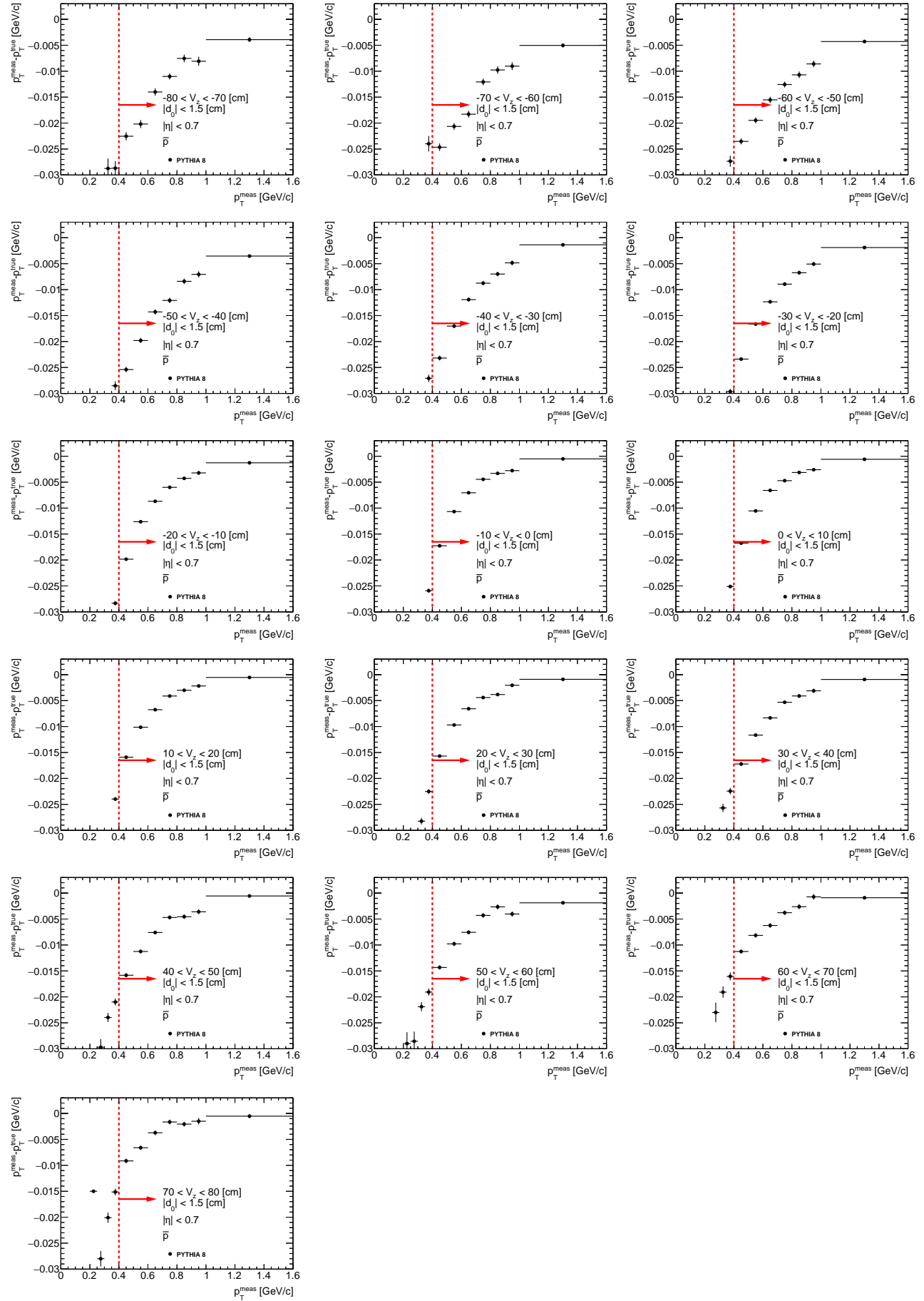


Figure C.6: Energy loss correction  $p_T^{meas} - p_T^{true}$  for  $p$  as a function of reconstructed transverse momentum  $p_T^{meas}$  ( $|\eta| < 0.7$ ) in single  $z$ -vertex bin whose range is given on each plot. Red lines and arrows indicate region accepted in analyses.

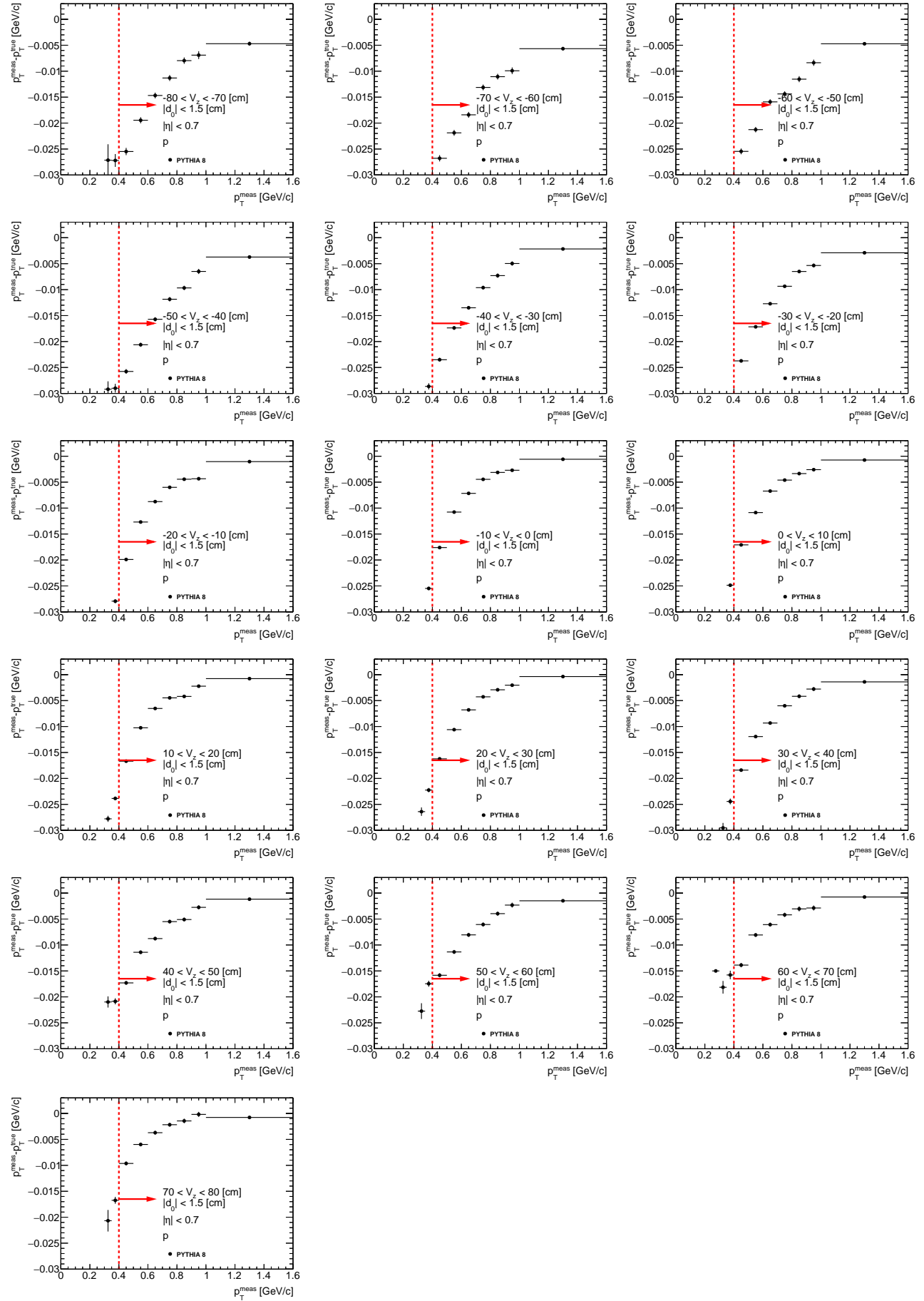


Figure C.7: Energy loss correction  $p_T^{meas} - p_T^{true}$  for negative particles as a function of reconstructed transverse momentum  $p_T^{meas}$  ( $|\eta| < 0.7$ ) in single  $z$ -vertex bin whose range is given on each plot. Red lines and arrows indicate region accepted in analyses.

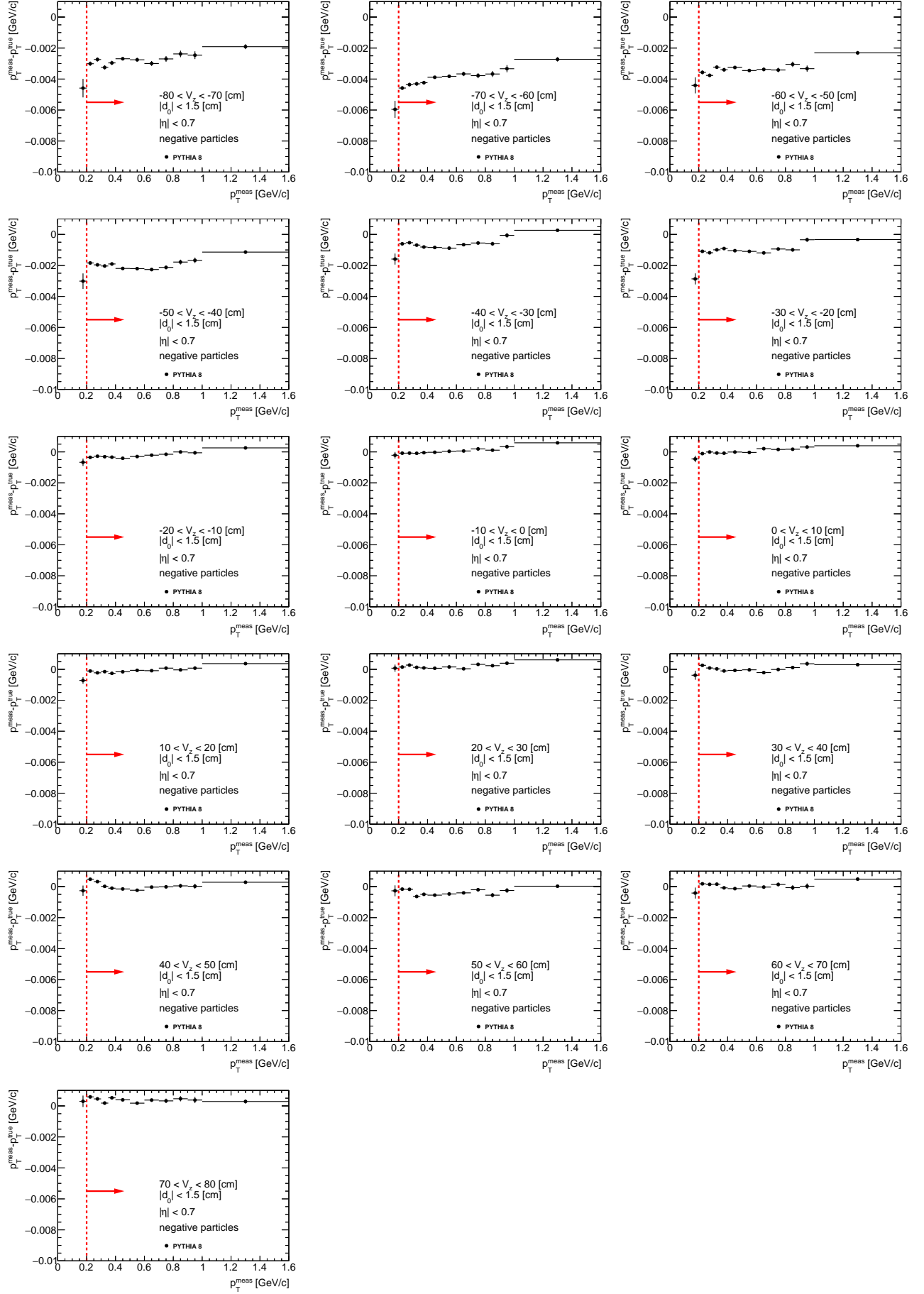


Figure C.8: Energy loss correction  $p_T^{meas} - p_T^{true}$  for positive particles as a function of reconstructed transverse momentum  $p_T^{meas}$  ( $|\eta| < 0.7$ ) in single  $z$ -vertex bin whose range is given on each plot. Red lines and arrows indicate region accepted in analyses.

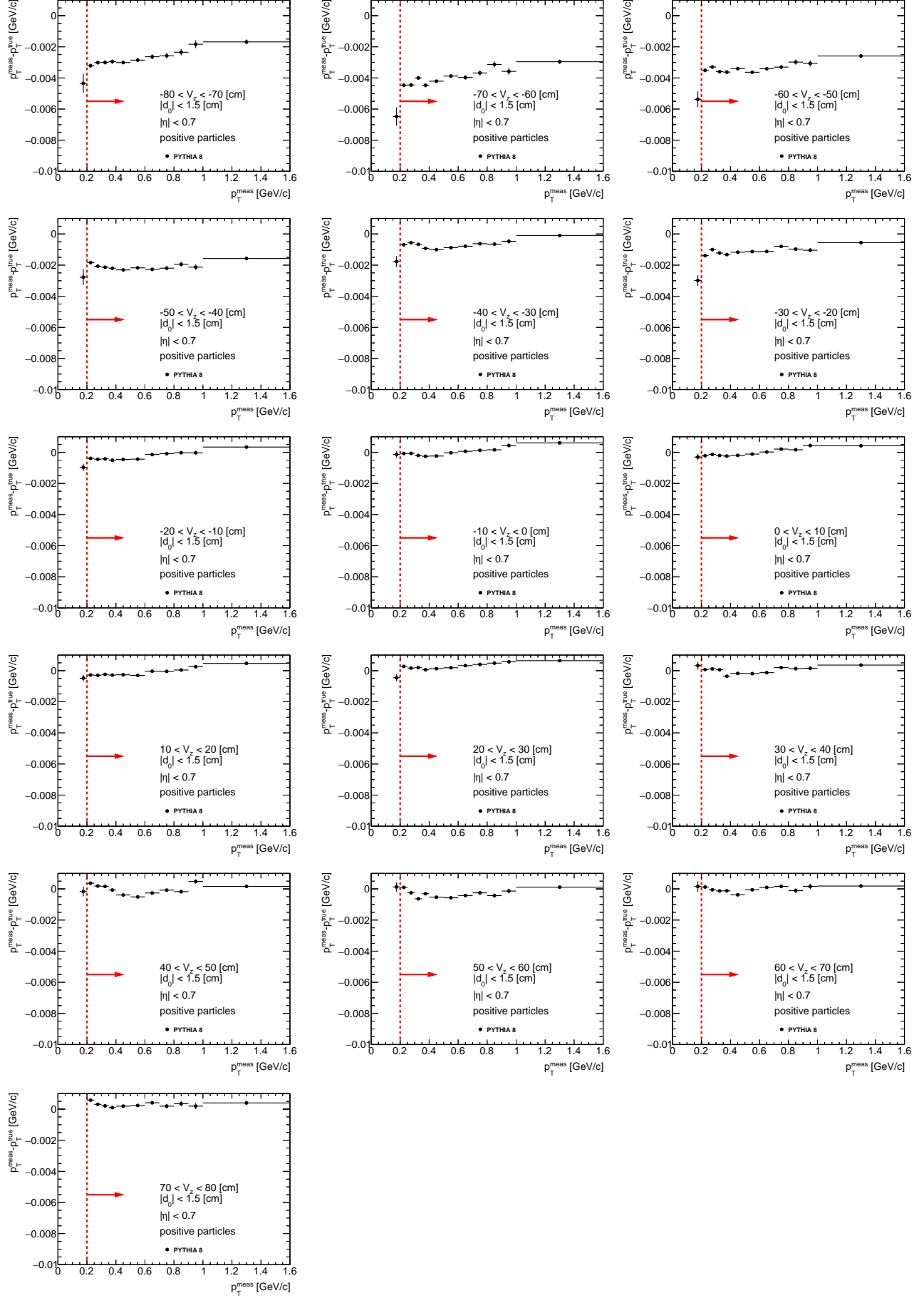
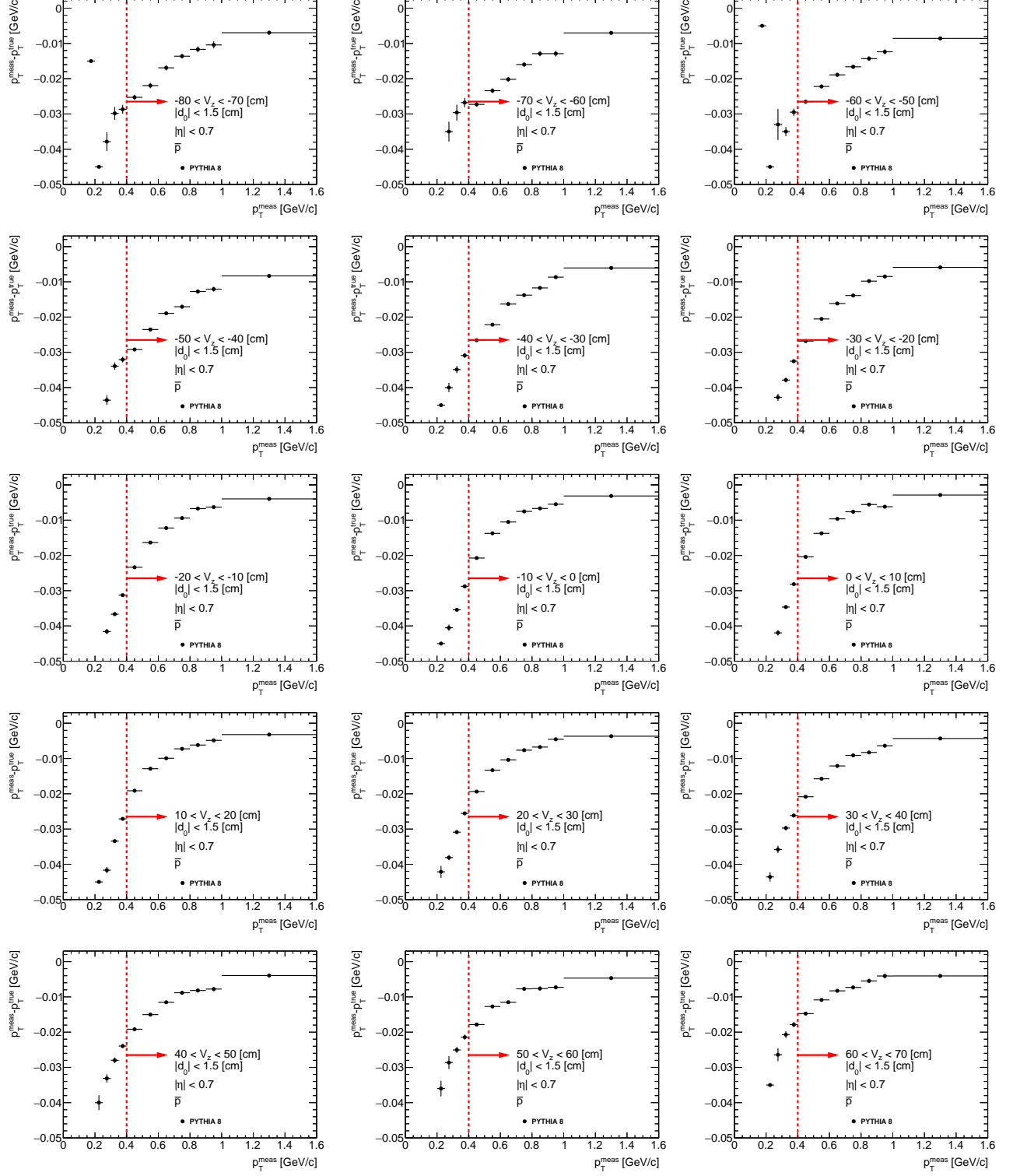


Figure C.9: Energy loss correction  $p_T^{meas} - p_T^{true}$  for  $\bar{p}$  as a function of reconstructed global track transverse momentum  $p_T^{meas}$  ( $|\eta| < 0.7$ ) in single  $z$ -vertex bin whose range is given on each plot. Red lines and arrows indicate region accepted in analyses. One may need the energy loss correction for reconstructed global proton and antiproton tracks to estimate the knock-out proton background. During the reconstruction, global tracks are corrected only for energy losses in TPC, whereas primary tracks have the information of dead material inside and in front of TPC. Since that, there is an offset of about 4 MeV for global tracks.



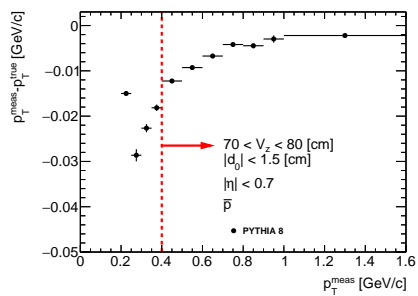
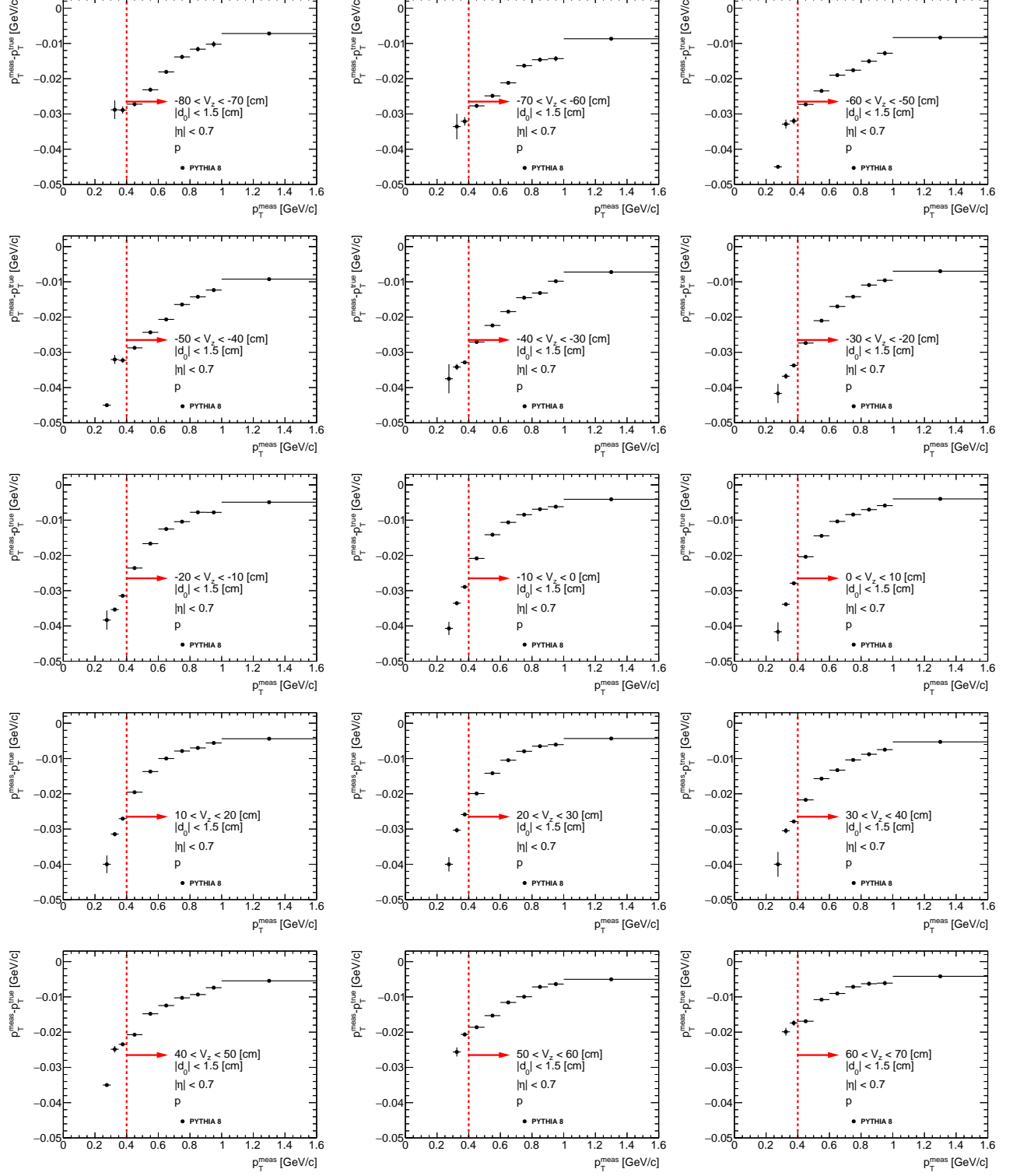
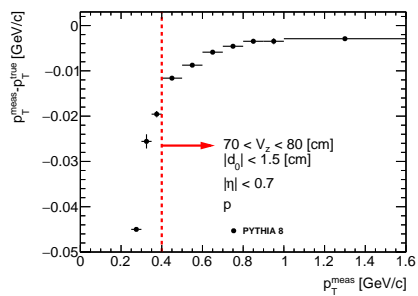


Figure C.10: Energy loss correction  $p_T^{meas} - p_T^{true}$  for  $p$  as a function of reconstructed global track transverse momentum  $p_T^{meas}$  ( $|\eta| < 0.7$ ) in single  $z$ -vertex bin whose range is given on each plot. Red lines and arrows indicate region accepted in analyses. One may need the energy loss correction for reconstructed global proton and antiproton tracks to estimate the knock-out proton background. During the reconstruction, global tracks are corrected only for energy losses in TPC, whereas primary tracks have the information of dead material inside and in front of TPC. Since that, there is an offset of about 4 MeV for global tracks.

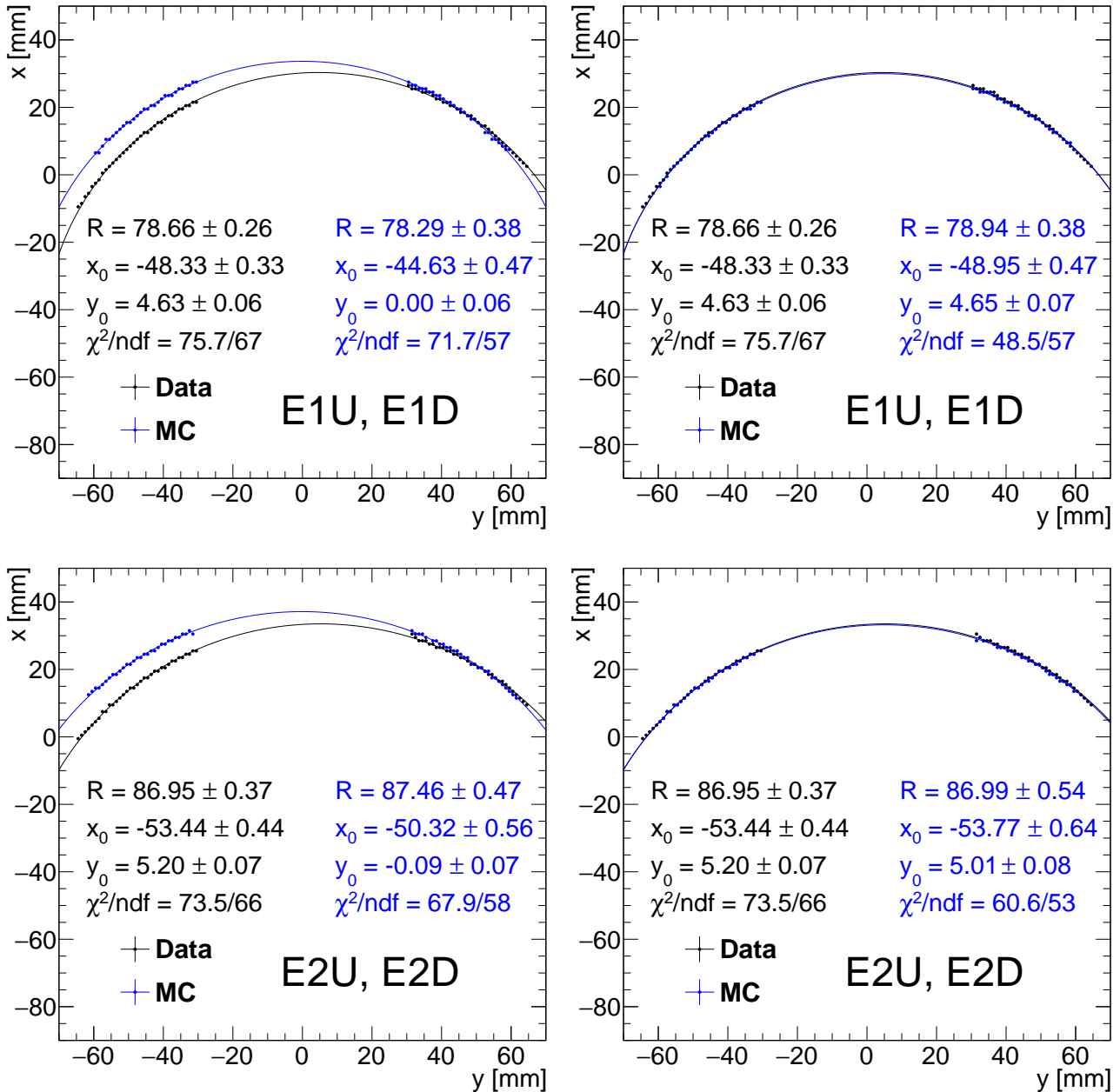


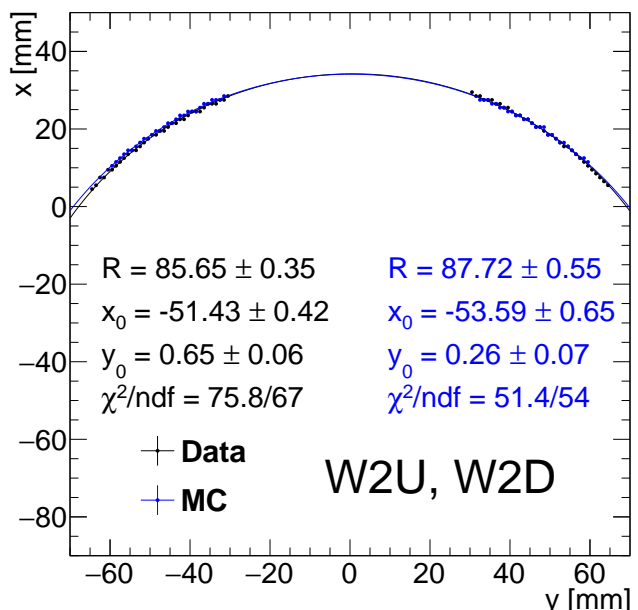
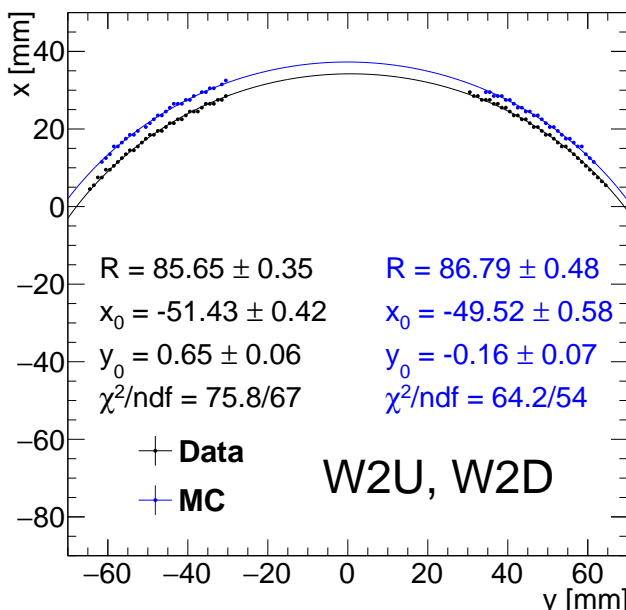
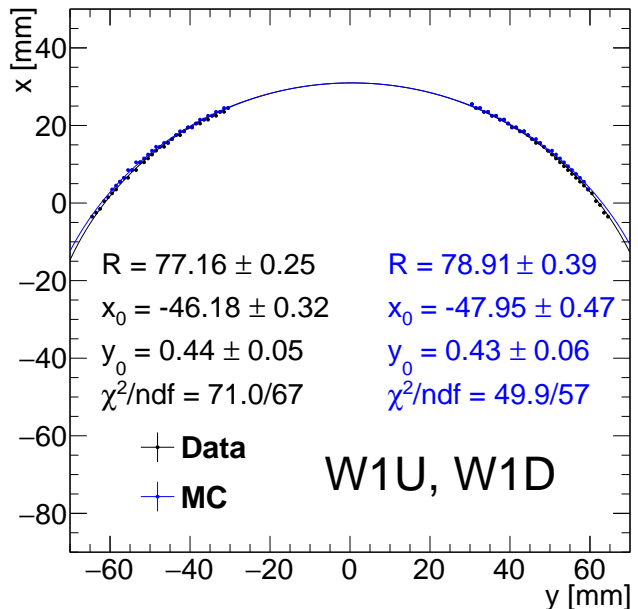
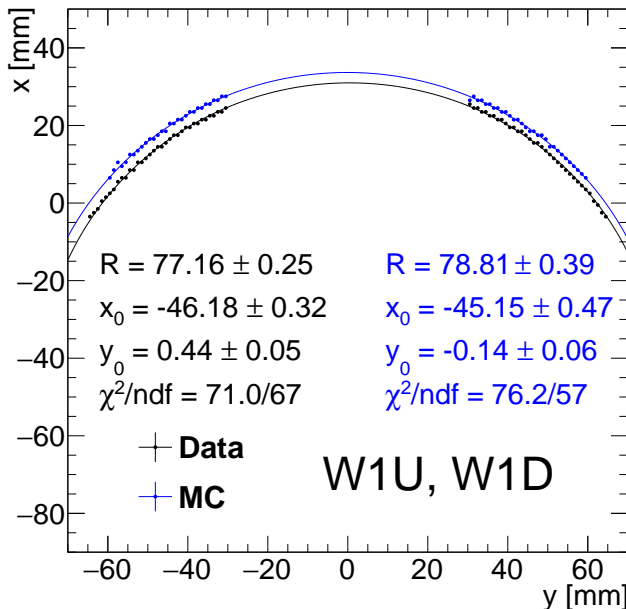


# Appendix D

## Apertures tuning in Geant4 simulation

Figure D.1: The DX aperture envelopes fitted with circles before (left) and after (right) the DX offsets introduced in the Geant4 geometry.

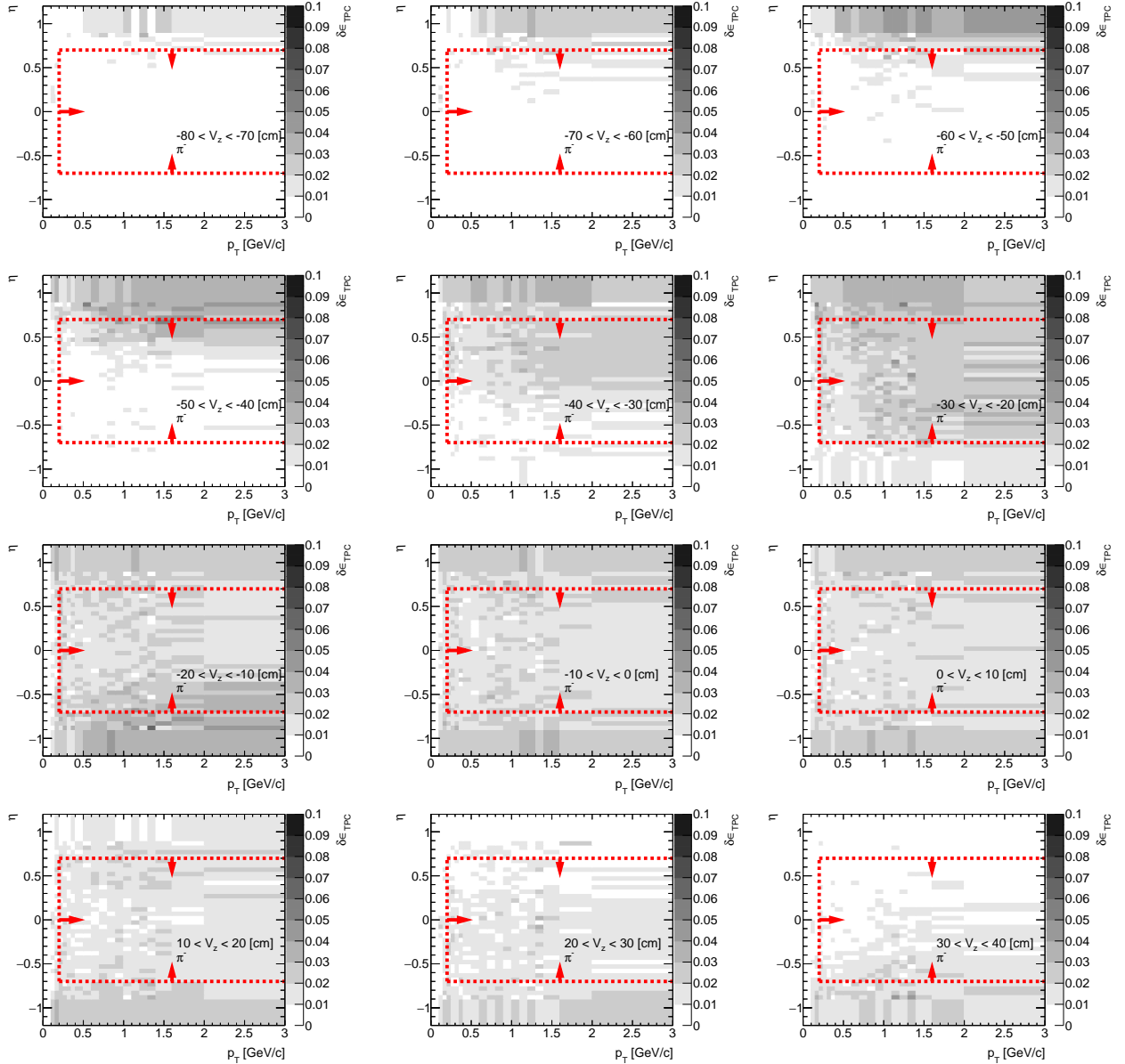




# Appendix E

## Dead material effect on TPC track reconstruction efficiency

Figure E.1: The amount of lost  $\pi^-$  due to the interaction with dead material in front of TPC in CD and SD MC samples. Each plot represents the fraction of lost  $\pi^-$ ,  $\delta\epsilon_{TPC}$  (z-axis), as a function of true particle pseudorapidity  $\eta$  (y-axis) and transverse momentum  $p_T$  (x-axis) in single  $z$ -vertex bin. Red lines and arrows indicate region accepted in the analysis.



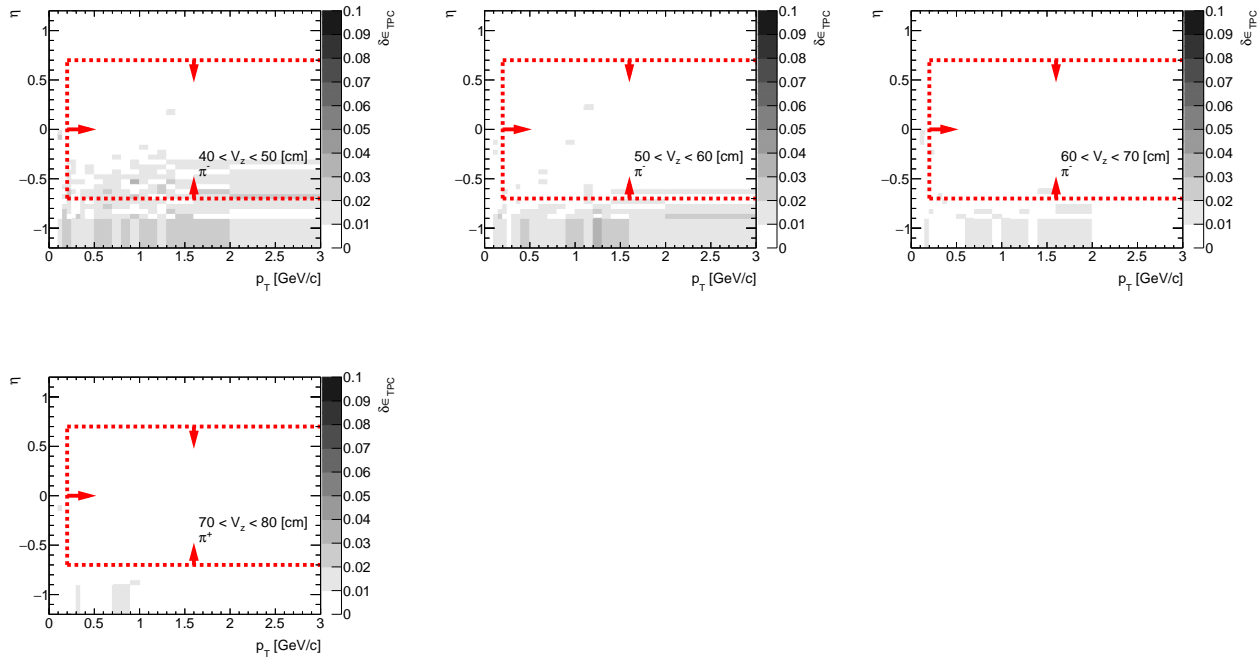


Figure E.2: The amount of lost  $\pi^+$  due to the interaction with dead material in front of TPC in CD and SD MC samples. Each plot represents the fraction of lost  $\pi^+$ ,  $\delta\epsilon_{TPC}$  (z-axis), as a function of true particle pseudorapidity  $\eta$  (y-axis) and transverse momentum  $p_T$  (x-axis) in single  $z$ -vertex bin. Red lines and arrows indicate region accepted in the analysis.

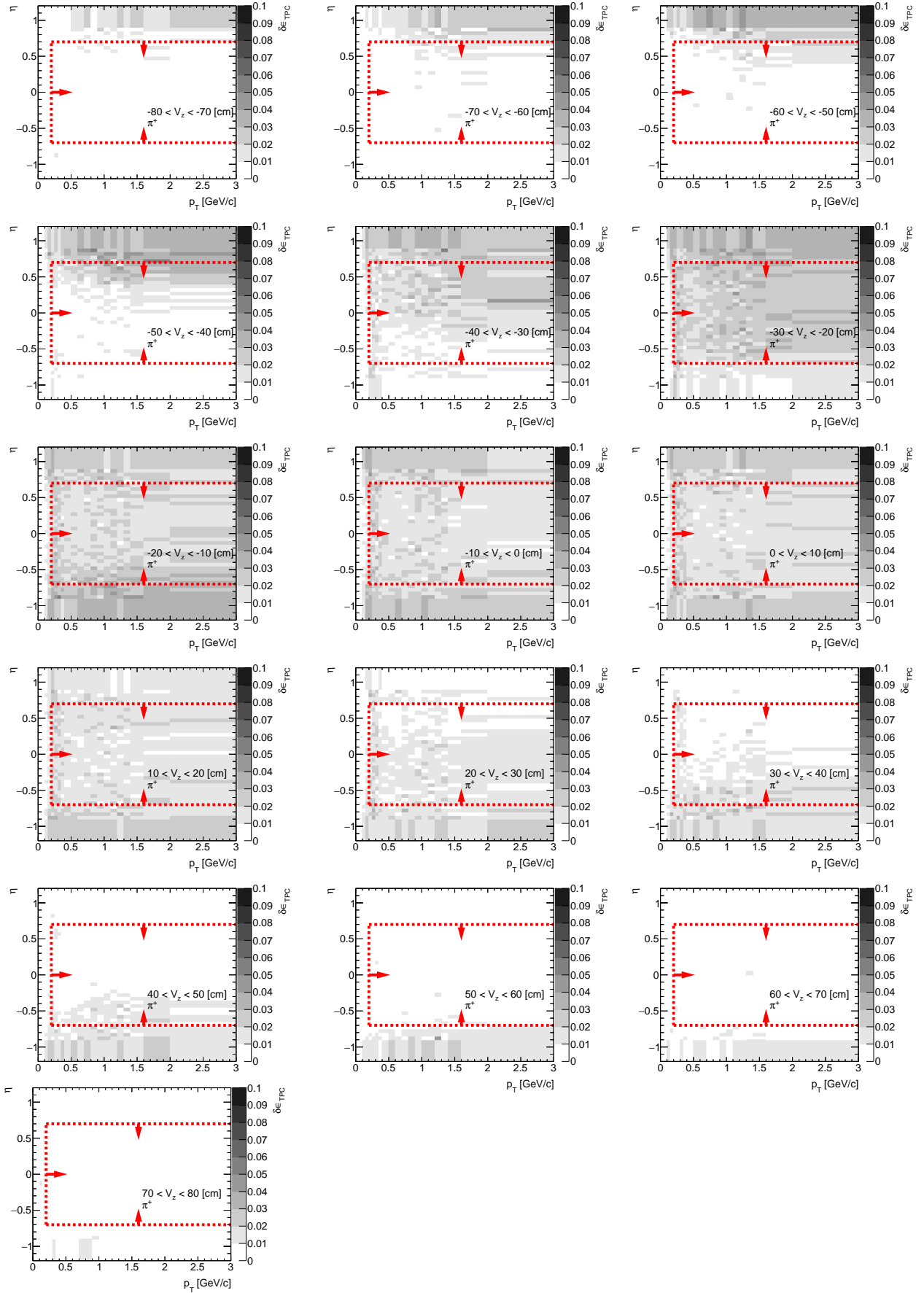


Figure E.3: The amount of lost  $K^-$  due to the interaction with dead material in front of TPC in CD and SD MC samples. Each plot represents the fraction of lost  $K^-$ ,  $\delta\epsilon_{TPC}$  ( $z$ -axis), as a function of true particle pseudorapidity  $\eta$  ( $y$ -axis) and transverse momentum  $p_T$  ( $x$ -axis) in single  $z$ -vertex bin. Red lines and arrows indicate region accepted in the analysis.

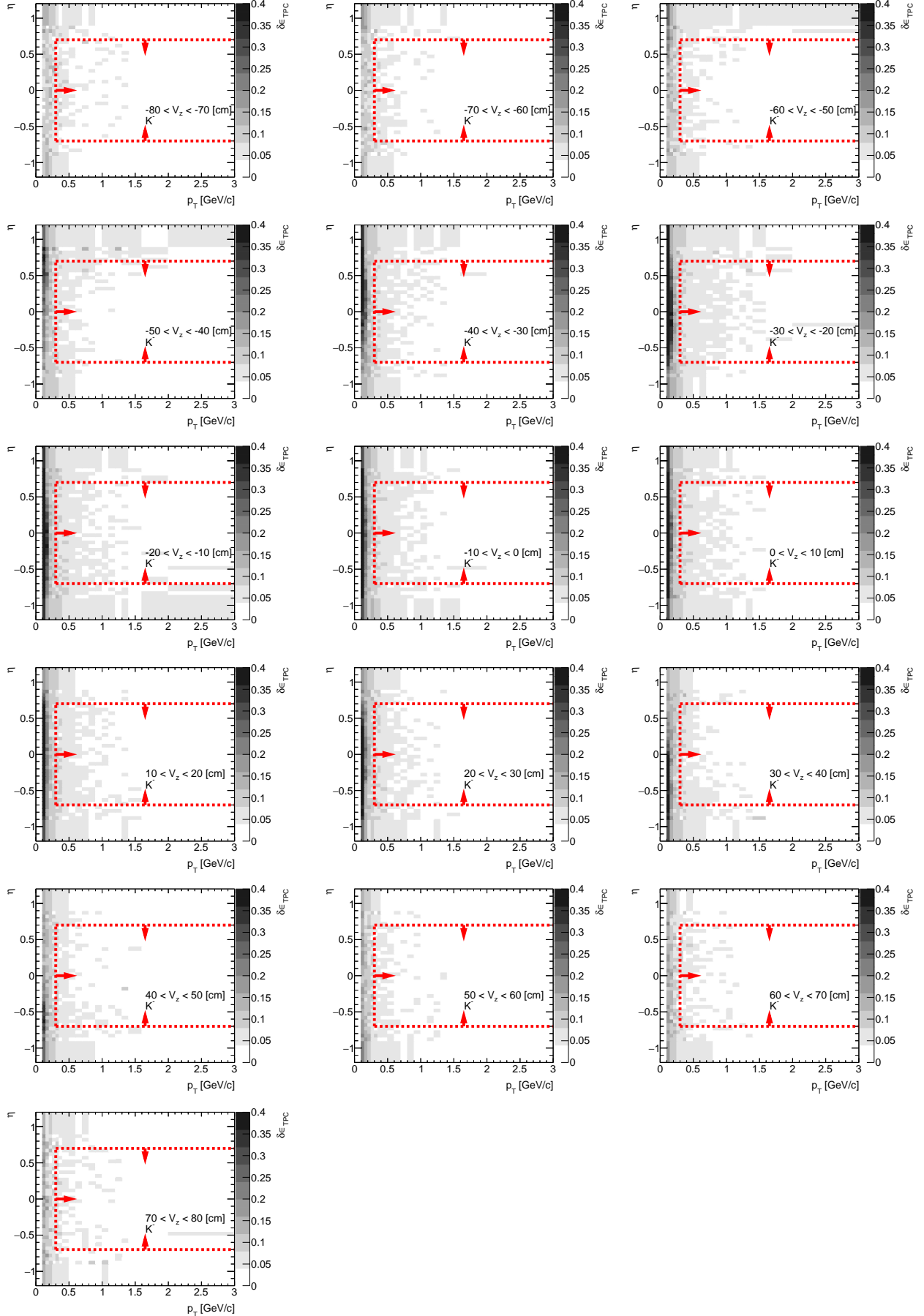


Figure E.4: The amount of lost  $K^+$  due to the interaction with dead material in front of TPC in CD and SD MC samples. Each plot represents the fraction of lost  $K^+$ ,  $\delta\epsilon_{TPC}$  ( $z$ -axis), as a function of true particle pseudorapidity  $\eta$  ( $y$ -axis) and transverse momentum  $p_T$  ( $x$ -axis) in single  $z$ -vertex bin. Red lines and arrows indicate region accepted in the analysis.

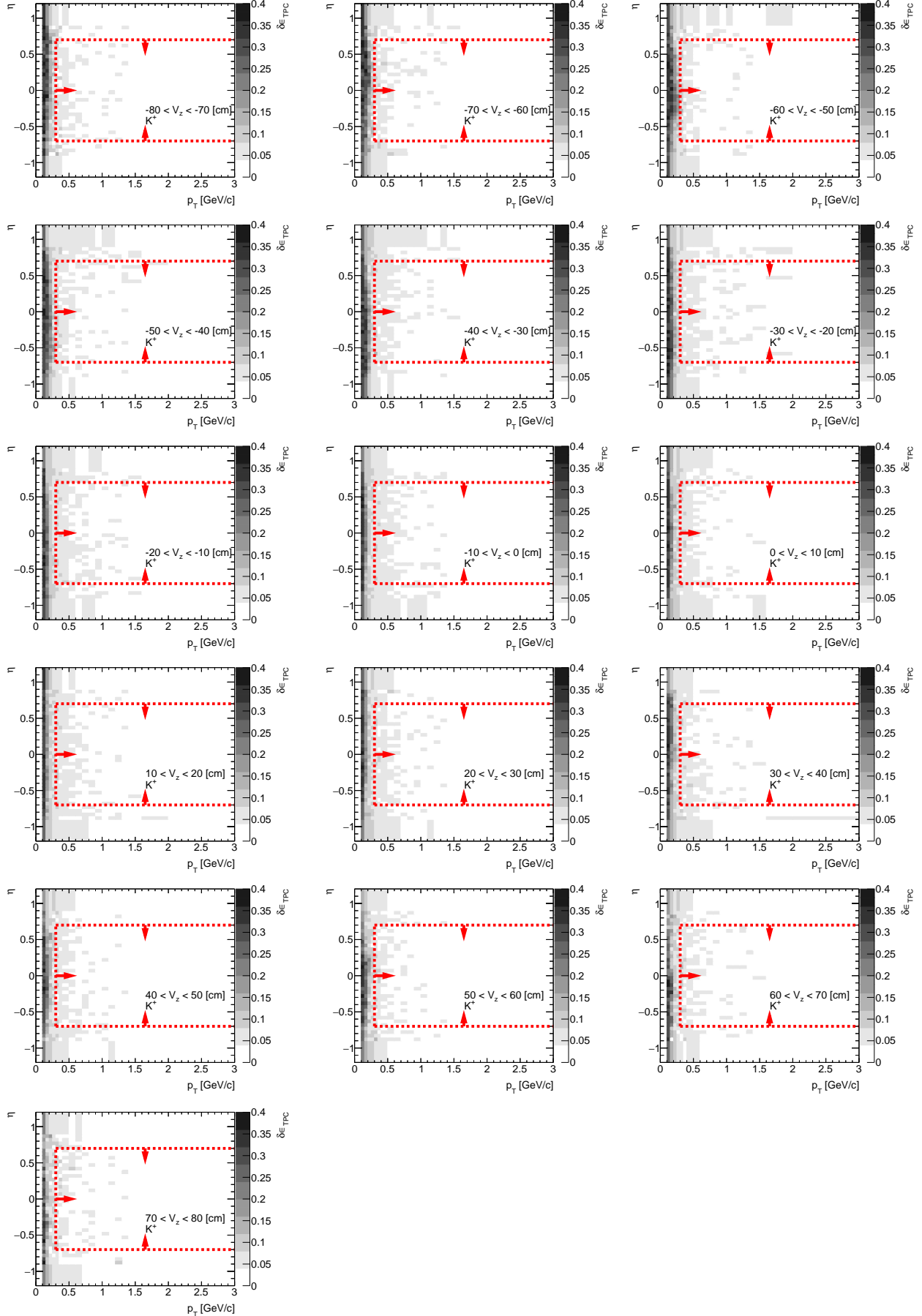


Figure E.5: The amount of lost  $\bar{p}$  due to the interaction with dead material in front of TPC in CD and SD MC samples. Each plot represents the fraction of lost  $\bar{p}$ ,  $\delta\epsilon_{TPC}$  ( $z$ -axis), as a function of true particle pseudorapidity  $\eta$  ( $y$ -axis) and transverse momentum  $p_T$  ( $x$ -axis) in single  $z$ -vertex bin. Red lines and arrows indicate region accepted in the analysis.

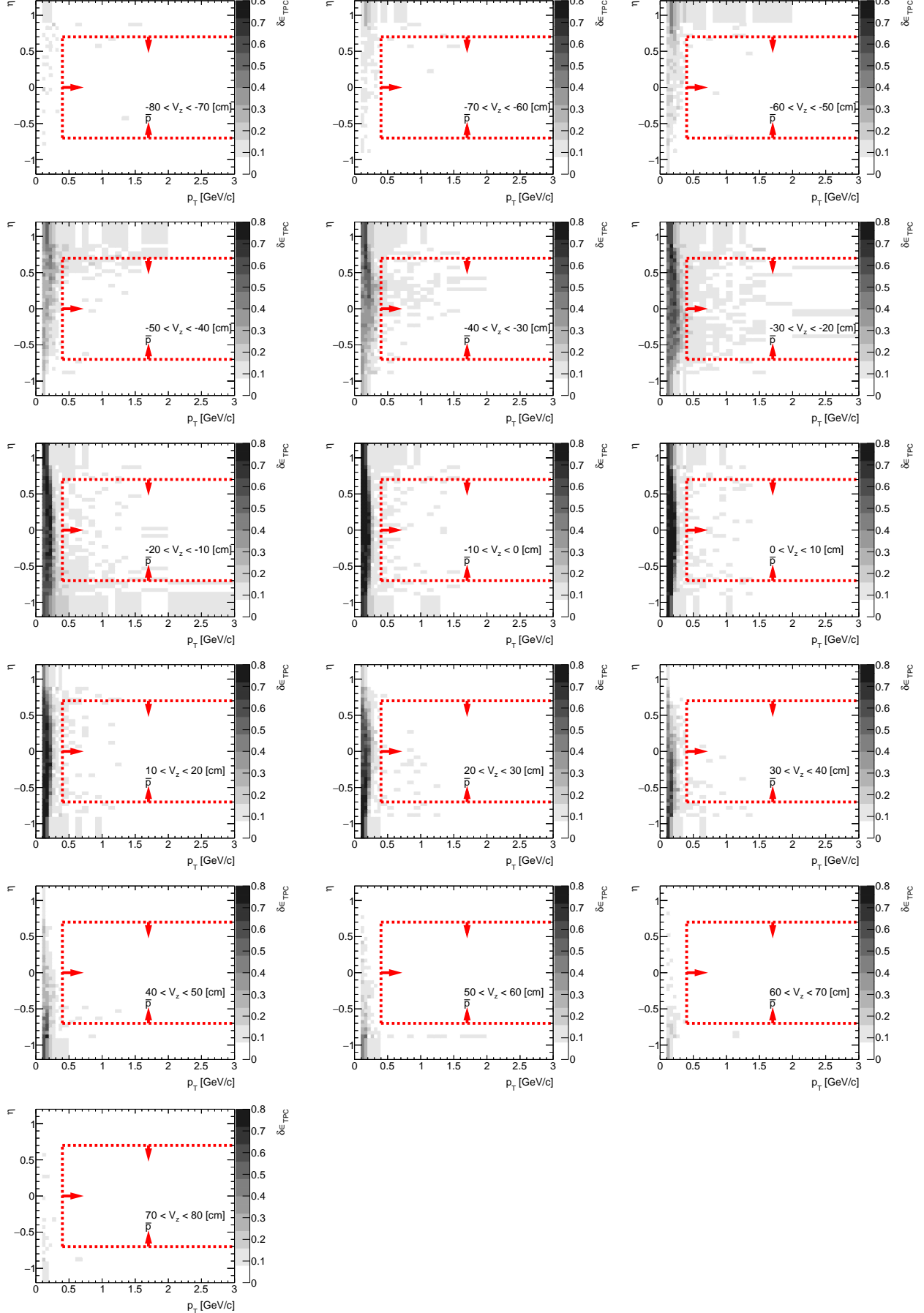


Figure E.6: The amount of lost  $p$  due to the interaction with dead material in front of TPC in CD and SD MC samples. Each plot represents the fraction of lost  $p$ ,  $\delta\epsilon_{TPC}$  ( $z$ -axis), as a function of true particle pseudorapidity  $\eta$  ( $y$ -axis) and transverse momentum  $p_T$  ( $x$ -axis) in single  $z$ -vertex bin. Red lines and arrows indicate region accepted in the analysis.

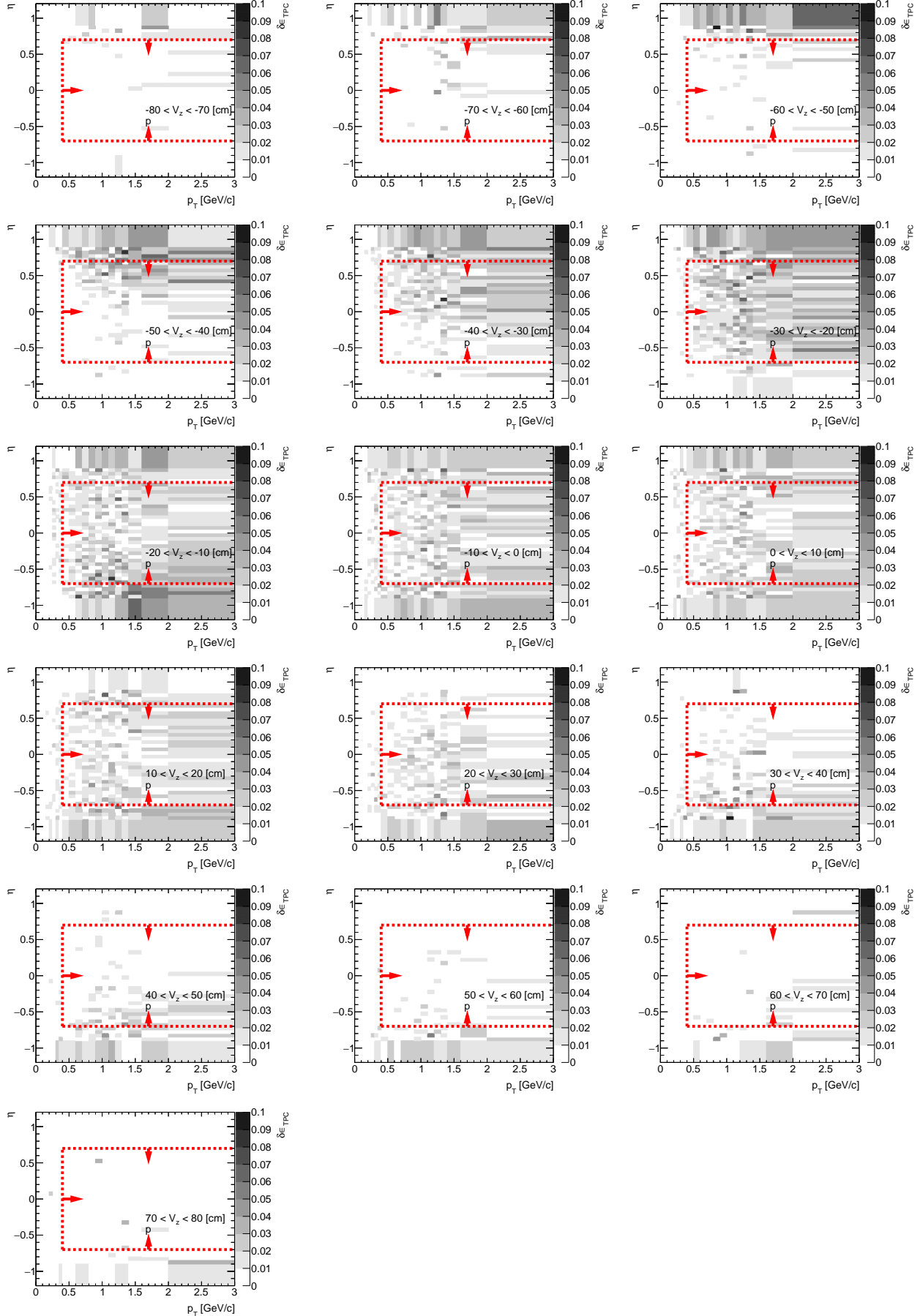


Figure E.7: The amount of lost negative particles due to the interaction with dead material in front of TPC in CD and SD MC samples. Each plot represents the fraction of lost negative particles,  $\delta\epsilon_{TPC}$  (z-axis), as a function of true particle pseudorapidity  $\eta$  (y-axis) and transverse momentum  $p_T$  (x-axis) in single  $z$ -vertex bin. Red lines and arrows indicate region accepted in the analysis.

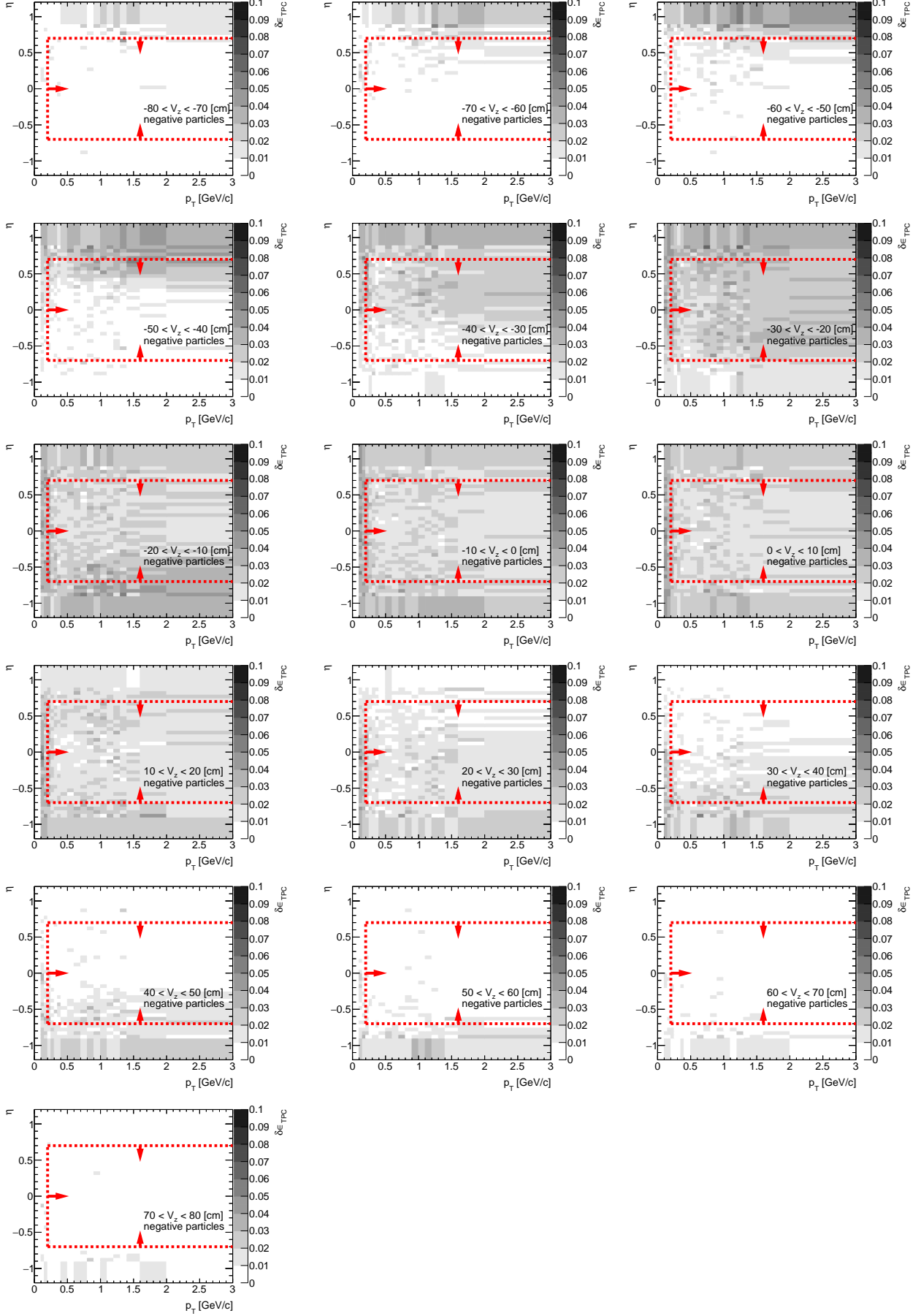
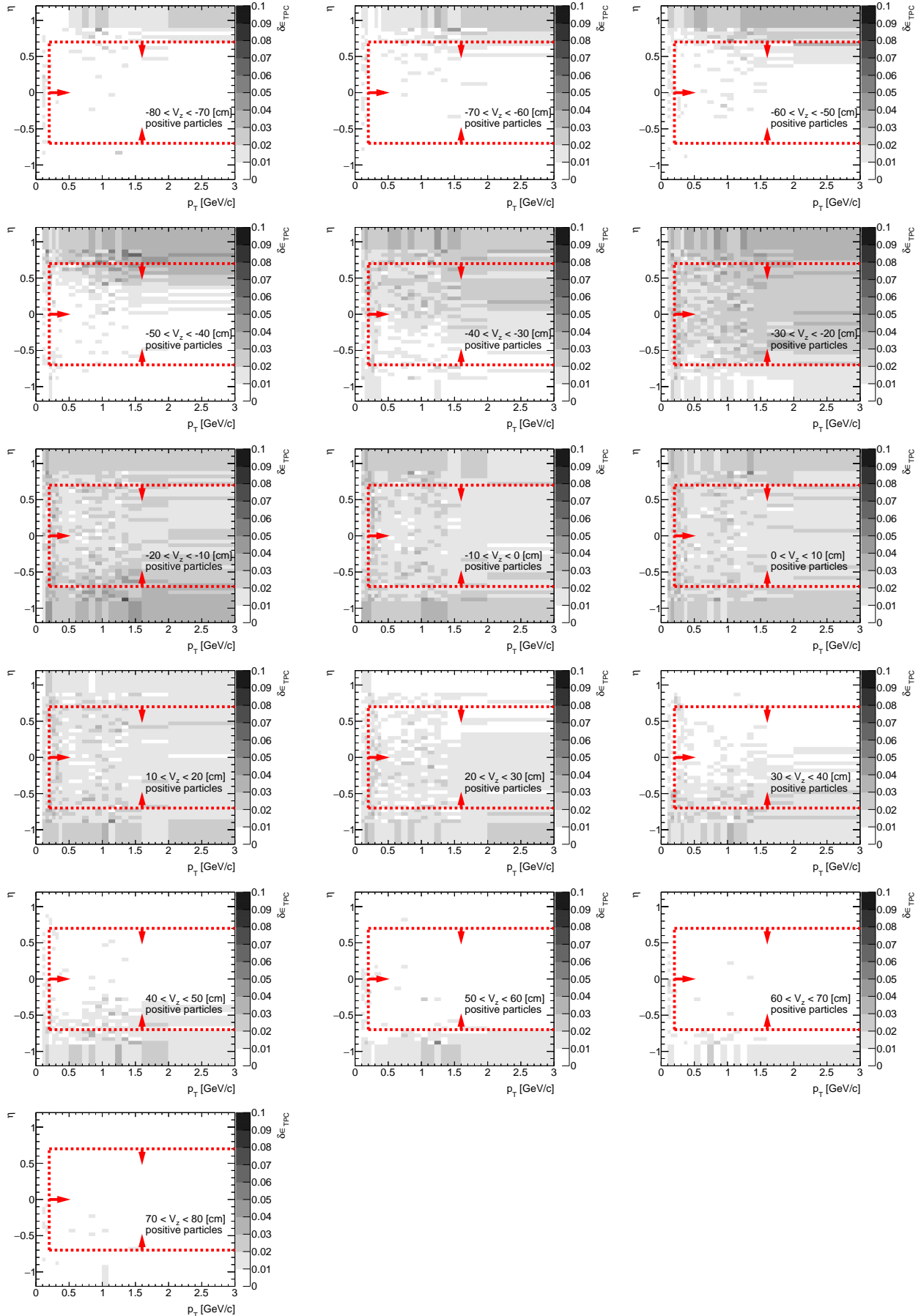


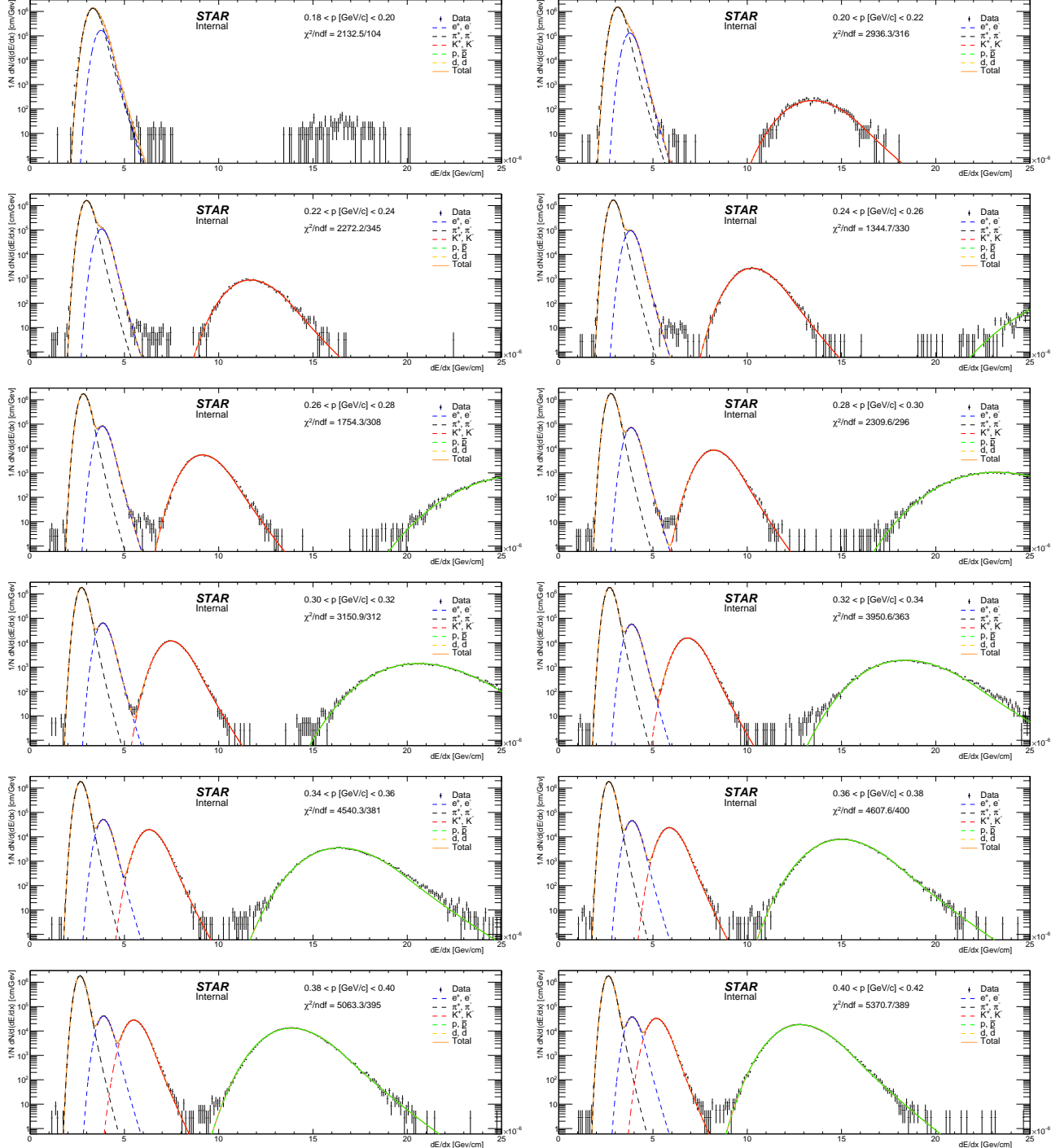
Figure E.8: The amount of lost positive particles due to the interaction with dead material in front of TPC in CD and SD MC samples. Each plot represents the fraction of lost positive particles,  $\delta\epsilon_{TPC}$  (z-axis), as a function of true particle pseudorapidity  $\eta$  (y-axis) and transverse momentum  $p_T$  (x-axis) in single  $z$ -vertex bin. Red lines and arrows indicate region accepted in the analysis.

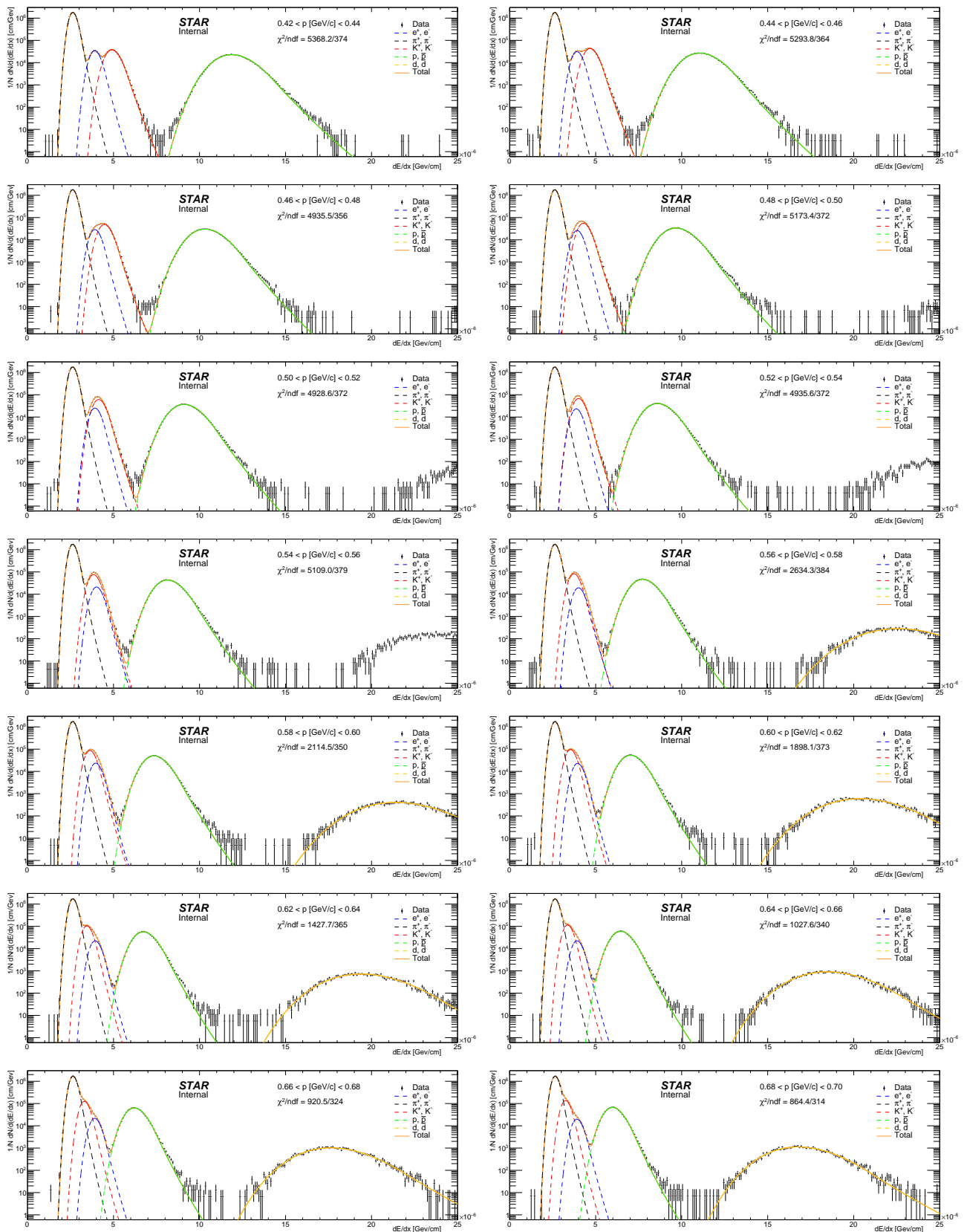


# Appendix F

## Fits to $dE/dx$ spectra, comparison of $dE/dx$ and $n_X^\sigma$ between data and MC

Figure F.1: Fits of sum of functions from Eq. (7.6) corresponding to different particle species to  $dE/dx$  spectra in the data in momentum bins.





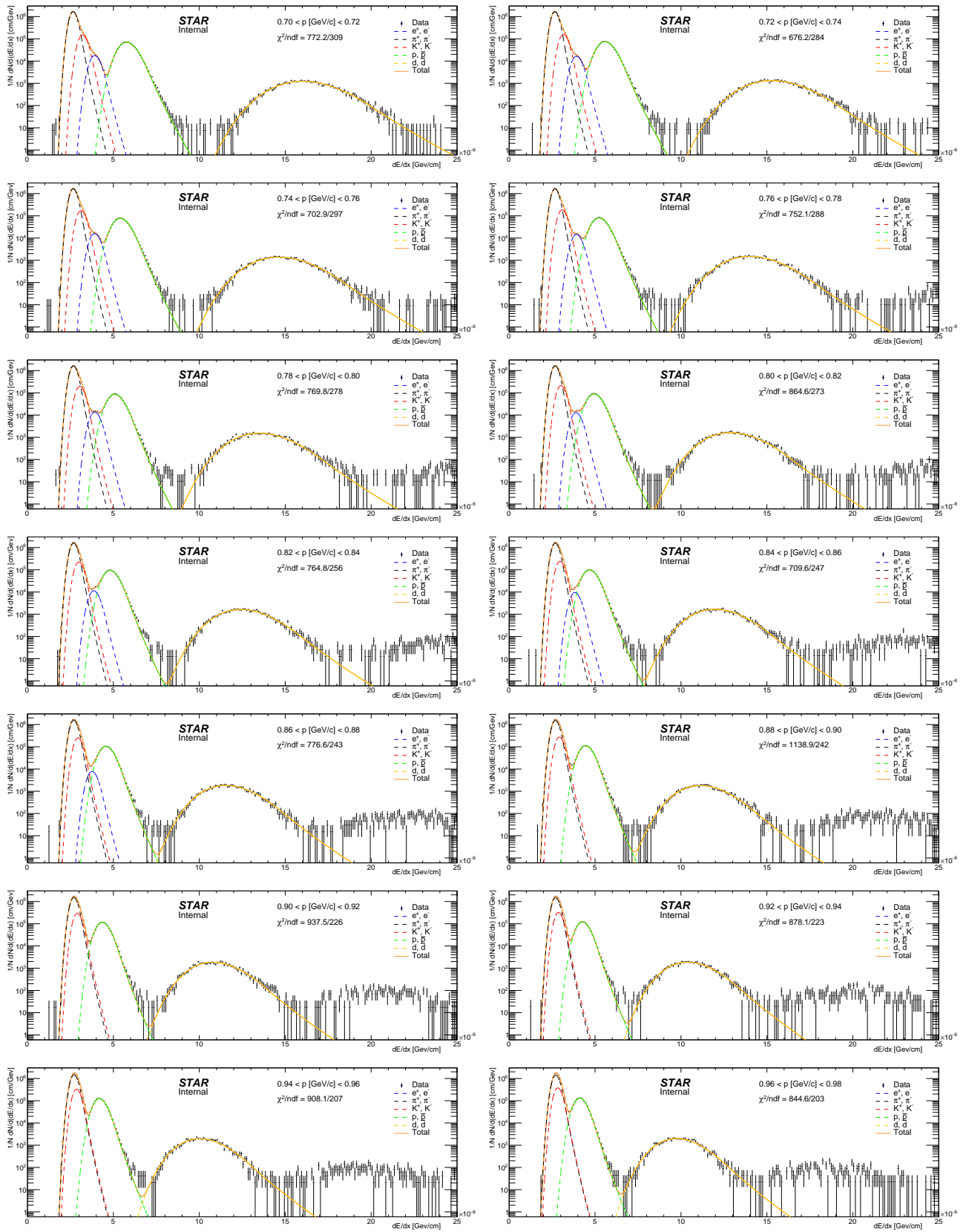
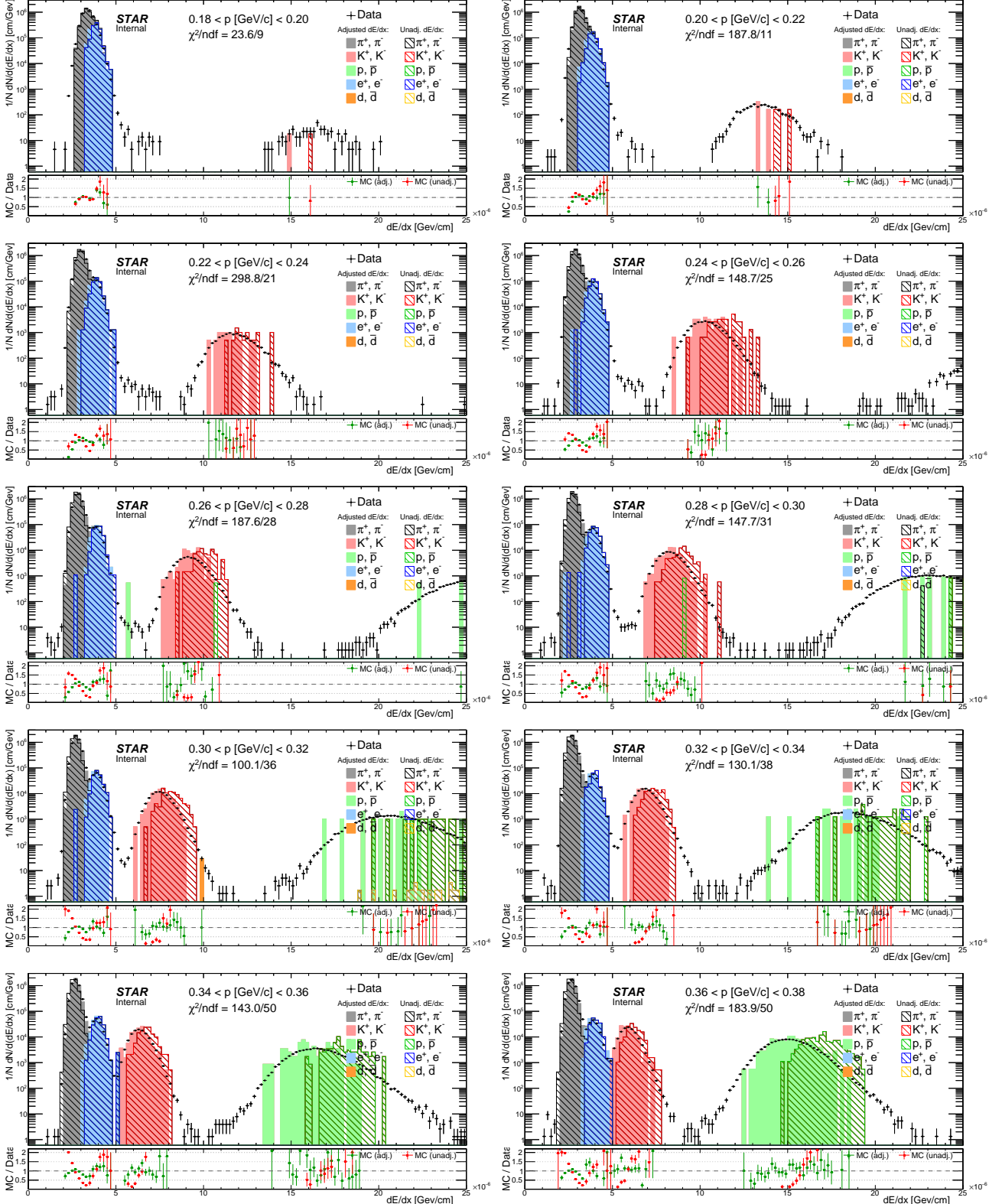
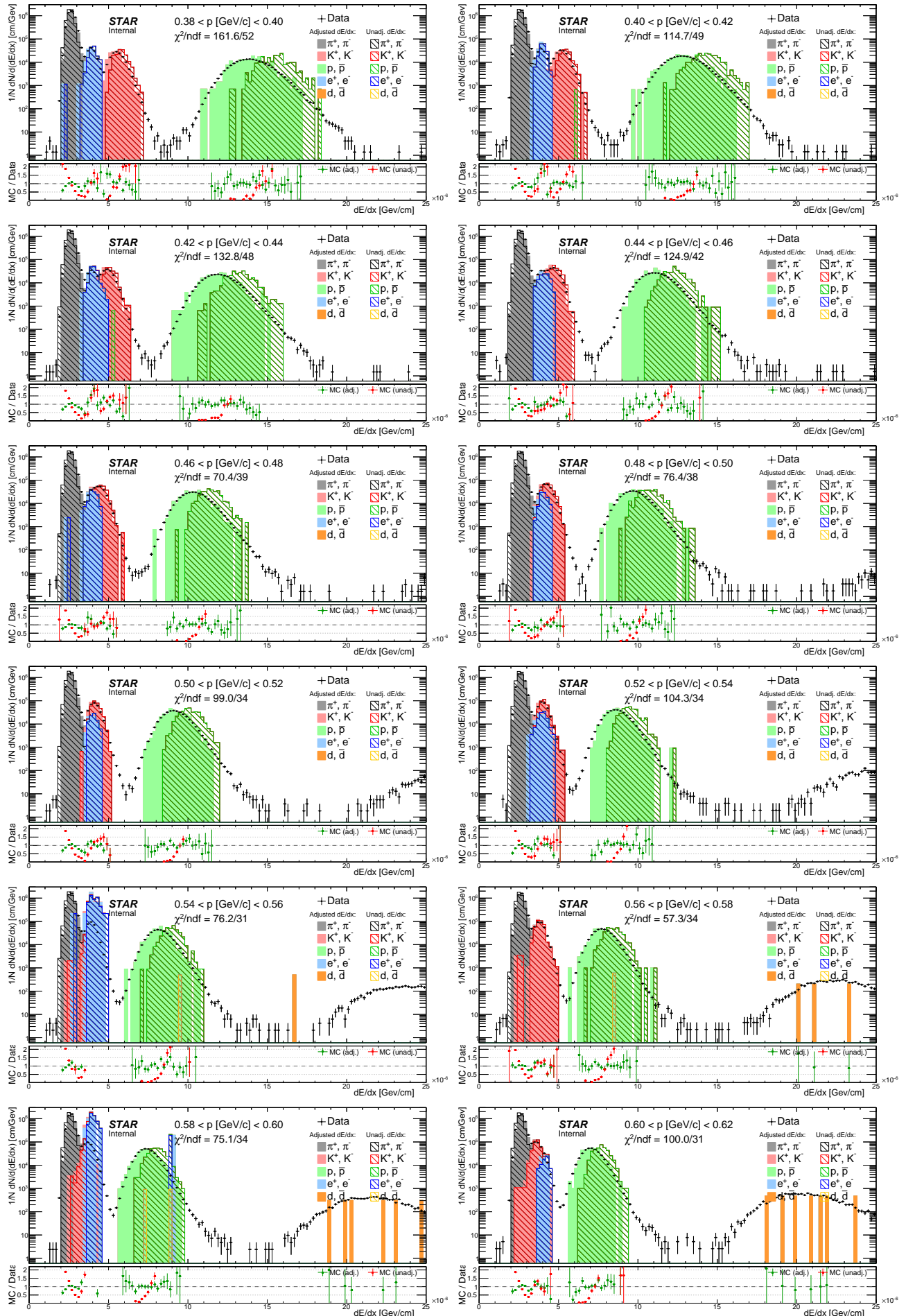
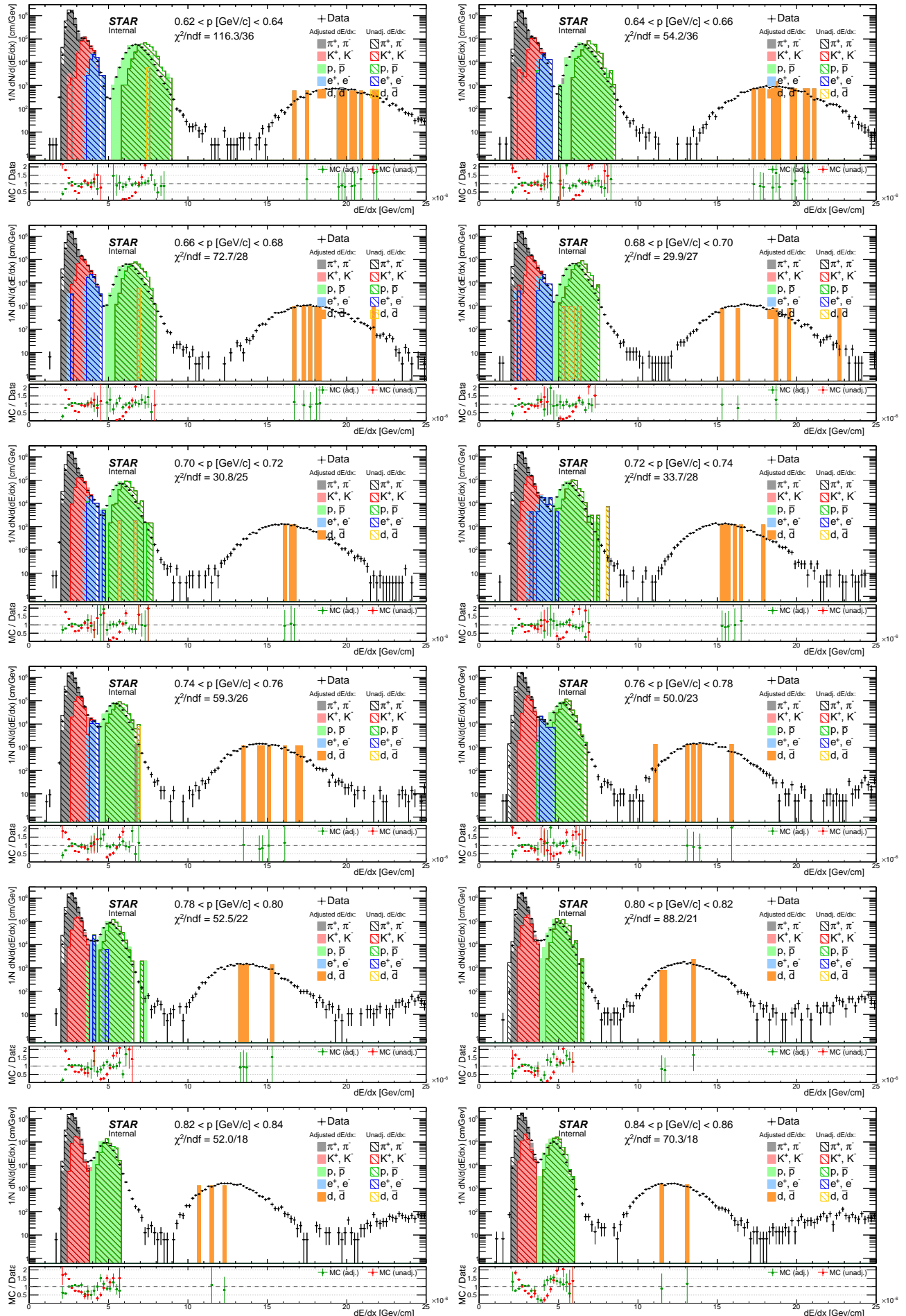


Figure F.2: Comparison of  $dE/dx$  spectrum between data and embedded MC (before and after  $dE/dx$  adjustment) in momentum bins.







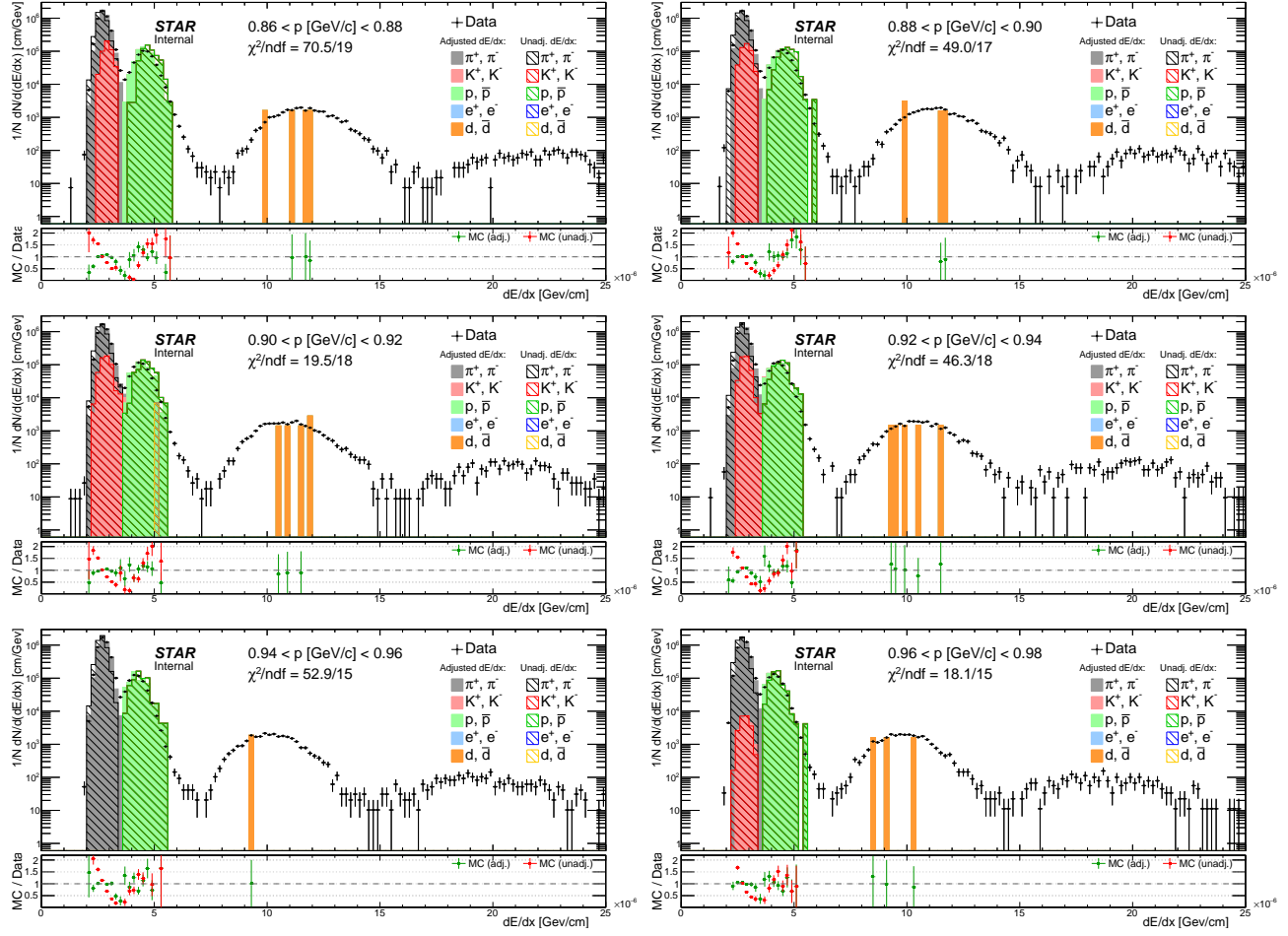
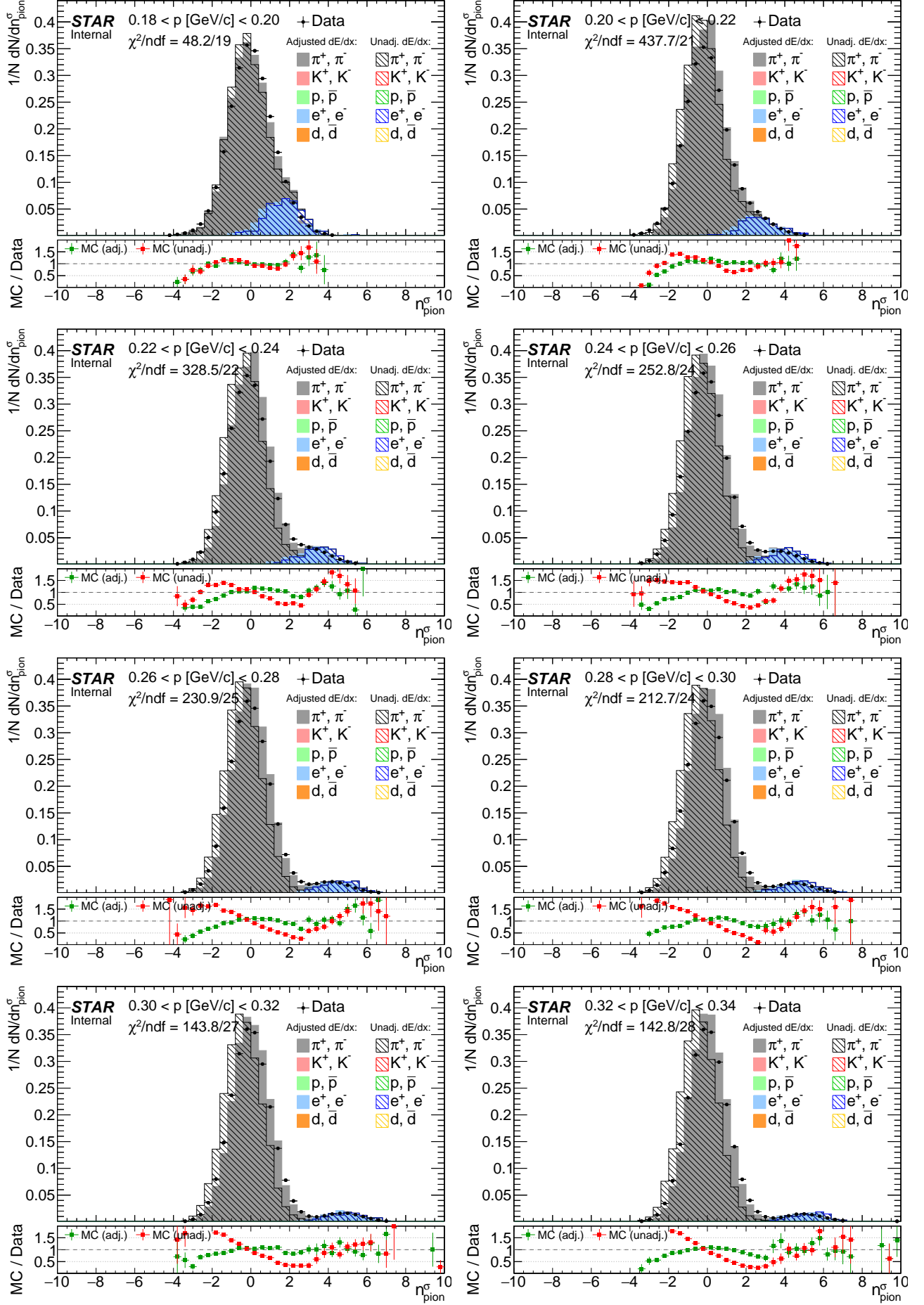
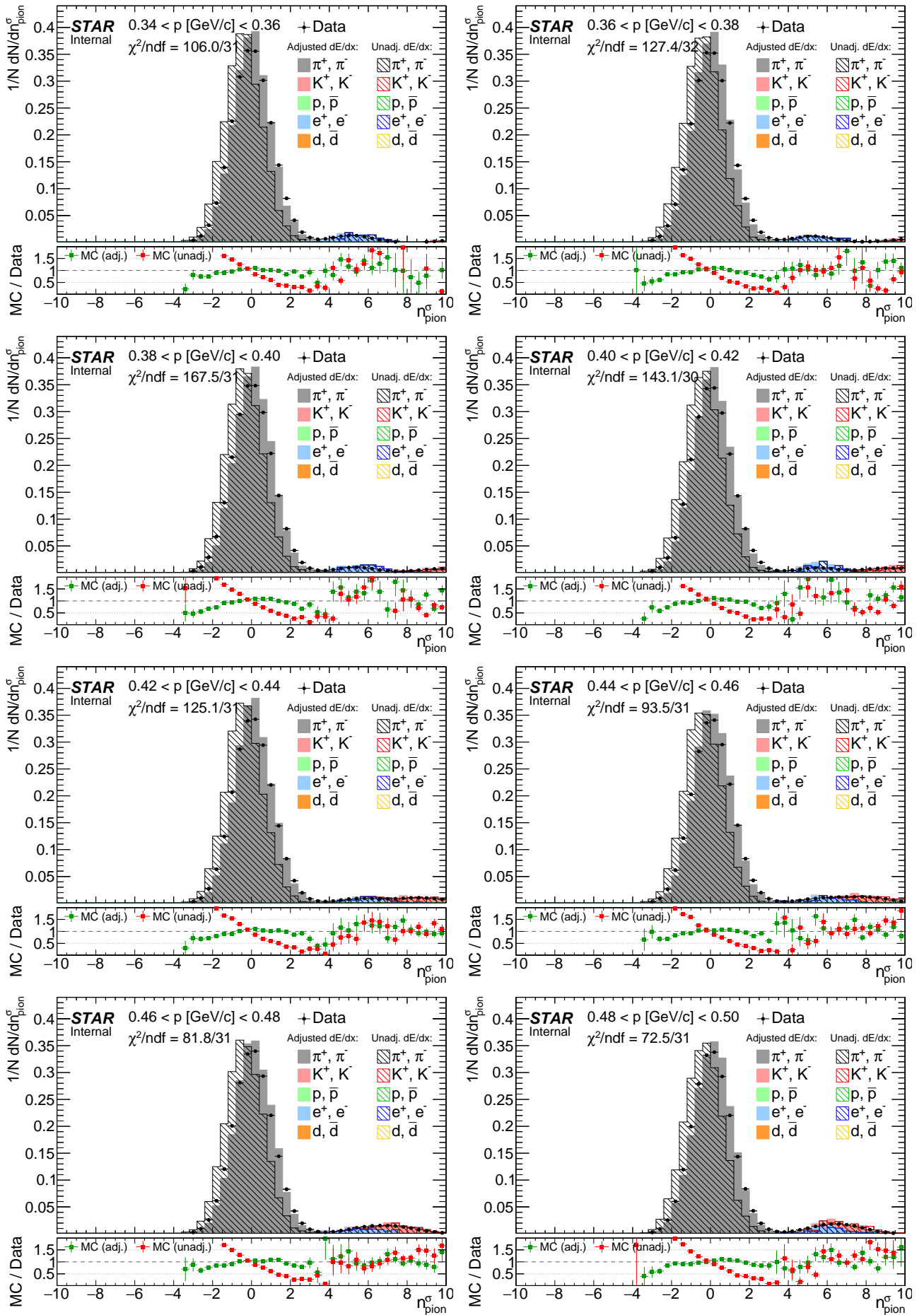
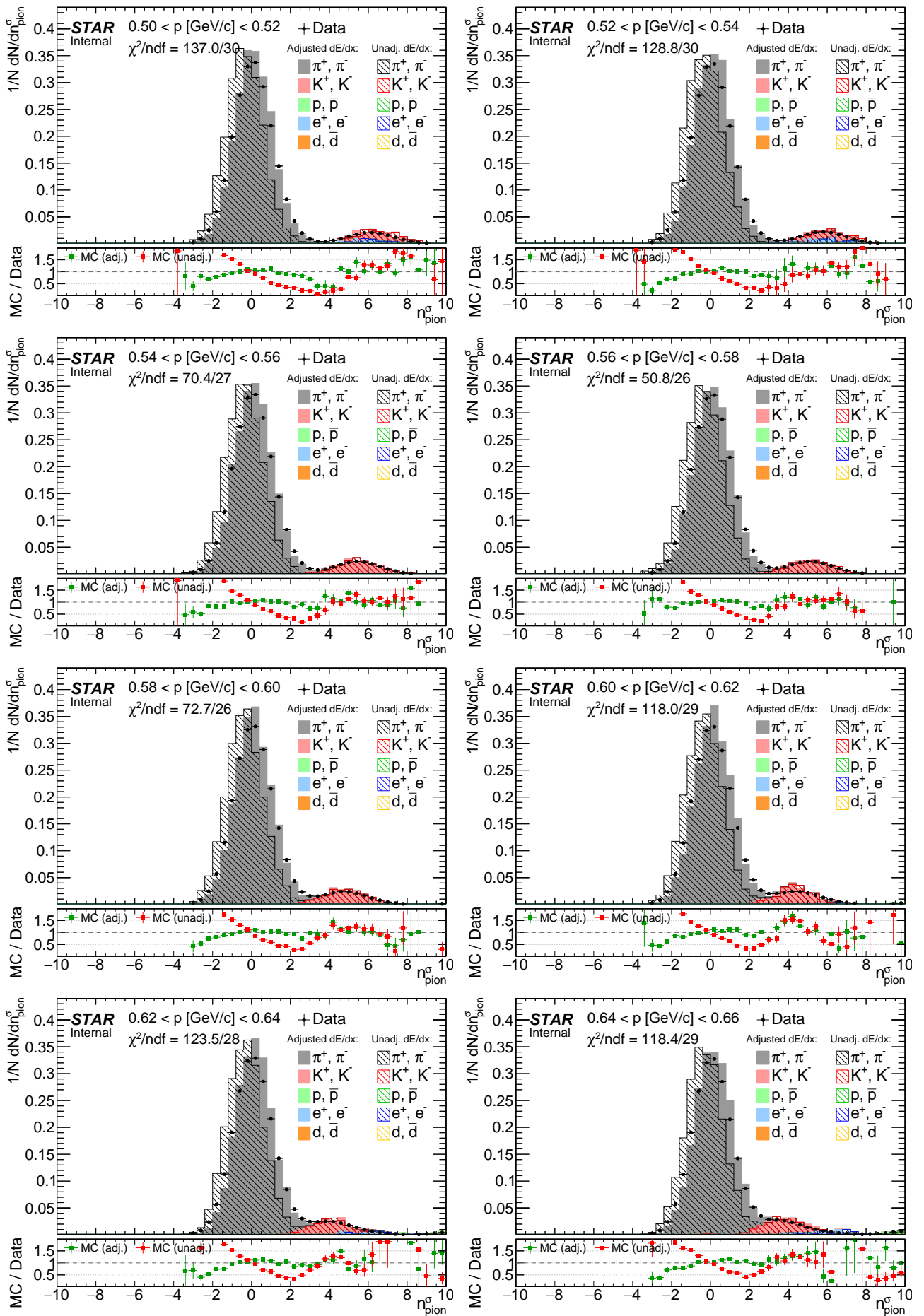
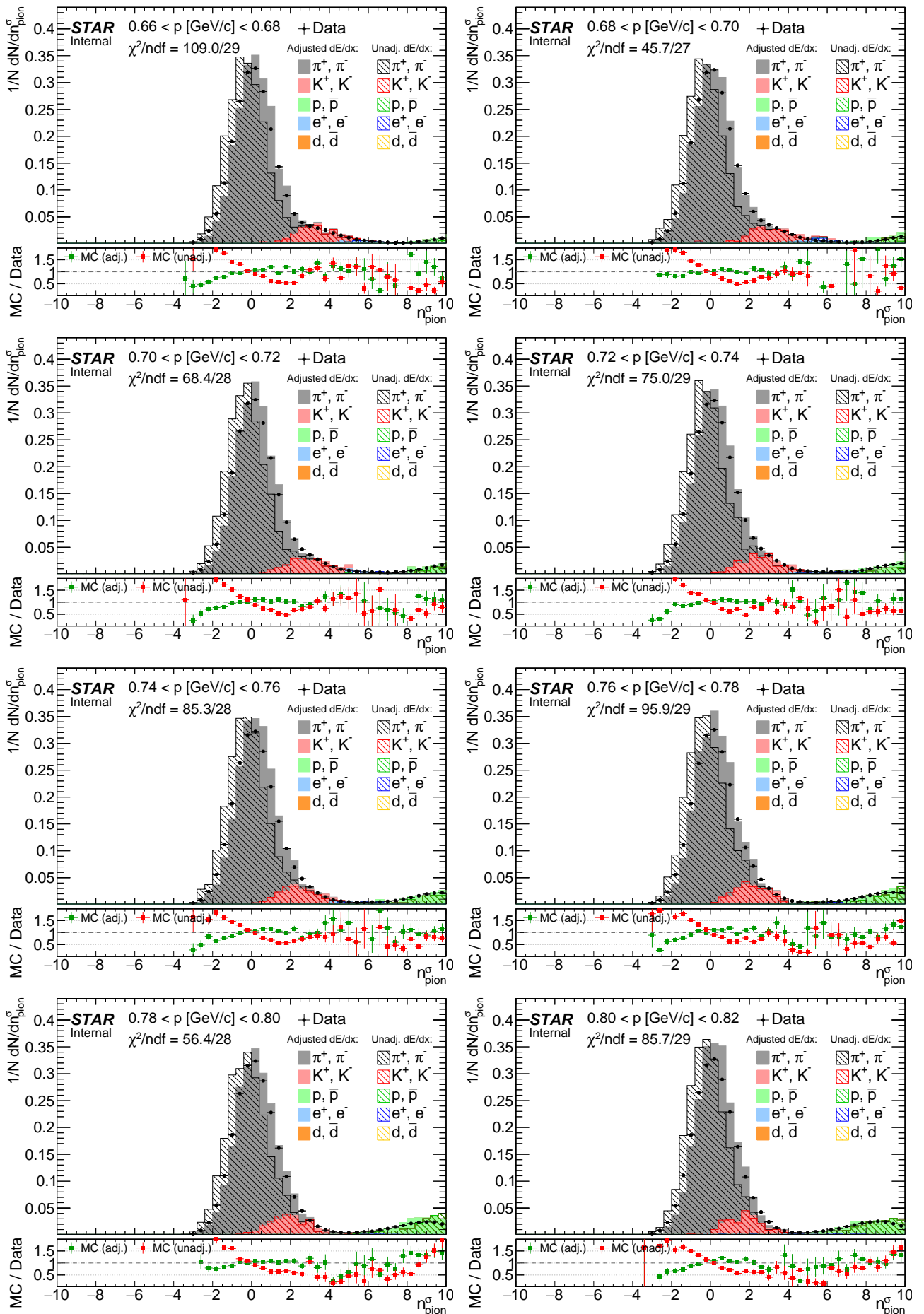


Figure F.3: Comparison of  $n_{\text{pion}}^{\sigma}$  distribution between data and embedded MC (before and after  $dE/dx$  adjustment) in momentum bins.









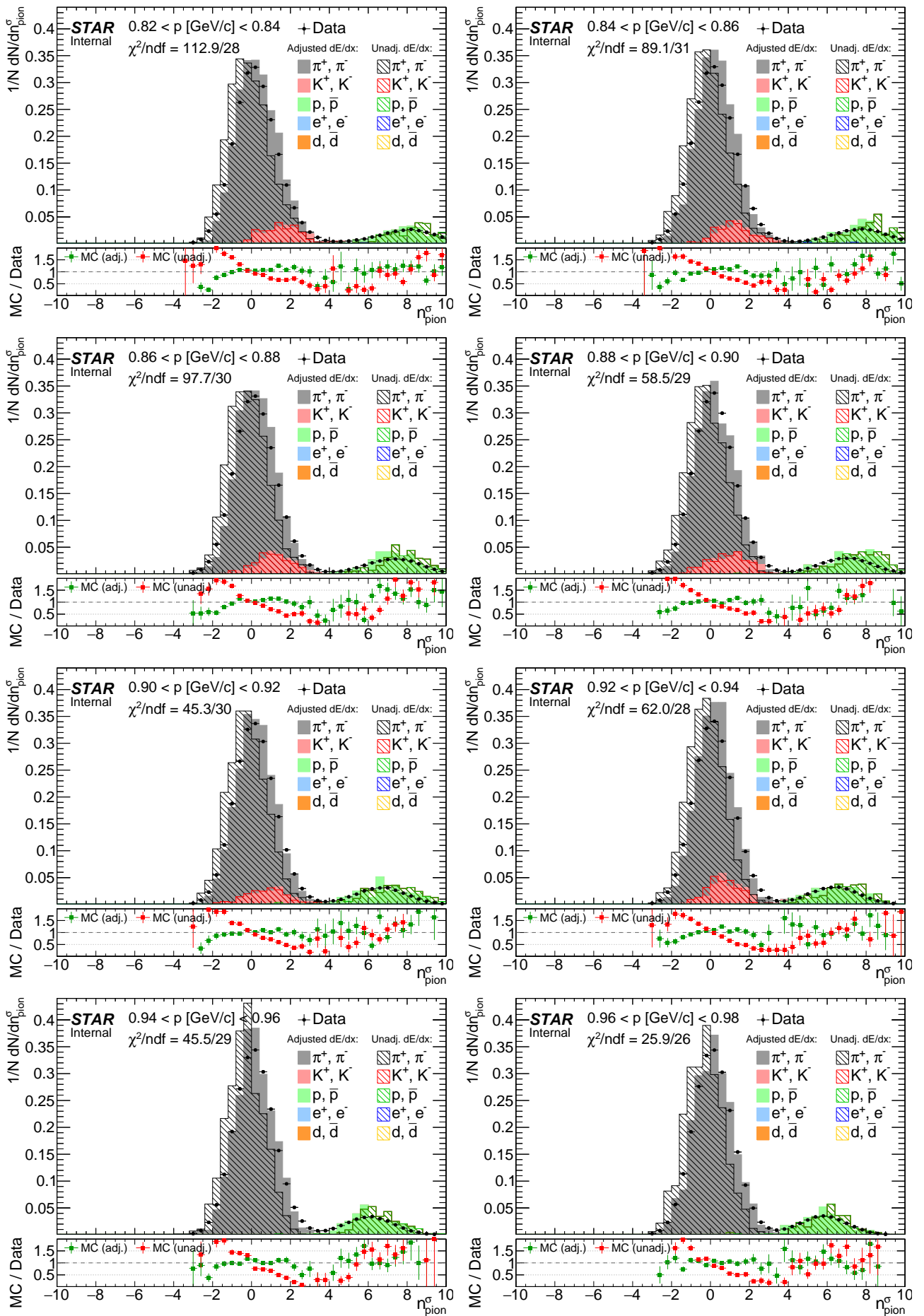
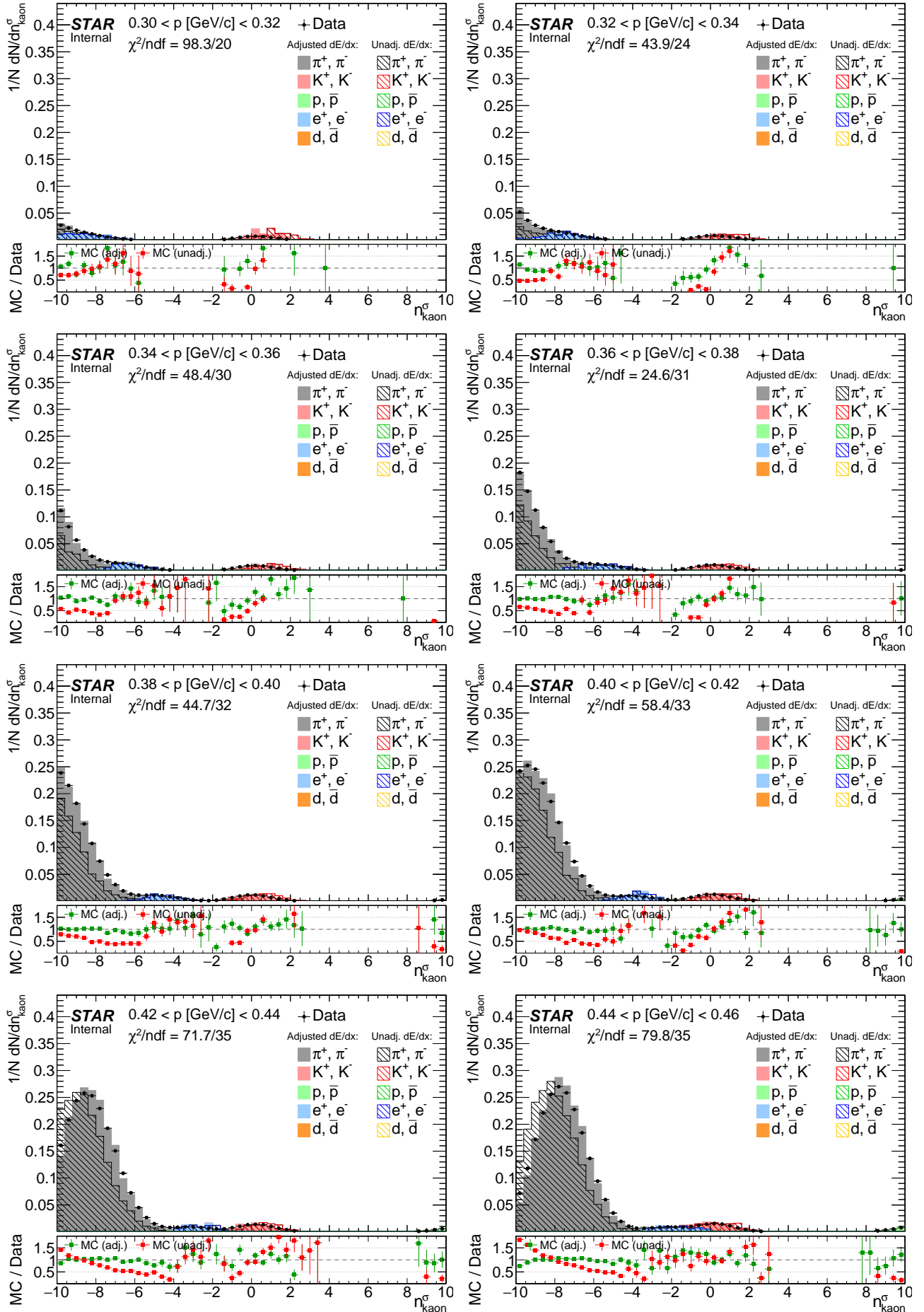
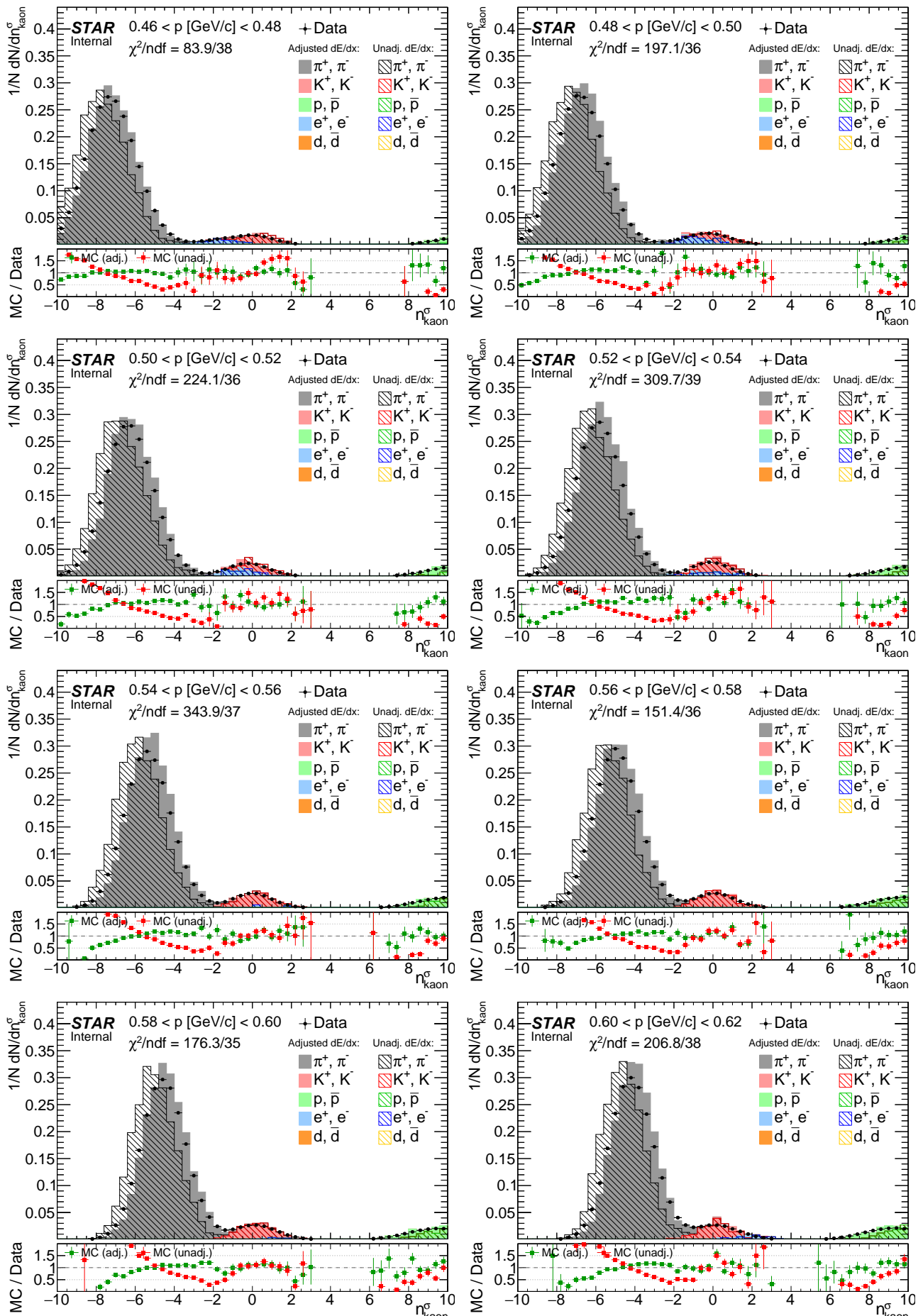
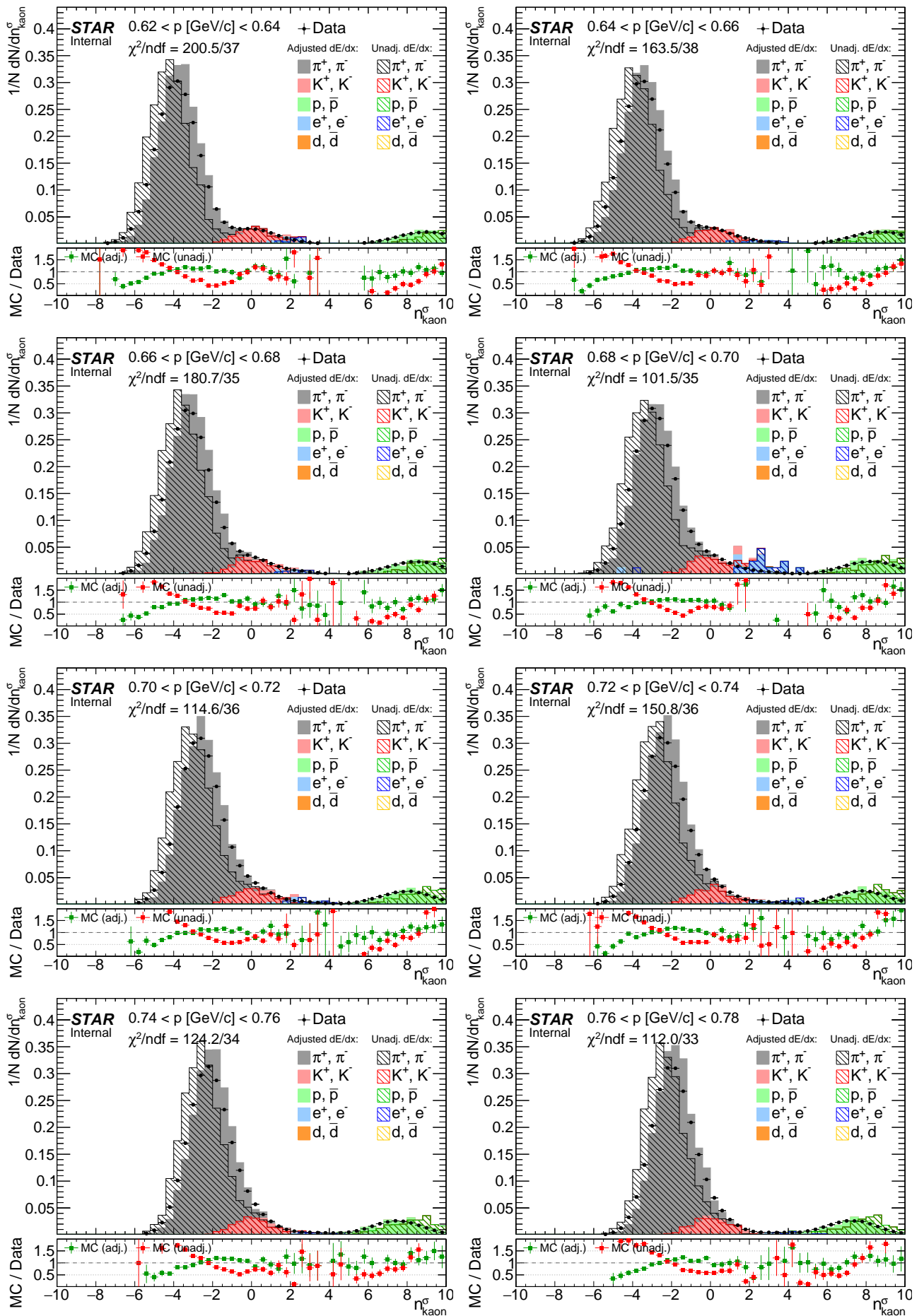
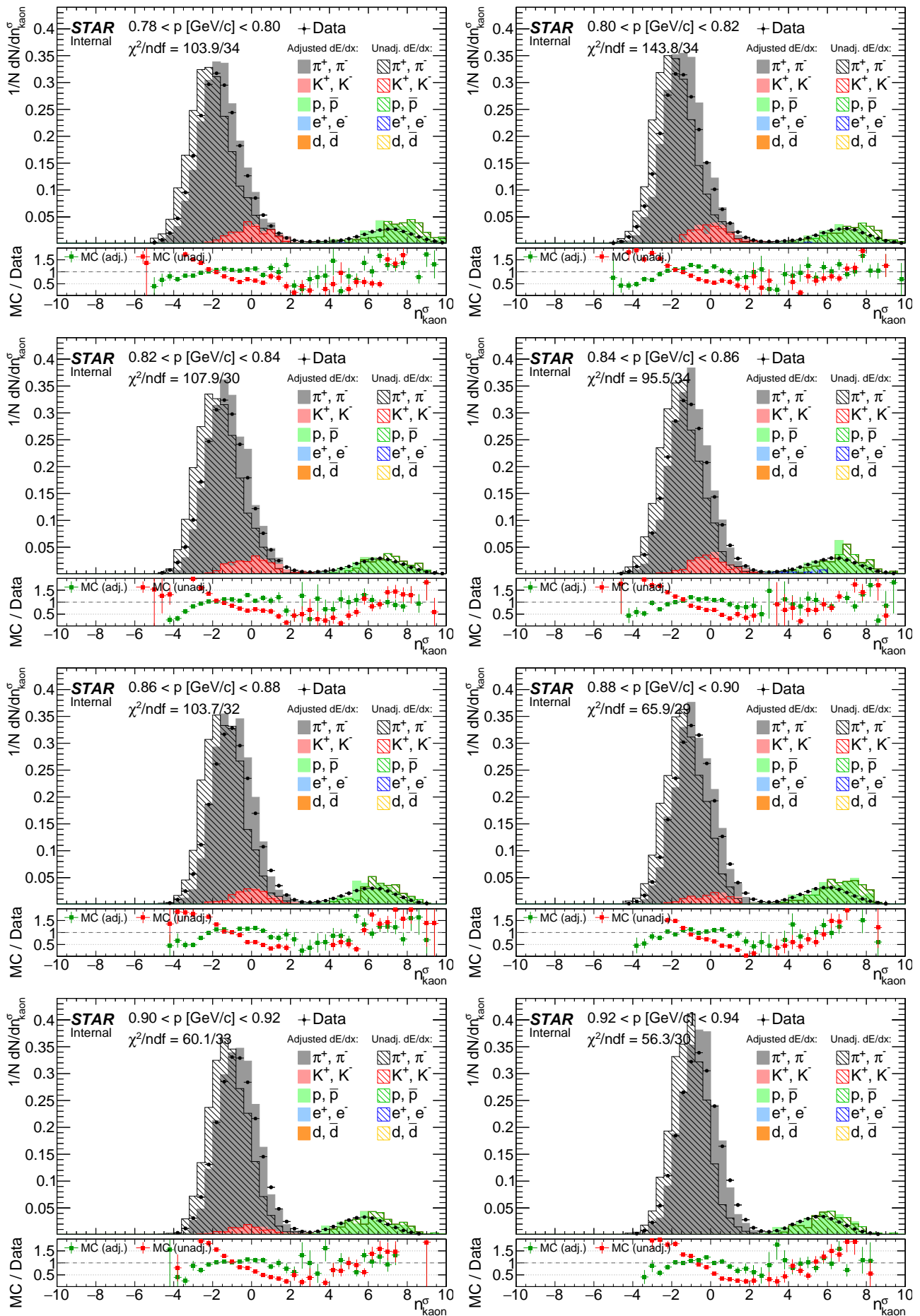


Figure F.4: Comparison of  $n_{\text{kaon}}^{\sigma}$  distribution between data and embedded MC (before and after  $dE/dx$  adjustment) in momentum bins.









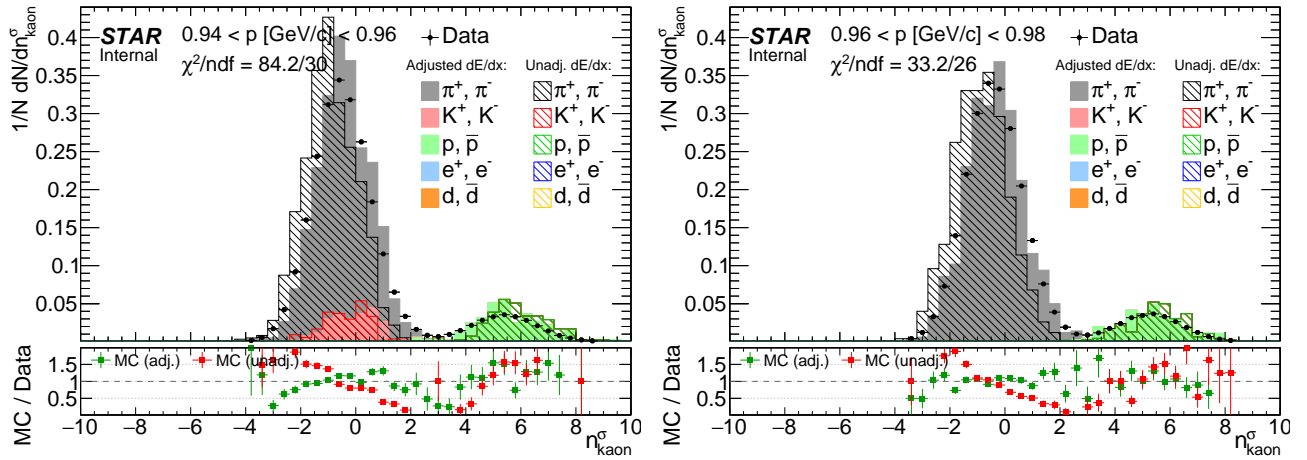
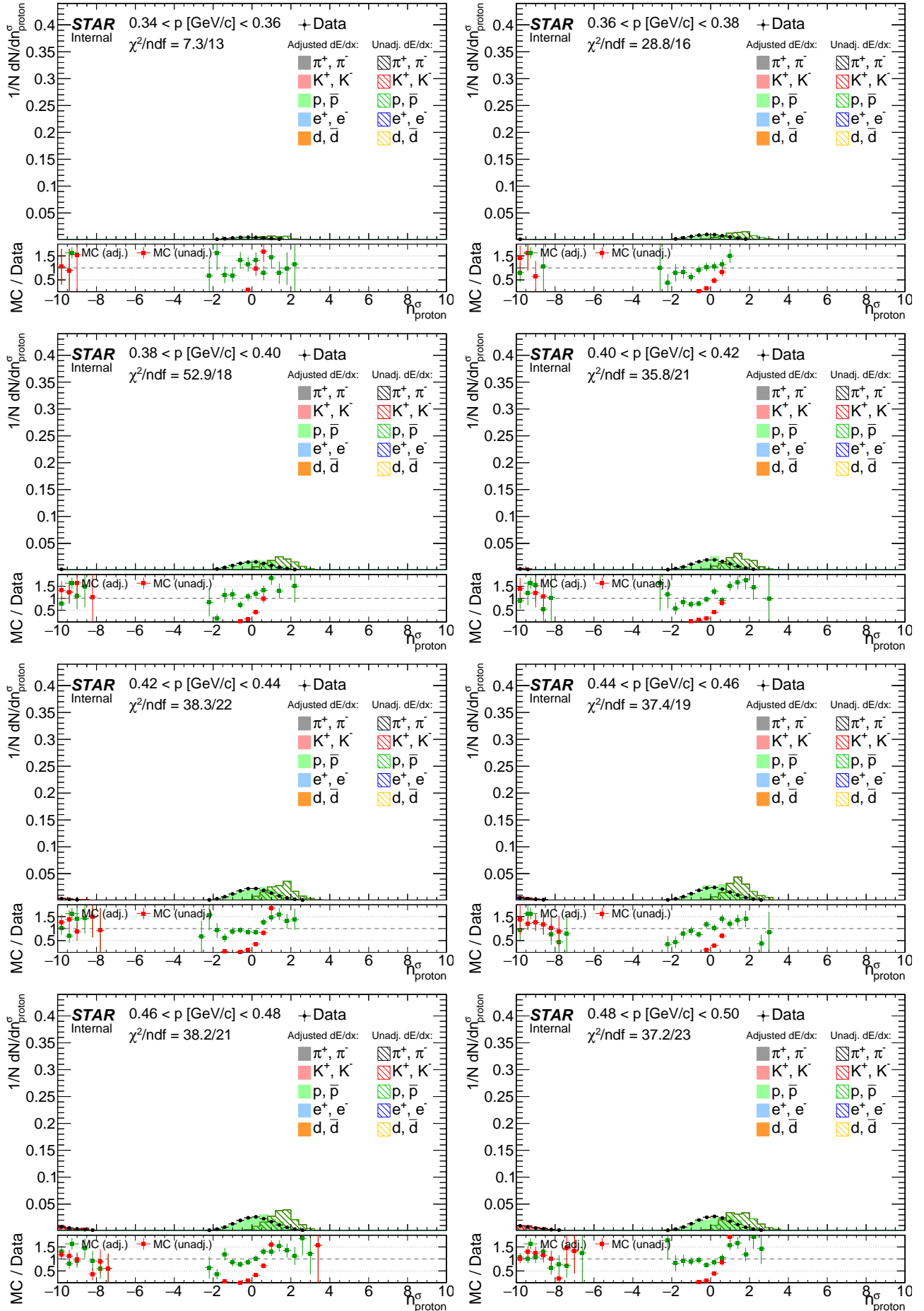
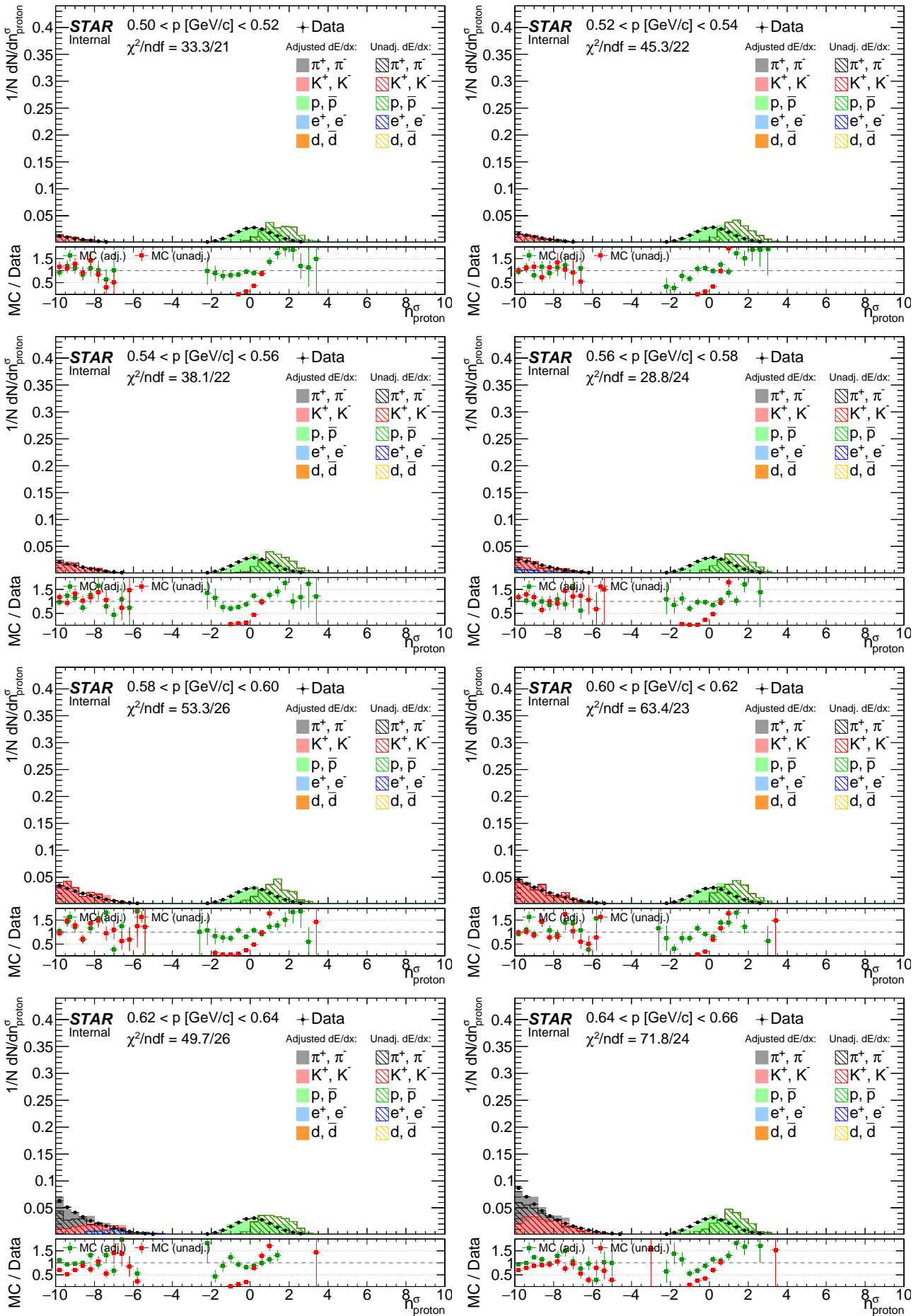
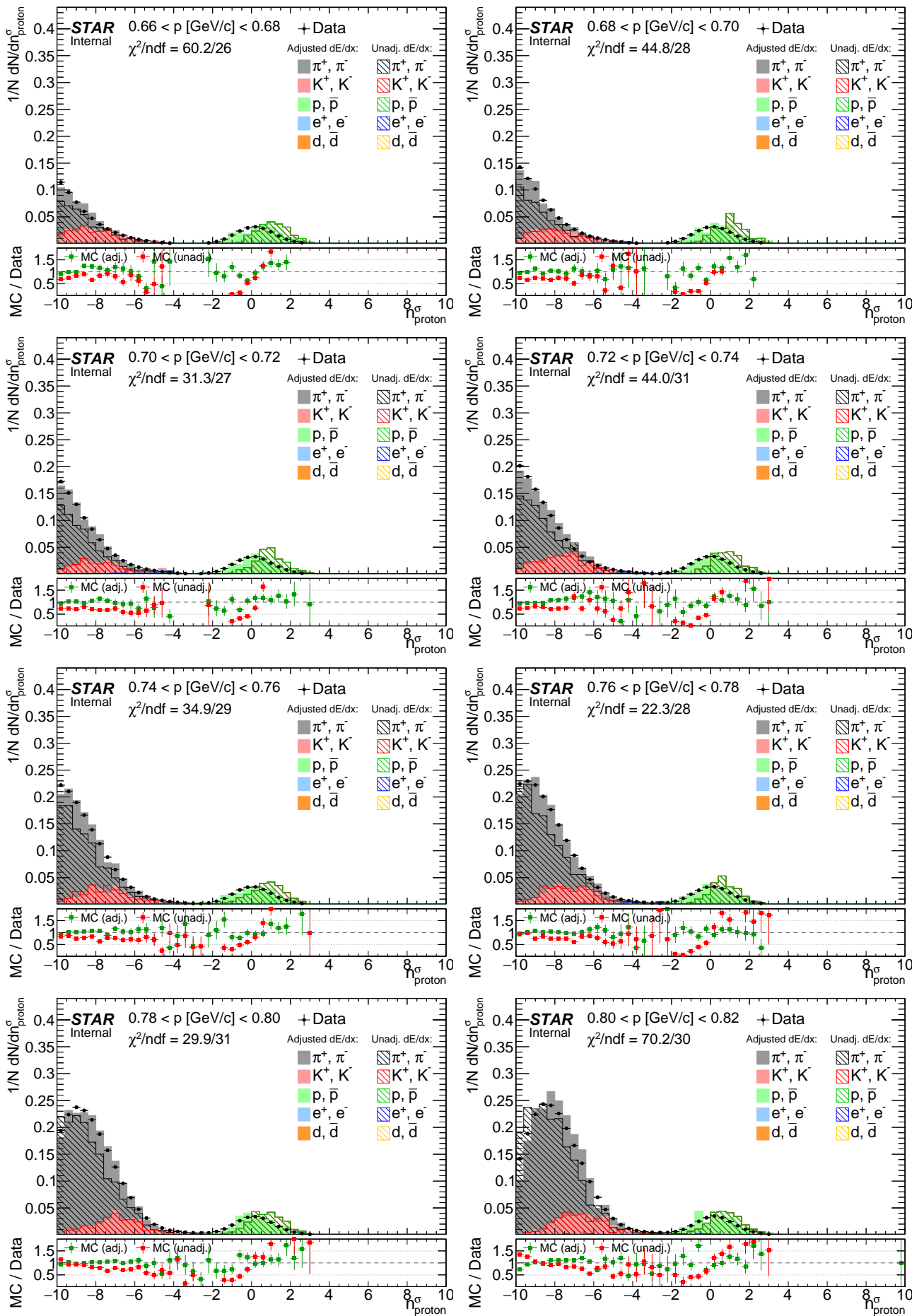
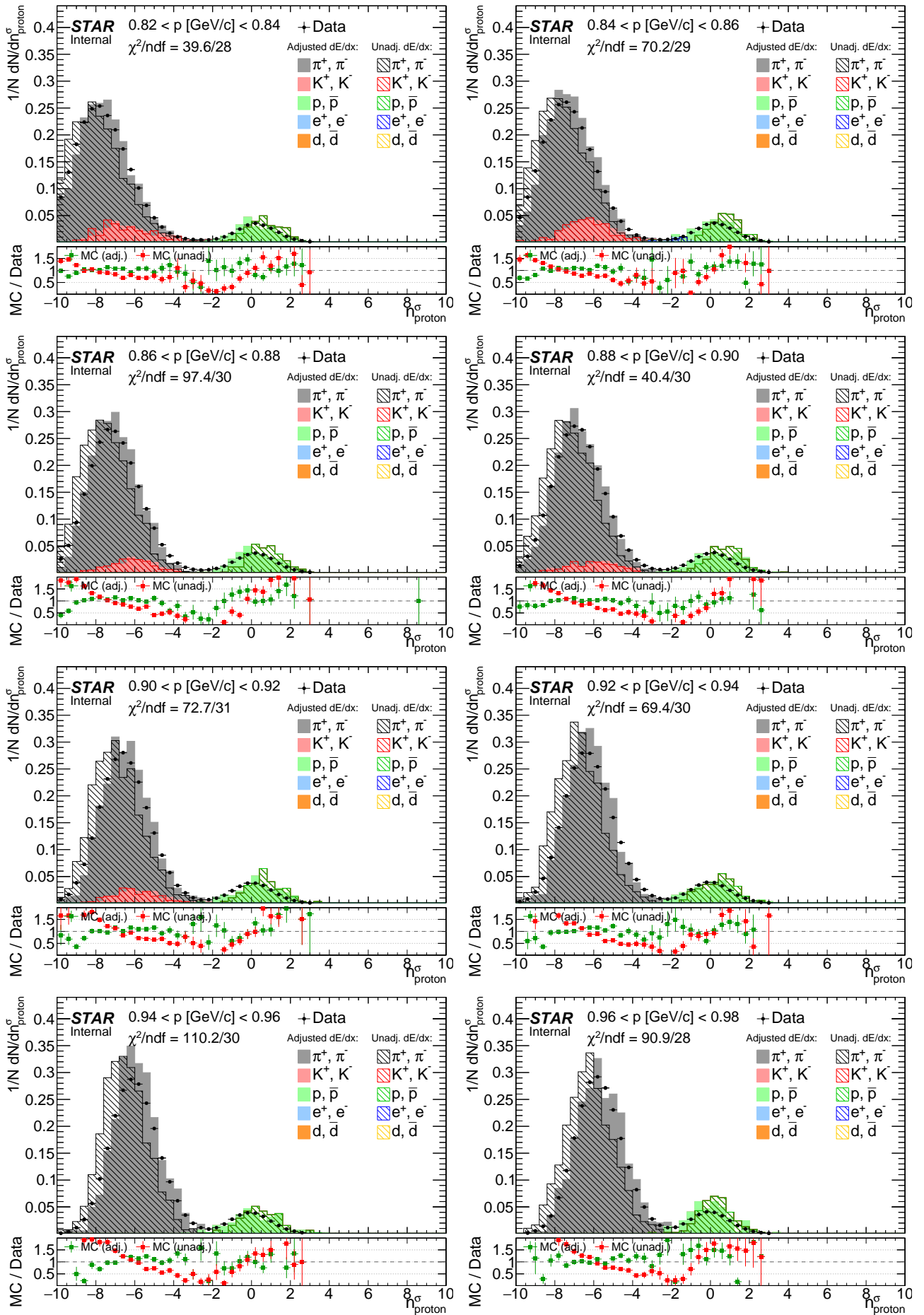


Figure F.5: Comparison of  $n_{\text{proton}}^{\sigma}$  distribution between data and embedded MC (before and after  $dE/dx$  adjustment) in momentum bins.









# Appendix G

## Tag&Probe fits for TOF hit reconstruction and matching efficiency

Figure G.1: Total transverse momentum  $p_T^{\text{miss}}$  of the  $p+\text{Tag}+\text{Probe}+p$  system in the data and signal+background embedded MC, in bins of  $p_T$  of a probe. Adjacent plots are for the same  $p_T$  bin, one for data (left) and the other for MC (right).

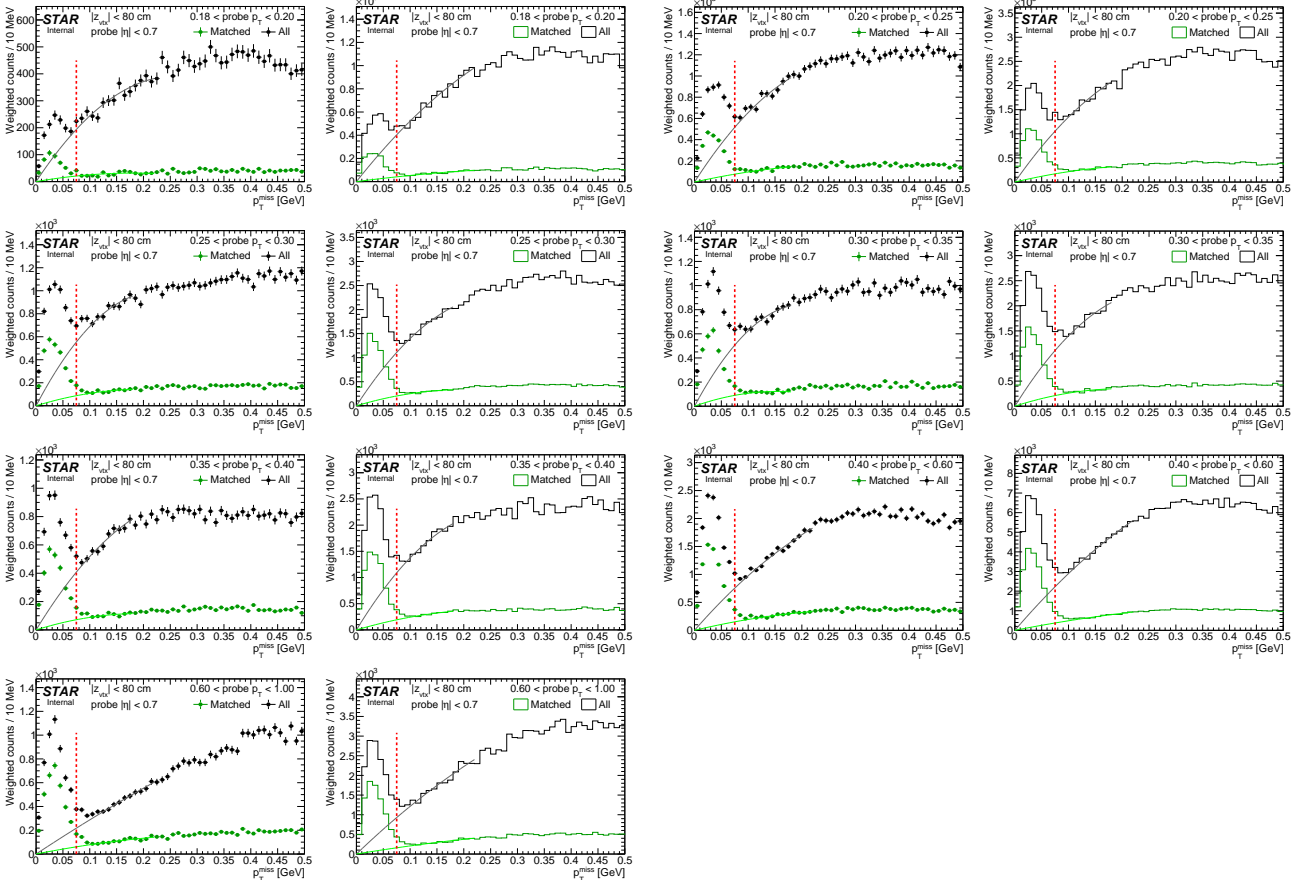
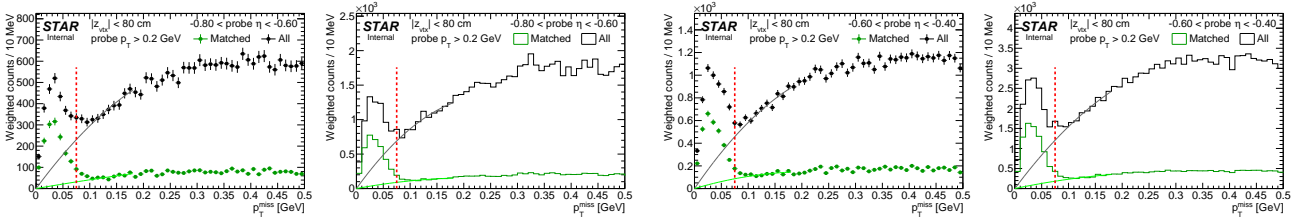


Figure G.2: Total transverse momentum  $p_T^{\text{miss}}$  of the  $p+\text{Tag}+\text{Probe}+p$  system in the data and signal+background embedded MC, in bins of  $\eta$  of a probe. Adjacent plots are for the same  $\eta$  bin, one for data (left) and the other for MC (right).



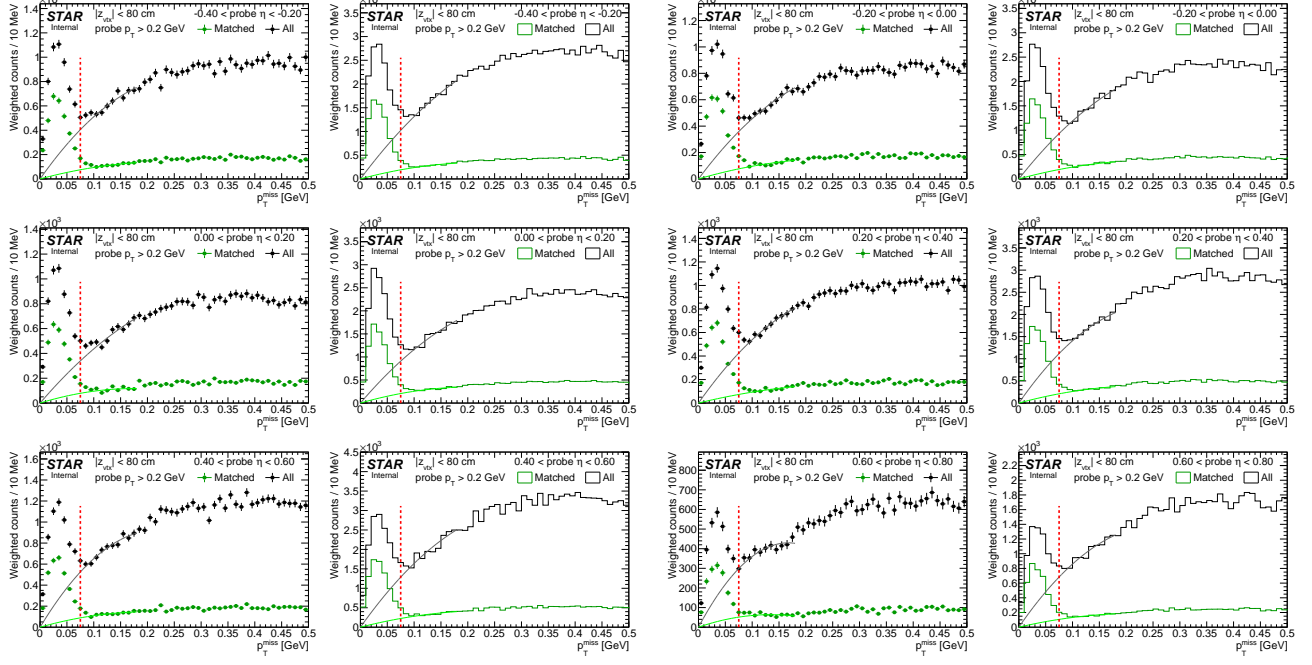


Figure G.3: Total transverse momentum  $p_T^{\text{miss}}$  of the  $p+\text{Tag}+\text{Probe}+p$  system in the data and signal+background embedded MC, in bins of  $z_{\text{vtx}}$  of a probe. Adjacent plots are for the same  $z_{\text{vtx}}$  bin, one for data (left) and the other for MC (right).

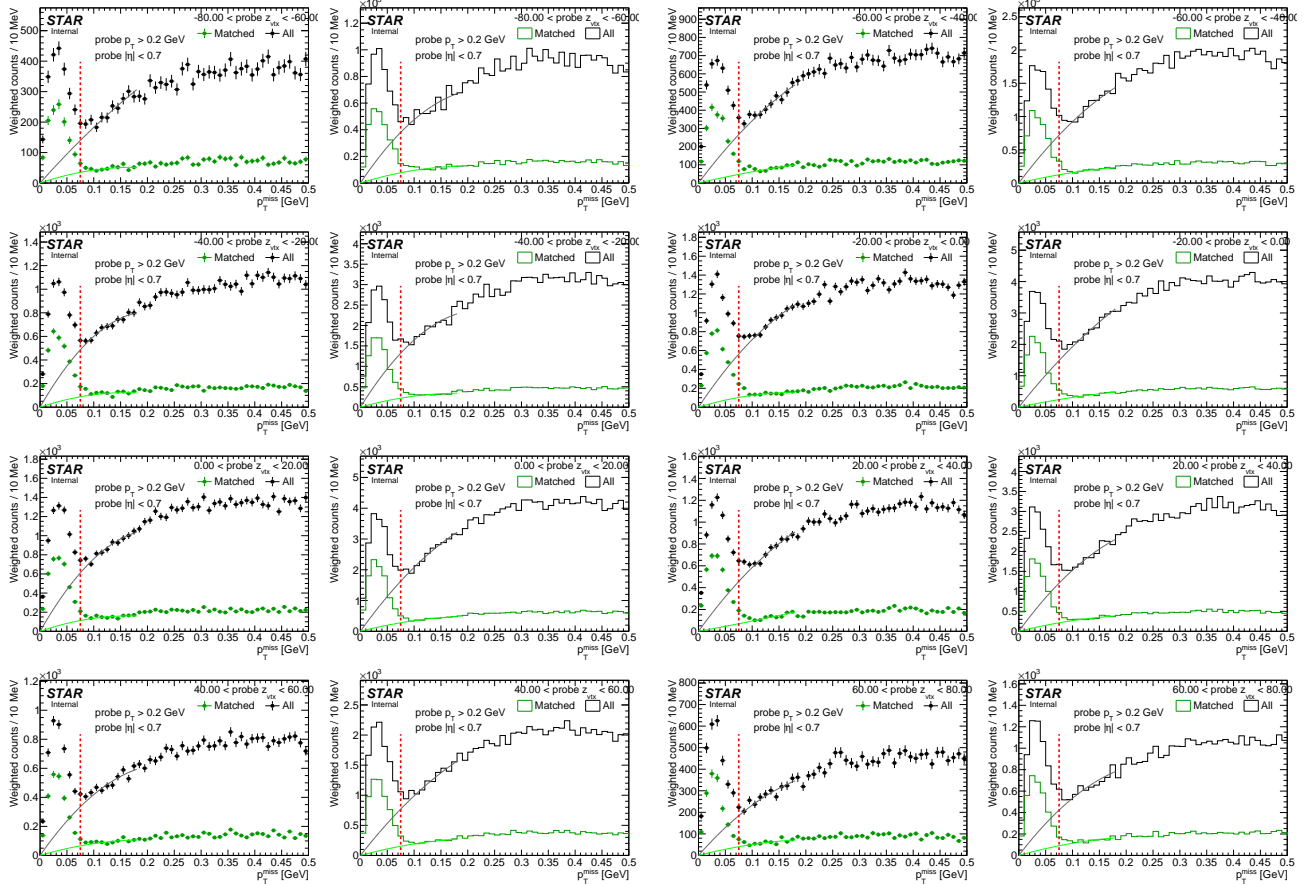


Figure G.4: Total transverse momentum  $p_T^{\text{miss}}$  of the  $p$ +Tag+Probe+ $p$  system in the data and signal+background embedded MC, in bins of  $p_T$  of a probe for probe pseudorapidity range  $-0.7 < \eta < -0.3$ . Adjacent plots are for the same  $p_T$  bin, one for data (left) and the other for MC (right).

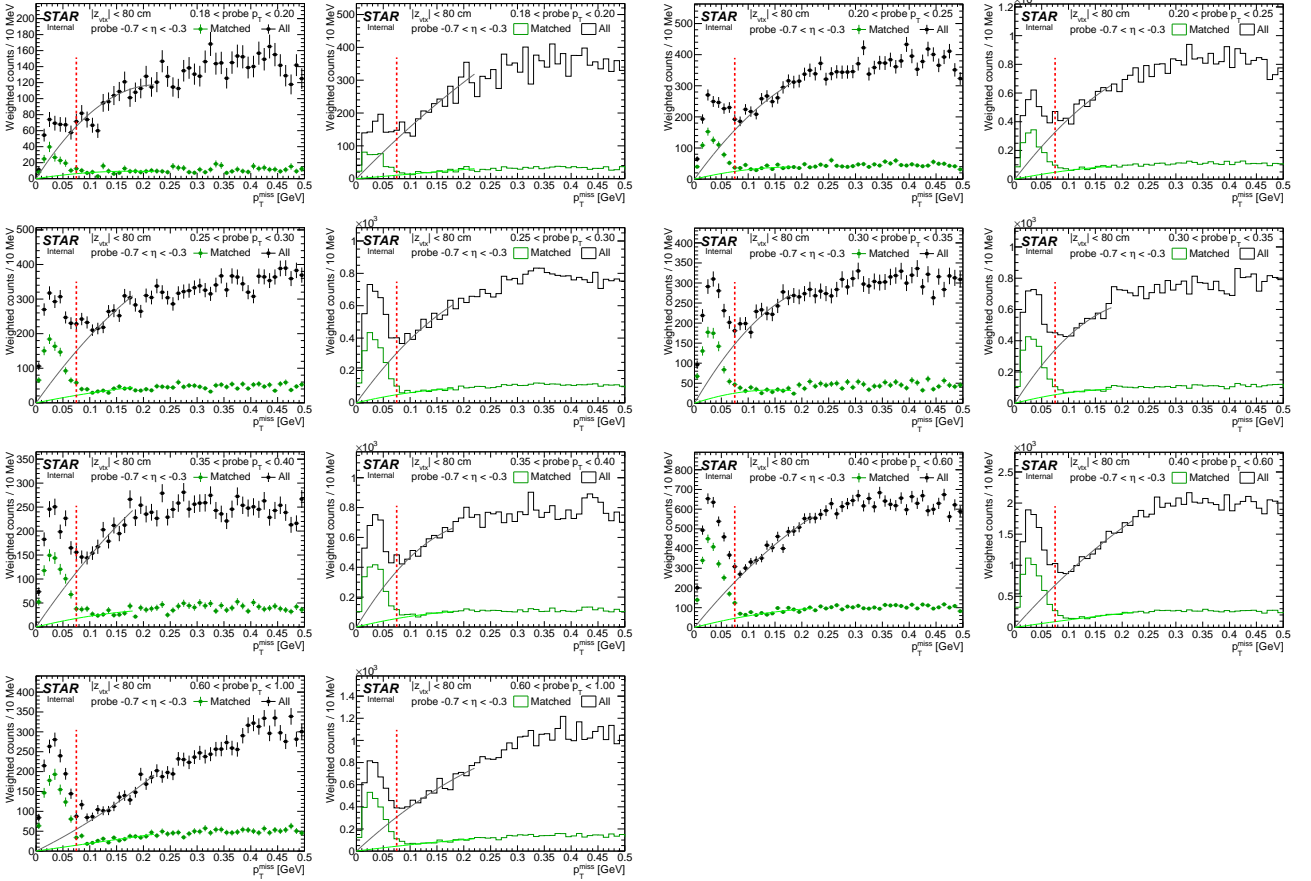
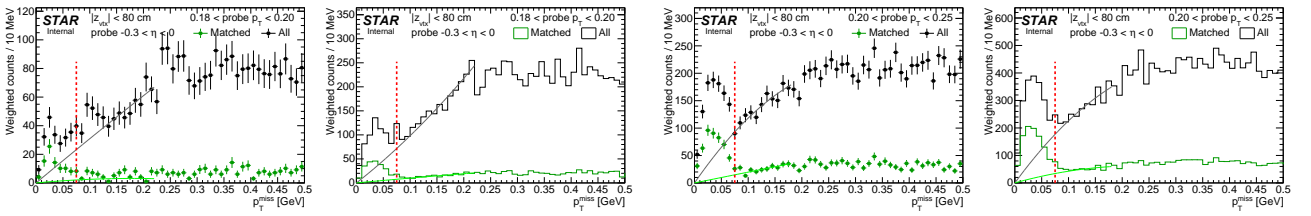


Figure G.5: Total transverse momentum  $p_T^{\text{miss}}$  of the  $p$ +Tag+Probe+ $p$  system in the data and signal+background embedded MC, in bins of  $p_T$  of a probe for probe pseudorapidity range  $-0.3 < \eta < 0$ . Adjacent plots are for the same  $p_T$  bin, one for data (left) and the other for MC (right).



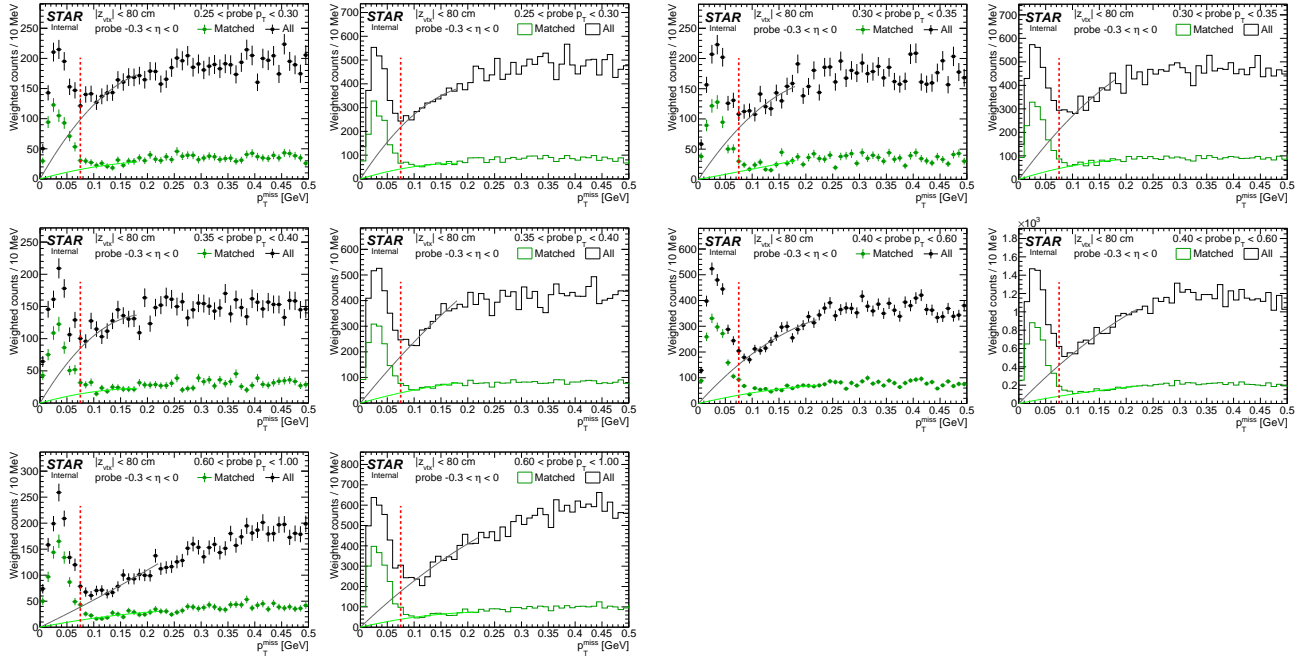


Figure G.6: Total transverse momentum  $p_T^{\text{miss}}$  of the  $p+\text{Tag}+\text{Probe}+p$  system in the data and signal+background embedded MC, in bins of  $p_T$  of a probe for probe pseudorapidity range  $0 < \eta < 0.3$ . Adjacent plots are for the same  $p_T$  bin, one for data (left) and the other for MC (right).

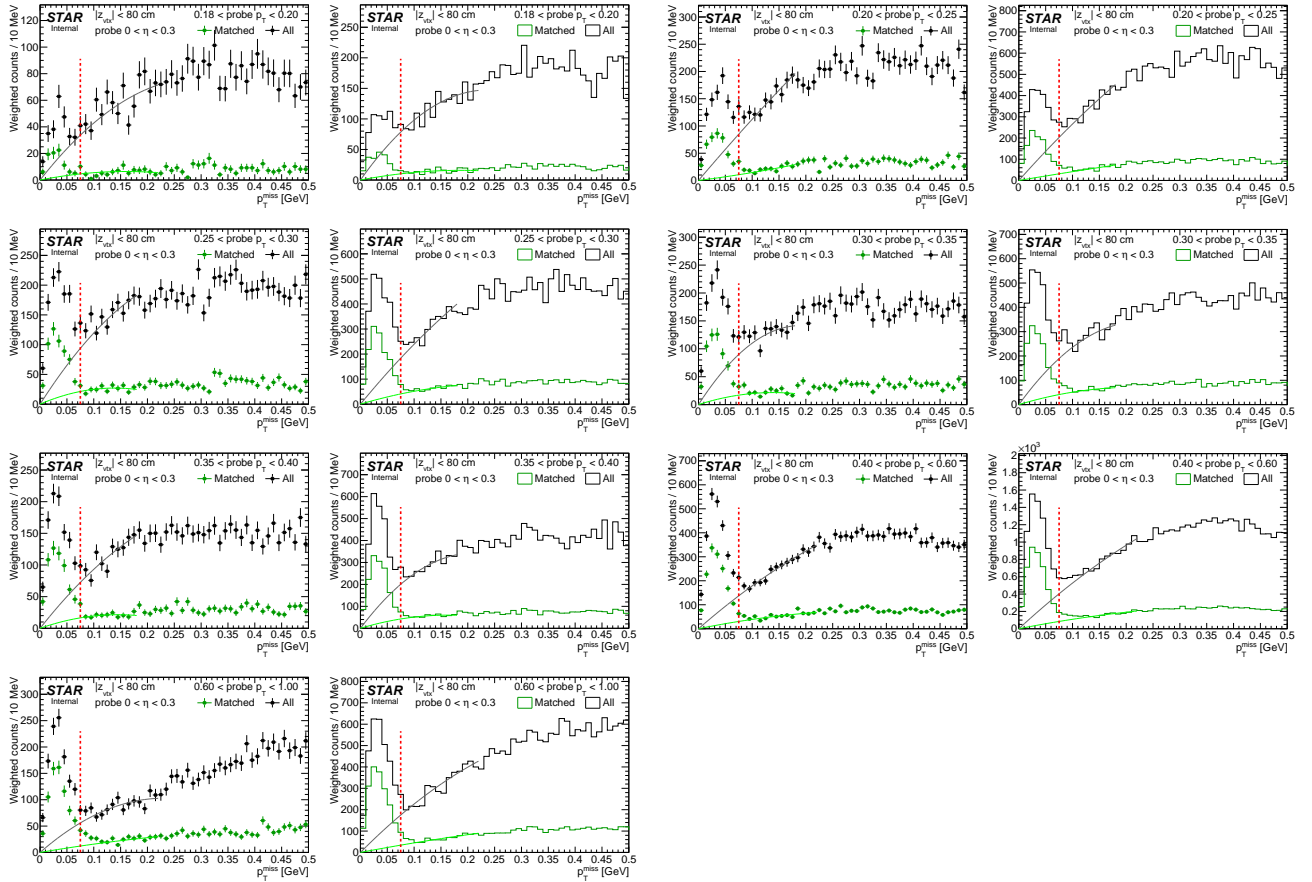
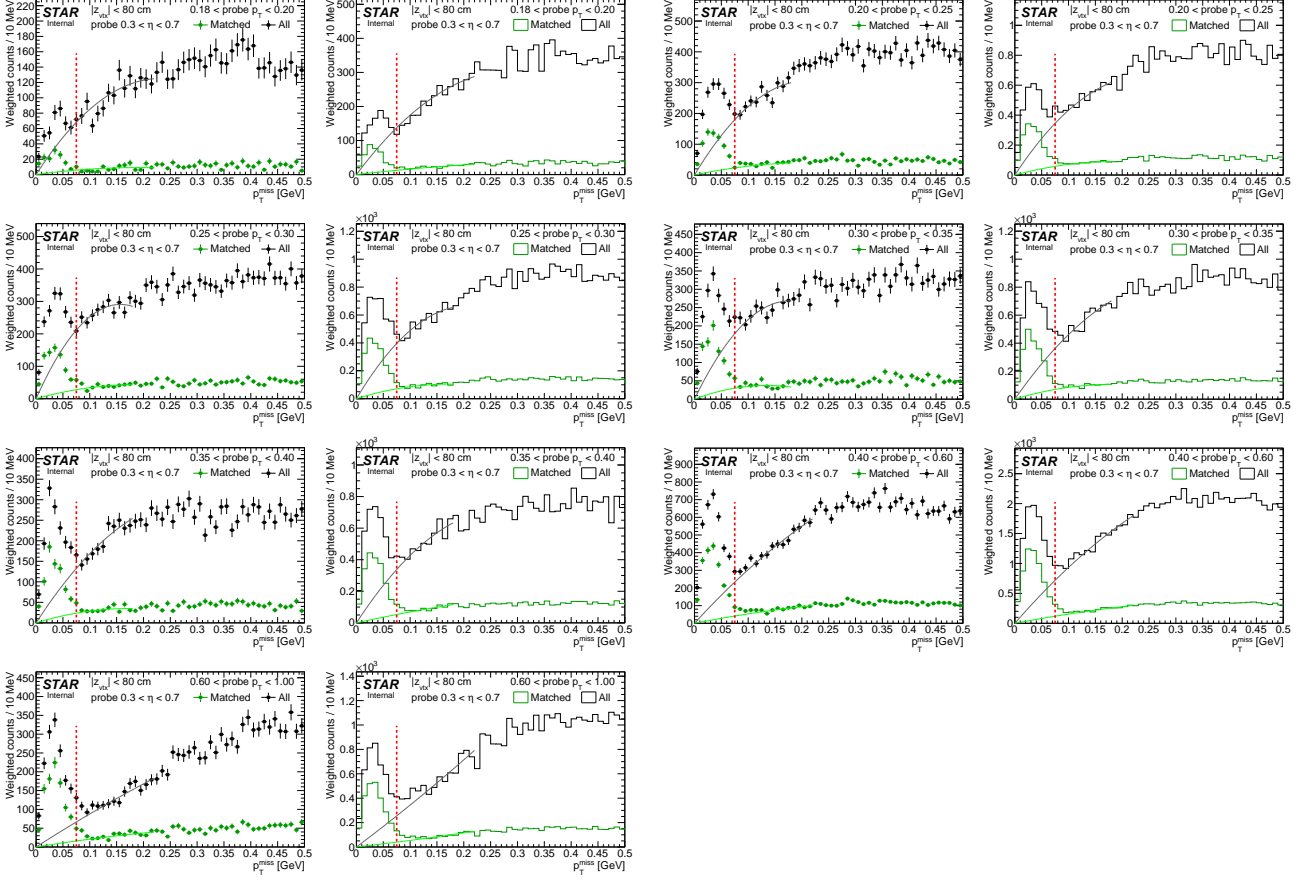


Figure G.7: Total transverse momentum  $p_T^{\text{miss}}$  of the  $p$ +Tag+Probe+ $p$  system in the data and signal+background embedded MC, in bins of  $p_T$  of a probe for probe pseudorapidity range  $0.3 < \eta < 0.7$ . Adjacent plots are for the same  $p_T$  bin, one for data (left) and the other for MC (right).



# Appendix H

## RP track reconstruction efficiency comparison between data and MC

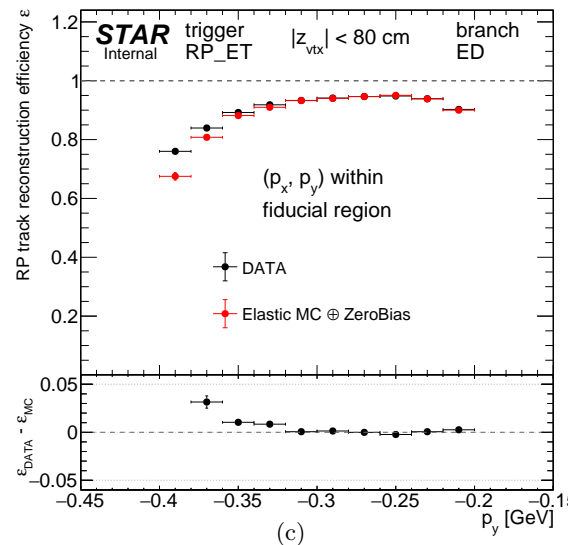
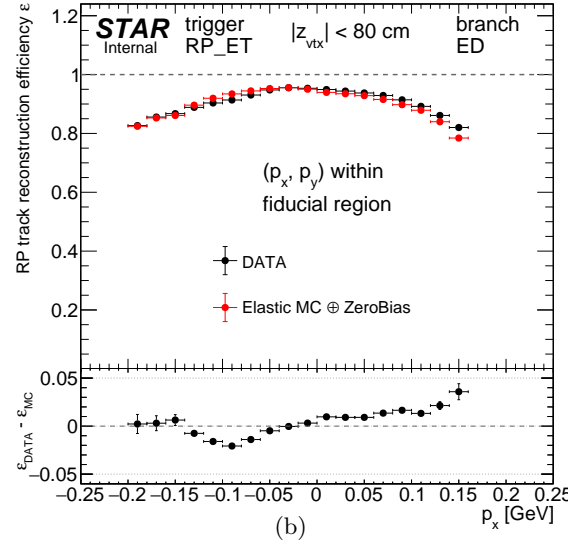
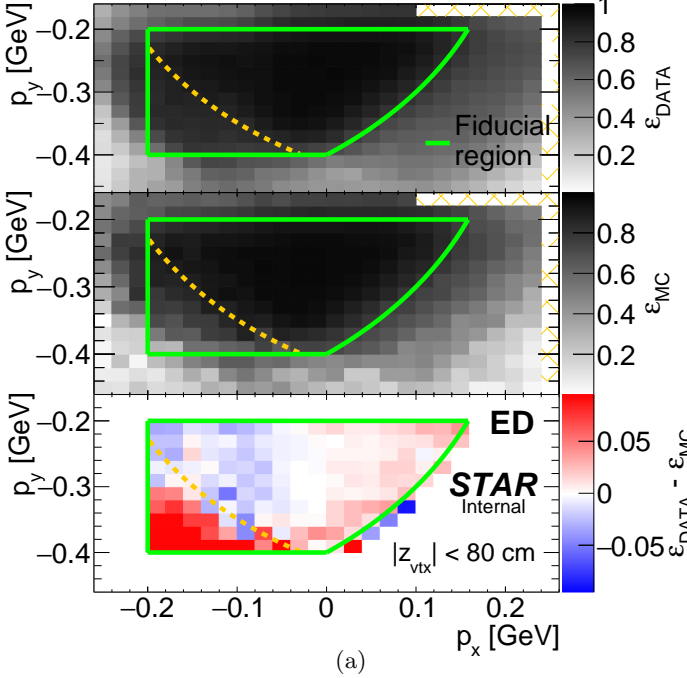


Figure H.1: Comparison of RP track reconstruction efficiency in branch ED estimated with the method described in Sec. 10.3.1 as a function of  $(p_x, p_y)$  of proton track (H.1a) and comparison of 1-dimensional projections of efficiencies in a fiducial region marked with green envelope:  $p_x$  (H.1b) and  $p_y$  (H.1c). Lower pad in each subfigure shows the difference between efficiency extracted from the data and elastic scattering MC embedded into zero-bias data. Hatched orange area marks bins without any entries (efficiency incalculable).

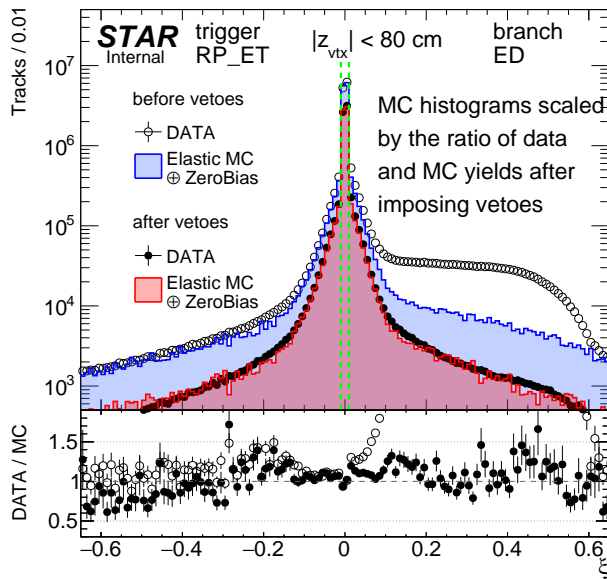
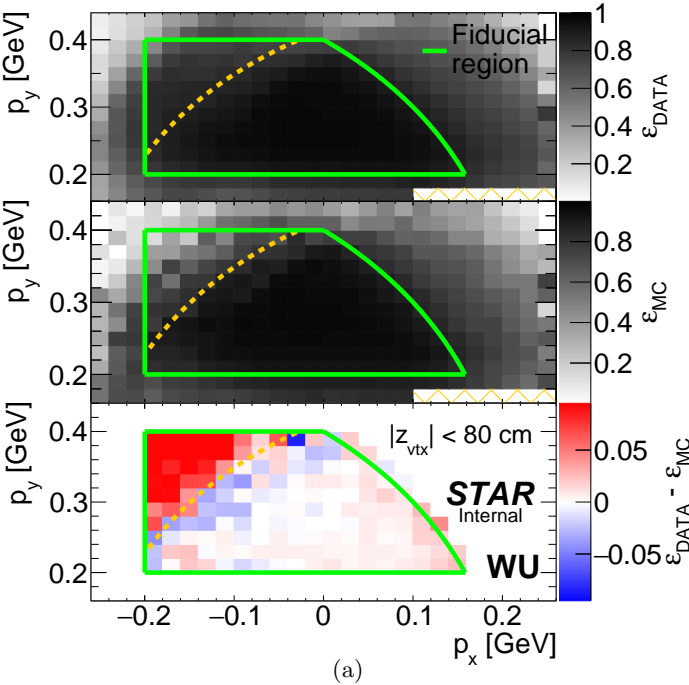
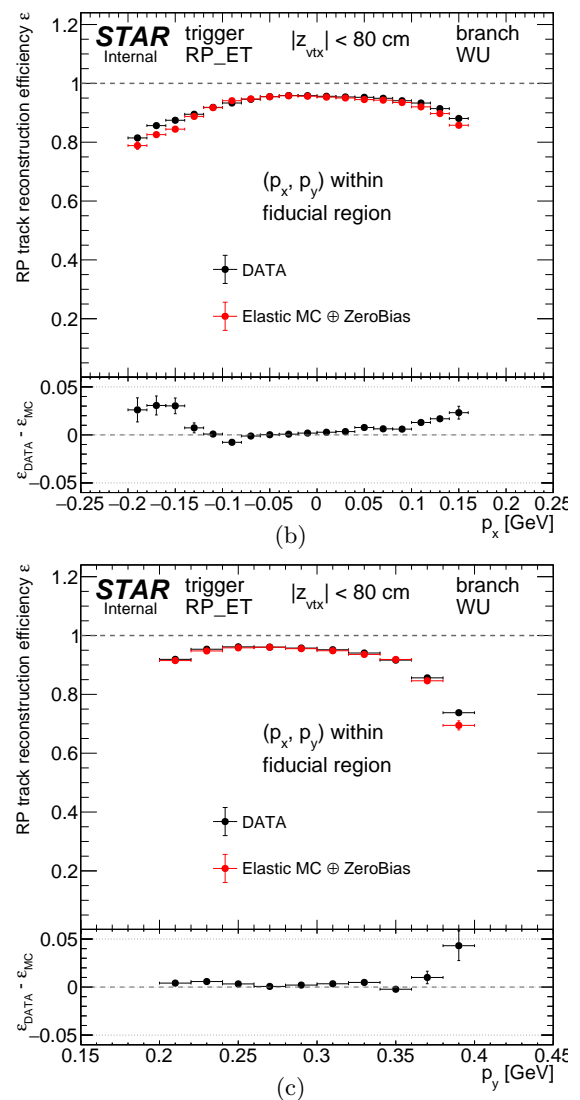


Figure H.2: Fractional momentum loss  $\xi$  of clean proton tracks in branch ED before and after implying vetoes. Data are represented by opened and filled circles, while elastic MC embedded into zero-bias data is drawn as filled histograms. MC histograms are scaled by the ratio of data and MC yields after imposing vetoes in other STAR detector subsystems. Lower pad shows the ratio of corresponding distributions in the data and MC. Dashed green vertical lines show the  $\xi$  range of tracks accepted for the RP track (and also track point) efficiency studies,  $|\xi| < 0.01$ .



(a)

Figure H.3: Comparison of RP track reconstruction efficiency in branch WU estimated with the method described in Sec. 10.3.1 as a function of  $(p_x, p_y)$  of proton track (H.3a) and comparison of 1-dimensional projections of efficiencies in a fiducial region marked with green envelope:  $p_x$  (H.3b) and  $p_y$  (H.3c). Lower pad in each subfigure shows the difference between efficiency extracted from the data and elastic scattering MC embedded into zero-bias data. Hatched orange area marks bins without any entries (efficiency incalculable).



(c)

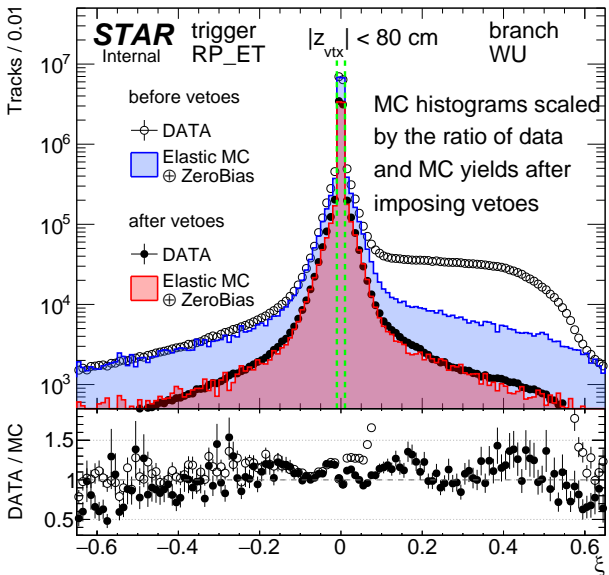
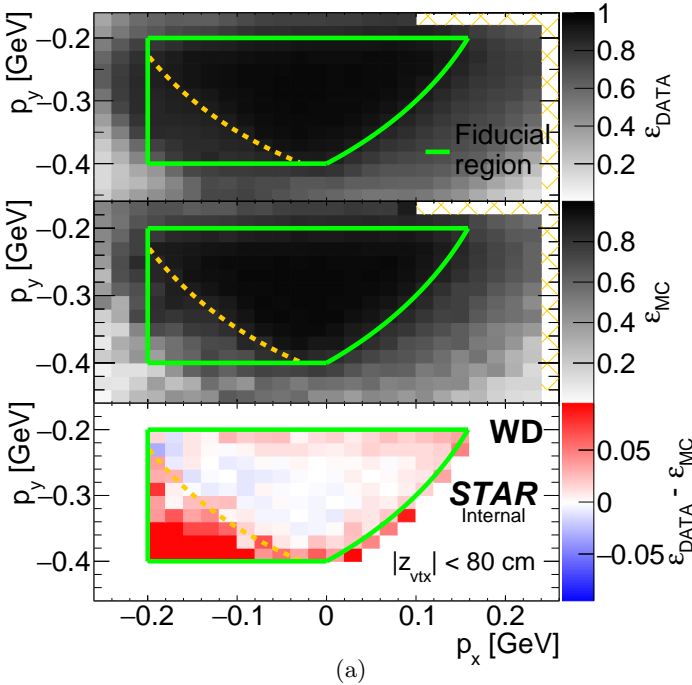
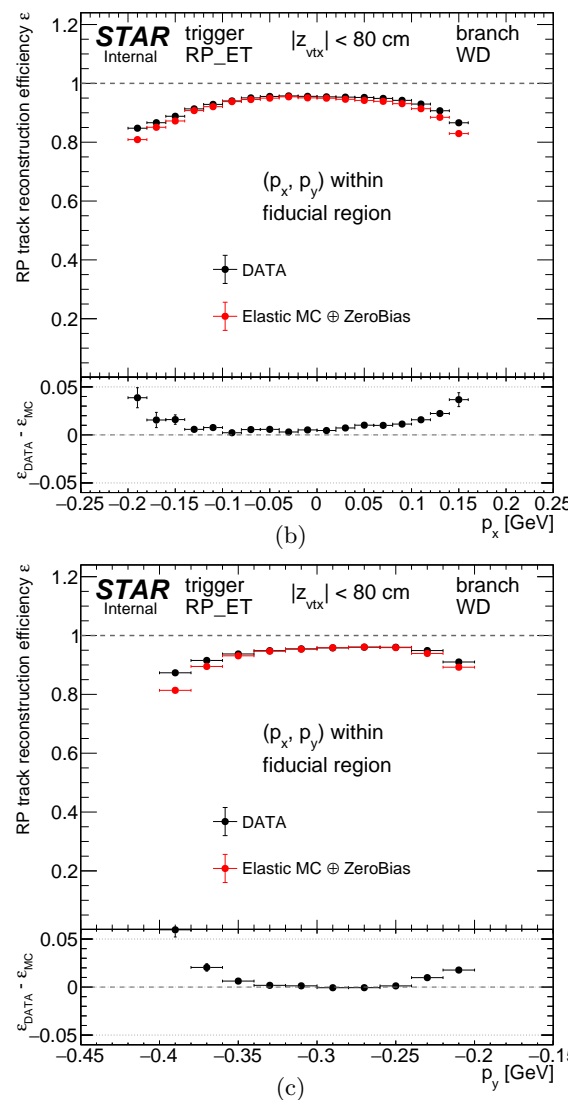


Figure H.4: Fractional momentum loss  $\xi$  of clean proton tracks in branch WU before and after implying vetoes. Data are represented by opened and filled circles, while elastic MC embedded into zero-bias data is drawn as filled histograms. MC histograms are scaled by the ratio of data and MC yields after imposing vetoes in other STAR detector subsystems. Lower pad shows the ratio of corresponding distributions in the data and MC. Dashed green vertical lines show the  $\xi$  range of tracks accepted for the RP track (and also track point) efficiency studies,  $|\xi| < 0.01$ .



(a)

Figure H.5: Comparison of RP track reconstruction efficiency in branch WD estimated with the method described in Sec. 10.3.1 as a function of  $(p_x, p_y)$  of proton track (H.5a) and comparison of 1-dimensional projections of efficiencies in a fiducial region marked with green envelope:  $p_x$  (H.5b) and  $p_y$  (H.5c). Lower pad in each subfigure shows the difference between efficiency extracted from the data and elastic scattering MC embedded into zero-bias data. Hatched orange area marks bins without any entries (efficiency incalculable).



(b)

(c)

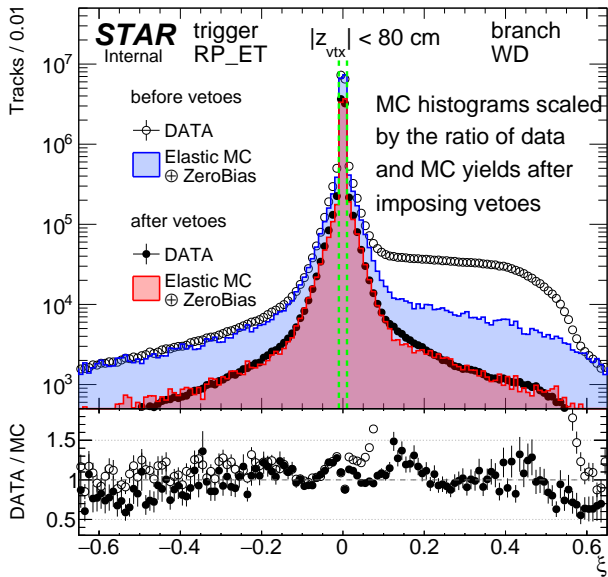


Figure H.6: Fractional momentum loss  $\xi$  of clean proton tracks in branch WD before and after implying vetoes. Data are represented by opened and filled circles, while elastic MC embedded into zero-bias data is drawn as filled histograms. MC histograms are scaled by the ratio of data and MC yields after imposing vetoes in other STAR detector subsystems. Lower pad shows the ratio of corresponding distributions in the data and MC. Dashed green vertical lines show the  $\xi$  range of tracks accepted for the RP track (and also track point) efficiency studies,  $|\xi| < 0.01$ .

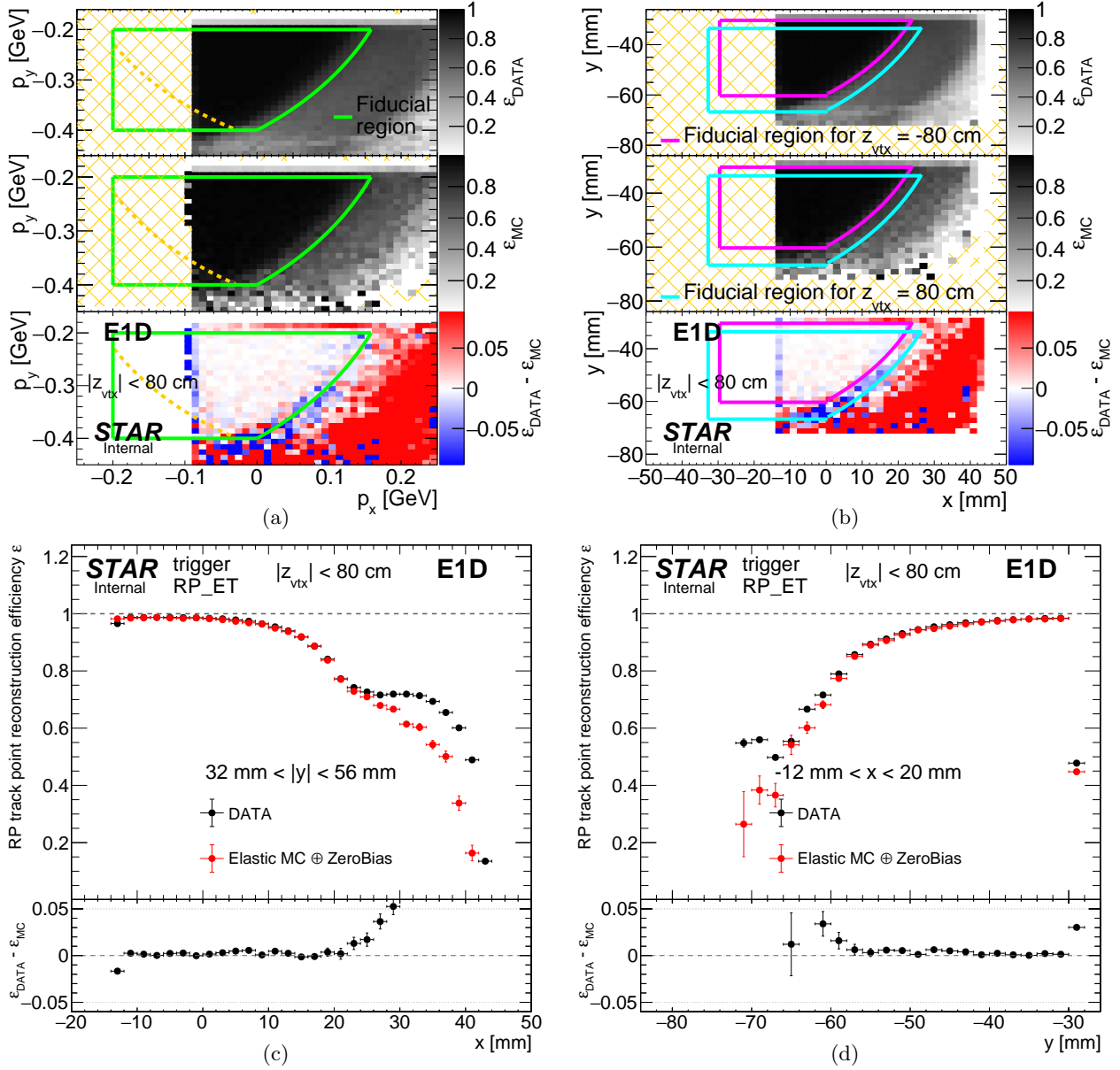


Figure H.7: Sample comparison of RP track point reconstruction efficiency (detector E1D) estimated with the method described in Sec. 10.3.2 as a function of  $(p_x, p_y)$  of proton track (H.7a),  $(x, y)$  position extrapolated from the reference RP (E2D) to the studied RP (H.7b), and comparison of 1-dimensional projections of efficiencies in selected ranges of hit position (given in the plot):  $x$  (H.7c) and  $y$  (H.7d). Lower pad in each subfigure shows the difference between efficiency extracted from the data and elastic scattering MC embedded into zero-bias data. Hatched orange area marks bins without any entries (efficiency incalculable). The fiducial region in  $(x, y)$  plot is represented by two envelopes which correspond to the extreme accepted values of  $z_{\text{vtx}}$ .

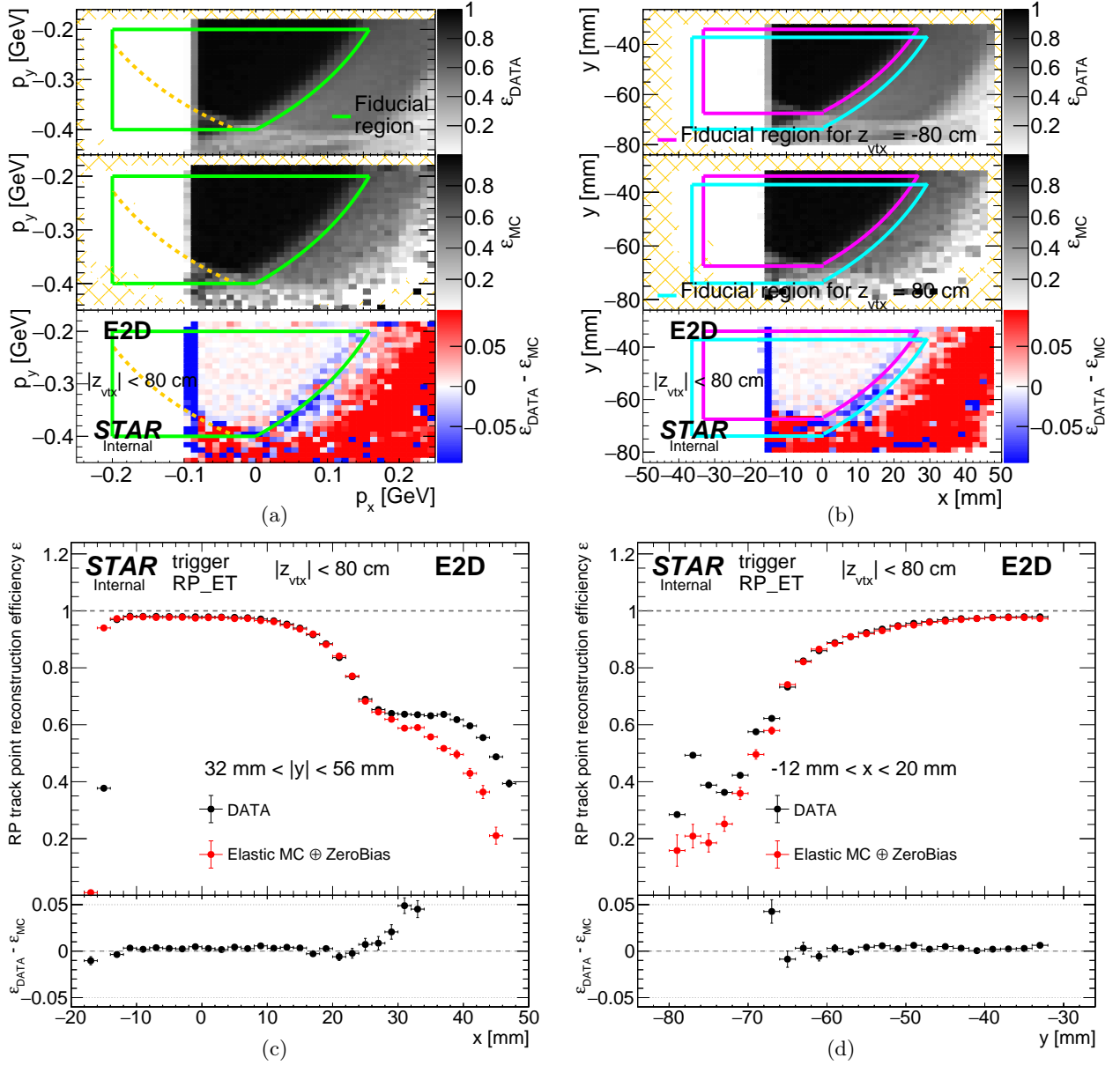


Figure H.8: Sample comparison of RP track point reconstruction efficiency (detector E2D) estimated with the method described in Sec. 10.3.2 as a function of  $(p_x, p_y)$  of proton track (H.8a),  $(x, y)$  position extrapolated from the reference RP (E1D) to the studied RP (H.8b), and comparison of 1-dimensional projections of efficiencies in selected ranges of hit position (given in the plot):  $x$  (H.8c) and  $y$  (H.8d). Lower pad in each subfigure shows the difference between efficiency extracted from the data and elastic scattering MC embedded into zero-bias data. Hatched orange area marks bins without any entries (efficiency incalculable). The fiducial region in  $(x, y)$  plot is represented by two envelopes which correspond to the extreme accepted values of  $z_{vtx}$ .

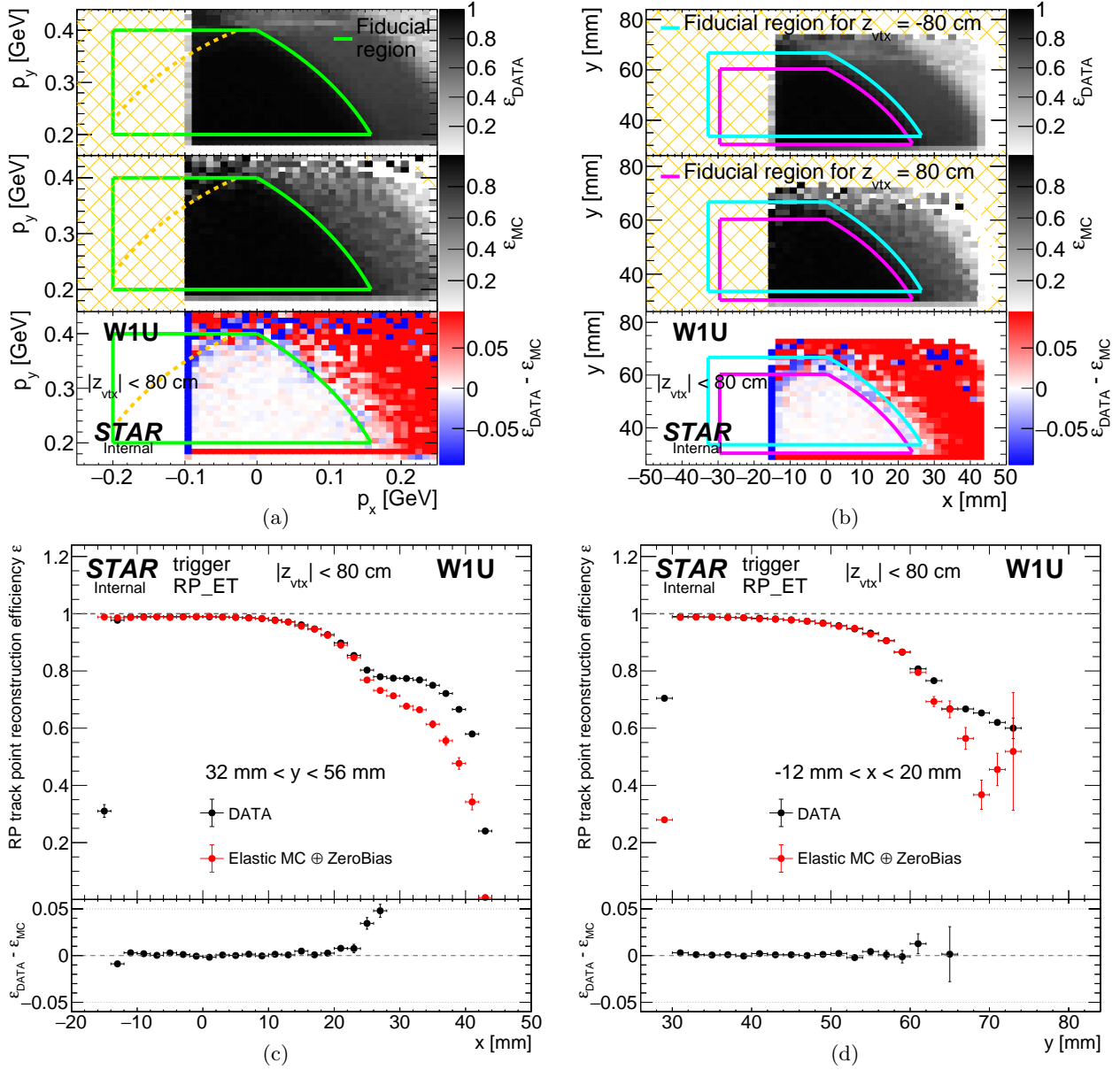


Figure H.9: Sample comparison of RP track point reconstruction efficiency (detector W1U) estimated with the method described in Sec. 10.3.2 as a function of  $(p_x, p_y)$  of proton track (H.9a),  $(x, y)$  position extrapolated from the reference RP (W2U) to the studied RP (H.9b), and comparison of 1-dimensional projections of efficiencies in selected ranges of hit position (given in the plot):  $x$  (H.9c) and  $y$  (H.9d). Lower pad in each subfigure shows the difference between efficiency extracted from the data and elastic scattering MC embedded into zero-bias data. Hatched orange area marks bins without any entries (efficiency incalculable). The fiducial region in  $(x, y)$  plot is represented by two envelopes which correspond to the extreme accepted values of  $|z_{vtx}|$ .

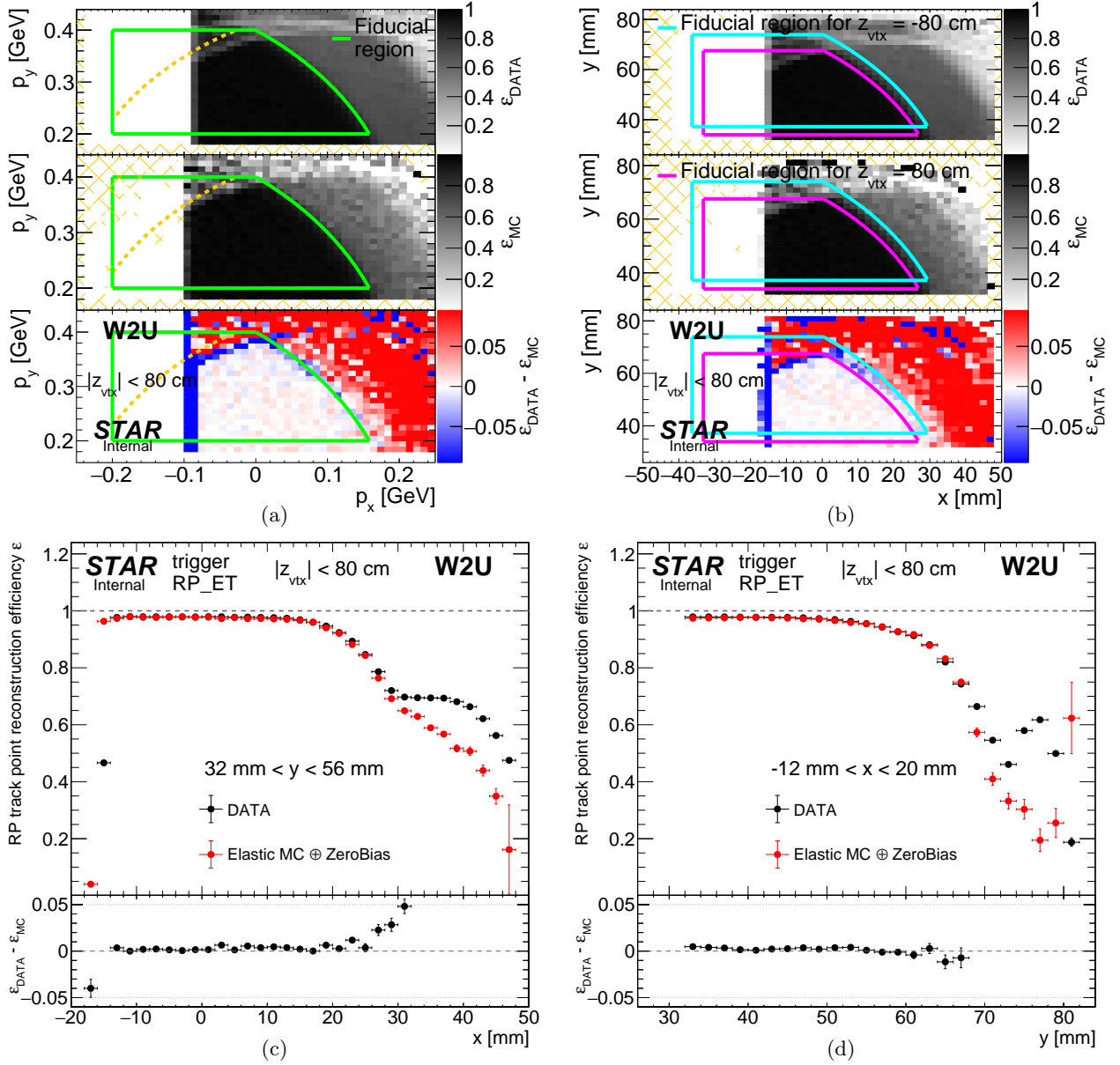


Figure H.10: Sample comparison of RP track point reconstruction efficiency (detector W2U) estimated with the method described in Sec. 10.3.2 as a function of  $(p_x, p_y)$  of proton track (H.10a),  $(x, y)$  position extrapolated from the reference RP (W1U) to the studied RP (H.10b), and comparison of 1-dimensional projections of efficiencies in selected ranges of hit position (given in the plot):  $x$  (H.10c) and  $y$  (H.10d). Lower pad in each subfigure shows the difference between efficiency extracted from the data and elastic scattering MC embedded into zero-bias data. Hatched orange area marks bins without any entries (efficiency incalculable). The fiducial region in  $(x, y)$  plot is represented by two envelopes which correspond to the extreme accepted values of  $z_{\text{vtx}}$ .

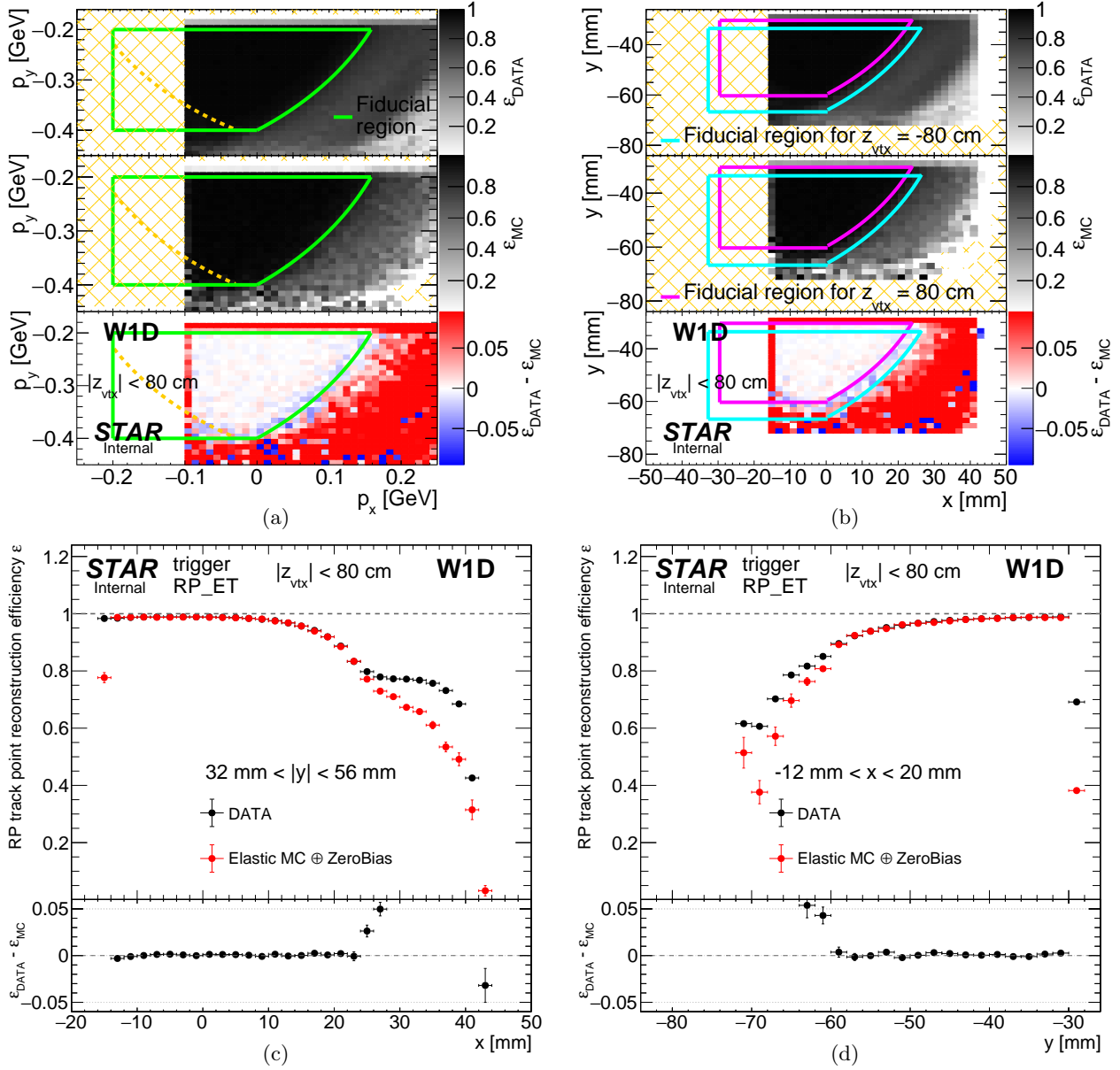


Figure H.11: Sample comparison of RP track point reconstruction efficiency (detector W1D) estimated with the method described in Sec. 10.3.2 as a function of  $(p_x, p_y)$  of proton track (H.11a),  $(x, y)$  position extrapolated from the reference RP (W2D) to the studied RP (H.11b), and comparison of 1-dimensional projections of efficiencies in selected ranges of hit position (given in the plot):  $x$  (H.11c) and  $y$  (H.11d). Lower pad in each subplot shows the difference between efficiency extracted from the data and elastic scattering MC embedded into zero-bias data. Hatched orange area marks bins without any entries (efficiency incalculable). The fiducial region in  $(x, y)$  plot is represented by two envelopes which correspond to the extreme accepted values of  $z_{vtx}$ .

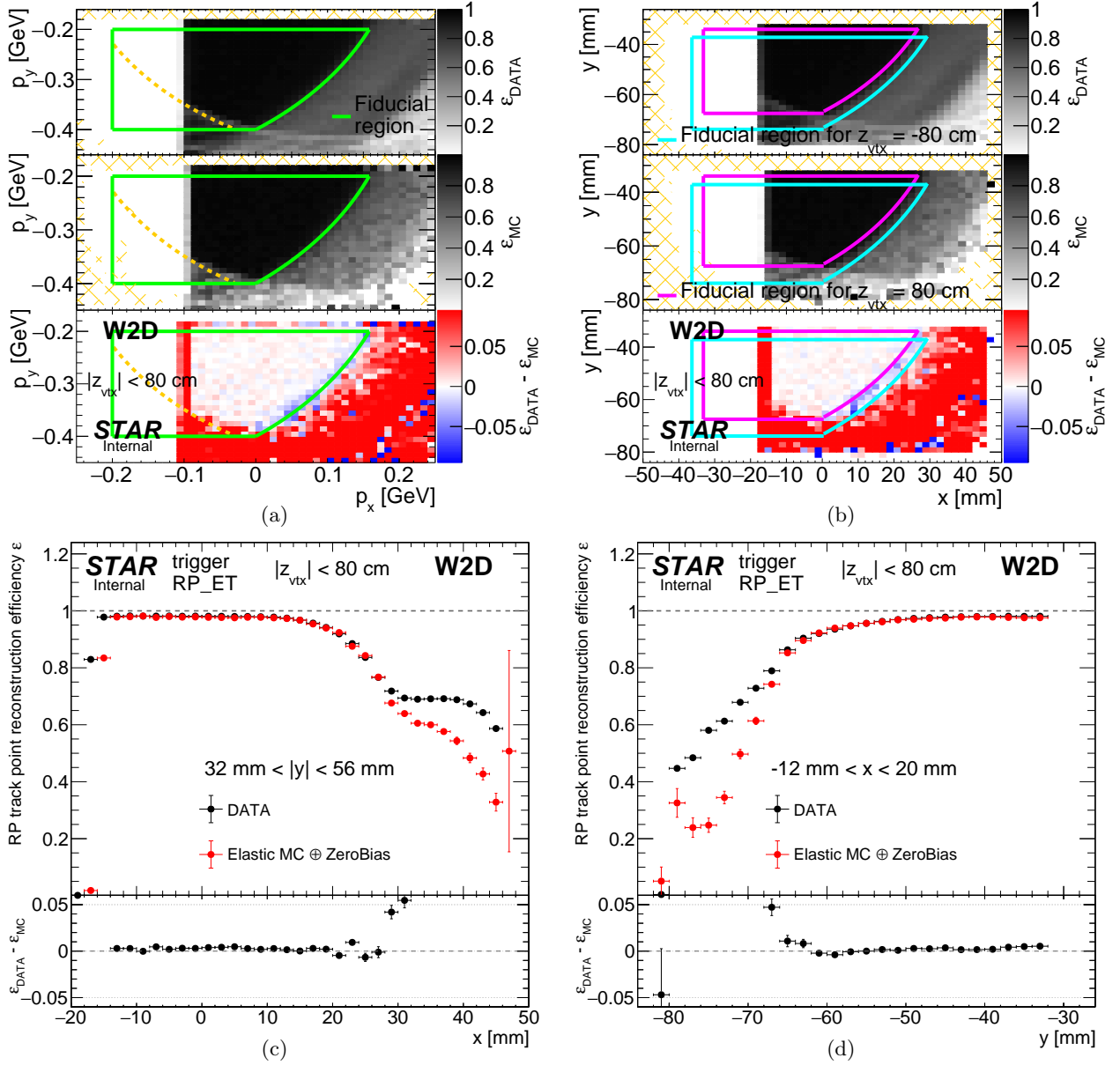


Figure H.12: Sample comparison of RP track point reconstruction efficiency (detector W2D) estimated with the method described in Sec. 10.3.2 as a function of  $(p_x, p_y)$  of proton track (H.12a),  $(x, y)$  position extrapolated from the reference RP (W1D) to the studied RP (H.12b), and comparison of 1-dimensional projections of efficiencies in selected ranges of hit position (given in the plot):  $x$  (H.12c) and  $y$  (H.12d). Lower pad in each subfigure shows the difference between efficiency extracted from the data and elastic scattering MC embedded into zero-bias data. Hatched orange area marks bins without any entries (efficiency incalculable). The fiducial region in  $(x, y)$  plot is represented by two envelopes which correspond to the extreme accepted values of  $z_{vtx}$ .

# List of Figures

1.1	Beam-detector distance of the Roman Pots in run 15.	5
3.1	Number of reconstructed global tracks, satisfying all quality criteria, matched with the same true level primary particle.	8
3.2	$dE/dx$ of the track matched to true level particle.	8
3.3	$\delta^2(\eta, \phi)$ distributions between true level particles and tracks assigned to them.	9
3.4	$\delta^2(\eta, \phi)$ distributions between true level particles and tracks assigned to them.	9
3.5	Distribution of $\delta^2(\eta, \phi)$ in CEP MC.	10
3.6	Number of reconstructed global tracks, satisfying all quality criteria and $\delta^2(\eta, \phi)$ cut, matched with the same true level primary particle.	10
3.7	$dE/dx$ of the closest track matched to true level particle passing the $\delta^2(\eta, \phi)$ cut.	11
3.8	TPC acceptance and reconstruction efficiency as a function of $p_T$ ( $ V_z  < 80$ cm, $ \eta  < 0.7$ ) obtained from two methods.	12
3.9	Density map of global TPC track first point $(\eta, \varphi)$ coordinates for runs with/without dead sector #19.	13
3.10	Sample TPC acceptance and reconstruction efficiency of $\pi^-$ .	13
3.11	Sample plotz of TOF acceptance, reconstruction and matching efficiency of $\pi^-$ .	15
4.1	Sketch of the tag&probe method.	16
4.2	TOF L0 multiplicity distribution for events with multiplicity reconstructed from offline hits $\geq 2$ .	16
4.3	Sample distributions of $p_T^{\text{miss}}$ of the $p + \text{Tag} + \text{Probe} + p$ system in the data and embedded MC.	17
4.4	Efficiencies for reconstruction of the vertex with single TOF-matched TPC track and association with this vertex of TOF-unmatched track.	18
4.5	Tag&Probe TOF efficiency from CEP data compared with the result from embedded CEP MC.	19
4.6	Tag&Probe TOF efficiency from CEP data compared with the result from embedded CEP MC (divided w.r.t. $\eta$ of the probe).	20
5.1	Sample energy loss correction for $K^-$ as a function of reconstructed transverse momentum $p_T^{\text{meas}}$	22
6.1	Schematic representation (top view) of the Roman Pot Phase II* at STAR.	23
6.2	Side view of the Roman Pot Phase II* setup with an illustration of Roman Pot track point and track.	23
6.3	Correlation between the hit position of constituent track point in the first RP station and the local angle of track in elastic scattering events.	24
6.4	View of the Geant4 implementation od the Roman Pot Phase II* detector setup.	26
6.5	Roman Pot vessel (photo).	26
6.6	Silicon Strip Detector packages stored in the protective atmosphere (photo).	26
6.7	Geant4 implementations of the Roman Pot vessel and SSD package with trigger counter.	26
6.8	Sample hit map of elastically scattered protons in the data and MC with extracted envelopes of the DX apertures.	27
7.1	Sample fit to $dE/dx$ spectrum in the data in single momentum bin.	30
7.2	Parameters of reconstructed track $dE/dx$ as a function of reconstructed momentum for a few particle species.	30
7.3	Sample comparison of $dE/dx$ spectrum between data and embedded MC in single momentum bin.	32
7.4	Sample comparison of $n_{\text{pion}}^\sigma$ , $n_{\text{kaon}}^\sigma$ and $n_{\text{proton}}^\sigma$ distribution between data and embedded MC in single momentum bin.	32
8.1	Sketch of helix modification procedure and $d_0$ calculation.	33

8.2	Example of comparison of $d_0$ histograms in the data and embedded MC in the procedure of TPC pointing resolution adjustment. . . . .	34
8.3	Example of $-\chi^2/\text{NDF}$ map in a parameter space in the procedure of TPC pointing resolution adjustment. . . . .	34
8.4	Best-fit parameters obtained in the procedure of the TPC track pointing resolution adjustment. . . . .	34
8.5	Comparison of distribution of pion $d_0$ and components of DCA vector in the data and embedded MC, before and after adjustment of TPC pointing resolution. . . . .	35
9.1	Comparison of primary track multiplicity, $p_T$ and $\eta$ distribution in zero-bias data and embedded MC (minimum-bias). . . . .	36
9.2	Comparison of $d_0^{(0,0)}$ distribution of global TPC tracks matched with TOF in zero-bias data and embedded MC (minimum-bias). . . . .	37
9.3	Invariant mass of two opposite-sign tracks and cosine of the opening angle between tracks forming a secondary vertex. . . . .	38
9.4	Multiplicity of tracks in reconstructed secondary vertices. . . . .	39
9.5	$\eta_{\text{vtx}}$ definition (sketch). . . . .	39
9.6	Comparison of raw $R_{\text{vtx}}^{\text{secondary}}$ and $z_{\text{vtx}}^{\text{secondary}}$ distribution in the data and embedded MC. . . . .	39
9.7	Comparison of DCA between all pairs of secondary track candidates selected for the secondary vertex reconstruction in the data and embedded MC. . . . .	40
9.8	Comparison of radial DCA of all primary tracks matched with TOF and passing quality criteria in events selected for secondary vertex analysis, between the data and embedded MC. . . . .	40
9.9	Comparison of background-subtracted $R_{\text{vtx}}^{\text{secondary}}$ and $z_{\text{vtx}}^{\text{secondary}}$ distribution in the data and embedded MC. . . . .	41
10.1	Number of events in embedded MC as a function of BBC_AND rate. . . . .	42
10.2	$\chi^2/\text{NDF}$ obtained in the search for the best $N_{\text{hits}}^{\text{fit}}$ cut value. . . . .	42
10.3	Sample comparison of TPC track quality cuts efficiency from tag&probe method. . . . .	43
10.4	$\chi^2/\text{NDF}$ obtained in the search for the best $N_{\text{hits}}^{\text{fit}}$ cut value. . . . .	43
10.5	$\pi^\pm$ TPC track reconstruction efficiency as a function of $p_T$ ( $ \eta  < 0.7,  V_z  < 80 \text{ cm}$ ) for embedded MC samples with $\langle \text{BBC\_AND} \rangle = 700 \text{ kHz}$ and $\langle \text{BBC\_AND} \rangle = 1400 \text{ kHz}$ . . . . .	44
10.6	Comparison of the BBC_AND rate in the data and embedded MC for SD and CD. . . . .	45
10.7	The amount of lost $\pi^-$ due to the interaction with dead material in front of TPC as a function of $p_T$ , $\eta$ in sample $z$ -vertex bin in CD and SD . . . . .	46
10.8	The systematic uncertainty to the TPC track reconstruction efficiency due to amount of dead material in front of TPC using MC samples for CD and SD . . . . .	47
10.9	$\pi^\pm$ TOF matching efficiency as a function of $p_T$ ( $ \eta  < 0.7,  V_z  < 80 \text{ cm}$ ) for embedded MC samples with $\langle \text{BBC\_AND} \rangle = 700 \text{ kHz}$ and $\langle \text{BBC\_AND} \rangle = 1400 \text{ kHz}$ . . . . .	48
10.10	The difference $\Delta\epsilon_{\text{TOF}} = \Delta\epsilon_{\text{TOF}}^{1400 \text{ kHz}} - 2 \cdot \Delta\epsilon_{\text{TOF}}^{700 \text{ kHz}}$ for $\pi^\pm$ as a function of $p_T$ and $\eta$ ( $ V_z  < 80 \text{ cm}$ )	49
10.11	Sketch of the track with points in HFT. . . . .	49
10.12	Distribution of $z$ -position of vertices with TPC tracks containing hits in HFT. . . . .	49
10.13	Distribution of $n^\sigma$ (kaon and proton) vs. transverse momentum for tracks containing HFT hits. .	50
10.14	Comparison of the TOF eff. correction from tag&probe method and the difference between TOF eff. calculated using standard method from the HFT-tagged tracks and efficiency from embedded single particle MC. . . . .	51
10.15	Difference between the TOF eff. correction estimated with the HFT-tagged tracks and with tag&probe method. . . . .	51
10.16	Systematic uncertainty of the TOF efficiency related to the TOF simulation accuracy. . . . .	52
10.17	Draft of the method of estimation of the RP track reconstruction efficiency for systematic uncertainty determination. . . . .	52
10.18	Fractional momentum loss $\xi$ of clean proton tracks before and after implying vetoes in the data and MC (branch EU). . . . .	53
10.19	Collinearity of a reference track and track reconstructed in studied branch. . . . .	54
10.20	Coparison of estimated RP track reconstruction efficiency in 2D and 1D (branch EU). . . . .	55
10.21	Draft of the method of estimation of the RP track point reconstruction efficiency for systematic uncertainty determination. . . . .	56
10.22	Difference between measured and extrapolated position of track point in E1U. . . . .	56
10.23	Coparison of estimated RP track point reconstruction efficiency in 2D and 1D (detector E1U). .	57
10.24	Coparison of estimated RP track point reconstruction efficiency in 2D and 1D (detector E2U). .	58
A.1	TPC acceptance and reconstruction efficiency of $\pi^-$ for runs with dead sector #19. . . . .	61

A.2	TPC acceptance and reconstruction efficiency of $\pi^-$ for runs with sector #19 back in operation.	63
A.3	TPC acceptance and reconstruction efficiency of $\pi^+$ for runs with dead sector #19. . . . .	65
A.4	TPC acceptance and reconstruction efficiency of $\pi^+$ for runs with sector #19 back in operation.	67
A.5	TPC acceptance and reconstruction efficiency of $K^-$ for runs with dead sector #19. . . . .	69
A.6	TPC acceptance and reconstruction efficiency of $K^-$ for runs with sector #19 back in operation.	71
A.7	TPC acceptance and reconstruction efficiency of $K^+$ for runs with dead sector #19. . . . .	73
A.8	TPC acceptance and reconstruction efficiency of $K^+$ for runs with sector #19 back in operation.	75
A.9	TPC acceptance and reconstruction efficiency of $\bar{p}$ for runs with dead sector #19. . . . .	77
A.10	TPC acceptance and reconstruction efficiency of $\bar{p}$ for runs with sector #19 back in operation. .	79
A.11	TPC acceptance and reconstruction efficiency of $p$ for runs with dead sector #19. . . . .	81
A.12	TPC acceptance and reconstruction efficiency of $p$ for runs with sector #19 back in operation. .	83
B.1	TOF acceptance, reconstruction and matching efficiency of $\pi^-$ . . . . .	86
B.2	TOF acceptance, reconstruction and matching efficiency of $\pi^+$ . . . . .	88
B.3	TOF acceptance, reconstruction and matching efficiency of $K^-$ . . . . .	90
B.4	TOF acceptance, reconstruction and matching efficiency of $K^+$ . . . . .	92
B.5	TOF acceptance, reconstruction and matching efficiency of $\bar{p}$ . . . . .	94
B.6	TOF acceptance, reconstruction and matching efficiency of $p$ . . . . .	96
C.1	Energy loss correction for $\pi^-$ as a function of reconstructed transverse momentum $p_T^{meas}$ . . . . .	98
C.2	Energy loss correction for $\pi^+$ as a function of reconstructed transverse momentum $p_T^{meas}$ . . . . .	100
C.3	Energy loss correction for $K^-$ as a function of reconstructed transverse momentum $p_T^{meas}$ . . . . .	101
C.4	Energy loss correction for $K^+$ as a function of reconstructed transverse momentum $p_T^{meas}$ . . . . .	102
C.5	Energy loss correction for $\bar{p}$ as a function of reconstructed transverse momentum $p_T^{meas}$ . . . . .	103
C.6	Energy loss correction for $p$ as a function of reconstructed transverse momentum $p_T^{meas}$ . . . . .	104
C.7	Energy loss correction for negative particles as a function of reconstructed transverse momentum $p_T^{meas}$ . . . . .	105
C.8	Energy loss correction for positive particles as a function of reconstructed transverse momentum $p_T^{meas}$ . . . . .	106
C.9	Energy loss correction for $\bar{p}$ as a function of reconstructed global track transverse momentum $p_T^{meas}$ . . . . .	107
C.10	Energy loss correction for $p$ as a function of reconstructed global track transverse momentum $p_T^{meas}$ . . . . .	109
D.1	The DX aperture envelopes fitted with circles before (left) and after (right) the DX offsets introduced in the Geant4 geometry. . . . .	111
E.1	The amount of lost $\pi^-$ due to the interaction with dead material in front of TPC as a function of $p_T$ , $\eta$ and $z$ -vertex in CD and SD . . . . .	113
E.2	The amount of lost $\pi^+$ due to the interaction with dead material in front of TPC as a function of $p_T$ , $\eta$ and $z$ -vertex in CD and SD . . . . .	115
E.3	The amount of lost $K^-$ due to the interaction with dead material in front of TPC as a function of $p_T$ , $\eta$ and $z$ -vertex in CD and SD . . . . .	116
E.4	The amount of lost $K^+$ due to the interaction with dead material in front of TPC as a function of $p_T$ , $\eta$ and $z$ -vertex in CD and SD . . . . .	117
E.5	The amount of lost $\bar{p}$ due to the interaction with dead material in front of TPC as a function of $p_T$ , $\eta$ and $z$ -vertex in CD and SD . . . . .	118
E.6	The amount of lost $p$ due to the interaction with dead material in front of TPC as a function of $p_T$ , $\eta$ and $z$ -vertex in CD and SD . . . . .	119
E.7	The amount of lost negative particles due to the interaction with dead material in front of TPC as a function of $p_T$ , $\eta$ and $z$ -vertex in CD and SD . . . . .	120
E.8	The amount of lost positive particles due to the interaction with dead material in front of TPC as a function of $p_T$ , $\eta$ and $z$ -vertex in CD and SD . . . . .	121
F.1	Fits to dE/dx spectra in the data. . . . .	122
F.2	Comparison of $dE/dx$ spectrum between data and embedded MC in momentum bins. . . . .	125
F.3	Comparison of $n_{\text{pion}}^\sigma$ distribution between data and embedded MC in momentum bins. . . . .	129
F.4	Comparison of $n_{\text{kaon}}^\sigma$ distribution between data and embedded MC in momentum bins. . . . .	134
F.5	Comparison of $n_{\text{proton}}^\sigma$ distribution between data and embedded MC in momentum bins. . . . .	139
G.1	Tag&Probe fits to $p_T^{\text{miss}}$ in bins of probe $p_T$ . . . . .	143

G.2	Tag&Probe fits to $p_T^{\text{miss}}$ in bins of probe $\eta$ . . . . .	143
G.3	Tag&Probe fits to $p_T^{\text{miss}}$ in bins of probe $z_{\text{vtx}}$ . . . . .	144
G.4	Tag&Probe fits to $p_T^{\text{miss}}$ in bins of probe $p_T$ . . . . .	145
G.5	Tag&Probe fits to $p_T^{\text{miss}}$ in bins of probe $p_T$ . . . . .	145
G.6	Tag&Probe fits to $p_T^{\text{miss}}$ in bins of probe $p_T$ . . . . .	146
G.7	Tag&Probe fits to $p_T^{\text{miss}}$ in bins of probe $p_T$ . . . . .	147
H.1	Coparison of estimated RP track reconstruction efficiency in 2D and 1D (branch ED). . . . .	148
H.2	Fractional momentum loss $\xi$ of clean proton tracks before and after implying vetoes in the data and MC (branch ED). . . . .	148
H.3	Coparison of estimated RP track reconstruction efficiency in 2D and 1D (branch WU). . . . .	149
H.4	Fractional momentum loss $\xi$ of clean proton tracks before and after implying vetoes in the data and MC (branch WU). . . . .	149
H.5	Coparison of estimated RP track reconstruction efficiency in 2D and 1D (branch WD). . . . .	150
H.6	Fractional momentum loss $\xi$ of clean proton tracks before and after implying vetoes in the data and MC (branch WD). . . . .	150
H.7	Coparison of estimated RP track point reconstruction efficiency in 2D and 1D (detector E1D). .	151
H.8	Coparison of estimated RP track point reconstruction efficiency in 2D and 1D (detector E2D). .	152
H.9	Coparison of estimated RP track point reconstruction efficiency in 2D and 1D (detector W1U). .	153
H.10	Coparison of estimated RP track point reconstruction efficiency in 2D and 1D (detector W2U). .	154
H.11	Coparison of estimated RP track point reconstruction efficiency in 2D and 1D (detector W1D). .	155
H.12	Coparison of estimated RP track point reconstruction efficiency in 2D and 1D (detector W2D). .	156

# List of Tables

4.1	Parameters of function describing the TOF efficiency as a function of pion track $p_T$ in bins of track $\eta$ . . . . .	21
7.1	Parameters of functions from Fig. 7.2 describing reconstructed track $dE/dx$ as a function of reconstructed momentum for a few particle species. . . . .	31
10.1	Summary of the TPC, TOF and RP efficiency systematic uncertainty. . . . .	59
B.1	Dead TOF modules masked in the MC. . . . .	85

# References

- [1] R. Sikora. <http://>.
- [2] L. Fulek. <http://>.
- [3] <https://online.star.bnl.gov/RunLogRun15/>.
- [4] <https://drupal.star.bnl.gov/STAR/system/files/survey.pdf>.
- [5] [https://drupal.star.bnl.gov/STAR/system/files/pawlik\\_alignment\\_28\\_Oct\\_2015.pdf](https://drupal.star.bnl.gov/STAR/system/files/pawlik_alignment_28_Oct_2015.pdf).
- [6] <https://www.star.bnl.gov/~pawlik/AutoIndex.php?dir=Geometry/pp2pp/>.
- [7] <https://online.star.bnl.gov/rp/pp200/>.
- [8] “Run 15 qa shift report, issue 11003: Sector 19, anodes 1-4 weak.”  
<https://www.star.bnl.gov/devcgi/qa/QAShiftReport/issueEditor.php?iid=11003>.
- [9] T. C. Huang *et al.*, “Muon Identification with Muon Telescope Detector at the STAR Experiment,” *Nucl. Instrum. Meth.* **A833** (2016) 88–93, [arXiv:1601.02910 \[physics.ins-det\]](https://arxiv.org/abs/1601.02910).
- [10] <https://www.star.bnl.gov/HyperNews-star/protected/get/startof/2730.html>.
- [11] **STAR** Collaboration, L. Adamczyk *et al.*, “Single Spin Asymmetry  $A_N$  in Polarized Proton-Proton Elastic Scattering at  $\sqrt{s} = 200$  GeV,” *Phys.Lett.* **B719** (2013) 62–69, [arXiv:1206.1928 \[nucl-ex\]](https://arxiv.org/abs/1206.1928).
- [12] K. Yip and J. Lee, “Analysis Note for the Single Transverse-Spin Asymmetries ( $A_N$ ) in elastic p+p collisions at  $\sqrt{s} = 200$  GeV.” Unpublished, February, 2012.
- [13] R. Sikora, “Study of elastic proton-proton scattering with the STAR detector at RHIC,” Master’s thesis, AGH-UST, Cracow, 2014-06-20. <https://drupal.star.bnl.gov/STAR/theses/masters/rafalsikora>.
- [14] R. Sikora, “Momentum reconstruction with the Roman Pot Phase II\* subsystem.”  
[https://drupal.star.bnl.gov/STAR/system/files/MomentumReconstruction\\_1.pdf](https://drupal.star.bnl.gov/STAR/system/files/MomentumReconstruction_1.pdf), August, 2015.
- [15] R. Sikora, “Naming convention and layout of the Roman Pot Phase II\* subsystem in the STAR experiment.” [https://drupal.star.bnl.gov/STAR/system/files/RomanPotNomenclature\\_0.pdf](https://drupal.star.bnl.gov/STAR/system/files/RomanPotNomenclature_0.pdf), October, 2014.
- [16] R. Sikora, “Description of Roman Pot data structure in StEvent.”  
[https://drupal.star.bnl.gov/STAR/system/files/RomanPotsInStEvent\\_0.pdf](https://drupal.star.bnl.gov/STAR/system/files/RomanPotsInStEvent_0.pdf), November, 2015.
- [17] R. Sikora, “Track reconstruction algorithm update.”  
[https://drupal.star.bnl.gov/STAR/system/files/Rafal\\_pp2pp-UPC\\_210October2015.pdf](https://drupal.star.bnl.gov/STAR/system/files/Rafal_pp2pp-UPC_210October2015.pdf), October, 2015.
- [18] <https://drupal.star.bnl.gov/STAR/subsys/romanpot/software/stmurusutil-roman-pot-data-analysis-utilities-afterburner>.
- [19] [https://drupal.star.bnl.gov/STAR/system/files/userfiles/265/TotalElastic200GeVAnalysisNote\(6\).pdf](https://drupal.star.bnl.gov/STAR/system/files/userfiles/265/TotalElastic200GeVAnalysisNote(6).pdf).
- [20] [https://drupal.star.bnl.gov/STAR/system/files/Rafal\\_AlignmentBiweekly\\_4March2016.pdf](https://drupal.star.bnl.gov/STAR/system/files/Rafal_AlignmentBiweekly_4March2016.pdf).
- [21] [https://www.star.bnl.gov/~pawlik/AutoIndex.php?dir=Geometry/pp2pp/README/&file=IP\\_and\\_MPT\\_positions.pdf](https://www.star.bnl.gov/~pawlik/AutoIndex.php?dir=Geometry/pp2pp/README/&file=IP_and_MPT_positions.pdf).

- [22] L. Fulek, “Geant4 simulation status.”  
[https://drupal.star.bnl.gov/STAR/system/files/fulek\\_January\\_20\\_2016.pdf](https://drupal.star.bnl.gov/STAR/system/files/fulek_January_20_2016.pdf), January, 2016.
- [23] R. Sikora, “Elastic proton-proton scattering in the STAR experiment at RHIC,” 2013.  
<https://misio.fis.agh.edu.pl/media/misiofiles/ff1d4d716fb2efde2d2e2e931070473b.pdf>.
- [24] L. Fulek, “Transport of particles through RHIC magnet lattice,” 2013.  
<https://misio.fis.agh.edu.pl/media/misiofiles/15450addc55712ecdb681873692cde5e.pdf>.
- [25] L. Fulek, “Study of proton-proton scattering with the diffractive dissociation of one of the protons in the STAR detector at RHIC collider,” Master’s thesis, AGH-UST, Cracow, 2014-06-18.  
<https://drupal.star.bnl.gov/STAR/theses/masters/rafalsikora>.
- [26] [https://drupal.star.bnl.gov/STAR/system/files/LFS\\_UPC\\_Geant4SimulationOfRomanPots\\_170October2016.pdf](https://drupal.star.bnl.gov/STAR/system/files/LFS_UPC_Geant4SimulationOfRomanPots_170October2016.pdf).
- [27] <https://www.star.bnl.gov/rt3/SelfService/Display.html?id=3272>.
- [28] S. Das, “A simple alternative to the Crystal Ball function,” arXiv:1603.08591 [hep-ex].
- [29] <https://www.star.bnl.gov/rt3/SelfService/Display.html?id=3332>.